N° d'ordre : 677

Année 1998

THÈSE

préeentée à

L'U.F.R. DES SCIENCES ET TECHNIQUES
DE L'UNIVERSITÉ DE FRANCHE-COMTÉ

en cotutelle avec

L'UNIVERSITE DE NEUCHATEL (SUISSE)

pour obtenir le

GRADE DE DOCTEUR DE L'UNIVERSITÉ DE FRANCHE-COMTÉ
Spécialité Sciences pour l'Ingénieur

MULTI-AXIAL SILICON BULK-MICROMACHINED ACCELEROMETERS WITH CAPACITIVE OR OPTICAL READ-OUT

par

Gerold Schröpfer

Soutenue le 14 Décembre 1998 devant la Commission d'Examen :

Président	D. HAUDEN	Professeur à l'ENSMM, Besançon
Rapporteurs	ESTEVE Daniel,	Directeur de Recherche au CNRS - LAAS, *Toulouse*
	RENAUD Philippe,	Professeur à l'EPFL, Lausanne
Examinateurs	DE LABACHELERIE Michel,	Directeur de Recherche au CNRS-LPMO, Besançon
	DE ROOIJ Nico,	Professeur à l'Université de Neuchâtel
	DUSSURGEY Charles,	Chef du Départ. Technique/Capteurs, Sextant Avionique, Valence

MULTI-AXIAL SILICON BULK-MICROMACHINED ACCELEROMETERS WITH CAPACITIVE OR OPTICAL READ-OUT

Everything should be made as simple as possible,
but not simpler.

Albert Einstein

Contents

1. Introduction 1

1.1 Basics on accelerometers 2
1.1.1 Definitions 2
1.1.2 Different configurations for suspended seismic masses 3
1.1.3 Additional features 4
1.2 Short overview of micromachining technologies 4
1.2.1 Overview of present micromachining technologies 5
1.2.2 Comparison between technologies for accelerometer applications 7
1.3 Short overview of read-out principles employed in accelerometers 8
1.3.1 Piezoresistive, capacitive and optical read-out 8
1.3.2 Other read-out principles 10
1.4 Recently developed multi-axial micromachined accelerometers 11
1.5 Applications of multi-axial accelerometers 17
1.6 Background and outline of the thesis 18
1.6.1 The PICS-Project: Research for the limits in microtechnology 18
1.6.2 Outline of the thesis 20

2. Design and modeling of mechanical accelerometer structures 21

2.1 Introduction 22
2.2 Different designs for a suspended seismic mass 23
2.2.1 In-plane structures 23
2.2.2 Out-of-plane structures 24
2.2.3 In- and out-of-plane structures 25
2.3 Analytical modeling 26
2.3.1 Equation of motion 26
2.3.2 Considerations about spring stiffness 27
2.3.4 Static modeling 28
2.3.5 Considerations about damping 29
2.3.6 Dynamic modeling 31

2.4	**Finite element simulation**	**33**
	2.4.1 Static analysis	34
	2.4.2 Modal analysis	37
2.5	**Comparison between theory and experiments for static displacements**	**38**
	2.5.1 Static measurements for in-plane structures	39
	2.5.2 Static measurements for out-of-plane structures	40
2.6	**Comparison of different designs**	**41**
2.7	**Mechanical-thermal noise**	**42**
2.8	**Conclusion of chapter 2**	**43**

3.	**Unconventional bulk-micromachining using underetching of (100) silicon**	**45**
3.1	**General aspects of anisotropic wet-etching of silicon**	**46**
3.2	**Fabrication of in-plane accelerometer-structures**	**48**
	3.2.1 Principle: underetching of {100} silicon planes	48
	3.2.2 Experimental results	50
	3.2.3 Design rules for the photolithography mask	52
3.3	**Etching simulation and limitations for in-plane structures**	**54**
	3.3.1 Simulation of the anisotropic etching	55
	3.3.2 Limitations in mechanical performance due to etching inaccuracy	59
3.4	**Fabrication of a monolithic tri-axial seismic mass system**	**60**
	3.4.1 Fabrication principle: two step anisotropic wet etching	60
	3.4.2 Discussion of maskless-etching	61
	3.4.3 Experimental results	62
	3.4.4 Overload protection	64
3.5	**Some other micromachined structures**	**65**
	3.5.1 Micromirror	65
	3.5.2 3D gyroscope	66
	3.5.3 Multi-axial accelerometer with a single seismic mass	67
	3.5.4 Seismic mass structure with octagonal shaped or double suspension beams	68
3.6	**Conclusion of chapter 3**	**69**

4. Multi-axial capacitive accelerometers 71

4.1 Introduction 72
4.2 Principles 73
4.2.1 Definition of capacitance 73
4.2.2 Simplified field approximation 73
4.2.3 Lateral capacitive transducer 74
4.2.4 Vertical capacitive transducer 75
4.2.5 Differential sensing 75
4.2.6 Capacitive transducer as actuator for closed-loop operation 76
4.3 Modeling of the capacitive transducer 77
4.3.1 Definition of capacitive sensitivity 77
4.3.2 Analytical modeling 77
4.3.3 Finite element simulation 80
4.3.4 Investigations concerning the capacitive sensitivity 85
4.3.5 Global simulation 86
4.3.6 Electrostatic force analysis 89
4.4 Fabrication process of the capacitive accelerometers 91
4.4.1 Silicon process for the accelerometer using thin film electrodes 91
4.4.2 Silicon process for the accelerometer using etched electrodes 93
4.4.3 Glass wafer processing 95
4.4.4 Anodic bonding 99
4.4.5 Mounting and connecting 101
4.5 Capacitive measurement circuits 102
4.5.1 Capacitive AC bridge circuits 102
4.5.2 Charge/discharge circuits 103
4.5.3 Sigma-delta modulation 104
4.5.4 Noise of capacitive detection 106
4.6 Characterization and limitations of the capacitive accelerometers 107
4.6.1 Employed evaluation methods 107
4.6.2 Measurements of the in-plane accelerometers 108
4.6.3 Measurements of the out-of-plane accelerometers 111
4.6.4 Possible optimizations of the capactive accelerometer 113
4.7 Conclusion of chapter 4 114

5. Multi-axial optical accelerometers 117

5.1 Introduction 118

5.2 Fabrication concepts for opto-mechanical sensors 119

5.2.1 Fabrication technologies 119

5.2.2 Different concepts for a fiber-optic interrogation 119

5.3 Principles 121

5.3.1 General detection principle using a Fabry-Perot cavity 121

5.3.2 Remote read-out based on coherence modulation 122

5.3.3 Optical multiplexing of several sensors 123

5.4 Modeling of the optical accelerometer 125

5.4.1 Mechanical structures for optical detection 125

5.4.2 Optical transmission function of the accelerometer 126

5.4.3 Coherence modulation and multiplexing 127

5.5 Fabrication process of the optical accelerometer 130

5.5.1 Fabrication of mechanical elements and silicon-fiber-sandwich 130

5.5.2 Assembling of the the opto-mechanical sensor 131

5.6 Experimental characterization 132

5.6.1 Measurements with spectrum analyzer 132

5.6.2 Measurement set-up using coherence modulation 134

5.6.3 Measurements using coherence modulation 135

5.6.4 Multi-axial and multiplexed measurements 136

5.7 Noise and optimized performance 139

5.7.1 Noise sources in the optical detection system 139

5.7.2 Optimized performance and limitations of the optical accelerometers 140

5.8 Conclusion of chapter 5 143

6. Conclusions and further work 145

6.1 Comparison between the capacitive and the optical accelerometers 146

6.2 Suggestions for further work 148

6.3 General Conclusions 149

7. Summary (in English) 151

8. Résumé (en français) 157

9. Remerciements 163

10. References 165

11. List of publications 177

CHAPTER 1

1. **Introduction**

1.1 **Basics on accelerometers**

1.2 **Short overview of micromachining technologies**

1.3 **Short overview of read-out principles employed in accelerometers**

1.4 **Recently developed multi-axial micromachined accelerometers**

1.5 **Applications of multi-axial accelerometers**

1.6 **Background and outline of the thesis**

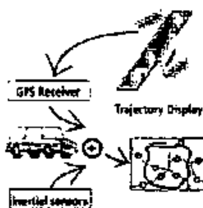

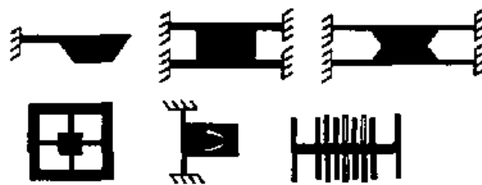

F=ma

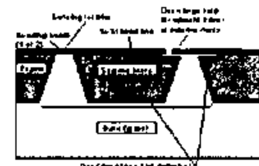

1. Introduction

1.1 Basics on accelerometers

1.1.1 Definitions

Accelerometers are devices which convert acceleration into an electrical signal. Since about two decades, micromachined or solid-state accelerometers have been used. All these devices measure acceleration based on Newton's second law of motion, which claims that acceleration results in a force F acting on a mass m:

$$\vec{F} = m \cdot \vec{a} \qquad (1.1).$$

Most times accelerometers consist of a seismic mass suspended by one ore more springs. The force applied to this suspended mass results in a displacement. Thus the displacement is directly related to acceleration. In addition, because the springs are elongated or shortened, depending on the direction of acceleration, stress arises in the springs. Therefore, acceleration can be determined by measuring the stress in the springs. Both methods, displacement and stress measurement, are used in present devices to detect the applied acceleration. The corresponding read-out principles, which convert these displacements or stresses into an electrical signal are piezoresistive, electrostatic, optical and other methods . They are shortly presented in section 1.3. Table 1.1 gives the definitions of some important terms concerning accelerometers.

Acceleration	Change in velocity per unit time.
Sensitive axis (or direction)	The direction in which the accelerometer is designed to respond.
Sensitivity	Change in output per unit g (1g=9.81ms^{-2}) of acceleration, often specified in mV/g. Mechanical sensitivity is defined as the displacement per unit g, specified in µm/g.
Cross(-axis) or transverse sensitivity	The response to acceleration in axes other than the sensitive axis. Often expressed in percentage of the main sensitivity.
Measurement or full scale range	Maximum acceleration which can be measured by the accelerometer. Expressed in g. Usually the range is bipolar, e.g. ±10g.
Bandwidth	The accelerometer output frequency range.

Table 1.1: Overview of some accelerometer expressions [Gal86, Mot97].

1.1.2 Different configurations for suspended seismic masses

Most designed accelerometers should only be sensitive to accelerations in one direction and should reject components of the acceleration vector in the other two directions. These devices are called single- or uni-axial accelerometers. One can divide uni-axial accelerometers in two categories. Firstly, out-of-plane devices where the seismic mass moves perpendicularly to the wafer-plane. Secondly, lateral accelerometers, where the seismic mass movement is parallel to the wafer surface [Del96].
There have been many different configurations presented for the arrangement of seismic mass and suspension beams. In the following the classical designs for micromachined accelerometers are listed:

- *Cantilever type*: the seismic mass is suspended from one side with one or more beams. This construction offers a high mechanical sensitivity. The center of the proof mass moves on an arc under acceleration. Unfortunately, this suspension type often results in high cross-axis sensitivities [Roy79, Pet82, Che82, Che84, Tsu87, Kan87, Bar88, Ger90, Rud90, Suz90, Hir91, Hua95, Pue98, Pla98].
- *Bridge type*: the mass is suspended with beams from at least two opposite sides. The mass moves in direction parallel to the sensitive axis [San87, Ter88, Pue88, All89, Cha90, All90, Tsc91, Yun92, Cra93].
- *Highly symmetrical type:* the mass is suspended at the upper and lower side symmetrically. Due to the large number of beams the deflection is relatively small. However, these structures offer very low cross-sensitivities [Hen90, Sch90, Sei90, Mat93, vKa95].
- *Surrounding mass-type:* mass is suspended to a frame at the inside of the mass. The effective mass is larger than for the other types and therefore this type offers a high sensitivity. But it shows also high cross-axis sensitivities [Yam90, Tak96, Tak97].
- *Mass suspended by torsion bars:* acceleration in the vertical direction results in a rotation of the mass around the suspension beams. Like the cantilever type, this design shows a high mechanical sensitivity [Rud83, Box90].
- *H-shaped or comb drive mass-beam structure.* this type is most used for surface-micromachined devices. The mass is shaped like an 'H'. A series of fingers originates from the central movable mass, each finger acting as one plate of a variable parallel-plate capacitor. The counter-electrodes are also comb-shaped and fixed on the substrate [Cha96, Off95, Lem97].

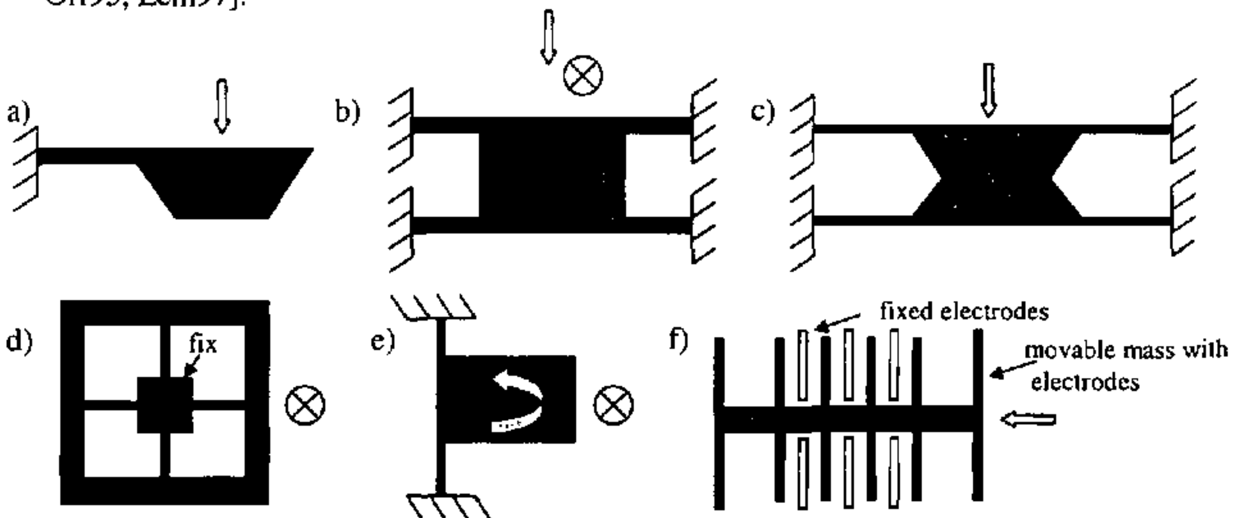

Figure 1.1: Different configurations for seismic mass suspension: a) cantilever type, b) bridge type, c) symmetrical type, d) surrounding mass, e) torsion bar, f) comb drive.

1.1.3 Additional features

Force balancing

The force balancing method consists in applying a counter force in the direction opposite to the inertial force, in order to compensate acceleration. The seismic mass remains in its initial equilibrium position and the force required to maintain equilibrium is a measure for the applied acceleration. To apply such a balancing force, the integration of an actuator is needed. The most used principle is the electrostatic actuation in connection with a capacitive read-out [vKa95, Lem97, Cha96]. In this case the same electrodes can be used for sensing and actuating. Other possibilities to apply an external force to the seismic mass are electromagnetic [Abb94] or thermal [SA30], methods by using coils or resistors, respectively. The main advantages of force balancing are a wider bandwidth of the device and a linear output by feedback of the sensor response. Also, the force balancing system can protect the accelerometer from shocks. However, the drawbacks of this method are the need of a complex electronic circuit and the increased power consumption, which depends on the actuation and detection principle.

In general, two different approaches for force balancing are possible. Firstly, excitation and feedback signals are continuously applied to the sensor and are separated in the frequency domain. Or secondly, sensing and feedback do not occur at the same time, meaning separation in the time domain.

Self test

The above presented force balancing method can also be used to self test or self calibration of the device [Pla98]. This means that a known force is applied to the seismic mass to verify if the accelerometer is still working. In addition to this self test feature, the same method can be eventually employed to calibrate the device. In each case an actuator has to be incorporated in the structure.

Overload protection

In order to protect the accelerometer from shocks which could damage or break the seismic mass structure, an overload protection should be incorporated in the sensor structure. As described above, an external force can be applied to compensate high forces. Another principle is the integration of overrange stoppers in the mechanical design, which prevent large deflections of the seismic mass. Such overrange stoppers can be realized at the same time as the seismic mass, or in an additional step before or after the fabrication of the mass.

1.2 Short overview of micromachining technologies

There are several technologies available for manufacturing solid-state accelerometers. The most common techniques are bulk- and surface-mircomachining of silicon. These techniques are derived from the IC industry and include photolithography, wafer doping, oxidation, thin film deposition, wet and dry etching and specially the possibility of batch processing. Batch processing means the fabrication of identical devices in parallel, most times hundreds or thousands of chips on one silicon wafer, and is one essential key to open the door to low cost

production. Further, there are the HARMST techniques (High-Aspect-Ratio MicroSysTems) with the LIGA-technique at its most known representative.
All these technologies are briefly described in this subsection. To conclude, these fabrication technologies are compared regarding advantages and disadvantages for micromachining of accelerometers.

1.2.1 Overview of present micromachining technologies

Bulk-micromachining
When using bulk-micromachining techniques, structures are formed by etching through the complete wafer. In the case of accelerometers these structures are seismic masses and spring suspensions. Perforating the wafer can be achieved by single or double-sided etching. Consequently the masses available for the acceleration-to-displacement conversion are relatively large (larger than milligram), which enables very sensitive devices to be fabricated. The most popular technique for bulk-micromachining is anisotropic wet etching and has been used for silicon micromachining for over two decades [Lee69, Roy79]. Here, anisotropy means that the shape of the achieved structures depends on the crystal orientation. Typically the suspension beams of wet etched accelerometers are horizontally located leading to an out-of-plane motion of the seismic mass. Horizontally and vertically located beams can be fabricated by wet etching of either (100) or (110) oriented wafers.

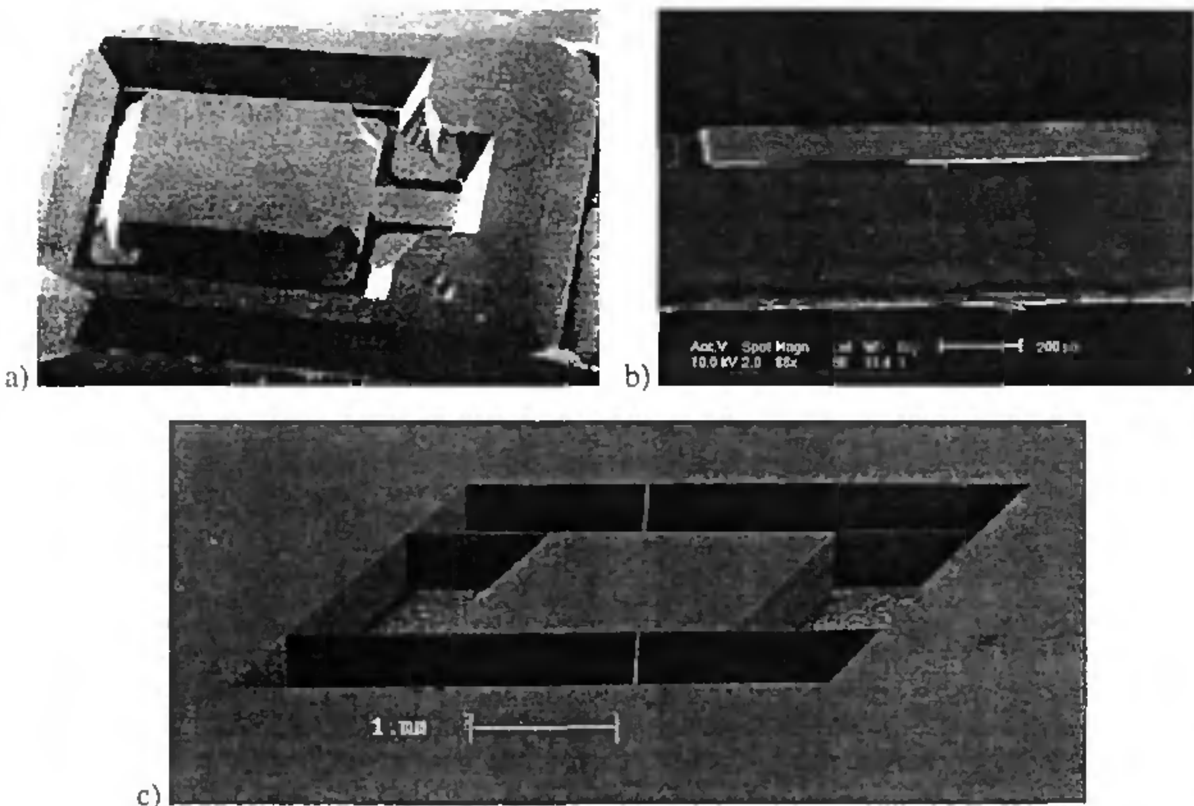

Figure 1.2: Examples of bulk-micromachined accelerometers: a) a device with a pyramid-shaped mass suspended by a cantilever fabricated in (100) silicon [Roy79]; b) a device fabricated by deep plasma etching (courtesy of Yannick Ansel); c) an in-plane accelerometer etched out of (110) silicon (courtesy of Torben Storgaard-Larsen [Sto96]).

Recently, many devices fabricated by deep plasma etching have been presented [Kla95, Del96, Li95, Mc95, Cle98]. With this technique the design becomes independent of the crystal orientation, which offers liberty in designing and optimizing micromachined devices. Unfortunately, machines enabling deep plasma etching in silicon are some orders of magnitude more expensive than a typical bench for wet etching. Apart from silicon, quartz can be bulk-micromachined. In that way well-known resonators in watches as well as accelerometers can be fabricated by wet etching [Del87].

Surface-micromachining

Using surface-micromachining, selective etching of sacrificial layers forms the masses and spring suspensions, which have a thickness of typically several microns and mostly consist of polysilicon. As a result the seismic masses are rather small (lower than one microgram) compared to bulk-micromachined devices. The motion of the seismic mass is usually in wafer-plane.

This technology requires more sophisticated processing techniques but enables on-chip electronics. Thanks to the integrated electronics the small sensor signals can be detected without perturbations.

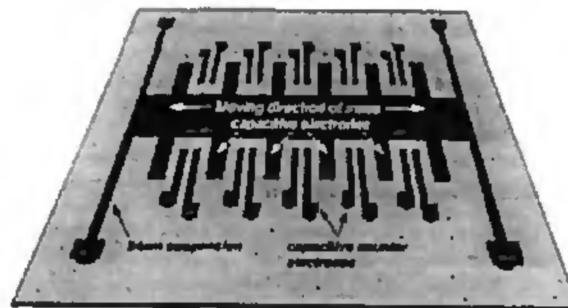

Figure 1.3: A surface-micromachined polysilicon accelerometer with comp-shaped electrodes for displacement sensing [Cha96].

HARMST techniques

HARMST means High -Aspect-Ratio MicroSysTems. The most known HARMST technique is LIGA (Lithographie Galvanoformung Abformung). The LIGA technique uses X-ray lithography to expose a thick resist layer deposited on a metal substrate. By subsequent electroplating, a metallic layer is grown in the resist mold. By this technique, a metallic mass and beam suspension can be fabricated with high aspect ratios (ratio between beam height and beam width). The movement of the mass is generally in wafer-plane. Also, UV lithography can be used (entitled "poor man's LIGA") resulting in structures with a lower aspect ratio.

Another recently developed technique is the fabrication of HARMST-devices by using a thick photoresist (Epson SU-8) to form the mould for electroplating [Lor96]. Using this process 300μm thick mechanical structures have been fabricated.

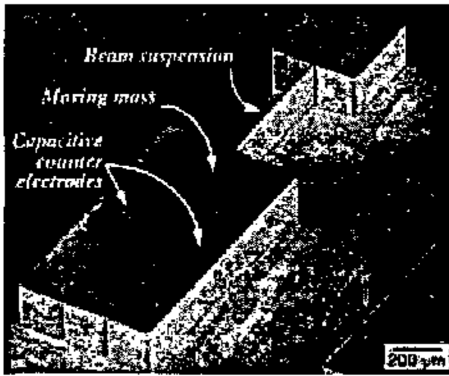

Figure 1.4: An accelerometer consisting of a seismic mass, one suspension beam and two counter electrodes for capacitive sensing fabricated in a LIGA process [Bur91].

1.2.2 Comparison between technologies regarding for accelerometer applications

Sensors built out of single crystal silicon show very low mechanical losses, good long-term stability, high elasticity and no hysteresis due to residual stresses. These good features are all due to the purity and high quality of single crystal silicon as a mechanical material. In structures fabricated by LIGA the mechanical material is electroplated Nickel or Copper, which do not have such excellent material properties as single crystal silicon. For example, residual stresses have been observed in electroformed metallic devices [Bal97]. Also polysilicon, used in surface micromachined devices, show less promising material properties. In general surface-miromachined devices are smaller than their bulk-micromachined counter parts.

property (general)	bulk-micromachining	surface-micromachining
process complexity	0	0/+
lateral dimensions	3-10 mm	100-500 µm
vertical dimensions	100-500 µm	0.5-2 µm
mechanical quality	++	0/+

Table 1.2: A general comparison between bulk- and surface-micromachining, partly taken from [Fre97].

Accelerometers fabricated by surface-micromachining have a some orders of magnitude lower seismic mass, which leads to a higher mechanical-thermal noise. The phenomenon of mechanical-thermal noise will be discussed more in detail in section 2.7. In the case of capacitive read-out, bulk-micromachined accelerometers have due to their size, larger electrodes leading to a higher capacitive sensitivity.

property (accelerometers)	bulk-micromachining	surface-micromachining
seismic mass	++	0
capacitivity	++	-
chip size	-	++

Table 1.3: A comparison between bulk- and surface-micromachining regarding accelerometer application, partly taken from [Fre97].

The problem of low cost is difficult to discuss and there is no general answer to which technology delivers the cheapest devices. Surface-micromachined devices with integrated electronics have the potential for low cost in case of a high volume fabrication. However other factors, especially packaging, often play an important role. For example, the most successful accelerometer in Europe for air-bag systems (1996 market share of 75%) was a piezoresistive accelerometer. For this device the seismic mass was mounted after micromachining of silicon. The read-out electronic was incorporated in a second chip (two-chip solution) [Ohl96], [SA20].

1.3 Short overview of read-out principles employed in accelerometers

1.3.1 Piezoresistive, capacitive and optical read-out

Piezoresistive read-out

For this detection method piezoresistors are placed on the suspension beams of the seismic mass. The strain sensing piezoresistors are placed at points of maximum stress during deflection of the mass. Generally, the piezoresistors are diffused into the beams, which makes the manufacturing simple and cheap. The piezoresistors are arranged in a half- or full-bridge configuration, which makes the electronic interface simple. Consequently this technique was mainly used for earlier devices [Roy79] and for low-cost applications they are still very attractive [SA20]. However there are some disadvantages, like a low output level (typically 10-100mV full-scale output) and relatively large temperature drift. Self-test features and closed-loop operation are only possible with increased complexity due the requirement of an additional actuation function (electrostatic or thermal).

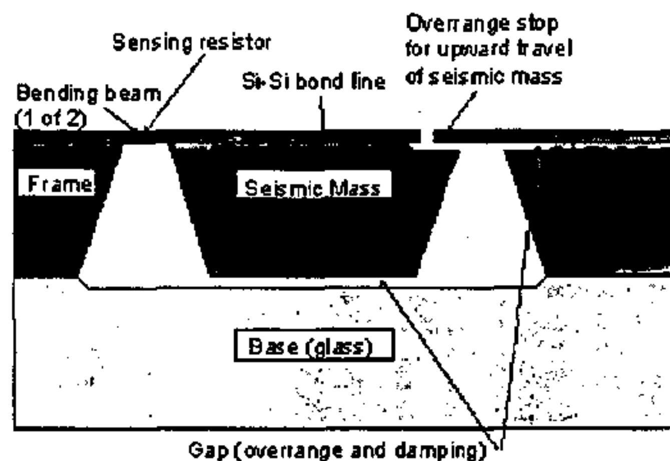

Figure 1.5: Piezoresistive accelerometer with integrated air damping and overrange protection demonstrated by [Bar88].

Capacitive read-out

If capacitive read-out is used for accelerometers, the sensing element typically comprises a moving seismic mass embedded between two fixed electrodes. The differential change in

capacitance between the capacitors is proportional to the displacement of the seismic mass from the center position. This method has a number of advantages, such as good linearity, high output levels and very low temperature drift. Furthermore, it can be used in force balancing for closed loop operation and self-testing without changing the sensor design. However, the electronics to measure the capacitive changes down to fF or even aF makes the signal processing complex in order to get rid of parasitic capacitances and electromagnetic interferences.

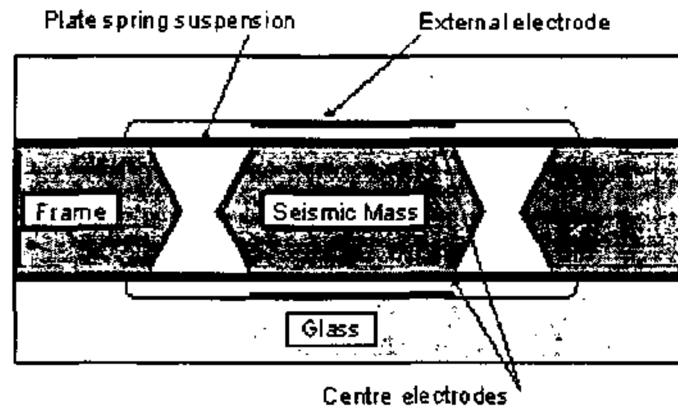

Figure 1.6: Capacitive accelerometer with symmetrical suspension and high resolution presented by [Sei90].

Optical read-out

There exist a number of different optical detection methods. Principally, one can divide them in intensity modulation and interferometric techniques. Light can be sent either through optical fibers or through a waveguide integrated into the substrate.

Figure 1.7 below illustrates an optical version of an intensity-modulated accelerometer. Due to the movement of the seismic mass, the amount of light coupled between two waveguides will change. The transmitted optical power becomes a function of the deflection of the seismic mass.

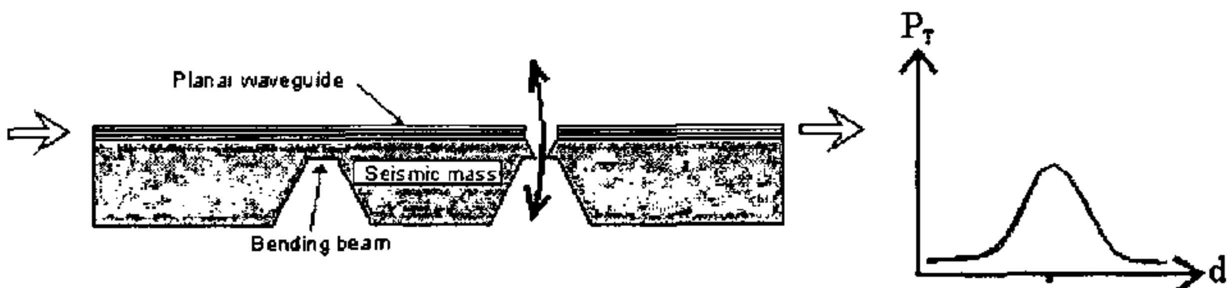

Figure 1.7: Accelerometer principle with optical interrogation based on intensity modulation (drawing courtesy of Torben Storgaard-Larsen).

Interferometric methods allow a very high resolution. As an example, figure 1.8 shows an accelerometer based on a Fabry-Perot interferometer. The Interferometer consists of two mirrors forming a Fabry-Perot cavity. The spectrum the reflected light becomes a function of the distance between the two mirrors, which changes due to accelerations.

Another optical accelerometer technique was developed by Torben Storgaard-Larsen, where the strain in the suspension system of the seismic mass is detected by a Bragg grating [Sto96]. In general, optical read-out techniques have the advantage that there are insensitive to electromagnetic interference.

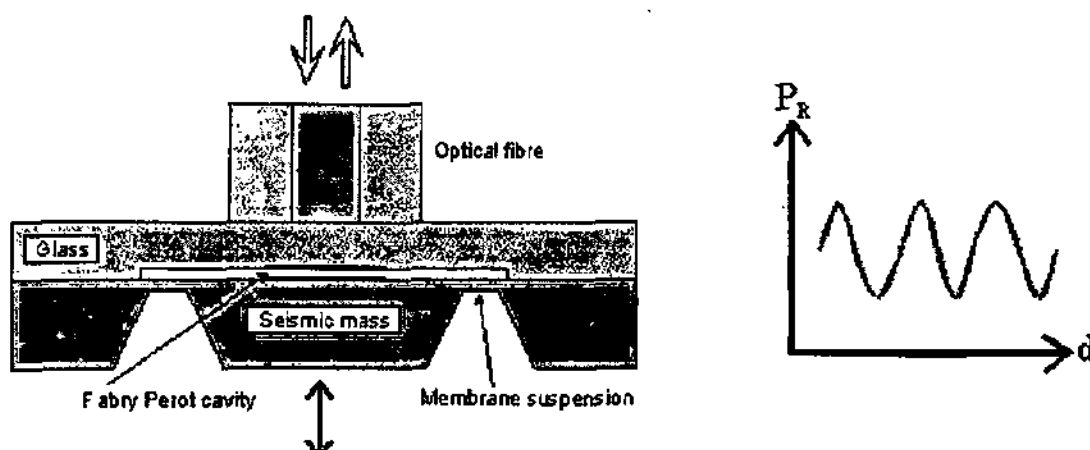

Figure 1.8: Principle of an optical accelerometer based on Fabry-Perot cavity (drawing courtesy of Torben Storgaard-Larsen).

1.3.2 Other read-out principles

Electron tunneling effect

Apart from the three above described categories there exist many other principles to detect the movement of the seismic masses. One of the most recent ones exploits *the electron tunneling effect* [Har98, Roc96]. The magnitude of the tunnel current between the seismic mass and a probe varies with the distance between them. With this method a very high resolution in the sub-μg range can be achieved. However, the electronic processing is complex and closed-loop operation can only be achieved with additional electrodes.

Piezoelectricity

Piezoelectric sensing is one of the most matures techniques employed in accelerometer design. Already used in quartz devices some decades ago, today piezoelectric layer can be deposited on the silicon suspension beams. These sensors have a high bandwidth and a high output signal, but suffer generally from the major disadvantage that they are not suitable for measuring static accelerations [Sch96].

Shift in resonant frequency

Very promising is also the *resonant frequency* read-out principle. This approach is based on the fact that the resonant frequency of a micro bridge changes, when submitted to tensile stress. The same property is used to tune a guitar string. By placing these resonant bridges in the suspension system of the seismic mass, the resonant frequency changes with the mass movement thus with acceleration. The beams are driven either electrothermally combined with a piezoresistive read-out, or electrostatically with capacitive sensing. Temperature drifts are small, because temperature mainly affects the amplitude and less the resonance frequency itself [Bun96, Bur95, Cha90, SA30].

Convection heat transfer
Very recently, one very simple but interesting accelerometer approach based on *convection heat transfer* has been presented [Le98]. This design varies form all other accelerometers. The air enclosed in the package functions as seismic mass and modifies the heat transfer between three suspended wires. One wire functions as heater, the other two as temperature sensors. First measurements indicate a remarkable performance (resolution of sub-mg) at extremely low-cost. A 2-axis accelerometer based on the same principle has also been fabricated and tested.

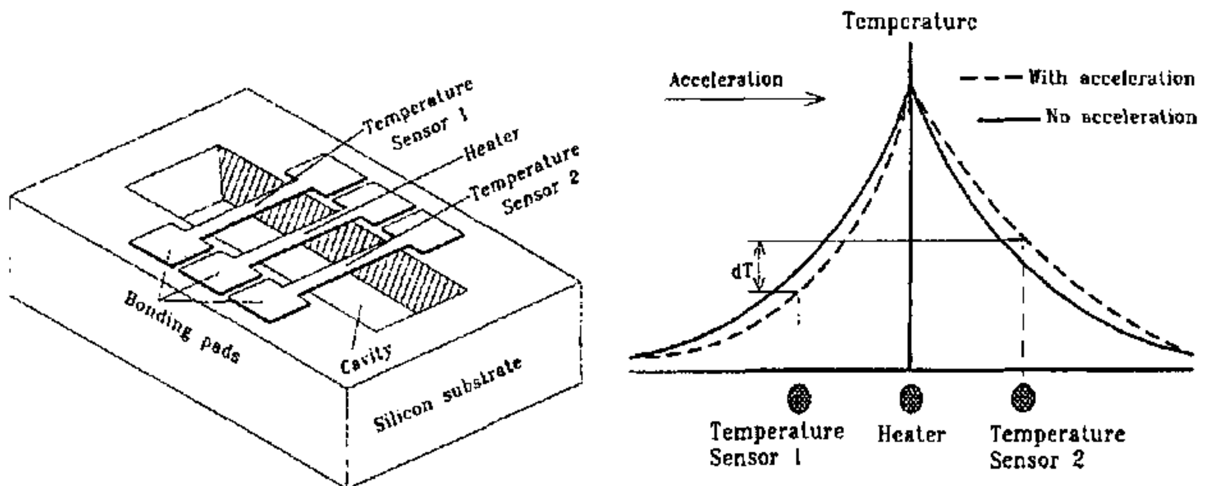

Figure 1.9: Accelerometer consisting of three wires: one works as a heater, the other two as temperature sensors [Le98].

... and more
In addition, read-out based on *electromagnetic* [Abb94], *thermal* [Hir92, Dau95] or *FET* [Pla96] effect have been demonstrated.

1.4 Recently developed multi-axial micromachined accelerometers

Multi-axial accelerometers designed to measure accelerations in two or three directions can be conventionally built by mounting three uni-axial devices together in a triad. Commercial devices built up by this triad assembling technique show high performance [Sag97], [Lit96]. However, accurate mounting of the uni-axial accelerometers makes these devices very costly. Alternatively, multiaxial monolithic accelerometers consisting of one chip with one or more seismic masses can be built. Recently, some inherently multi-axial accelerometers have been reported and are described briefly in this section.

Probably the first monolithic tri-axial accelerometer was presented by Okada [Oka92]. It is composed of a silicon diaphragm on which a glass seismic mass is bonded. When the seismic mass moves under acceleration, the diaphragm changes its shape. This change is detected by piezoresistors, which are aligned on the surface of the silicon diaphragm. There are three sets of piezoresistors configured in Wheatstone bridges to measure each axis independently.

T. Mineta proposed a capacitive triaxial accelerometer based on a surrounding mass structure. The sensor has a seismic mass whose center of gravity is raised above suspending beams, so that vertical and lateral accelerations can be detected capacitively by parallel shift and tilt of the seismic mass, respectively. The main disadvantage of this device are the cross-sensitivities which are over 10% and have to be eliminated by an arithmetic operation.

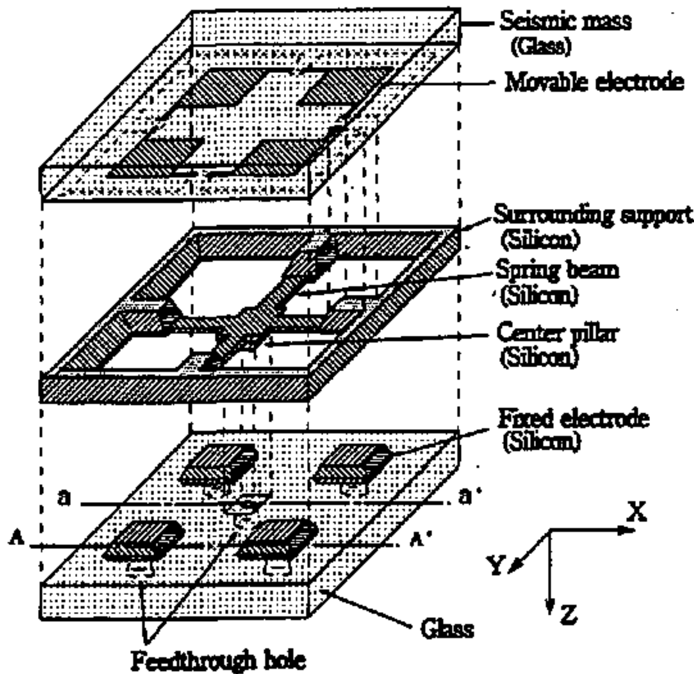

Figure 1.10: Schematic of a triaxial accelerometer based on a surrounding mass structure [Min96].

Andersson [And95] described a tri-axial accelerometer composed of four seismic masses, which are sensed piezoresitively. Main and Cross-sensibilities are not presented.

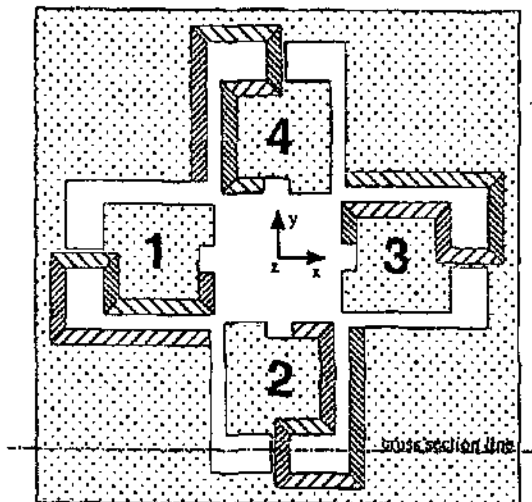

Figure 1.11: Tri-axial piezoresistive accelerometer consisting of four seismic masses [And95].

A tri-axial accelerometer with Zinc oxide layers as strain-sensing elements has been designed by Scheeper [Sch96]. The device consists of several seismic mass structures, which have

piezoelectric elements in the suspension beams. By changing the electrode configuration the direction of sensing can be chosen. Measurement results have been recently reported [dRe98]. The resolution in the vertical direction is about 0.1mg/√Hz while the resolution in the lateral direction is 100 times larger.

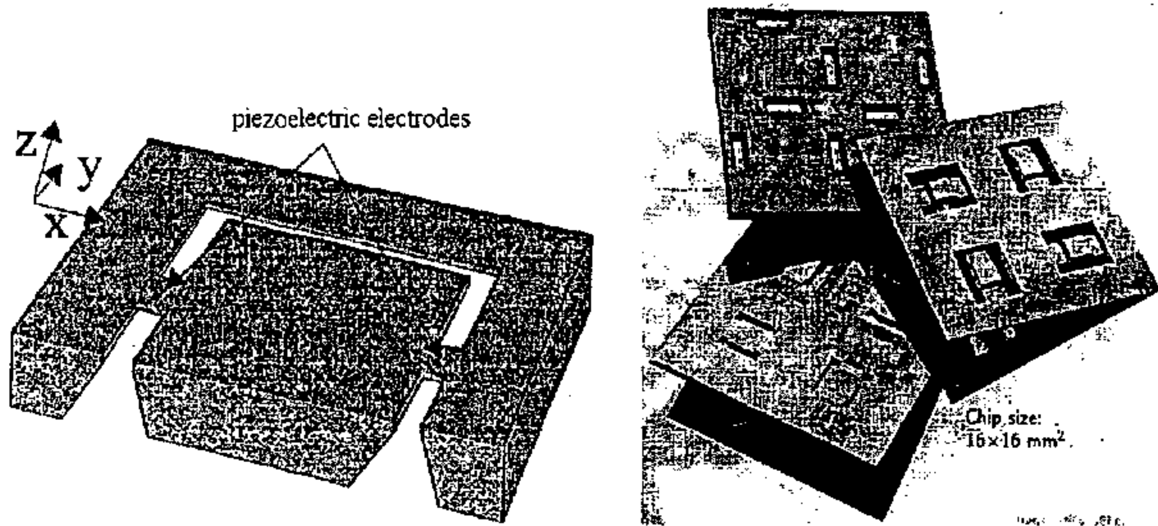

Figure 1.12: Principle (left) and realization (right) of a three-dimensional accelerometer with piezoelectric sensing based on ZnO-layers [Sch96], [dRe98].

In 1996 Th. Velten presented a two-axis accelerometer consisting of a double seismic mass (also called twin mass) with piezoresitive read-out. The piezoresistors are arranged in a Wheatstone bridge and can be switched to get the vertical or one lateral acceleration measurement. To build a three-dimensional accelerometer two of these devices are necessary.

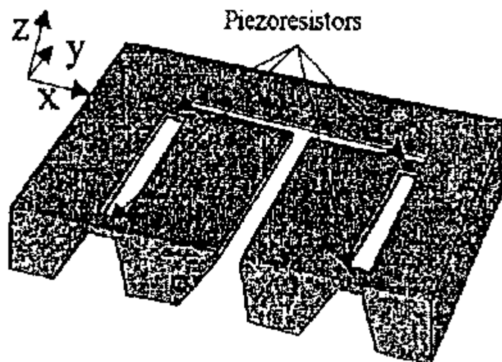

Figure 1.13: Two-axial accelerometer with piezoresitive read-out [Vel96].

A very unconventional approach was presented by Lötters [Löt97]. His tri-axial accelerometer is based on the idea of one central cubic seismic mass made of Tungsten surrounded by capacitors. Due to the high symmetry, off-axis sensitivities are reduced to smaller than 5%. Resolutions are below 1mg for a measurement range of ±5g. Unfortunately, fabrication of this sensor with batch fabrication facilities conventionally used in microtechnology is not possible, making the device less attractive for mass applications.

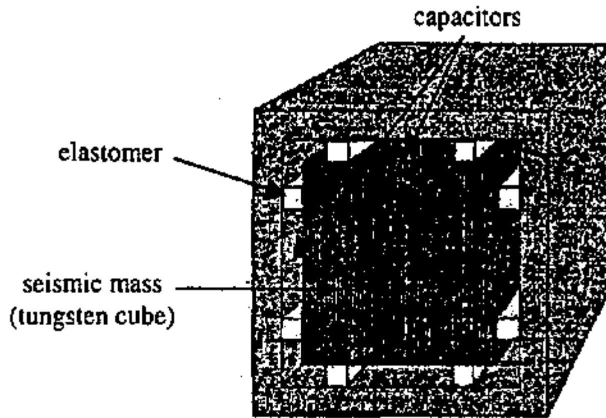

Figure 1.14: An unconventional highly symmetrical triaxial accelerometer consisting of a cubic seismic mass [Löt97].

A 3-axis force balanced surface-micromachined accelerometer was recently presented by Lemkin [Lem97]. Here, four beams, as shown in the figure below, suspend one mass. Due to lateral accelerations, the distance between the comb shaped electrodes changes, which can be sensed capacitively. Due to vertical accelerations the distance and capacitance to the substrate varies. Capacitance position sense and force feedback are accomplished using the same air-gap capacitors through time multiplexing. The zero sense capacitors are in the order of 100fF making an on-chip interface electronic necessary. Resolutions are under 1mg/√Hz for a measurement range of ±11g and ±5g in lateral and vertical directions, respectively.
Ahmad [Ah97] has proposed a similar design for a two-axis surface-micromachined accelerometer.

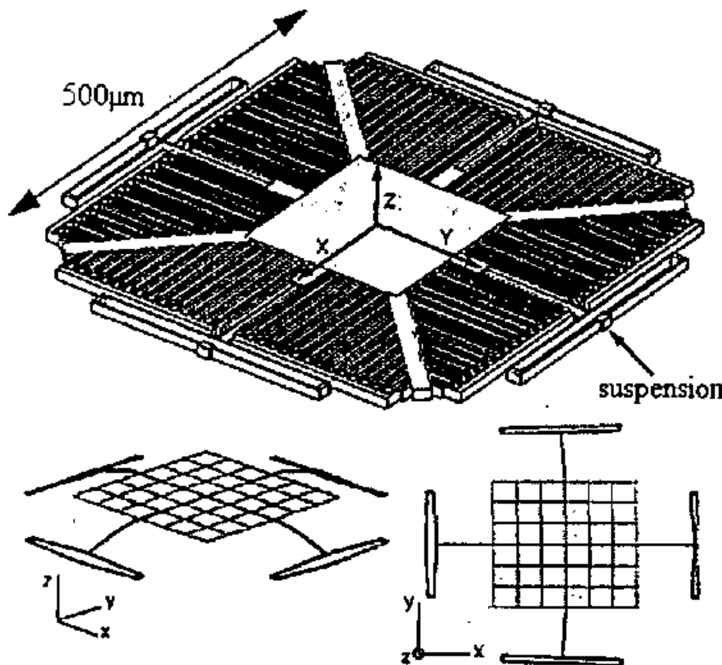

Figure 1.15: Undeformed 2.3μm thick surface micromachined triaxial accelerometer (top) with comb shaped electrodes. Simulations of deformation due to applied vertical (bottom left) and lateral (bottom right) accelerations are shown [Lem97].

In addition to the above described devices, a twin-mass like tri-axial accelerometer with piezoresitive read-out has been demonstrated by J. Plaza [Pla97]. The device shows cross-axis sensitivities between 1.6% and 8.8% depending on the sensing direction. It has been fabricated using a combination of surface and bulk technologies based on BESOI wafers. In comparison to the piezoresistive twin-mass accelerometer of [Vel96] this device is suitable for full 3D measurement.

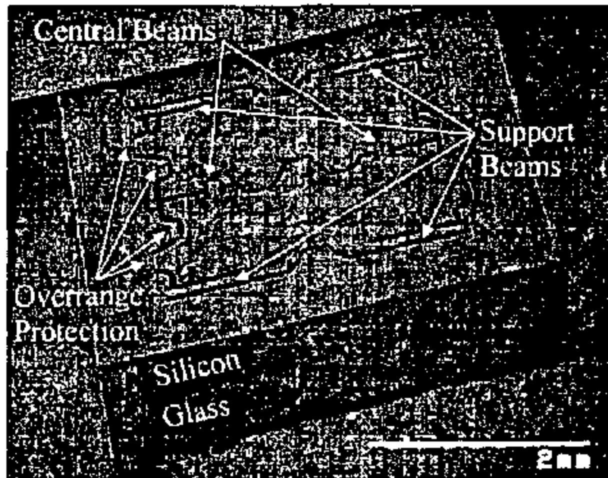

Figure 1.16: SEM view of twin mass 3D piezoresitive accelerometer [Pla97].

Taking a surrounding mass structure H. Takao has built two- and three-axis accelerometers. The displacements of the seismic mass are detected by strain sensing in the suspension either with piezoresistors [Tak96] or by stress sensitive differential amplifiers (transistors) [Tak97]. The monolithic tri-axial device is fabricated using silicon on insulator (SOI) and offers a measurement range of ±10g. Cross-sensitivities are about 25%, thus have to be compensated.

Puers and Reyntjens [PuS98] have very recently reported a very small device. The seismic mass has a four-leafed clover shape and its three-dimensional movements are sensed by four capacitors. The smallest design has a dimension of 2.5mm × 2mm × 2mm and is designed for a range of ±5g. Resolution and cross-sensitivities are not yet reported.

Further, Kwon presented a three axis piezoresistive accelerometer using polisilicon layer [Kw97]. The design is a bridge-type structure with a glass base underneath a silicon wafer, which has a polysilicon layer on top.

Very recently, Kruglick and co-workers demonstrated a fully integrated CMOS 3-axis accelerometer consisting of three single suspended polysilicon masses assembled on one chip. The sensing is based on the piezoresistive behavior of gate polysilicon in standard CMOS [Kru98]. This device offer through the employed standard CMOS process low cost.

The only commercial available monolithic tri-axes accelerometer has been recently released by British Aerospace [BA98]. The sensing element is composed of an upper fixed electrode and a lower moveable electrode bonded to a seismic mass. When acceleration is applied, the lower electrode moves with the seismic mass and capacitance values change. Differences or summation of the capacitance values gives the acceleration in three directions.

The above mentioned multi-axial accelerometers are listed and compared in table 1.4. In conclusion, it can be said that a number of monolithic triaxial accelerometers have been proposed. However, resolutions below 100μg/√Hz and cross-sensitivities lower 1% for a typical measurement range between ±1g and ±10g have not been achieved up to now.

Ref.	seismic mass design	read-out principle	surface [mm²]	range [g]	cross-axis sensitivity	Resolution [mg/√Hz]	Bandwidth [Hz]
[Oka92]	diaphragm	piezoresitive	?	±50	5%	?	1500
[Jon94]	surrounding mass	capacitive	18×18	±1	1...7.3%	?	?
[And95]	cantilever	piezoresitive	?	±2	10%	?	?
[Min96]	surrounding mass	capacitive	10×10	±3	10%	?	400
[Tak96]	surrounding mass	piezoresitive	7×5	±4	5.7%	?	2200
[Vel96]	twin mass (2D)	piezoresitive	?	±5	>2%	10	300
[Tak97]	surrounding mass	piezojunction	8×8	±10	25%	?	1500
[Lem97]	comb shape	capacitive	4×4	±5...11	2%	1	7000
[Kw97]	bridge type	piezoresitive	5×5	±24	16%	?	?
[Pla97]	twin mass	piezoresitive	4×4	±	1.6-8.8%	1	350
[Löt97]	cubic	capacitive	5×5	±5	< 5%	1	>400
[PuS98]	4-leaf clover	capacitive	?	±2...5	?	?	?
[dRe98]	bridge type	piezoelectric	16×16	?	?	0.1...10	1500, no DC
[Le98]	air (2D)	heat transfer	3×5	±1	?	0.5	20
[Kru98]	cantilever	piezoresitive	~6×6	>±10	~10%	10	1000
[BA98]	bonded mass	capacitive	<54×54	±2	3%	1	10

Table 1.4: Numerical summary of realized monolithic multi-axial accelerometers. Cross-axis sensitivities are for the accelerometer itself without any electronic compensation.

1.5 Applications of multi-axial accelerometers

Silicon inertial sensors, especially accelerometers, have been developed rapidly during the last decade and are considered after silicon pressure sensors as the most mass-produced mechanical sensors [Son97]. One of the most known applications is the use of accelerometers as crash sensors in airbag safety systems. These devices achieve typically a noise floor of around 10mg/√Hz over a measurement range of ±50g and are built to measure acceleration in only one direction. With these specifications, applications in a range of motion control systems are possible.

However, substantial improvements regarding resolution and multiaxial measurement open the way to far more mass applications. Some potential applications are summarized in table 1.5. It should be noted that each application may need to fulfill different specific requirements, like extremely high resolution and low drift in the inertial navigation system, low power consumption in implanatable medical systems, or harsh environment for the position measurement of an oil-drill head.

Market area (main requirements)	**Applications**
Automotive (low cost, reliable, harsh environment, life time)	• Advanced airbag systems • Active suspension • ABS/Anti-skid • Navigation (µg)
Medical (reliable, small size, low power, life time)	• Monitoring of body motion (µg) • Gesture recognition • Pacemaker
Industry (harsh environment, reliable)	• Robotics (µg) • Machine monitoring • Attitude control (µg) • Transportation/handling of fragile goods • Oil drilling/position of drill head (µg)
Consumer (low cost, low power, small size, life time)	• Camcorder • 3D mouse • Games/Toys • Sport equipment • Electronic inch rule (µg) • Electronic 3D pencil (µg) • Electronic city-guide (µg)
Military and Aerospace (reliable)	• Navigation (µg)
Geology	• Earth quake monitoring (µg)

Table 1.5 Fields of application for high resolution and multi-axial accelerometers (partly from [Son97, Löt97]). If high resolution is required the application is marked with (µg).

1.6 Background and outline of this thesis

The work presented in this thesis was done in the framework of a french-swiss research project, which is entitled PICS (Projet International de Coopération Scientifique).

1.6.1 The PICS-Project: Research for the limits of microtechnology

The PICS research program is intended for studying the limits of the microtechnologies [PIC97]. With the research on a navigation microsystem, the following limits can be investigated: metrology limits, complexity limits and integration limits.
With the satellite Global Positioning System (GPS) exist an important source of information for navigation systems. However, it can suffer from loss of signal, especially in urban areas. There is a need for additional information, which can be provided by a vehicle based system (wheel sensor, speedometer, ea.) or by an Inertial Navigation System (INS). Such an INS has to compute the position and the orientation by the measurements of accelerometers and angular rate sensors. The position can be calculated by integrating the acceleration twice over time. The necessary zero-point stability is obtained by a calibration procedure with a GPS receiver (see figure 1.17). Micromachined accelerometers and angular rate sensors will make such systems economically realistic, if their signal drift is minimized by a suitable data processing.

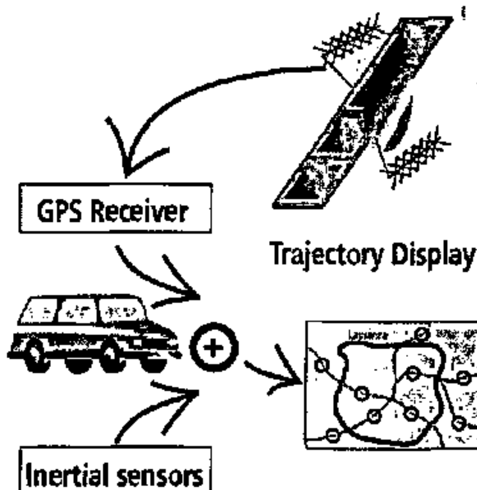

Figure 1.17: Schema of an inertial navigation system.

The research work of PICS for the limits in a navigation microsystem has been divided in four parts: the realization of micromachined accelerometers and angular rate sensors [Gré98], the behavior modeling of the inertial sensors [Ans98] and the data processing of a navigation system [Mar98] (see figure 1.18).

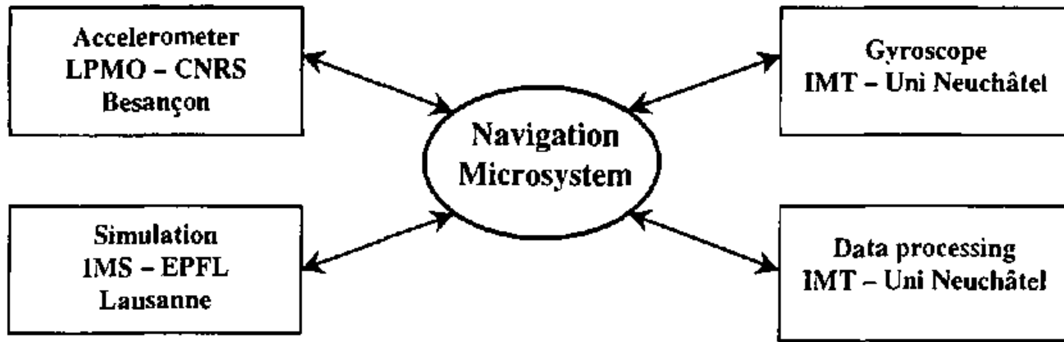

Figure 1.18: Puzzle out of four parts. The PICS program consists of four single research projects: micromachined multiaxial accelerometers (Gerold Schröpfer ea, LPMO/CNRS Besançon), silicon angular rate sensor (Florence Grétillat ea. IMT Neuchâtel), Simulation of inertial sensors (Yannick Ansel ea., IMS-EPFL Lausanne) and navigation system data processing (Catherine Marsetti ea., IMT Neuchâtel).

We can establish at least the following requirements for the accelerometer part within this project:

- Measurement range: ±1g ... ±2g
- Resolution: < 100µg/√Hz
- Bandwidth: 10Hz ... 100Hz
- Cross-sensitivities: < 1%
- Nonlinearity: < 1%

A Three-axial acceleration measurement is necessary, including highly precise orientation of the three axis. The seismic masses should be large to obtain high sensitivity. Therefore, the aim of the following work is not to minimize the accelerometer size, but rather search for new mechanical structures that can provide the high precision of orientation as well as a high sensitivity regarding each single axis. In addition, a sensitive technique for mass displacement detection has to be found to obtain a high resolution.
Although no miniaturization of the 3D accelerometer is necessary, the device should be micromachined in order to use the advantages of possible cost reduction due to batch processing. The chosen fabrication concept should enable a high stability of sensor performance.

1.6.2 Outline of the thesis

This thesis describes the research work towards some new possibilities in silicon wet etching and their application to the design and fabrication of accelerometers with capacitive and optical read-out. It is divided into seven main chapters. An introduction on accelerometers and micromachining was given in chapter 1.

The second chapter deals with different designs of seismic mass systems for measuring in- and out-of-waferplane accelerations. The static and dynamic mechanical behavior of these structures is modeled analytically as well as by finite element simulations. Theoretical predictions are compared to first static measurements performed by an external optical comparator. The various designs are compared not only regarding sensitivity, but also in terms of nonlinearity, variation of sensitivity due to fabrication tolerances, chip size and cross-sensitivities.

In the third chapter some new principles and experimental results on a non-conventional bulk-micromachining using underetching of {100} silicon planes are reported. The fabrication process is discussed in detail and design rules are derived. Simulations of the anisotropic etching were performed to find the geometrical variations of the structures when mask misalignments and crystal misorientations of the silicon wafer occur. This novel technique was used to fabricate the seismic mass elements employed in accelerometers but also for other silicon microstructures.

The fourth chapter presents capacitive accelerometers. Modelisation of these devices is achieved by analytical methods as well as by finite element simulators. Emphasis is also put on the micro-fabrication of these sensors. The developed processes are described in detail. The multi-axial capacitive accelerometers are characterized to show the performance of the fabricated devices. Finally, the study of limitations and performance optimization for these devices concludes this section.

Multi-axial accelerometers with optical detection are discussed in chapter 5. All steps in sensor development are presented: design and modeling, fabrication, and experimental characterization. Using only one light source these devices can be multiplexed for measuring accelerations along two or three directions.

In the sixth chapter a comparison of optical and capacitive accelerometers is given, and some suggestions for further work are proposed.

Finally, a detailed summary in English and French is given.

CHAPTER 2

2. Design and modeling of mechanical accelerometer structures

2.1 Introduction

2.2 Different designs for a suspended seismic mass

2.3 Analytical modeling

2.4 Finite element simulation

2.5 Comparison between theory and experiments for static displacements

2.6 Comparison of different designs

2.7 Mechanical-thermal noise

2.8 Conclusion of chapter 2

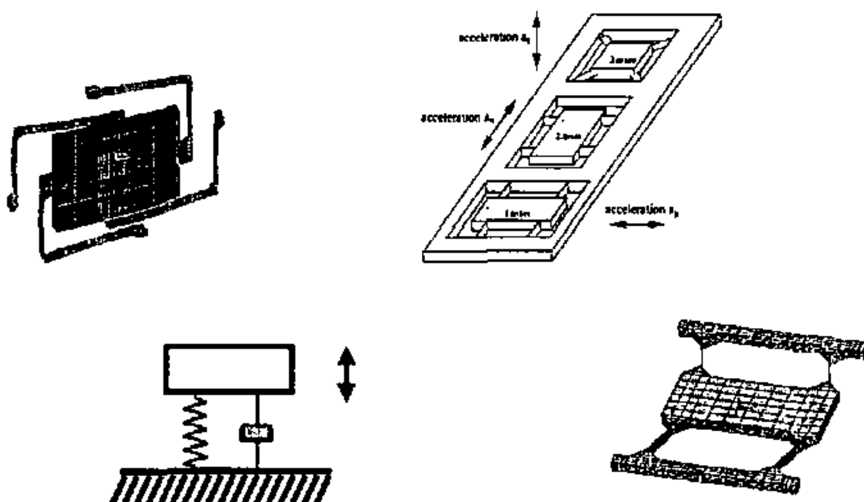

2. Design and modeling of mechanical accelerometer structures

2.1 Introduction

The purpose of this chapter is to present and describe new mechanical designs suitable for three-dimensional acceleration measurement. There exist two possibilities to build a monolithic 3D accelerometer system on one chip. One can integrate in one chip three different seismic masses, each one uniaxially sensitive to aspecific direction, having low cross-axis sensitivities (two lateral structures and one vertical structure, see figure 2.1). Alternatively, one can use a single seismic mass sensitive to all directions. In this thesis the main emphasis is put on a system composed of three individual masses, but the other principle is also studied. The implementation of the proposed designs in real micromachined devices is described in the third chapter, which deals with unconventional bulk-micromachining of (100) silicon.

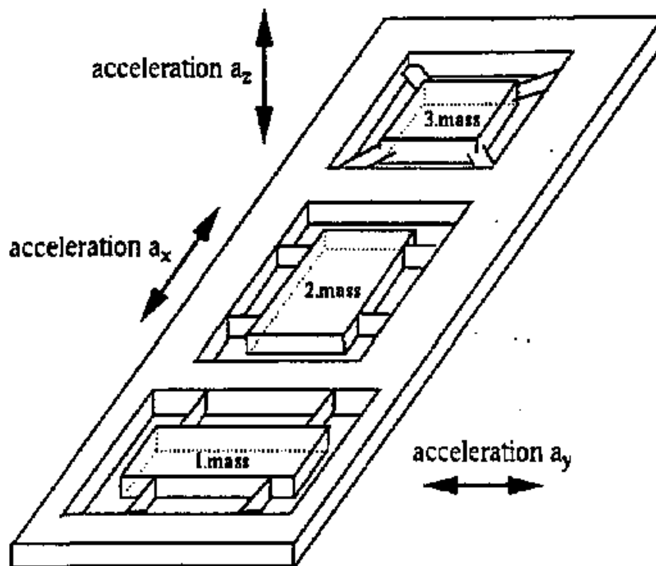

Figure 2.1: Three-dimensional monolithic accelerometer composed of three seismic masses (two laterally sensitive structures and one vertically sensitive structure). Each mass is sensitive in only one direction and not sensitive in the other one (low cross-sensitivities). In the presented case each mass is symmetrically suspended by four thin beams.

In the following, design and modeling of different seismic mass systems are described. Analytical formulae describe the mechanical displacements due to accelerations, damping and resonance frequencies. These formulae construct a simple model which represents the static and dynamic mechanical behavior of the accelerometers. Also, the main characteristics are simulated by Finite Element Methods (FEM) to confirm and complete the analytical model. In addition, first measurements have been made to compare the theoretical results with experimental ones.

Analytical and FEM calculations are used to investigate design parameters in order to find the best choice not only regarding a large main sensitivity and low cross-axis sensitivities, but also considering nonlinearity, chip size, and variation of sensitivity due to the accuracy of the fabrication process.

Finally, the fundamental limit in the measurement of the mechanical displacements is considered by describing the mechanical-thermal noise of the seismic mass structures.

The modeling and the limitations of the complete sensors with optical or capacitive read-out will be treated in further chapters. The following analytical and FEM models describe the mechanical part for both types of accelerometer.

2.2 Different designs for a suspended seismic mass

The proposed designs have been divided into three categories. Firstly, in-plane or lateral structures having a main mechanical sensitivity parallel to the wafer. Secondly, out-of-plane structures consisting of a seismic mass with a sensitivity in the vertical direction which is orthogonal to the substrate. And thirdly, in- and out-of-plane structures being sensitive to accelerations parallel as well as perpendicular to the wafer plane.

2.2.1 In-plane structures

The mechanical designs of accelerometers with a lateral sensitivity offer two significant advantages over the vertically sensitive structures. Firstly, the fabrication of suspension beams and seismic masses is generally done for in-plane accelerometers in one manufacturing (etching) step. Secondly, they show a high degree of symmetry which allows one to increase the seismic mass without changing its center of gravity.

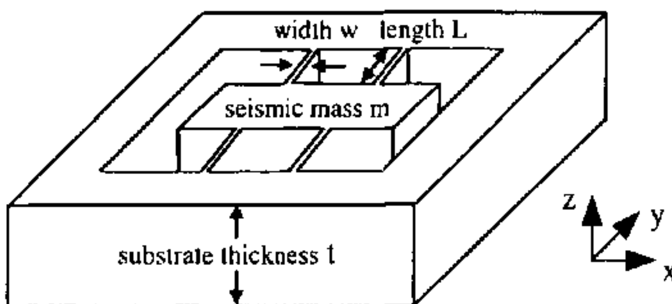

Figure 2.2: 3D schematic of a four-beam suspended proof mass with a pure translational movement in the x-direction (design 1, in-plane structure).

In the following section four different designs for accelerometers with in-plane sensitivity are proposed (see figure 2.3). All four designs have seismic masses supported by thin vertical beams. These beams show a high aspect ratio, which is the ration t/w between beam thickness t (or better beam height) and beam width w. This high aspect ratio together with a symmetrically shaped mass ensures a translational movement parallel to one direction of the wafer plane and rejects movements in the other directions. The presented mechanical designs differ in the arrangements, number and dimensions of suspension beams. Thus, assuming a fixed chip size, the four structures have different mechanical main and cross-axis sensitivities. Generally, design 1 and 2 are less sensitive to transverse and rotational accelerations than design 3 and 4. Numerical values and more details about the differences between each design will be given in the next sections.

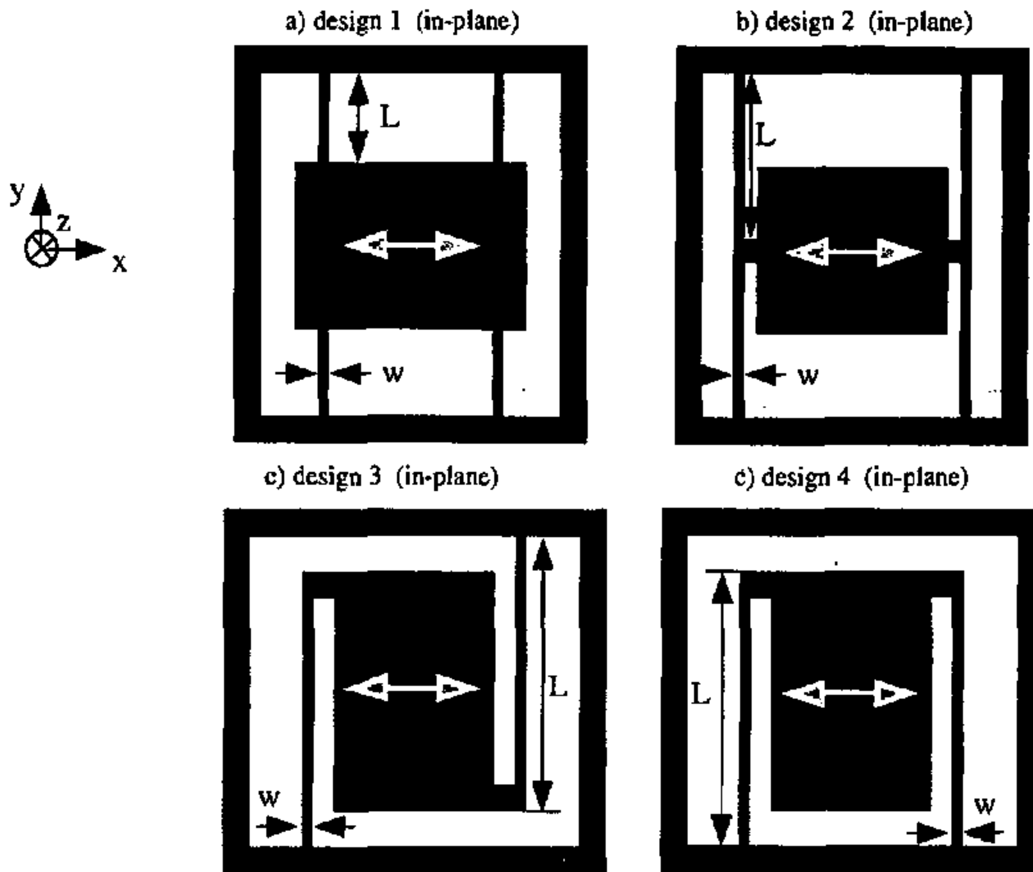

Figure 2.2 : Simplified 2D layouts of four different designs with in-plane sensitivity (with main sensitivity in x-direction): a) seismic mass suspended at the sides with 4 vertical beams, b) seismic mass suspended at the ends with 4 vertical beams (H-shaped), c) seismic mass with two vertical suspension beams asymmetrically clamped (S-shape), and d) seismic mass with two vertical suspension beams symmetrically clamped. The arrows in the mass centers indicates the main sensitive direction.

2.2.2 Out-of-plane structures

Designs with out-of-plane sensitivity (i.e., seismic mass movement perpendicular to the wafer plane) are traditionally more used in bulk-micromachined accelerometers than the in-plane structures. For out-of-plane devices, which have a main sensitivity perpendicular to the substrate, horizontally located suspension beams are needed. Due to the used fabrication technique of ansiotrophic wet etching, these beams are often placed at the surface of the wafer, leading to transverse sensitivities caused by lateral accelerations. Placing the beams in the middle of the substrate or increasing the number of beams reduces these transverse sensitivities.

Here, three different designs with vertical sensitivity are proposed (see figure 2.5). Each design shows a quadratic seismic mass suspended symmetrically by four horizontally located beams. These beams with a thickness t and a width w are fixed either at the corners (design 5) or at the sides (design 6 and 7) of the proof mass, but always in the middle of the wafer, which can not be seen in the 2D top views of figure 2. The thickness t of the beams is very small compared to beam width w. As well as in the case of the in-plane structures, a symmetrically shaped seismic mass is added to the symmetrical arrangement of the suspension beams necessary to enable a pure translational movement rejecting transverse or tilt motions.

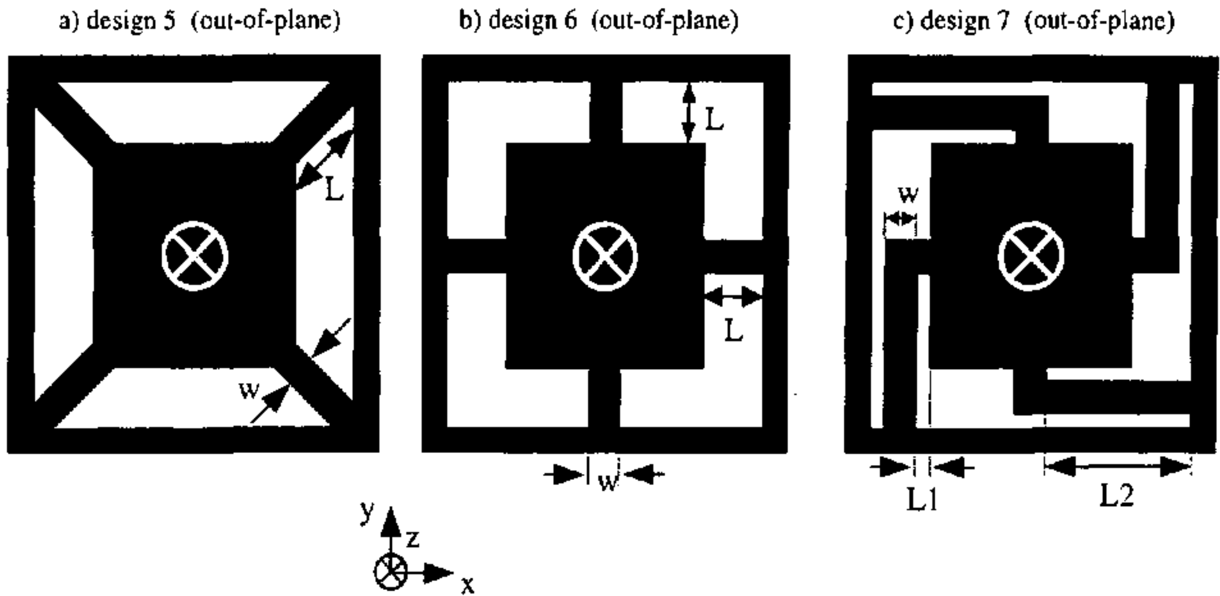

Figure 2.4: Simplified 2D layouts of three different designs with out-of-plane sensitivity (main sensitivity in z-direction): a) seismic mass suspended in the corners with four horizontally located beams, b) seismic mass suspended at the sides with four horizontally located beams and c) seismic mass with four horizontally located S-shaped suspension beams.

2.2.3 In- and out-of-plane structures

The above presented structures (design 1 to 7) have been designed in order to be insensitive to all accelerations, which are not along the main sensitive axis. The following designs (entitled design 8 and 9, figure 2.5) have large sensitivities in all three directions (x-,y- and z-axis). This allows to construct a monolithic triaxial accelerometer consisting of only one seismic mass.

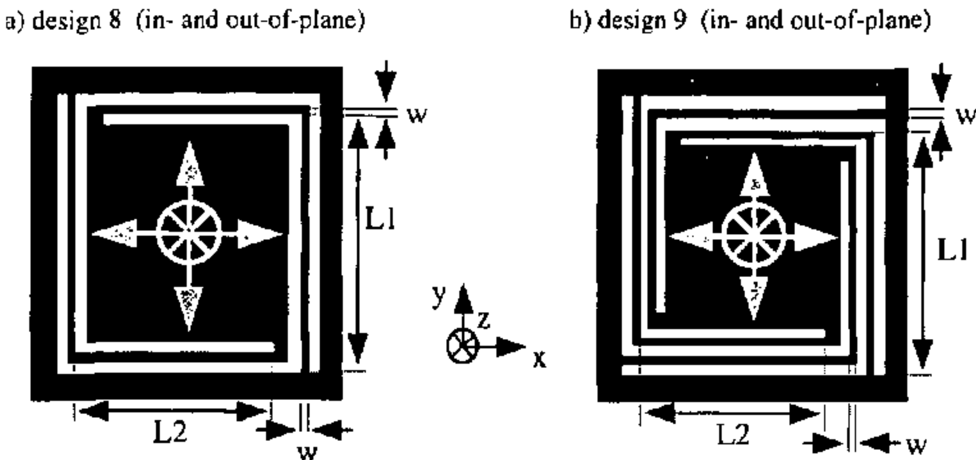

Figure 2.5: 2D layouts of two designs with in- and out-of-plane sensitivity (sensitive in all directions): a) seismic mass suspended with two vertical S-shaped beams and b) seismic mass highly symmetrically suspended by four vertical S-shaped beams.

For both designs of figure 2.5 the proof mass is suspended by vertical beams having the same thickness t as the substrate enabling movement and sensitivity in the in-plane directions (x- and y-axis). Due to the increased length of the beams, these structures become also sensitive to accelerations in out-of-plane direction. While for design 8 the lateral sensitivities in x- and y-direction are not inevitably the same, design 9 offers the inherent matching of the these two mechanical sensitivities due to high degree of symmetry. Unfortunately, both designs are not only sensitive to translational forces, but also to rotational ones.

2.3 Analytical modeling

In the following a simple analytical model is presented to describe the mechanical behavior of the above described mechanical design, the static as well as the dynamic one.

2.3.1 Equation of motion

The analytical model consists of a second order damped spring-mass-system as shown in figure 2.6 [Gab93]. The seismic mass m is suspended with a spring of stiffness k. When an acceleration is applied to the sensor, e.g. in x-direction (a_x), the inertial force $F_x = m\ a_x$ extend or compress the spring depending on the sign of the acceleration and a relative displacement Δx of the proof mass is produced.

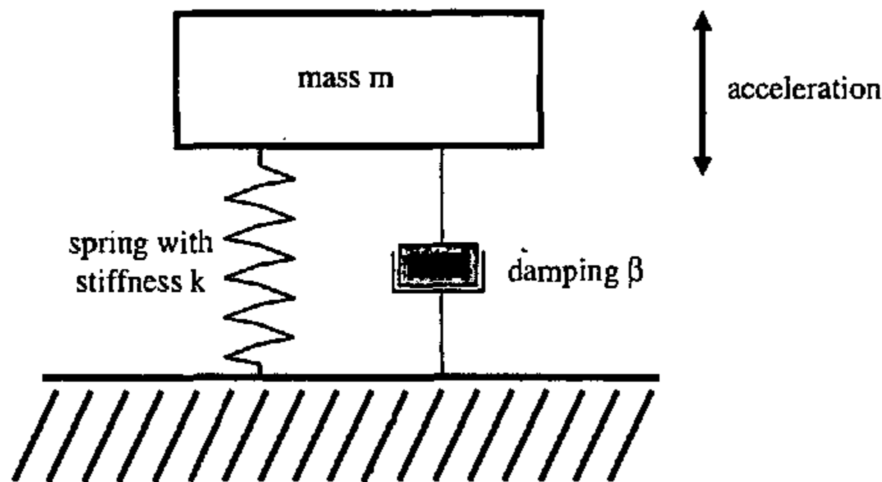

Figure 2.6: Simplified accelerometer model: second order damped spring-mass-system.

In the case of an inertial force in the x-direction, the equation of motion for an open loop system without electrostatical feedback is given by

$$m\frac{d^2\Delta x}{dt^2} + \beta_x \frac{d\Delta x}{dt} + k_x \cdot \Delta x = m \cdot a_x \qquad (2.1).$$

The parameters β_x and k_x describe respectively the damping and the spring stiffness of the system in the x-direction. For accelerations in the y- or z-direction equation 2.1 can be applied similarly. The influence of electrostatical forces will be discussed in a later section (see in chapter 4 which deals with the capacitive device).

2.3.2 Considerations about spring stiffness

In reality, the accelerometer is composed of a mass supported by N beams. The sensitive direction regarding acceleration is in-wafer-plane (x- or y-direction) or out-of-plane (z-direction). The spring constants of the beams are different in the three directions of space. In order to describe the three-dimensional behavior of the sensor, the model can be expanded to one mass supported by three springs representing the different spring constants along the three directions of space (k_x, k_y, k_z).

For the proposed designs, the spring constant along one direction is N-times the spring constant of one single beam. For example, if the x-direction is the sensitive direction (design 1 to 4), the total spring constant is [Ger91]

$$k_x = \frac{N \cdot \hat{E} \cdot t \cdot w^3}{L^3} \qquad (2.2),$$

where $\hat{E}$ is an effective Young modulus of (100) silicon, L the length, w the width and t the thickness of the beams (see figure 2.3). For $t/w > 5$, $\hat{E}$ equals $E/(1-v^2)$ where v is the Poisson ratio. Considering the designs 1 to 4, the thickness t nearly equals the thickness of the wafer (in our case 360µm - 380µm). The displacement in the x-direction due to an acceleration in this direction is mainly caused by bending. Elongation or compression can be neglected. For the accelerations in the y-direction it is vice versa. The displacement is due to elongation and compression of the beams while a displacement due to bending is some orders of magnitude smaller and can be neglected. With Hook's law the total stiffness in the y-direction is [Ger91]

$$k_y = \frac{N \cdot E \cdot t \cdot w}{L} \qquad (2.3).$$

Still considering only the in-plane designs, for acceleration along the z-axis one has a mixture of bending and elongation/compression.

For the out-of-plane designs (design 5 and 6) similar spring constants can be assumed. One just have to switch the parameters beam width w and beam thickness t.

In the case of the designs 7 to 9 the suspension beams are not straight shaped, but show an angle of 90° in their shape. In general, the equation for the equivalent total spring constant for N springs in parallel is given by the total sum of the individual spring constants. For N springs in series, the inverse equivalent spring constant of the system can be calculated by adding up the individual inverse spring constants. Using this rule, one can calculate approximately the stiffness for the main sensitive axis for deign 7 to 9 in the following way

$$k_z = \frac{4 \cdot \hat{E} \cdot t^3 \cdot w}{L1^3 + L2^3} \qquad (2.4) \qquad \text{(design 7)},$$

$$k_x^{-1} = \left(\frac{2 \cdot \hat{E} \cdot w \cdot t^3}{L1^3}\right)^{-1} + \left(\frac{2 \cdot E \cdot w \cdot t}{L2}\right)^{-1} \qquad (2.5) \qquad \text{(design 8)},$$

$$k_y^{-1} = \left(\frac{2 \cdot \hat{E} \cdot w \cdot t^3}{L2^3}\right)^{-1} + \left(\frac{2 \cdot E \cdot w \cdot t}{L1}\right)^{-1} \qquad (2.6) \qquad \text{(still design 8)},$$

$$k_x^{-1} = k_y^{-1} = \left(\frac{2 \cdot \hat{E} \cdot w \cdot t^3}{L1^3 + L2^3}\right)^{-1} + \left(\frac{2 \cdot E \cdot w \cdot t}{L2 + L1}\right)^{-1} \qquad (2.7) \qquad \text{(design 9)}.$$

2.3.3 Static modeling

To simplify the discussion of the static behavior, we will only study design 1. But it has to be mentioned that for all other designs the given formulae and drawn conclusion can also be applied in a similar way.

In the static modeling only the time independent terms of the equation of motion (2.1) are considered. Thus damping is not taken into account.

The deflection of a suspension beam is given by (with $y \leq L$ and the moment of inertia I of the beam) [Roc71]

$$x(y) = m \cdot a_x \cdot \left(\frac{L^3}{2 \cdot N \cdot \hat{E} \cdot I}\right) \cdot \left(3\left(\frac{yv}{L}\right)^2 - 2\left(\frac{y}{L}\right)^3\right) \qquad (2.8).$$

This leads for $y = L$ to the displacement Δx of the seismic mass due to an acceleration a_x along x-axis of (considering design 1)

$$\Delta x = x(y = L) = \left(\frac{m \cdot a_x \cdot L^3}{N \cdot \hat{E} \cdot w^3 \cdot t}\right) \qquad (2.9).$$

This simple calculation is true for displacements Δx which are small compared to the width w and thickness t of the suspension beams (small deflection theory). Regarding formulae 2.2 and 2.9 we find the equation of motion reduced to the static case

$$k_x \cdot \Delta x = m \cdot a_x \qquad (2.10).$$

With equation 2.10 we define the mechanical sensitivity S_x as

$$S_x = \frac{\Delta x}{a_x} \quad (2.11) \qquad \text{or} \qquad S_x = \frac{m}{k_x} \quad (2.12).$$

The mechanical sensitivity of a device is given by the ratio of mass m over the spring constant. This equals the ratio of displacement over acceleration regarding one direction.

From formulae 2.2 and 2.12 it is clear that it is possible to increase the mechanical sensitivity S_x of design 1 (or design 2, 3, 4, 8 and 9) by:

- Increasing the mass m of the sensor ($S_x \sim m$).
- Increasing the length L of the suspension beams ($S_x \sim L^3$).
- Decreasing the width w of the suspension beams ($S_x \sim w^{-3}$).
- Decreasing the thickness t of the suspension beams ($S_x \sim t^{-1}$).

For the designs 5-7 similar conclusions can be drawn to increase the mechanical sensitivity.

Mechanical cross-sensitivities are defined as displacement in one direction over acceleration in another direction, e.g.,

$$S_{yx} = \frac{\Delta y}{a_x} \quad (2.13) \qquad \text{or} \qquad S_{xz} = \frac{\Delta x}{a_z} \quad (2.14).$$

Often mechanical cross-sensitivities are given as a percentage of the main sensitivity, e.g.,

$$\frac{S_{xz}}{S_z} = \frac{\Delta x}{\Delta z} \quad (2.15).$$

2.3.4 Considerations about damping

In this subsection, the damper mechanisms occurring in the proposed structures are described and equations for the corresponding damping constants are given. In the model shown in figure 2.6 the damper determines the damping coefficient of the system β (β_x, β_y, β_x for all directions, respectively) and allows or prohibits the resonance peak to occur. The first case is called sub-critical damping, the second super-critical damping. The force acting on the damper is equal to the product of the damping constant β and the speed of the change in spring length.

The damping of the seismic mass is determined by the medium between the mass surface and the substrate and also by the geometrical dimensions. Often air is used as a damping medium. Following [Löt97], we distinguish between three types of damping, pictured in figure 2.7.

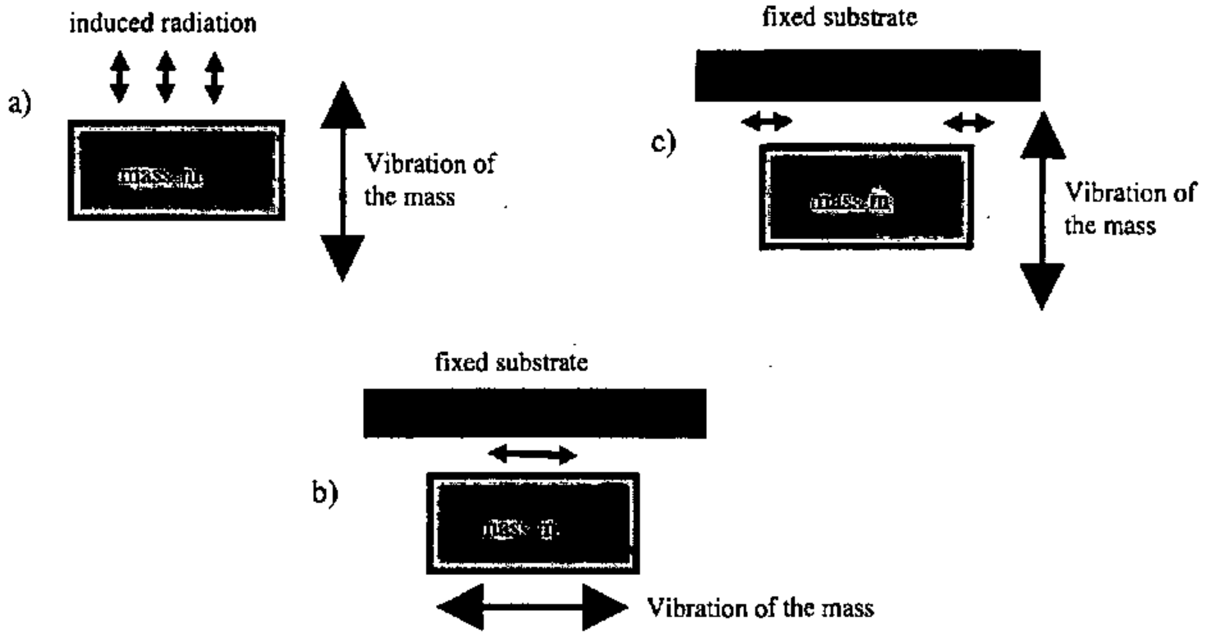

Figure 2.7: Schematic overview of the three damping types considered for the proposed accelerometer structures: a) radiation resistance, b) lateral film damping and c) squeeze film damping.

a) Radiation resistance

The vibration of the seismic mass induces an acoustical flow into the surrounding medium, perpendicular to the area of the mass (see figure 2.7a). By considering the radiation of sound, a complex reaction force can be calculated [Mo68]. The real part of the reaction force is a frequency dependent frictional force and describes the damping of the seismic mass due to energy losses. The imaginary part of the reaction force describes the effective mass of the vibrating medium and can be generally neglected with respect to the weight of the seismic mass. In the case of narrow gaps the damping due to radiation can be neglected.

For small gaps (typically $<10\mu m$) only two types of damping have to be considered: lateral film damping and squeeze film damping. While for the in-plane structures (design 1, 2, 3, 4, 8 and 9) the lateral film damping is the dominant type, the squeeze film damping is more important in the case of the out-of-plane designs (design 5, 6 and 7).

b) Lateral film damping

When the seismic mass is moving in parallel with the fixed substrate the damping medium in the gap starts vibrating with the velocity of the seismic mass at the contact interface with the seismic mass and with velocity 0 at the interface with the fixed substrate. This velocity gradient in the medium causes the damping mechanism which is called lateral film damping (see figure 2.7 b)). By solving the Navier-Stokes differential equation for the movement of an incompressible viscous liquid or gas one can finally find an expression for the lateral film damping constant $\beta_{Lateral}$ [Cho94]:

$$\beta_{Lateral} = \frac{\mu \cdot A}{d} \qquad (2.16).$$

μ is the dynamic viscosity of the damping medium (liquid or gas), A the surface of the seismic mass and d the gap between seismic mass and fixed substrate.

c) Squeeze film damping

When the distance between proof mass and fixed substrate is considerably small, e.g. in the range of some µm, the vibration of the mass perpendicular to the substrate causes a flow directed inside or outside the gap. When the mass moves towards the substrate the damping medium is squeezed out of the gap and when the mass moves away from the substrate the damping medium is forced to flow into the gap. This flow causes damping. The corresponding mechanism is called squeeze film damping. The damping constant can be described as [An93] (viscosity μ, surface A, gap $d < 10\mu m$)

$$\beta_{Squeeze} = \frac{12 \cdot \mu \cdot A^2}{\pi \cdot d^3} \qquad (2.17).$$

In [Bou97], [Vei95] and [Dar97] one can find more complete analytical calaculations and modeling by circuit simulation concerning squeeze film damping in accelerometers.

Generally, most time air is used as damping medium in existing accelerometers. But also silicone oil has been employed as a damping medium, especially for piezoresitive accelerometers ([Ric94], [Tsc92]). The silicon oil provides also good shock resistance.

2.3.5 Dynamic modeling

The resonance frequencies are determined by the seismic mass and the spring stiffness of the suspension beams. The undisturbed fundamental resonance frequencies for vibrations in only one direction are represented, e.g. in the x-direction, by

$$\omega_x = 2 \cdot \pi \cdot f_x = \sqrt{\frac{k_x}{m}} \qquad (2.18) \qquad \text{(equivalent for y and z).}$$

The resonance frequency for a tilt motion of the seismic mass around the y-axis is given by

$$f_{R,x} = \frac{1}{2 \cdot \pi} \cdot \sqrt{\frac{k_{R,y}}{I_{R,y}}} \qquad (2.19),$$

where $k_{R,y}$ is the spring constant and $I_{R,y}$ the moment of inertia for a rotational movement around the y-axis. The formulae for rotations around the x- or z-axis are equivalent to 2.19.

From equations 2.12, 2.18 and 2.19 one fundamental aspect of all seismic mass systems becomes visible: Mechanical sensitivities and resonance frequencies are related. Combining equations 2.12 and 2.18 one find that the sensitivity is proportional to the inverse squared resonance frequency. Any increase in the mechanical sensitivity means always a decrease in the mechanical resonance frequency. A compromise between these two parameters has to be found when designing accelerometers.

By Laplace transformation of equation 2.1 one can derive the mechanical transfer function of the second order damped spring-mass-system from acceleration to displacement (here representative for the x-direction)

$$H(\omega) = \frac{\Delta x}{a_x} = \frac{m}{k_x} \cdot \frac{1}{\left(\frac{j\omega}{\omega_x}\right)^2 + \frac{\beta_x \cdot j\omega}{\sqrt{k_x \cdot m} \cdot \omega_x} + 1} \qquad (2.20).$$

Generally, the Q-factor is defined as the ratio between the average stored energy in the resonant circuit and the dissipated energy per period in the circuit. In the above used model of a damped mass-spring-system Q is equal to the reciprocal of the damping term, e.g., for the vibrations along the x-axis,

$$Q_x = \frac{\sqrt{k_x \cdot m}}{\beta_x} \qquad (2.21)$$

and can thus be expressed by the basic system parameters m, k_x and β_x.

By using the presented transfer function 2.20, the mechanical behavior of the accelerometer can be simulated, and parameters can be adapted in order to achieve a desired sensitivity, bandwidth and damping. The damping modifies the frequency response of the sensor. Strong damping or overdamping narrows the frequency range, and underdamping produces a high resonance peak.

In figure 2.8 the mechanical transfer function of an in-plane design is displayed for five different damping media. For the simulated device the moveable seismic mass has a surface of 5580μm × 2570μm. The cavity between mass and fixed substrate is 5μm. Air and silicone oil with a viscosity of 10cs (Centi-Stokes) results in under damping. The resonance peak occurs clearly at the first resonance of 1025Hz. Silicone oil with a viscosity of 100cs or 1000cs overdamps the device and therefore decreases the useable bandwidth. In the case of silicon oil with a viscosity of 44cs the accelerometer is critically damped. The Q-factor is thus 0.7.

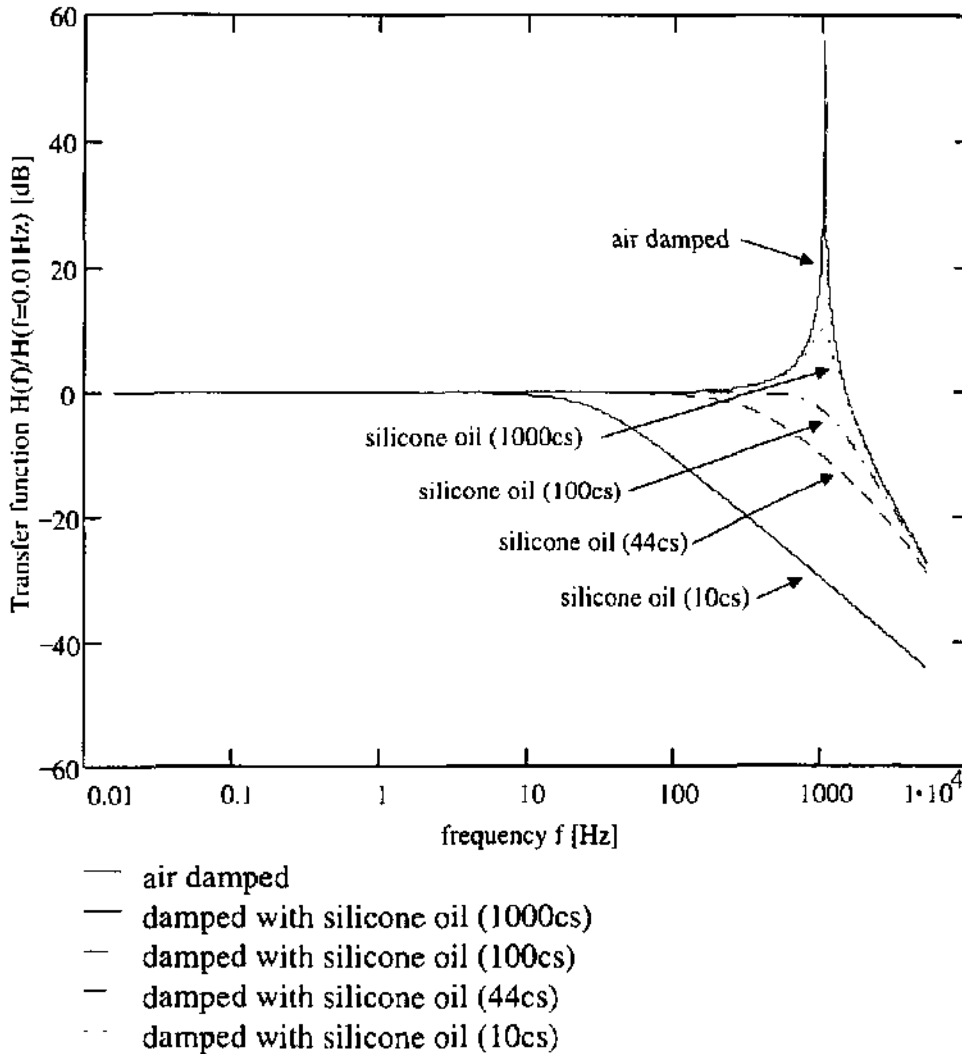

Figure 2.8: Mechanical transfer function for an in-plane accelerometer (design 1, 2, 3 or 4). Five different damping media (air, silicon oil N° 1 μ=1000cs, silicon oil N° 2 μ=100cs, silicon oil N° 3 μ=44cs and silicon oil N° 4 μ=10cs) have been considered and only lateral film damping is assumed (equation 2.16). The mechanical sensitivity is in this case S_x=236nm/g corresponding to a first resonance frequency f_x of 1025Hz.

2.4 Finite element simulation

The previously given analytical formulae are based on a model which is simplified in such a way that it still fits best the reality and that it consists of a system of forces, moments and shapes which can be analytically described. Such an analytical discussion is very helpful to obtain a global view. However, there are some important features to be considered in the accelerometer design which can not be sufficiently modeled by the analytical approach. For example, *cross-sensitivities* or *nonlinear effects* due to large displacements. In these cases explicit analytical formulae can not be easily given. Also, it is difficult to predict the *higher modes* of resonance vibrations and their *corresponding frequencies* by using only analytical methods, specially for complicated shaped structures. With *arbitrarily shaped beams*, like in

design 7 or 9, the sensitivity can be increased without increasing the chip size. For these structures, the mechanical behavior is calculated more efficiently by creating a FEM model than using an analytical approach.

In a first step the static behavior of the sensor due to an external acceleration is simulated (displacement and stress). In the second step a dynamic analysis is performed focusing on the different modes of vibration. Both, static and dynamic behavior of the accelerometer structures, are investigated using the commercial finite element simulator ANSYS 5.3. Anisotropic ANSYS SOLID 64 elements are used to model the structure of the sensor

2.4.1 Static analysis

In the static analysis a constant acceleration acts on the whole device while the frame is fixed. The acceleration is applied successively along the three directions of space. From the resulting displacements one can calculate the mechanical sensitivities as well as the mechanical cross-axis-sensitivities. The results of a simulation for the first fabricated structure which is of type design 1 are presented. The mechanical sensitivity in the main sensitive direction S_x (about 6nm/g) is very low (see table 2.1). The sensitivity can be increased without increasing the chip size by taking thinner, longer or less beams as proposed in design 2, 3 or 4 (see figure 2.2 and 2.9).

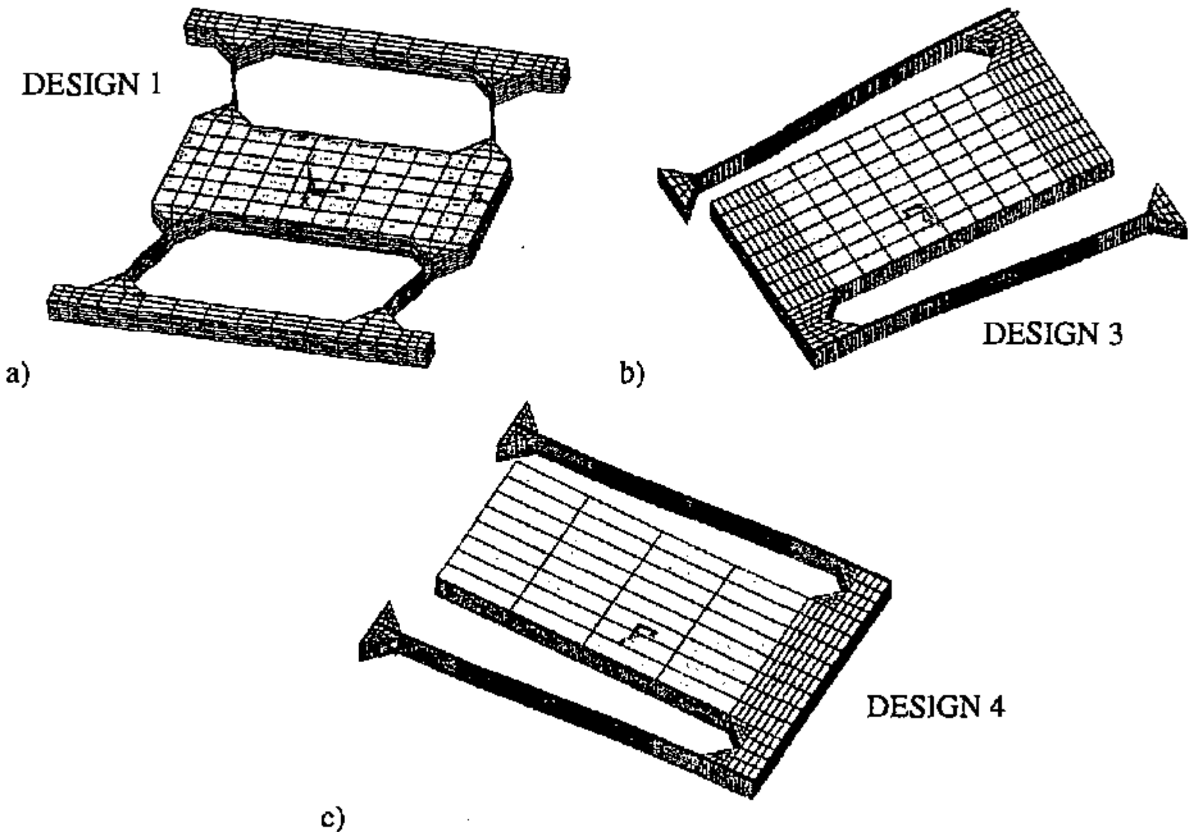

Figure 2.9: FEM simulations (ANSYS 5.3) for three different in-plane designs: a) design 1: the seismic mass is suspended bridge-like with 4 beams, b) design 3: seismic mass with two suspension beams asymmetrically clamped (S-shape) and c) design 4: seismic mass with two suspension beams symmetrically clamped.

dimension design 1 case A:
beams: length L × thickness t × width w = 360 × 380 × 11 μm^3
seismic mass: m = 4.2 mgr

dimension design 1 case B:
beams: length L × thickness t × width w = 1000 × 360 × 15 μm^3
seismic mass: m = 33 mgr

constants:
density ρ = 2330 kg/m^3
Young modulus $E=1.3\times10^{11}$ Nm^{-3} (for <100> directions)
Poisson ration ν = 0.28

calculated performance:	*analytical model case A*	*FEM (ANSYS) case A*	*analytical model case B*	*FEM (ANSYS) case B*
mechanical sensitivity S_x	6.65 nm/g	6.31 nm/g	472 nm/g	429 nm/g
mechanical cross sensitivity S_{xy}/S_x	0	< 0.001 %	0	< 0.001 %
mechanical cross sensitivity S_{xz}/S_x	0	< 0.01 %	0	< 0.01 %
1st resonance frequency	6.1 kHz	6.0 kHz	0.72 kHz	0.76 kHz
2nd resonance frequency	70.5 kHz	70.3 kHz	12.6 kHz	11.6 kHz
3rd resonance frequency	73.5	72.4 kHz	20. 6 kHz	18.4 kHz
5th resonance frequency	190.9 kHz	201.8 kHz	46.5 kHz	44.9 kHz

Table 2.1: Dimensions, mechanical properties and theoretical performance for design 1 with two different dimensions (case A and case B).

Cross-axis sensitivities

The mechanical cross-axis sensitivities which do not appear in the analytical model can be calculated with ANSYS. The computed mechanical cross-sensitivities in y- and z-direction are in case of the design 1, in the order of 0.01% and 0.001%, respectively (percentage of S_x). This demonstrates the strong reduction of cross-sensitivities. This is mainly due to the symmetrically bridge-like suspension by four high-aspect-ratio beams.

Nonlinear displacement

With large displacements the stress in the suspension beams increases and changes the stiffness of the beams. The relationship between displacement and acceleration (or applied force) becomes nonlinear. Since the stress depends on the displacement vs. acceleration curve, an explicit formula can not be given. Numerical algorithms or FEM methods can be applied [Cho97]. In our case, ANSYS has been used to simulate the nonlinear effects of design 1, 3 and 4. As it can be seen from figure 2.10 the response of design 3 and 4 is nearly linear for accelerations up to 100g. Design 1 shows a strong nonlinear behavior for this range. Reducing the input range to ±1g, the nonlinear effect becomes less than 1% for all designs (see table 2.2). For all designs the same mechanical sensitivity of nearly 1μm at 1g acceleration is assumed. The strong nonlinear effect of design 1 for higher accelerations can be explained by regarding the thin (small beam width w) suspension beams for this structure. In this beams the stress causing nonlinearity is higher than for design 3 or 4 which have larger beams. These in-plane designs are more deeply investigated and compared in the subsection 2.6.

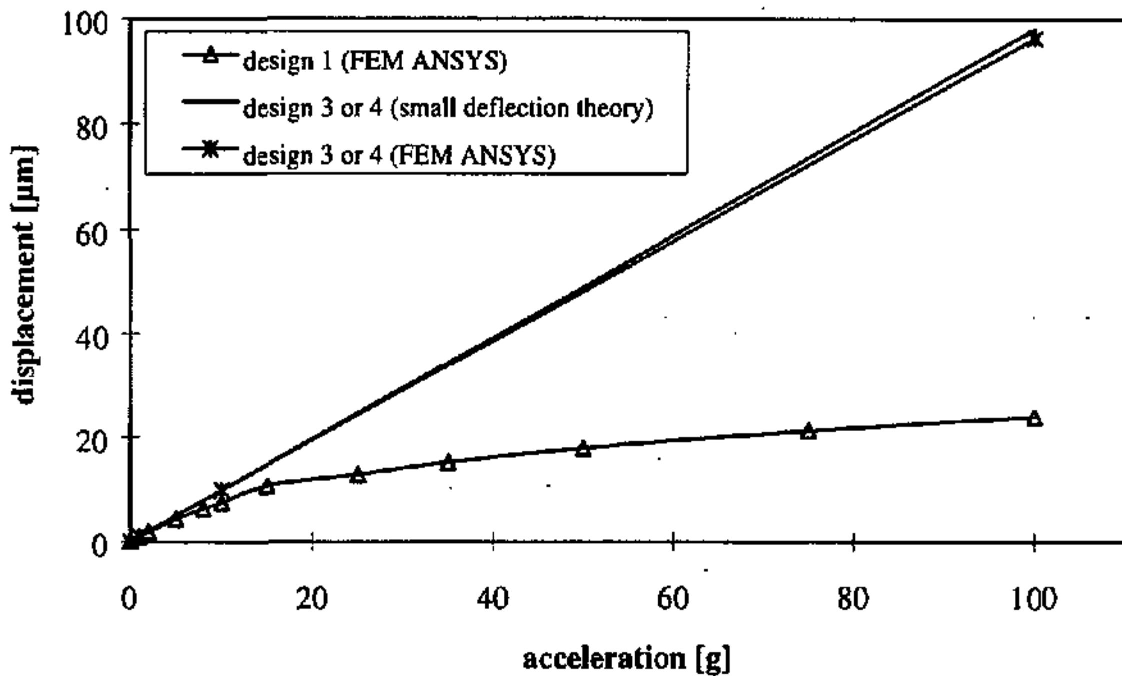

Figure 2.10: Calculated displacement of the two designs due to acceleration. In the range of 100g design 3 and 4 show a nearly linear response.

acceleration range	Nonlinearity of mech. sensitivity: 4 beams (design 1)	2 beams (design 3, 4)
+/- 1 g	0.4 %	0.001 %
+/- 10 g	20.5 %	0.02 %
+/- 100 g	74.2 %	1.9 %

Table 2.2 :Comparison between both designs regarding nonlinearity.

Arbitrarily shaped beams (in- and out-of-plane structures)

Figure 2.11 shows the FEM model of a complicated shaped structure. The seismic mass is suspended by four L-shaped beams and sensitive to lateral and vertical inertial forces. Data resulting from a static simulation are displayed on the right side of figure 2.11. Due to the in-plane symmetry, the sensitivities in the lateral directions (x, y) are identical. For the structure in figure 2.11 an applied force at one edge of the seismic mass leads to an rotational movement with a maximum lateral displacement of 0.4µm/mN. This equals a corresponding torque of approximately 10^{-6} Nm. Comparing the sensitivities of rotational with linear inertial forces, we find for the in figure 2.11 presented structure a cross-sensitivity of about 25% for the linear mechanical sensitivity with respect to in-plane rotational forces. This demonstrates the high sensitivity to angular accelerations. For a pure linear accelerometer one have to use a differential read-out technique to cancel these strong rotational transverse sensitivities. On the other side, one can exploit this effect to construct an angular rate sensor. The rotational

sensitivity for the vertical axis (z-direction) is typically more than on order of magnitude smaller for this structure.

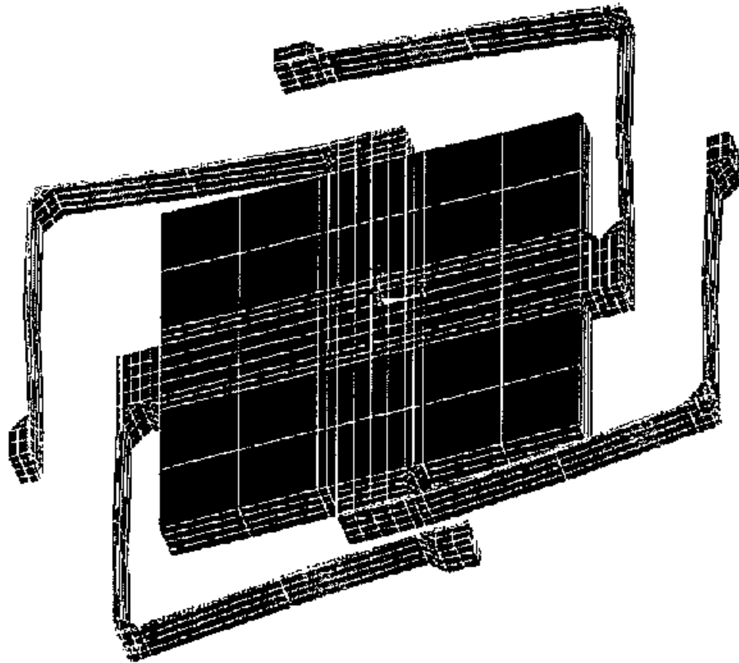

In- and out-of-plane design:

main sensitivities [µm/g]:
$S_y = 0.186\mu m/g$
$S_x = 0.186\mu m/g$
$S_z = 0.025\mu m/g$

cross-axis sensitivities [%]:
$S_{yx} / S_y = S_{xy} / S_x = 1.6\%$
$S_{yz} / S_y = S_{xz} / S_x = 0.07\%$
$S_{zy} / S_z = S_{zx} / S_z = 0.02\%$

Figure 2.11: FEM model (left) of a structure sensitive to accelerations parallel to the in- and out-of-plane directions, like design 8 and 9. Data regarding mechanical sensitivities is given on the right side. Dimensions of the structure are: L1 = L2 = 2620µm, w = 45µm, l = 360µm, m=13.4mgr.

2.4.2 Modal analysis

A modal analysis shows the different shapes of resonance vibration. In addition, a calculation of the corresponding resonance frequencies is useful to estimate the possible bandwidth of the device.

Vibration modes and resonance frequencies

The dynamic analysis of design 1 with two different geometries is given in table 2.1 (case A and case B). The first resonant frequency of the structure corresponds to a vibration along the main sensitive axis (x-direction). The second resonant frequency was found for vibrations in the vertical (z-) direction). The third fundamental frequency is a rocking mode where the seismic mass tilts around the y-axis. For case A, the frequency of the third mode is close to the second mode, but this is not generally true, as demonstrated with case B. The fourth frequency is much larger and consists of a tilt- or rocking mode around the x-axis. In the fifth resonance mode, resonance occurs for vibrations along the y-axis. Table 2.1 shows a comparison between analytical model and the performances computed with ANSYS of design 1 for two different dimensions (case A and B). For design 3 and 4 similar resonance modes can be found.

One have to consider the trade-off between mechanical sensitivity and resonance frequency, meaning that any increase of the sensitivity by a factor X will reduce the first resonant frequency of the structure by a factor $X^{-1/2}$. For example, increasing the sensitivity of design 1

(case A) by a factor X=144 from 6.6nm/g to 950nm/g reduces the first resonance frequency from 6.1kHz to 508Hz.

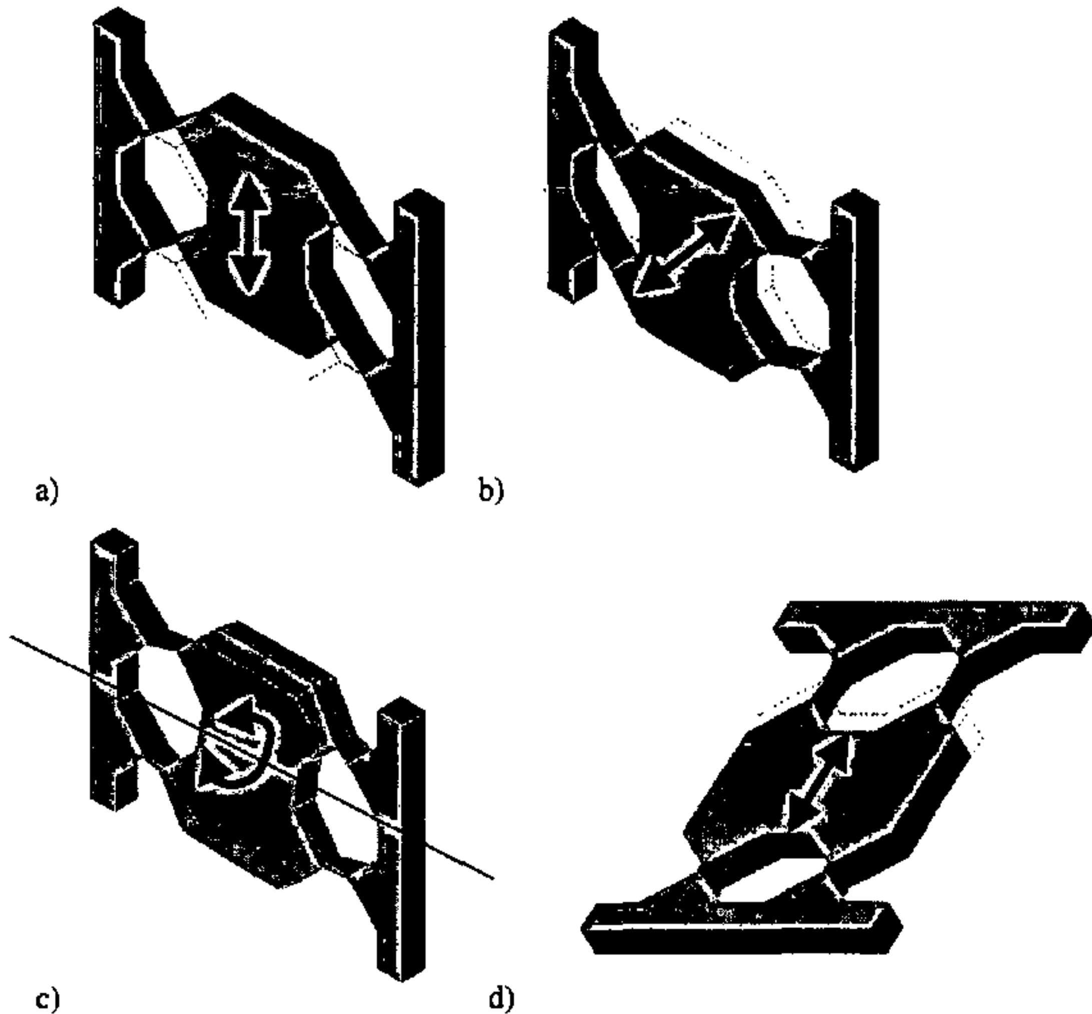

Figure:2.12: Different resonance modes for design 1: a) 1st mode (translational vibration in x-direction), b) 2nd mode (vibration in z-direction), c) 3rd mode (tilt-mode around y-axis) and d) 5th mode resonance (vibration in y-direction).

2.5 Comparison between theory and experiments for static displacements

In order to check the analytical and the finite element model experimentally, static measurements were performed. Static mechanical tests were carried out by loading the seismic mass with microweights. The corresponding deflection was measured with a non-contact optical comparator, as shown in figure 2.13.

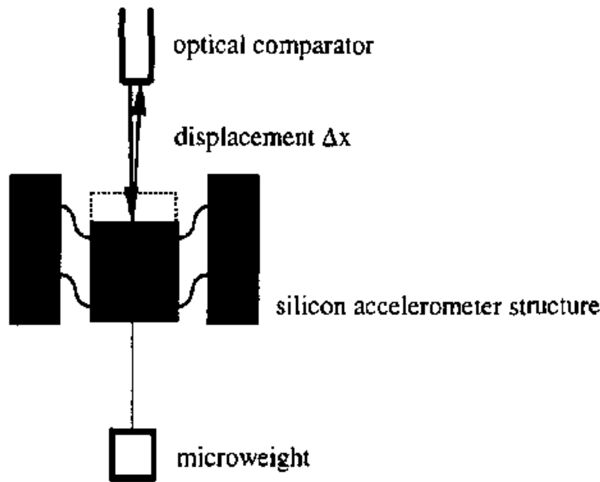

Figure 2.13: Measurement setup to determine experimentally the displacement of the seismic mass due to an external force. The accuracy of the optical comparator is 1-2μm.

2.5.1 Static measurements for in-plane structures

Linear displacements (small deflection theory)

In the FEM simulation a force corresponding to the microweights was applied in the middle of the mass. Considering design 1 (table 2.1, case A), the computed mechanical sensitivity is 154.3μm/mN. The results show that experimental results agree nicely with the simple linear analytic model as well as with the FEM simulation (see figure 2.14) for small displacements (displacements smaller than beam width w).

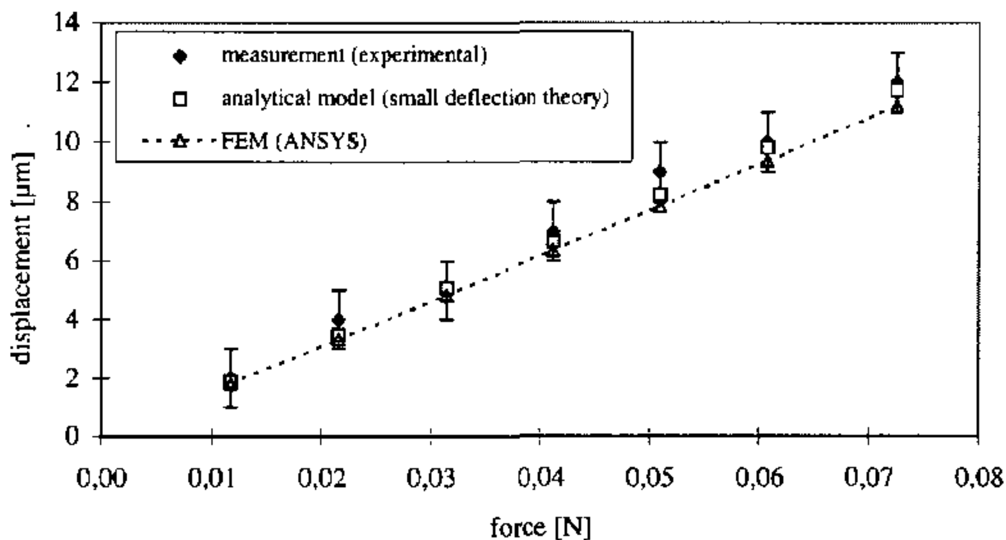

Figure 2.14: Comparison between experimental results and data obtained from the analytical model and the FEM simulation, considering only linear displacements (for design 1 with dimensions as shown in table 2.1).

Nonlinear displacements (large deflection theory)

Considering in-plane structures with a higher mechanical sensitivity, larger displacements will occur leading to nonlinear effects. Here, the simple linear analytical model, also called small deflection theory, reaches its limit and theoretical description by FEM or other numerical simulation which can handle these nonlinear effects becomes necessary (large deflection theory). But still, accurate description of the nonlinear effects for large displacements is difficult. As it can be seen in figure 2.15 the theoretical response obtained by ANSYS overestimates the nonlinear effect. For the accelerometer application treated in this thesis, inertial forces are small, thus generally small and therefore linear displacements can be assumed. From experiments we can conclude that nonlinearity remains neglectable as far as the displacement is smaller than the beam width. This is in disagreement with the nonlinear analysis performed by ANSYS where the nonlinearity appears for smaller displacements. This means that in reality less stress is in the beams as predicted by ANSYS. One explication for this mismatch could be that the beam clamping is not precisely represented in the ANSYS model.

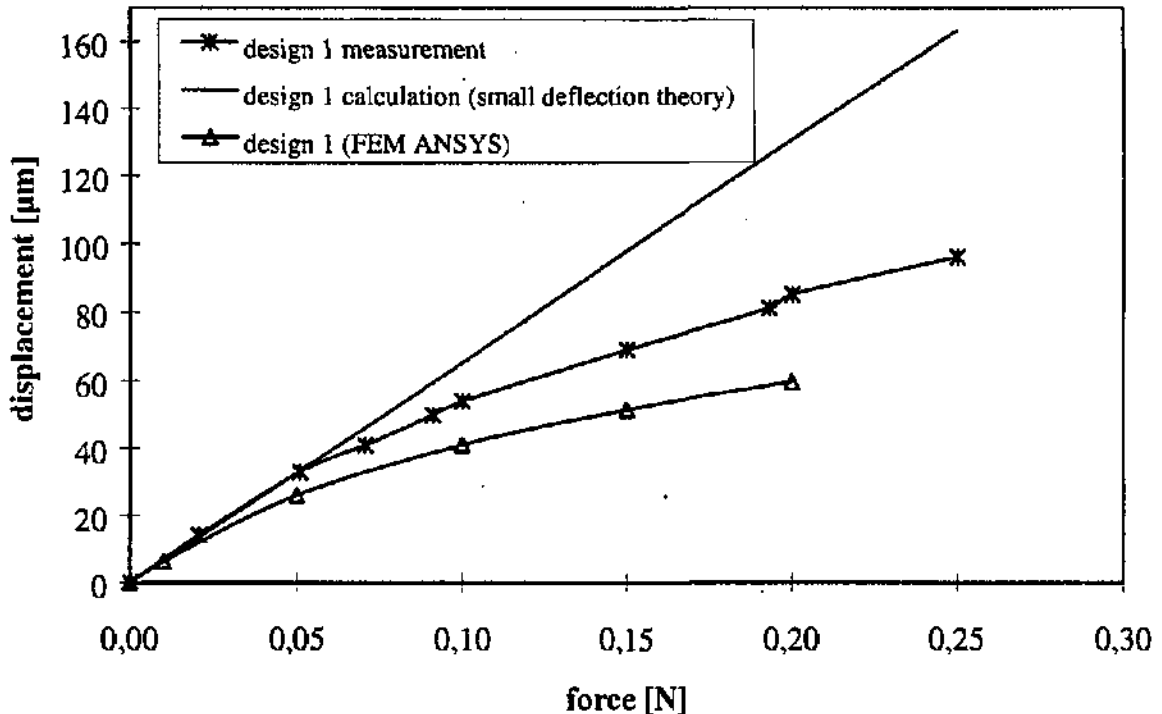

Figure 2.15 : Experimental and theoretical mechanical displacement of a structure like design 1, with high sensitivity. The displacement is due to an applied force. The measured nonlinearity is lower than calculated with FEM (ANSYS). The measurements have been done with an external optical comparator.

2.5.2 Static measurement for out-of-plane structures

For the out-of-plane structures (design 5, 6 or 7) measurements have been made as well. In figure 2.16 the experimental determined displacements are compared with the small deflection theory (analytical model). As in the case of the lateral structures the nonlinearity dominates in the displacement vs. force curve for displacements larger than the beam thickness.

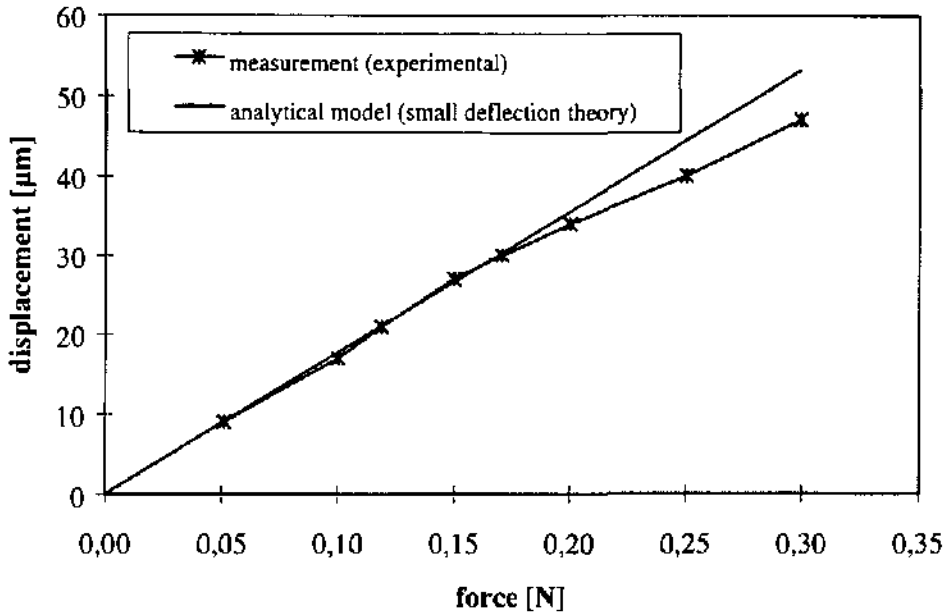

Figure 2.16: Displacement measurement for an out-of-plane structure (design 6) with a beam thickness t of 32µm.

2.6 Comparison of different designs

As earlier mentioned, the mechanical sensitivity can be increased in several ways. Increasing the sensitivity by decreasing the beam width w leads to an increase of the nonlinearity. Due to thinner beams, the stress increases and with that, the nonlinearity. Therefore an increase of the beam length can be recommended to improve the sensitivity. For the design 1, pictured in figure 2.2a), an increase in the beam length would take much more space on the chip. Design 2, 3 or 4 present alternative designs, which offer the improvement of longer beams without scarifying more space on the chip. A comparison between the designs 1, 3 and 4 regarding mechanical cross-sensitivities and dimensions is shown in table 2.3.

	design 1 (4 beams)	**design 3** (2 beams sym.)	**design 4** (2 beams asy.)
S_y [µm/g]	0.941	0.981	0.981
S_{yx}/S_y	0.0003%	0.001%	0.04%
S_{yz}/S_y	0.0009%	0.001%	0.002%
S_z/S_y	0.1%	2%	1.9%
S_x/S_y	0.008%	0.02%	0.02%
beam length L	1275µm	4440m	4440
beam width w	10µm	45µm	45µm
chip size [µm²]	8100 × 6000	4100 × 6000	4100 × 6000

Table 2.3 : Comparison based on FEM results between the three structures from figure 2.9 (design 1,3 and 4) regarding mechanical sensitivity and cross-sensitivities (mass m=10.2mgr., beam thickness t=380µm).

The fabrication process described later can manufacture beams only with a certain accuracy for the width. This accuracy of the suspension beam width depends on several parameters, like for example the variation of the wafer thickness, the initial misalignment of crystal axis in the silicon wafer and the alignment accuracy of the lithography. As it can be concluded from the analytical formulae for small displacements (2.2 and 2.12) the mechanical sensitivity varies less for larger beams (see table 2.4). Also, due to larger beam width, the linearity is well improved in design 3 and 4 (see fig. 2.10, table 2.2).

Accuracy of beam width	Variation in sensitivity	
	4 beams (design 1)	2 beams (design 3, 4)
+/- 1 µm	30 %	6 %
+/- 0.1 µm	3 %	0.6 %

Table 2.4: Comparison of the different structures regarding reproducibility (variation of sensitivity due to beam width accuracy in the fabrication process). The mechanical sensitivity is assumed to be identical for all structures (about 1µm/g).

2.7 Mechanical-thermal noise

The most fundamental noise source that can be found in all accelerometers is the mechanical-thermal noise. Mechanical-thermal noise is a direct consequence of the molecular motion associated with thermal equilibrium (Brownian motion). The Mechanical agitation of the seismic mass due to thermal energy set the noise floor in highly sensitive micromachined accelerometers. This noise floor does not depend on the read-out principle, but only on the mechanical parameters such as mass m, Q-factor and mechanical sensitivity S. Considering the spring-mass model for the accelerometer (figure 2.6 and equation 2.1) with a frequency independent damping, the noise equivalent acceleration a_{min} for equilibrium thermal noise is given by [Gab93, Gab95]

$$\frac{a_{min}}{\sqrt{\Delta f}} = \sqrt{\frac{4 \cdot k_B \cdot T \cdot \omega_x}{m \cdot Q_x \cdot \Delta f}} = \sqrt{\frac{4 \cdot k_B \cdot T}{m \cdot Q_x \cdot \sqrt{S_x} \cdot \Delta f}} \qquad (2.22).$$

As we can see from equation (2.22), a_{min} consists of a constant part, $(4\ k_B\ T)^{1/2}$, and a part only depending on the sensor mechanics, $(S_x^{-1/2}\ m^{-1}\ Q^{-1})^{1/2}$. Taking parameters of a bulk-micromachined accelerometer, such as a mass of 10mgr, a mechanical sensitivity of S_y=1µm/g and an assumed Q-factor of 1, the minimum detectable acceleration equals 0.2µg/√Hz. For surface-micromachined accelerometers this limit is generally some orders of magnitude higher due to the much lower mass. Surface-machined devices with a high resolution, like [Cha96] and [Lem97], are therefore limited by their mechanical-thermal noise.
Decreasing the equivalent thermal acceleration noise could be done by increasing either the seismic mass m, the Q-factor or the mechanical sensitivity. However, in practice all these possibilities to reduce the thermal noise floor are critical [Gab93]. Increasing the seismic mass is in contrast to miniaturization. Increasing the mechanical sensitivity reduces the resonance

frequency and with that, the usable bandwidth. A large Q-factor can cause the problem of introducing oscillations with a long duration when rapid acceleration changes should be measured.

2.8 Conclusion of chapter 2

Different designs

In this chapter presents nine different mechanical designs for accelerometers, so called seismic mass systems. Four of them are devoted acceleration measurements parallel to the waferplane and three to measure accelerations that are perpendicular to the waferplane. Combining two lateral accelerometers and one vertically sensitive accelerometer in one substrate offers the three-dimensional measurement of accelerations with one monolithic chip. Due to the highly symmetrical suspension with high-aspect ratio beams the movements of the masses are purely translational and mechanical cross-sensitivities are very small (<0.1%). Alternatively, two designs are presented for measuring accelerations in- as well as out-of-waferplane, opening the way to a 3D accelerometer consisting of one single seismic mass. However, this possibility leads to higher mechanical cross-sensitivities.

Analytical modeling

The analytical modeling of these structures is based on a second order spring-mass-system. Explicit formulae for the spring stiffness allows to calculate the mechanical sensitivity of these designs. The damping for the in-plane structures is caused mainly by lateral film damping, while for the out-of-plane structures the dominant damping type is squeeze film damping. Finally, the mechanical transfer function describing the dynamical behavior is given. The analytical model is very suitable to describe the mechanical response of the accelerometer structures for small displacements.

Finite element simulations

However, to calculate effects such as nonlinearity due to large displacements (displacement > beam width), mechanical cross-sensitivities, higher resonance modes or more complicated shaped beams, finite element simulations are preferable. Using ANSYS the static and dynamic behavior of the proposed designs is computed. In general, considering small displacements, predictions from the FEM analysis and from the analytical model agree within 10%.

Displacment measurements

In addition, static measurements with an external optical comparator have been performed to confirm the theoretical calculation. Here as well analytical and experimental results agree well for small dispalcements. However, nonlinear displacements due to higher forces are overestimated by ANSYS.

Comparison of different designs

Comparing the different mechanical designs, we have to find a tradeoff between cross-sensitivities, chip size, variation of sensitivity due to fabrication tolerances and linearity. Designs offering longer instead of thinner beams seem to be the best choice to improve the main sensitivity. As one fundamental aspect in designing accelerometers, one has to consider that mechanical sensitvity and first resonance frequency are related. Limiting the first resonance frequency to 500Hz to a operate in a bandwidth of at least 100Hz, we can increase the mechanical sensitivity up to 1μm/g.

Thermal-mechanical noise

Finally, investigating the level of thermal-mechanical noise, one can derive that for bulk-micromachined accelerometers the detection limit is not determined by mechanical-thermal noise, but by the read-out mechanism. Therefore, bulk-micromaching of silicon is very suitable to obtain accelerometers with resolutions in the μg-range and even below.

CHAPTER 3

3. Unconventional bulk-micromachining using underetching of (100) silicon

3.1 General aspects of anisotropic wet-etching of silicon

3.2 Fabrication of in-plane accelerometer-structures

3.3 Etching simulation and limitations for in-plane structures

3.4 Fabrication of a monolithic tri-axial seismic mass system

3.5 Some other micromachined structures

3.6 Conclusion of chapter 3

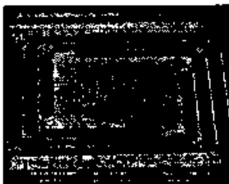

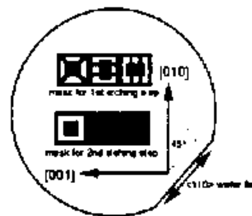

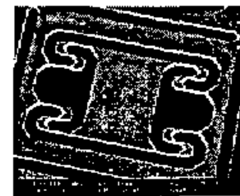

3. Unconventional bulk-micromachining using underetching of (100) silicon

Anisotropic wet etching of silicon is the most mature bulk-micromachining technology. After a short introduction discussing the general aspects of anisotropic silicon etching, we will describe and investigate some unconventional methods employing wet etching to fabricate two and three dimensional accelerometer structures.

3.1 General aspects of anisotropic wet-etching of silicon

Crystal structure of silicon
A silicon wafer is a single crystal and has the same crystal structure as diamond, i.e. every atom is bound by four neighbors in a tetrahedral configuration. This configuration is also called face centered cubic. Apart from higher order crystal planes, we can count three fundamental atomic planes in the crystal silicon, which can be identified by their so called Miller indices: {100}, {110} and {111}.

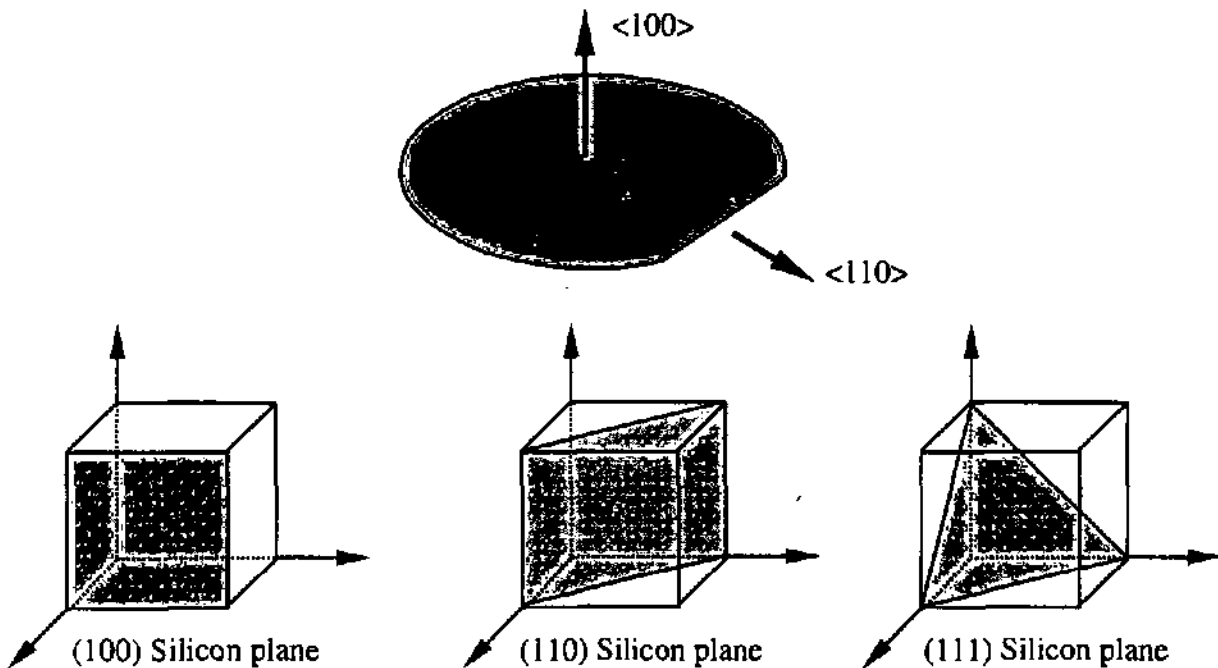

Figure 3.1: Schematic of a (100) silicon wafer (top) and the three most important planes in the silicon crystal demonstrating the cubic lattice structure (bottom).

Anisotropic wet etching
The most important feature of silicon etching in KOH and other agents is the anisotropy of the etch rate, i.e. different etch rates for different crystal directions. The {111}-planes have the slowest etching rate and are therefore almost inert to etchants, while the relative etching rates for the other planes depend on the type of etchant, temperature, concentration, additives etc. KOH

etches the {110}-planes faster than the {100}-planes. For EDP (Ethylene Diamine Pyrocatechol) this ratio is inversed [Ros94].
There exist different explanations of the strong anisotropy of the etchrate. Kenndal suggests that a thin protective oxide layer grows on the {111}-planes, making them nearly inert during etching [Ken75]. But this does not explain the difference between the etchrates of {110}- and {100}-planes. Another explication for the anisotropy in etching is the difference in activation energies of the crystal planes [Sei87, Pal85]. The different activation energies orginate from different binding forces of the surface atoms of different crystal planes.
KOH is the most common agent, because it is easy to handle, readily available and it etches fast. The often declared disadvantage of KOH is that it contains potassium and traces of sodium, which contaminates wafers and furnaces, and make it IC incompatible. However, very recently Munch ea. suggested a protection method for the front side of fully processed CMOS wafers against KOH attack [Mun98]. The scientists from ETH Zürich demonstrated with the help of secondary ion mass spectroscopy that the total alkaline contamination after KOH is not higher than in the unetched layers if the etched layer is cleaned using the standard RCA cleaning procedures
A possible alternative to KOH is EDP. EDP is IC-compatible, but it is strongly poisonous and inconvenient to work with. More promising is tetramethyl-ammonium-hydroxides (TMAH). In addition, there exist etchants that etch silicon isotropically, e.g. hydrofluoric acid [Ros94].
Most times anisotropic etching of (100) silicon wafers is used to fabricate devices with pits or V-grooves which have {111}-sidewall faces along the <110>-mask directions, taking advantage of the low etching rate of {111}-planes (see figure 3.2a). If the mask is not aligned parallel to the <110>-wafer flat, but turned 45° and therefore aligned along the <100> direction, U-grooves will be generated having perpendicular walls (see fig. 3.2b).
In the following section the unconventional etching technique with a 45° mask alignment is used to fabricate accelerometer-structures. When this work was started, only very few papers have already been published dealing with this technique. Among the first publications one can find work from Tenerz [Ten89] and Choi [Cho92]. But in the last three years this technique became more popular, and some more papers appeared using the underetching of vertical {100} silicon planes to fabricate MEMS [Nik96, Nik97, Che97, Frü97, Han98, 1, 2, 9, 13].

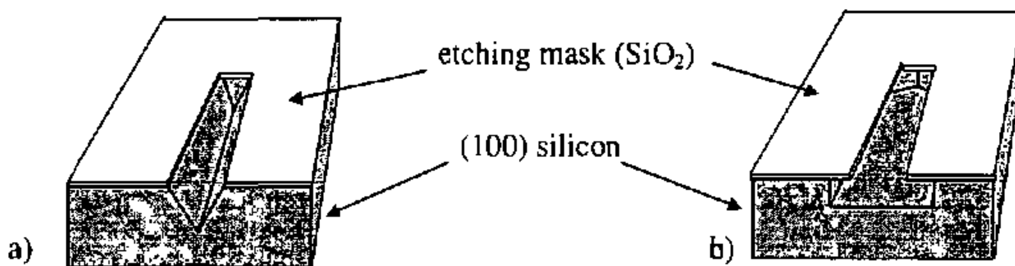

Figure 3.2: V-groove, bounded by {111}-planes with an angle of 54.7° from the surface (a). Here, the rectangular mask pattern is aligned parallel to the <110> wafer flat. U-groove, bounded by {100}-planes by an angle from 90° to the wafer surface (b). The mask pattern is in this case turned by 45° regarding the <110> wafer flat.

3.2 Fabrication of in-plane accelerometer-structures

This section describes the method to fabricate symmetrical structures with high aspect ratio and vertical sidewalls suspension beams. Experimental results are presented to demonstrate the fabrication principle. The contents of this section has been published in [1].

3.2.1 Principle: underetching of {100} silicon planes

The fabrication principle is bulk-micromachining based on the anisotropic etching of a double sided polished (100) silicon wafer. As mentioned above, {111} planes in silicon have the lowest etch rate among all planes and act therefore as an etch-stop surfaces. In (110)-oriented silicon wafers this property is used to fabricate beams with vertical sidewalls [Tir95, Sto96]. However, in that case the vertical {111} planes intersect each other at an angle of 109.48°, leading to parallelogram-shaped structures, which does not allow to make two identical devices at right angle. On a (100) wafer it is not possible to achieve vertical sidewalls if the pattern is aligned in the usual direction, which is parallel to the <110> wafer flat. That is the reason why, in many conventional bulk-micromachined accelerometers, the seismic mass is pyramidal and not symmetrically shaped. The emerging planes appearing at the intersection of (100)-(001) planes makes a 45° angle with the <110> wafer flat. Thus, uniform and flat vertical {100} sidewalls in a (100) wafer are achievable, if the pattern is aligned with a ±45° angle from the wafer flat (see figure 3.3 and 3.4). However, this alignment will also result in a large undercut of the mask which is equal to the etch depth d_{etch}. In order to obtain a beam width of w, the width of the mask pattern w_M must therefore be equal to

$$w_M = w + 2\, d_{etch} \qquad (3.1).$$

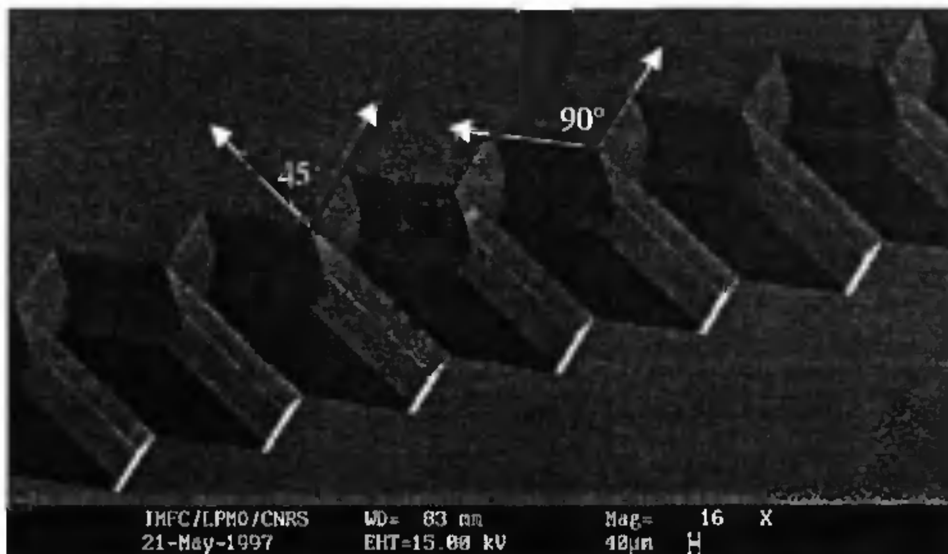

Figure 3.3: SEM view of a row of vertical beams etched in (100) silicon.

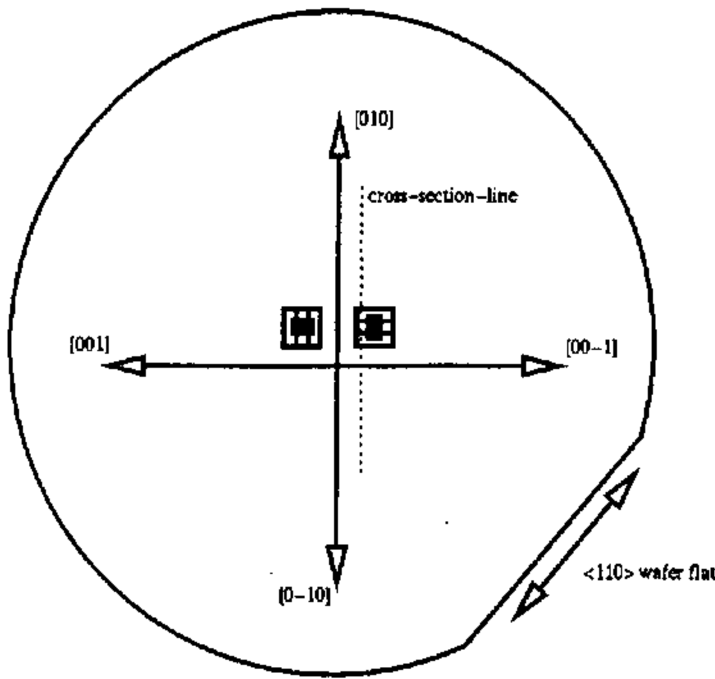

Figure 3.4: The mask pattern is aligned with a rotation of 45° from the <110> wafer flat. Due to the crystal orientation of the {100} planes, two identical structures rotated by 90° are feasible on the same wafer within the same etching step.

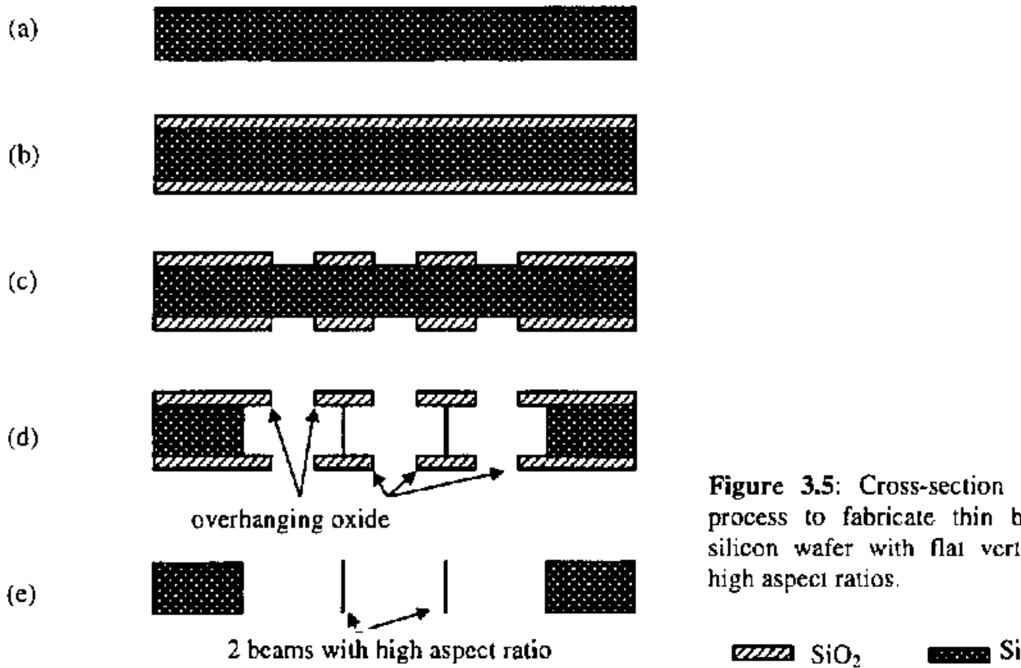

Figure 3.5: Cross-section of the fabrication process to fabricate thin beams on a (100) silicon wafer with flat vertical sidewalls and high aspect ratios.

Figure 3.5 shows the fabrication process. Thermal SiO_2 is used as a mask material. The pattern is aligned at 45° from the <110> wafer flat on both sides of the silicon wafer (see figure 3.4) with a double side aligner. This alignment gives the possibility to fabricate two perpendicular devices, or two perpendicular beams with vertical sidewalls, on one (100) silicon wafer in the same etching process. For an improved alignment, a further step can be integrated : test structures may be etched into the wafer to reveal {100} planes, as shown in figure 3.6 [Ens96]. These structures can be used as marks for a more precise alignment. Another possibility is to cleave the wafer parallel to the <110> crystal orientation.

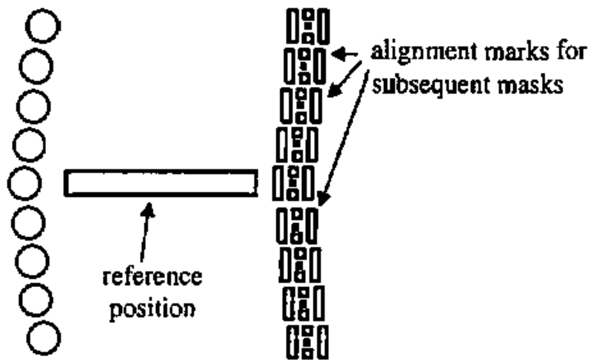

Figure 3.6: Circular shaped test-structures positioned on an arc used to reveal the crystal orientation of a (100) silicon wafer. When silicon is etched through these masks, squares are formed that are misaligned or displaced regarding each other. The three most closely structures indicate the <110> direction. Associated with each circular window is an alignment aid for subsequent mask, which is etched at the same time [Ens96].

After exposure and development of the photoresist (in our case AZ 5024), the thin oxide layer was etched in a buffered HF solution (BHF). During the subsequent etching process in the KOH solution, the dimensions of the structure are controlled by time and also visually in the first experiments. Later, the width of the vertical beams was controlled by a test structure, which has been included with a mask-beam width $w_{M,test} = w_M - w$. This structure will fall down if the desired beam width w_M is achieved [Ren97]. Experimentally, we achieved to control by this mean the beam width with an accuracy of typically +/- 1µm. When the wafer is etched through, a lower temperature of the KOH solution may be used in order to lower the etching rate and to achieve a higher accuracy [Nik96]. When the desired dimension is achieved, the overhanging oxide is removed with a buffered HF solution.

3.2.2 Experimental results

To demonstrate the described process, 93 structures were fabricated on a 3-inch (100) silicon wafer. We used a KOH solution (KOH/H_2O 41% wt.) at 55°C. With this combination of temperature and concentration smooth surfaces can be produced. Figure 3.7 shows a beam of one device when the wafer is just etched completely through. Note the very symmetric approach of the {111} planes at the end of the beam, due to the double side etching. At this stage, the beam width is 97 µm. The sidewalls of the beam are vertical with flat surfaces. The oxide is not yet removed in order to enable further etching.

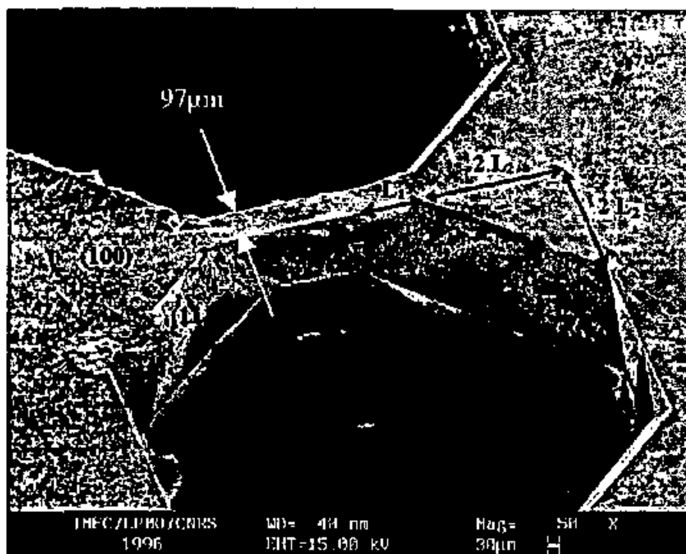

Figure 3.7: Close up view of one beam. The beam width is 97 µm. Note the very symmetric approach of the {111} planes at the end of the beam.

A beam width of 11 µm was accurately achieved when etching was continued, as shown in figure 3.8. In the middle of the wafer, the edges of the {111} planes intersect. These edges were attacked by the etch solution and etched away. The vanishing of the sharp edges changes the clamping conditions of the beam, which improves the mechanical sensitivity of the structure. For the given structure, FEM simulation shows that the sensitivity is increased by a factor 8.5 due to etching of the {111} plane edges. The whole device is shown in figure 3.9. The symmetry is remarkable and the achieved aspect ratio (beam thickness t over width w) is 35.

At the upper part of the beam's sidewalls in figure 3.9 an imperfection of the crystal plane is visible. This imperfection is due to the alignment error of the double sided alignment. A little misalignment, typically on the order of 1 µm leads to a step between the upper and lower part of the beam's sidewall. This step will be etched perpendicularly to the wafer plane which causes the imperfection to moves during further etching, towards the wafer surface. For the other side of the beam's sidewall, an inverted step can be seen and will move towards the opposite wafer surface (see schematic in figure 3.10).

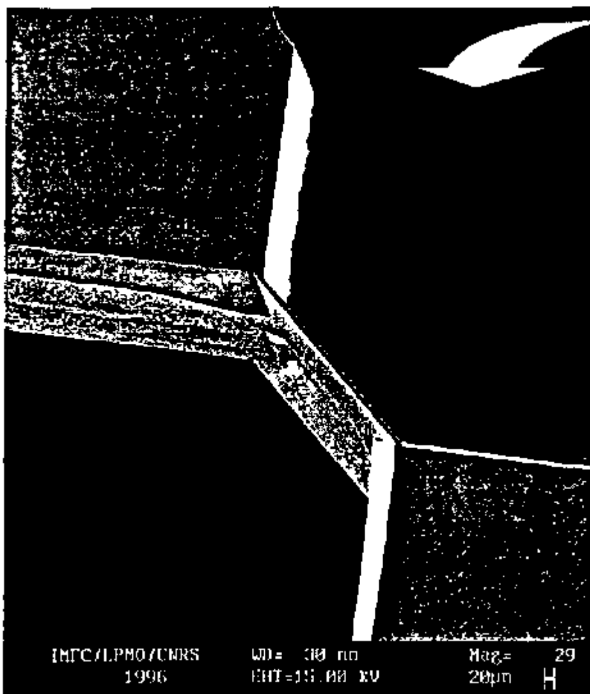

Figure 3.8: Close up view of the beam in figure 3.7 after continued etching. The beam width is now 11 µm corresponding to an aspect ratio of 35.

Figure 3.9 (right): SEM view of the complete symmetrical structure.

Beam cross-section just after etch-through

Step propagation after further etching

Figure 3.10: Cross-section of the vertical suspension beam shown in figure 3.8. It illustrates the moving of a step due to mask misalignment towards the wafer surface.

Undercut directions

The planes on which the underetching stops are illustrated in figure 3.11. The undercut plane's directions can be identified from the direction of their intersections with the wafer plane. The angle α between the traces of two planes is given by :

$$\cos(\alpha) = \frac{\vec{r}_1 \cdot \vec{r}_2}{|\vec{r}_1| \cdot |\vec{r}_2|} \qquad (3.2)$$

where $\vec{r}_1$ and $\vec{r}_2$ denote the projection on the wafer surface of the undercut plane's directions. Table 3.1 shows that the angles calculated from equation 3.2 agree very well with those measured from the fabricated structure.

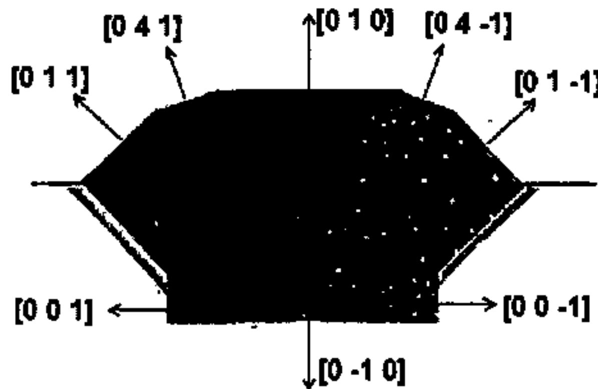

Figure 3.11: Undercut directions for one part of the seismic mass.

$\angle(\vec{r}_1, \vec{r}_2)$	$\text{angle}_{\text{theoretical}}$	$\text{angle}_{\text{measured}}$
$\angle$([0 4 1], [0 -4 1])	151.93°	152° ± 1°
$\angle$([0 1 1], [0 1-1])	90°	90° ± 1°
$\angle$([0 -1 0], [0 4 1])	165.96°	166° ± 1°
$\angle$([0 -4 -1], [1 1 0])	149.04°	150° ± 1°

Table 3.1. Angles between undercut directions (theoretical and measured).

3.2.3 Design rules for the photolithography mask

In the following section, design rules for the layout of the photolithography mask are developed. Figure 3.12 shows pictures of the mask and the fabricated structure, respectively. It illustrates how the etching progressed from the initial mask to the final structure.

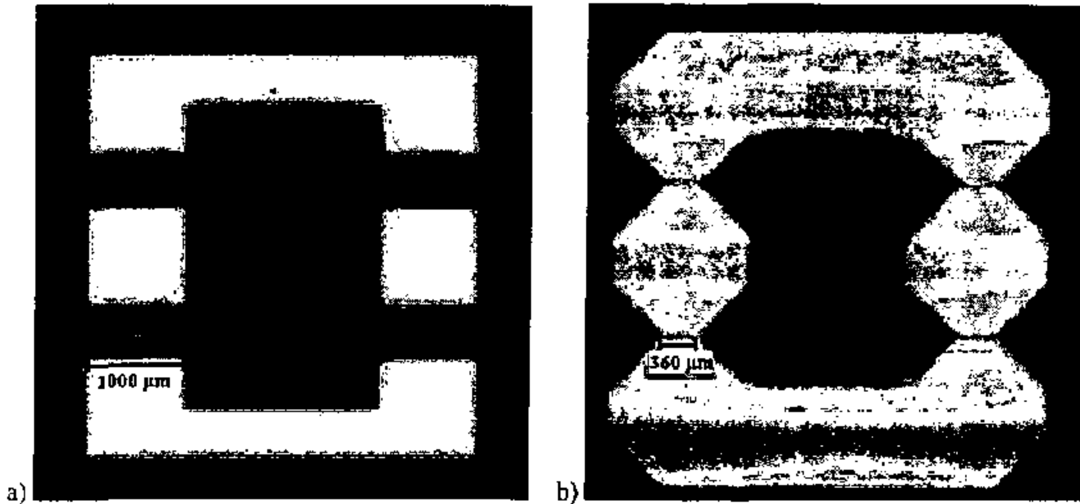

Figure 3.12:. Pictures of the photolithography mask (a) and of the fabricated mechanical silicon structure (b). Both are on the same scale.

The mask area for the beam is given by $w_M \times L_M = 500\ \mu m \times 1000\ \mu m$. w_M is the mask width and L_M is the mask length for the beam. To calculate the real size of the fabricated beam, one has to take the etching duration into consideration. The time required to etch from both sides the wafer completely through is given by $T_1 = ½\ t \times (R_{<100>})^{-1}$, where t is the wafer thickness and $R_{<100>}$ the etch rate in the <100> directions. Considering etching conditions reported in paragraph 3.2.2 (KOH 41% at 55°C), the etch rate $R_{<100>}$ is approximately 0.255 µm/minute. In this condition, for a 380µm thick wafer, T_1 equals approximately 12 hours and 25 minutes.
The etch time to reach a desired beam width w, with a given mask parameter w_M, is given by $T_2 = (w_M - w) \times (R_{<100>})^{-1}$. If a clamping with {111} planes (as shown in figure 3.7) is desired, T_1 must be equal to T_2 :

$$T_1 = T_2 \quad \Leftrightarrow \quad ½\, t \times (R_{<100>})^{-1} = (w_M - w) \times (R_{<100>})^{-1} \qquad (3.3).$$

Thus, the mask beam width is then given by

$$w_M = t + w \qquad (3.4).$$

If a clamping like in figure 3.8 is desired, the mask beam width must be larger than t + w, e.g. 500 µm.
The effective length L of the fabricated beam, which is the distance between the two clamped ends, is given by $L = L_M - 2\,L_1 - 2\,L_2$, where L_1 and L_2 are indicated in figure 3.7. L_1 equals $t \times [2\tan(54.74°)]^{-1}$, where the angle 54.74° denotes to the angle between the {100} surface of the wafer and the {111} clamping planes. L_2 is given by $R_{<100>} \times T_1 = t$. To summarize, one gets the following design rule for a mask beam length L_M and an effective length L of the fabricated beam:

$$L_M = L + \frac{t}{\tan(54.74°)} + t \approx L + 1.707 \cdot t \qquad (3.5).$$

In the case of the fabricated structure in figure 3.9, the realized beam length is 360µm while the calculated beam length equals 352µm: the difference is due to the fact that etching was continued after the wafer was etched through.

More lateral accelerometer structures

Using the same technique of underetching employed above for the fabrication of a seismic mass suspended by four beams, other types of in-plane accelerometer structures have been realized. Figure 3.13 a) and b) show SEM images of masses suspended by only two long beams (design 3 and 4, see section 2.1.1). One mass suspended by folded beams is demonstrated in c). And figure 3.13 d) shows a realization of design 2 as proposed in section 2.1.1. Due to the vertical beams, all structures have a main mode in the in-plane direction, and are nearly insensitive to out-of-plane accelerations due to the high aspect ratio of the beams.

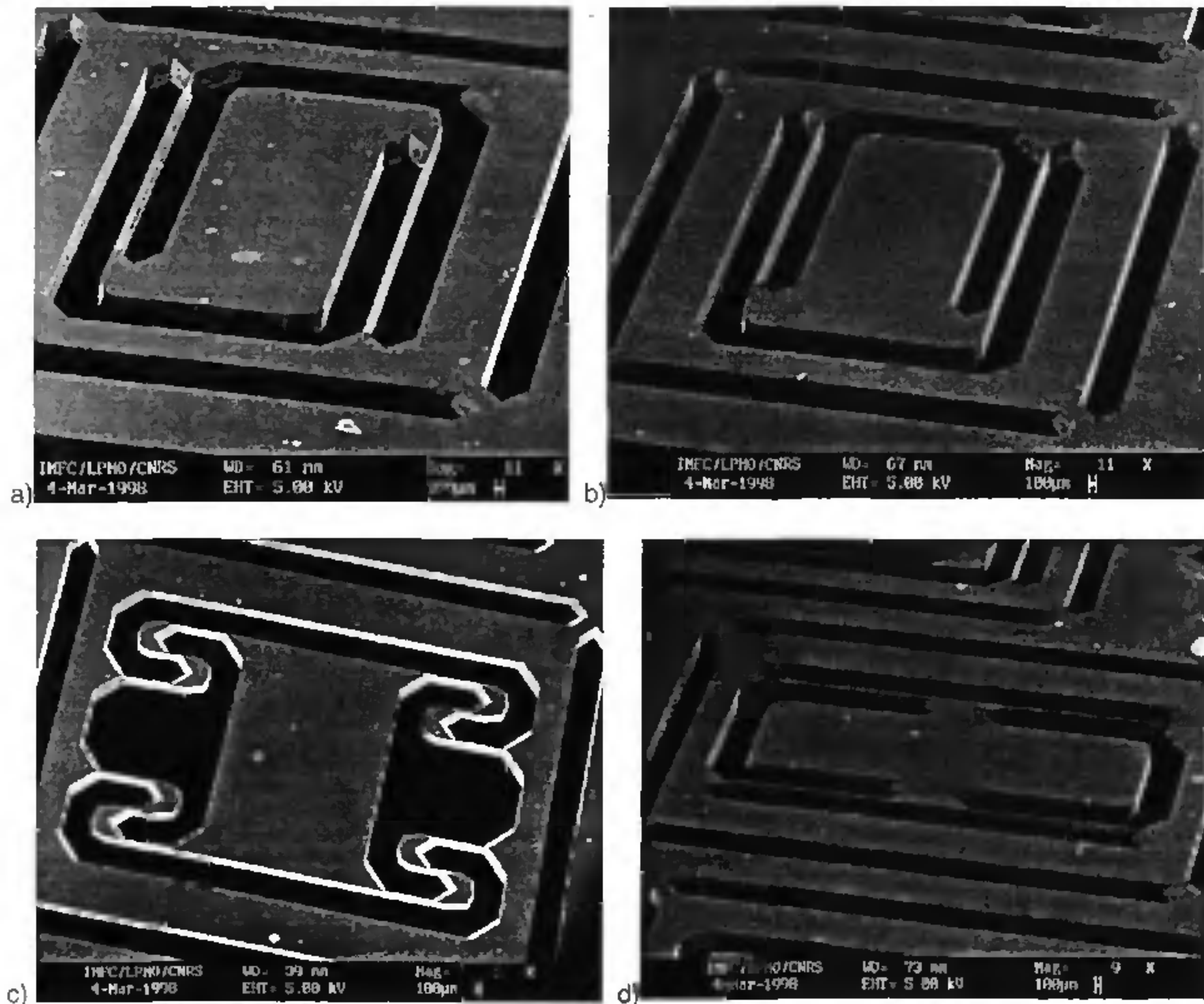

Figure 3.13: Some seismic masses with a different configuration of suspension beams. All structures are etched in one step.

3.3 Etching simulation and limitations for in-plane structures

The above demonstrated etching process is able to produce silicon structures within a certain fabrication tolerance. Due to the tolerances for different batches, variations in the accelerometer's mechanical performance will occur. For example, the sensitivity will vary due to the accuracy of the suspension beam width and length. This accuracy depends on the initial misorientation of the crystal axis in the wafer, the variation of the wafer thickness, and the alignment accuracy of the lithography mask. A 3D etching simulation tool was developed at the IMFC by C. Tellier ea.

[Tel91, Tel97, Bra91]. By using this tool, the variations in the structure's geometry are investigated to determine the variations in sensor performance. By this way, the limits of the technique of underetching of vertical {100} silicon planes is shown. This section describes the joint work between the LCEP and LPMO both members of the IMFC.
After a short introduction into the simulation of anisotropic etching, the theoretical results for the etched structures are presented. Further on, the influence on the mechanical performance is discussed. The main results concerning the etching simulation have been published in [13].

3.3.1 Simulation of the anisotropic etching

Numerical simulation of 3D etching shapes
The employed simulation software is based on a tensorial model for the anisotropic wet etching of crystals [Bar91, Tel91]. In this model the starting surface is decomposed into a succession of planar surface elements corresponding, for silicon, to crystallographic planes. The orientation of the surface element is defined by two angles of cut (φ, θ). To each surface element a so called dissolution slowness vector is associated which characterizes completely the anisotropic dissolution process. In the case of chemical wet etching of silicon in KOH, the anisotropic process is essentially governed by the very large dissolution slowness of the {111} planes (see figure 3.14).
The displacement of the surface element can be evaluated from the equation of slowness surface. Thus it is possible to construct numerically the etched shape of any structure when suitable tests are made to eliminate elements which disappear with prolonged etching. By varying the two angles of cut (φ, θ), the simulation tool allows to investigate the effect of misalignment of the mask-pattern and misorientation of the crystal axis in- and out-of-waferplane. Variations of the etching due to different wafer thickness within one silicon wafer are not considered.

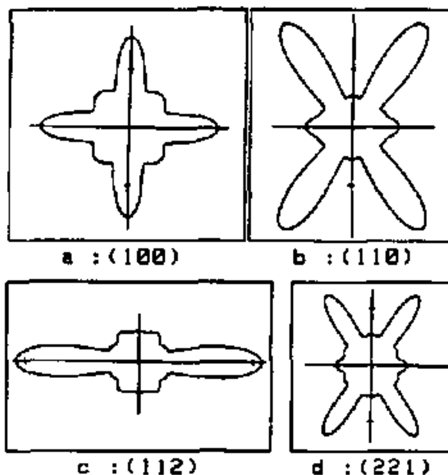

Figure 3.14 : Some cross-sectional polar graphs of the dissolution slowness surface. a) – d) are for the (100), (110), (112) and (221) cross-sectional planes, respectively. In the case of the (110), (112) and (221) sections logarithmic polar plots are drawn owing to a maximum dissolution slowness of the {111} planes [Tel97].

Etching simulation without misalignment or misorientation
In figure 3.15 one see a lateral seismic mass suspended by four vertical beams. The structure was fabricated by the etching process described in section 3.2. In order to compare the experimental results with theoretical shapes, simulations have been performed in a first step without any misalignment of the lithography mask (φ=0°) and without any misorientation of the crystal axis within the silicon wafer (θ =0°). For the seismic mass, as well as for the suspension beams, the numerical results agrees with the experimental observations. This opens the way to further simulations with different configurations for the cut angles φ and θ.

Figure 3.15: a) SEM image of a lateral seismic mass suspended by four vertical beams. b) etching simulation of the left end of the seismic mass and c) of one beam (without any mask misalignment (φ=0°) or crystal misorientation of the wafer (θ =0°)). d) shows the orientation of the lithography mask for the beam which is simulated in c).

Etching simulation for three different cases of misalignment and misorientation

Three different cases for the cut angles φ and θ are investigated. Figure 3.16 shows the simulation of anisotropic etching for one vertical, double-clamped beam for these three configurations. The reference case with φ =0° and θ=0° is shown in figure 3.15 c) and d). In case A, the influence of mask-misalignment is studied, which is the deviation from the parallel alignment to the <100> direction. One can observe with increasing misalignment a decrease in the beam width w and length L by Δw and ΔL, respectively (figure 3.18). In addition, the beam becomes unsymmetrical. Cases B and C represent misorientation of the wafer surface relative to the crystal axis. For case B the main effect is a decrease of the beam length with increasing crystal misorientation while the beam width increases slightly. Thus, for case A and B together, which will also simultaneously occur in practice, the change of the beam width could be partly compensated. Some features of the simulations are well confirmed by experiments (see figure 3.18). In case C the beam length decreases linearly while the effect on the beam width is small.

a) **Case A**: Mask misalignment with no wafer misorientation ($\varphi \neq 0°$, $\theta = 0°$) :

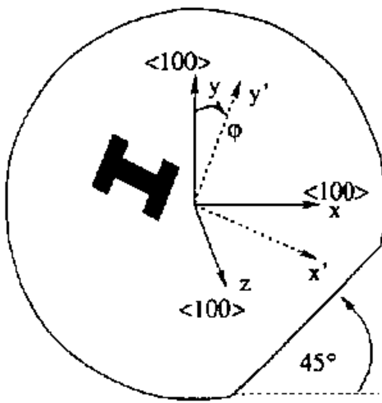

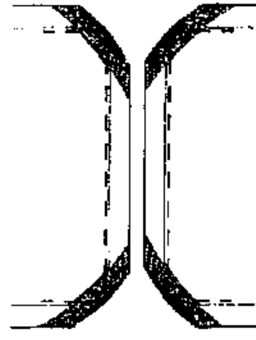

Case A : φ=2.5°, θ = 0°

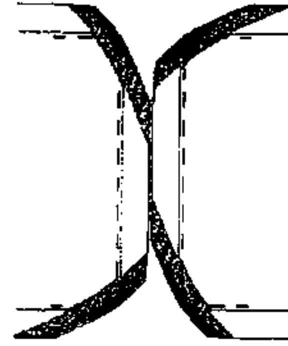

Case A : φ= 10°, θ = 0°

b) **Case B**: Rotation of crystal axes about the in-plane crystal axis (y) with an angle θ and beam aligned perpendicular to y-axis ($\varphi = 0°$, $\theta \neq 0°$) :

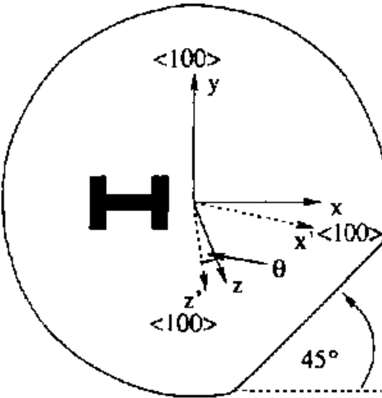

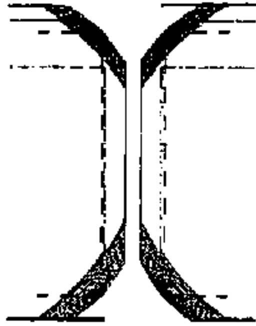

Case B : θ = 5°, φ= 0°

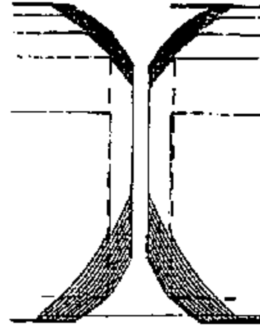

Case B : θ = 10°, φ = 0°

c) **Case C**: Same case as b) with beam aligned along y-axis ($\varphi = 90°$, $\theta \neq 0°$) :

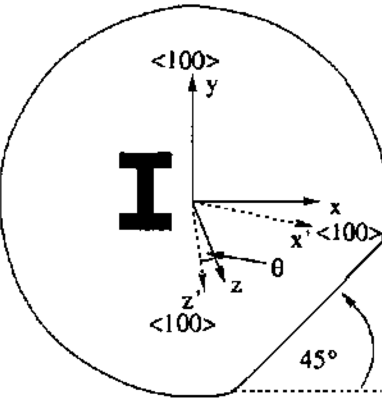

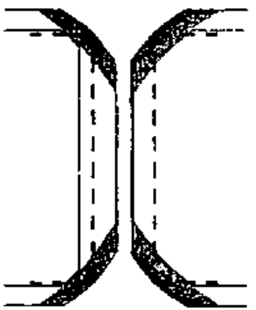

Case C : θ = 2.5°, φ= 90°

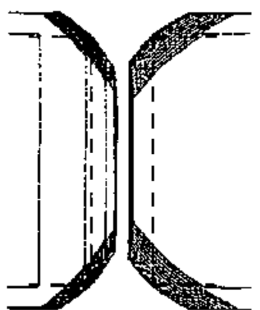

Case C : θ = 7.5°, φ= 90°

Figure 3.16: Etching simulation for three different cases of misorientation and misalignment. To demonstrate the geometrical effects the pictures show cases with large angles (θ, φ), although alignment tolerances around 1° are easily achievable.

a) Case A ($\varphi \neq 0°$, $\theta = 0°$):

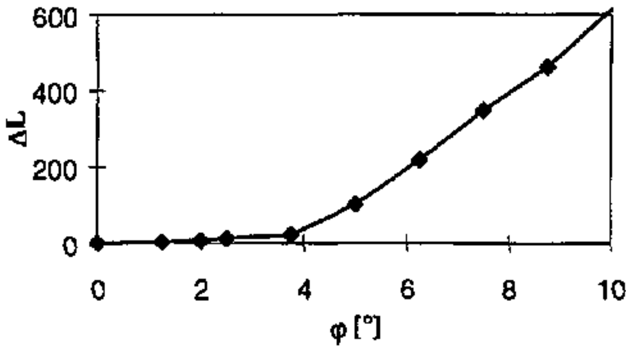

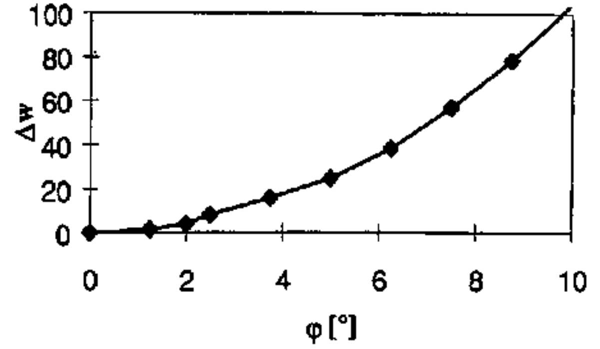

b) Case B ($\varphi = 0°$, $\theta \neq 0°$):

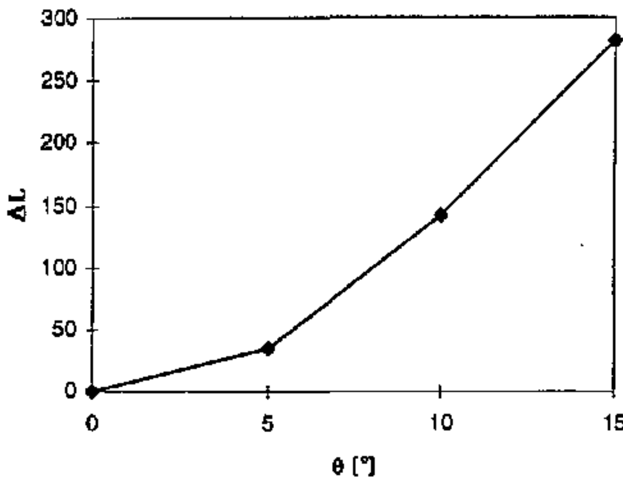

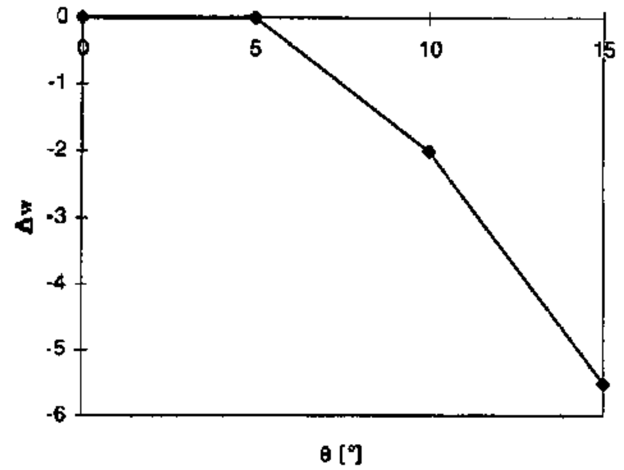

c) Case C ($\varphi = 90°$, $\theta \neq 0°$):

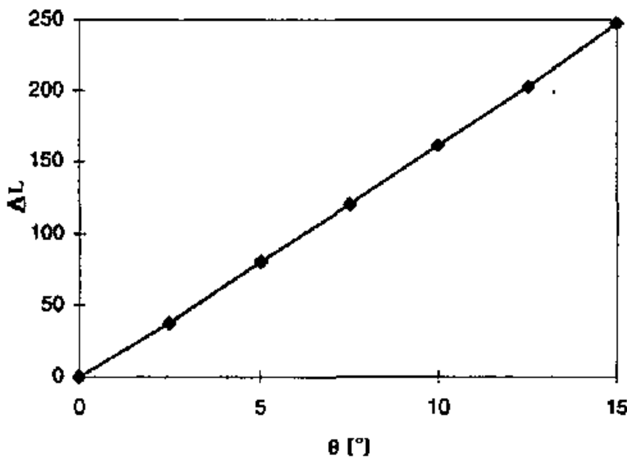

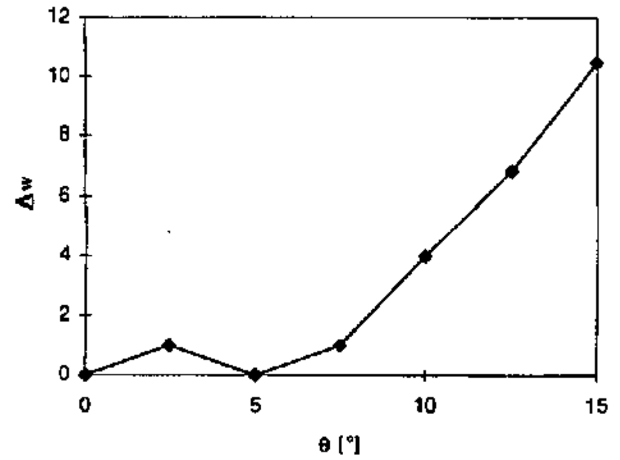

Figure 3.17: Results of the etching simulation for the three different cases A, B and C of figure 3.16. *Case A* (a): increase in the beam length deviation ΔL with increasing angle φ of the mask misalignment (left), and increase in the deviation of the beam width Δw (right). *Case B* (b): increase in the beam length deviation ΔL with increasing angle θ of the crystal misorientation (left) and decrease in the deviation of the beam width Δw (right), which means that the beam becomes larger. *Case C* (c): linear increase in the beam length deviation ΔL with increasing angle θ of the crystal misorientation (left) and small increase in the deviation of the beam width Δw (right).

Figure 3.18: Image of one end of a realized clamped beam as simulated. One can clearly see the unsymmetrical suspension which is mainly due to the in-plane misalignment (φ, case A) of the lithography mask (compare with figure 3.16 a).

The deviations in beam length and width for all three cases are represented in the diagrams of figure 3.16 and summarized in table 3.2 for angles of 1° and 0.1°. By performing a pre-etch to reveal the crystal directions in the silicon wafer, the angle of mask misalignment φ can be typically reduced to 0.1° [Ens97]. The angle θ can be reduced, only by using precisely cut wafers. Fortunately the effects regarding θ are less important than those for φ.

	Case A		**Case B**		**Case C**		**Case A + B**	
	φ = 1°	*φ=0.1°*	*θ = 1°*	*θ=0.1°*	*θ = 1°*	*θ=0.1°*	*φ,θ = 1°*	*φ,θ=0.1°*
Δw	1.2μm	0.4μm	-0.1μm	-0.01μm	0.4μm	0.1μm	1.1μm	0.4μm
ΔL	2.4μm	0.2μm	0.4μm	0.3μm	14.8μm	1.2μm	6.2μm	0.5μm
Sensitivity variation:								
Design 1 (4 beams)	37%	12%	3.9%	0.4%	8.5%	2.7%	32.8%	11.9%
Design 2 (4 beams)	20%	6.1%	1.5%	0.2%	4.4%	1.4%	17.6%	6.2%
Design 3,4 (2 beams)	7.8%	2.6%	0.9%	0.1%	1.7%	0.6%	6.9%	2.6%

Table 3.2: Deviations in beam width and length, and in mechanical sensitivity due to wafer misorientation and mask misalignment. Values are derived from the etching simulations. For the mechanical sensitivities, the initial value (φ = θ = 0°) is 1μm/g.

3.3.2 Limitations in mechanical performance due to etching inaccuracy

The mechanical sensitivity of an accelerometer depends on the weight of the seismic mass, but also on the rigidity of the suspension beams. With formula 2.2 we see that the sensitivity is proportional to the cubic beam length L^3 and the inverse cubic beam width w^{-3}. Considering the four different designs for in-plane accelerometers (design 1 to 4, see section 2.2), one can conclude that long and large beams instead of short and thin beams should be used to improve sensitivity in order to keep variations in sensitivity of devices from different batches as small as possible. The influence of the variation of the seismic mass can be estimated in our cases to be less than 1%, depending on the mass size.

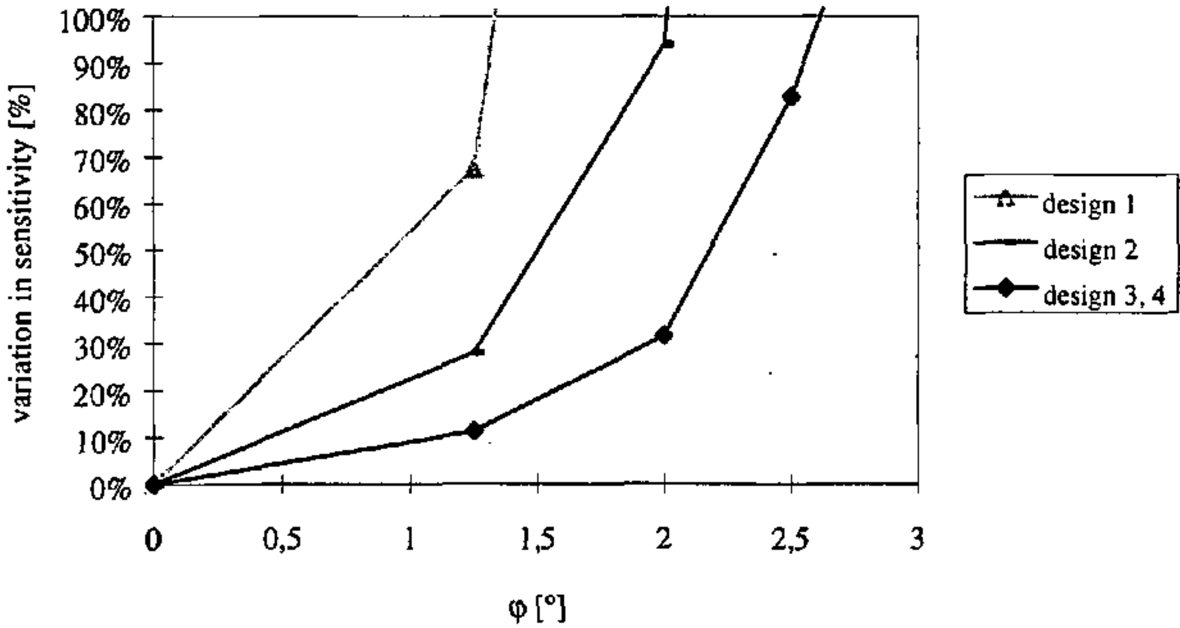

Figure 3.19: Variation of the mechanical sensitivity for the four different in-plane accelerometer designs (presented in section 2.2) as a function of mask misalignment. Design 1 and 2: the seismic mass is suspended bridge-like by four vertical beams. Design 3 and 4: the seismic mass has only two suspension beams which are symmetrically or asymmetrically attached to the mass.

3.4 Fabrication of a monolithic tri-axial seismic mass system

The unconventional fabrication method presented in section 3.2 allows one to build a two-axis accelerometer-system in a single etching operation, by simultaneously building two sensor elements rotated by 90° with respect to each other. The 90° angle is precisely defined by the intrinsic crystal orientation. This has been experimentally verified by measuring the intersecting angles. In addition, the high optical quality of the beam surface indicate the true {100} crystal planes, which are revealed during the underetching.

In order to measure accelerations in three dimensions we need to include a third seismic mass element sensitive to vertical acceleration. The fabrication and integration of this third element is described in the following section, which is partly published in [2, 9].

3.4.1 Fabrication principle: two step anisotropic wet etching

The fabrication of the two lateral accelerometer-structures is described in detail above. In order to include a third seismic mass, which is sensitive in the out-of plane direction, we used a technique which Li, Bao, and Shen [Li96, Li97] called "maskless etching". For the collective etching of all three suspended masses two double sided lithography steps are necessary.

A schematic of the layout and orientation of the two masks is shown in figure 3.20. The etching masks for the two lateral structures are rotated by 90° from each other and by 45° from the <110> wafer flat. For the horizontally located beams the mask can be parallel or perpendicular to the wafer flat.

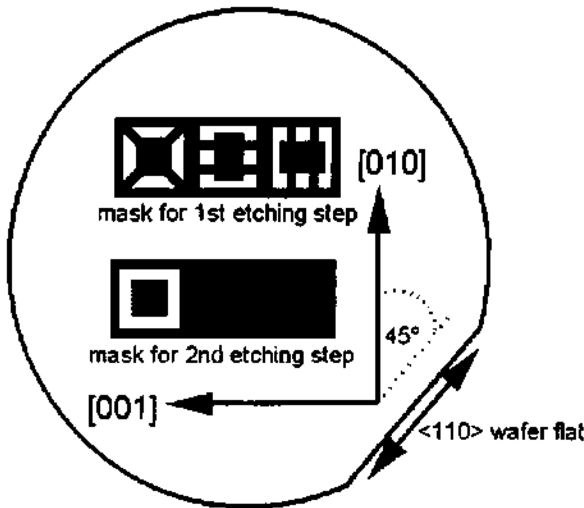

Figure 3.20: Schematic of the layout and orientation of the masks for the two etching steps.

In order to fabricate at the same time as the in-plane structures the seismic mass with horizontally located suspension beams, a pre-etching was performed. After a pre-etching of typically 20μm to 30μm the SiO_2-mask in the region of the beams is removed by a second lithography step. The SiO_2-masks for the lateral structures are not influenced by this second step. The etching of the horizontally located beams continues in vertical and lateral directions. While in vertical direction the final beams are bounded by {100} planes, the beams are limited in lateral directions by {311} planes, which are revealed during the second etching step. A more detailed description of the maskless etching step follows in the paragraph below.

3.4.2 Discussion of maskless-etching

The cross-sectional evolution of the maskless etching step is shown in figure 3.20.

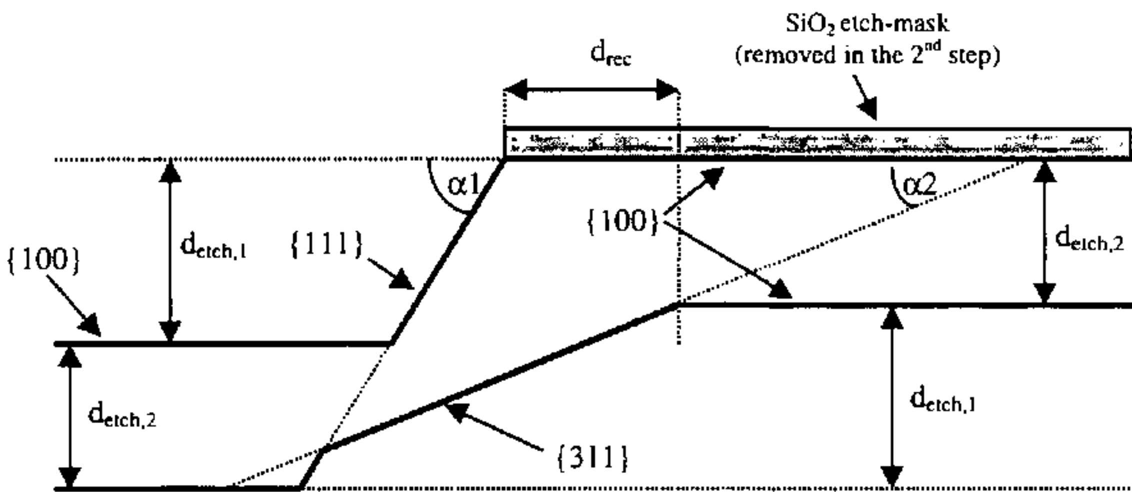

Figure 3.21: Cross section evolution for the second etching step (maskless-etching) to fabricate the horizontally located beams.

We consider a structure after pre-etching with a etch depth of $d_{etch,1}$ (upper thick line). Thus the structure has a height of $d_{etch,1}$ and consists of a {111} sidewall, a top and bottom {100} plane (see fig. 3.21). This is before maskless etching. If the mask on the top of the step is removed and

etching is continued, this is called maskless-etching. The overall step height $d_{etch,1}$ will remain constant as both the top and bottom planes are etched at the same rate, $R_{<100>}$. However, the profile of the sidewall changes due to the emergence of the fast etching {311} plane (with the etch rate $R_{<311>}$) starting at the convex edge on the {111} sidewall. The ratio $R_{<100>}/R_{<311>}$ is a function of KOH concentration and it is usually larger than 1, i.e. ≈ 1.7 for 41%wt KOH. The profile of the structure after maskless-etching is shown by the lower thick line in fig. 3.21. Here, the {111} sidewall is partly replaced by a {311} plane. The top edge of the sidewall recesses due to the fast etching {311} plane and the recession distance d_{rec} can be expressed by (assuming 41%wt KOH) [Li96]

$$d_{rec} = \left(\frac{R_{<311>} / R_{<100>}}{\sin(\alpha 2)} - \frac{1}{\sin(\alpha 2)} \right) \cdot d_{etch,2} \approx 1.9 \cdot d_{etch,2} \qquad (3.6).$$

$\alpha 2$ (25.24°) is the included angle between the {311} sidewall and the {100} bottom, $d_{etch,2}$ is the maskless-etching depth. If the etching time is long enough, the {111} sidewall will be completely replaced by the {311} plane. This is the case for the horizontally located beams described in the next section. After such a complete replacement, the {311} sidewall will move laterally while the {100} top and bottom planes are etched.

Design rules

As a design rule for the thickness $t_{horizontal}$ of the horizontal beams one can find

$$t_{horizontal} \approx 2\, d_{etch,1} \qquad (3.7)$$

at perforation of the wafer, where $d_{etch,1}$ is the depth of the pre-etch. As mentioned above, the rate for the lateral undercutting of the horizontally located beams (so called edge recession) can be estimated to be approximately two times the etching rate of the downward etching for a 41%wt KOH solution (see equation 3.6). For a horizontally located beam edge recession will take place on two sides. Thus, the beam width $w_{M,horizontal}$ of the mask-layout should be larger than two times the edge recession and thus approximately four times larger than the maskless etching depth $d_{etch,2}$. For $d_{etch,2}$ one can derive the following relation (t is wafer thickness)

$$d_{etch,2} = t/2 - d_{etch,1} \qquad (3.8).$$

The maskless-etching method can also be used to form silicon structures with more than two levels [Li97].

3.4.3 Experimental results

Figure 3.22 shows the etching result for the 3D seismic mass system. For the fabrication of this structure, the processes of underetching vertical {100} planes (section 3.2) and of maskless-etching (section 3.4.2) have been combined. The suspended seismic masses are aligned along the <100> directions of the silicon crystal. The highly symmetrical suspension of each mass by four beams minimizes the effect of mechanical cross-sensitivities.

A vertically and a horizontally located suspension beam are shown in figure 3.23. For both beams the crystal planes, which bound the beams, are identified. The beam dimensions in this case are

830μm × 20μm × 370μm for the vertical beam and 1100μm × 400μm × 20μm for the horizontal beam.

For the out-of-plane structure the suspension beams can be positioned either at the edges of the mass (as in fig. 3.22 and 3.23) or at the sides (see fig. 3.24). In the case where the horizontally located beam are clamped at the edges of the mass, stress will be concentrated in one point. While for the other case (fig. 3.24) the stress will be distributed continuously over the beam. Thus this configuration increases the limit of breakage due to higher forces. The horizontal beam in figure 3.23 is aligned along the <110> direction and the beam in figure 3.24 is parallel to the <100> direction.

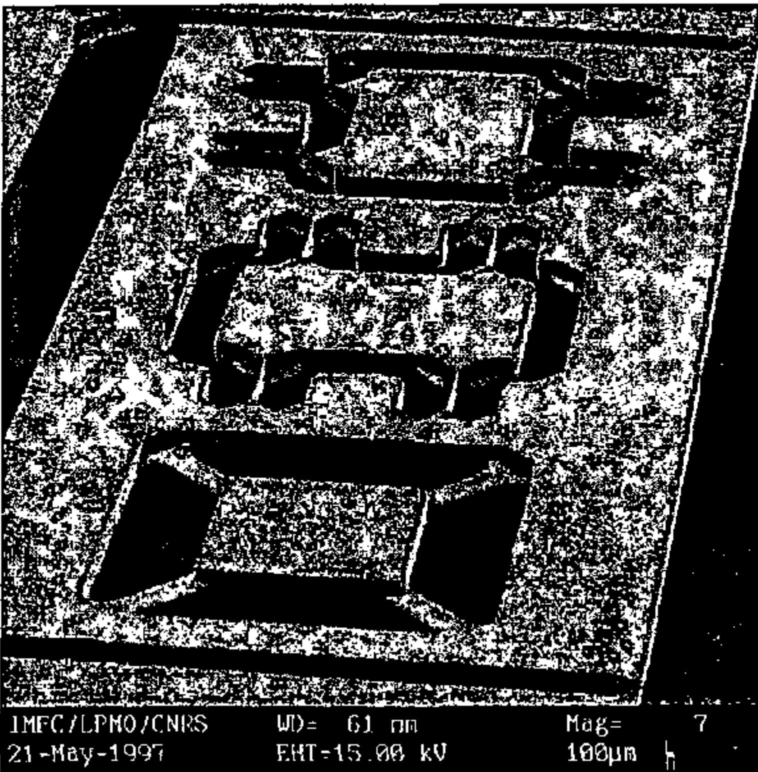

Figure 3.22: SEM view of the 3D monolithic silicon seismic mass system which has been collectively etched in (100) silicon.

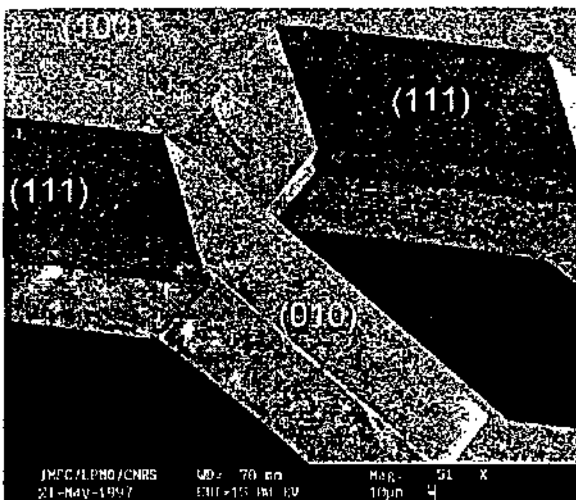

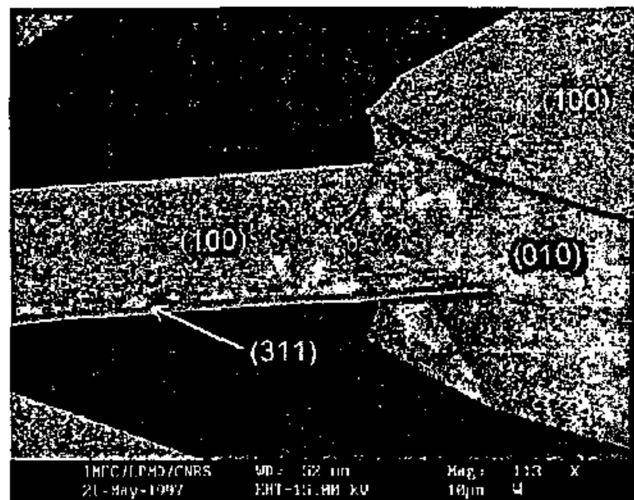

Figure 3.23: Zoom of figure 3.21: Vertical suspension beam (left) and horizontally located suspension beam (right). In this case the horizontally located beam supports the mass at the corners.

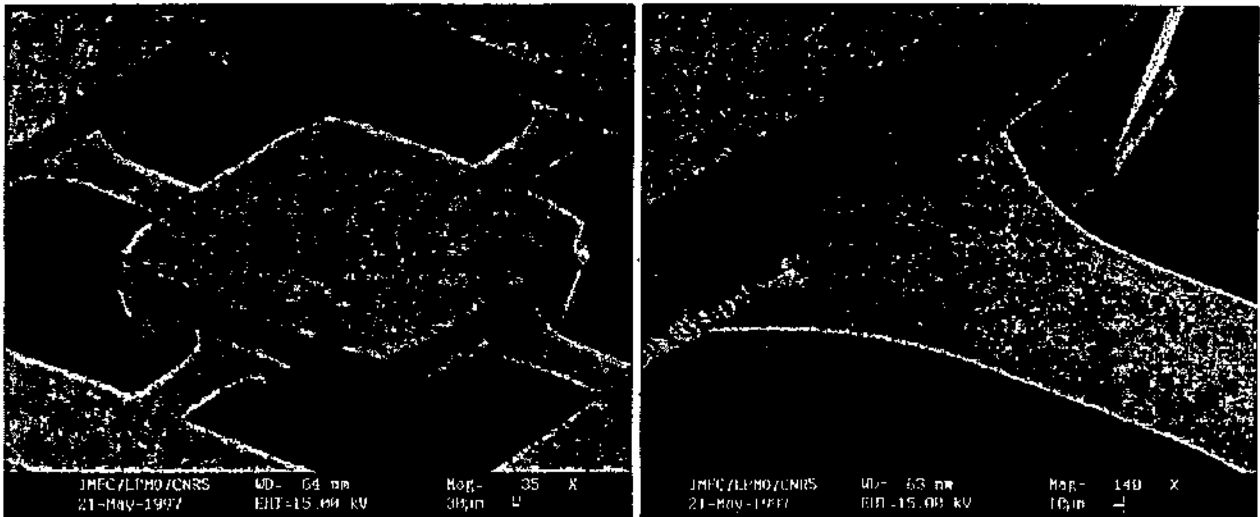

Figure 3.24: Out-of-plane structure with suspension beams positioned at the sides of the mass (left) and zoom of one suspension beam.

As mentioned in section 3.2.1, test structures have been included to control the width of the vertical beams. In order to implement a test structure to control the thickness of the horizontally located beams an additional photolithography and etch step would be necessary.

Measurements have been performed to investigate the mechanical sensitivities, e.g. displacement due to acceleration. For the above presented device, the mechanical sensitivities are 50nm/g and 80nm/g ($g = 9.81 m/s^2$) for the lateral and vertical sensitive devices, respectively. This agrees well with the theoretically expected one (see formula in section 2.3.4). By continuing the etching after perforation, the beam width or thickness is decreased, which leads to an increase in sensitivity.

3.4.4 Overload protection

One problem encountered in practical applications for micromachined accelerometers is the breakage of the beams due to a shock acceleration higher than the operation range. A device is subjected to an acceleration up to several hundred g due to a drop on the ground or crash with a hard surface. An accelerometer should be able to survive such high accelerations to be of practical use.

For the sensitive direction of the in-plane structure, this stress σ occurring in the beam due to acceleration forces is approximately given by [Che97]

$$\sigma = \frac{3 \cdot m \cdot a \cdot L}{2 \cdot w^2 \cdot t} \qquad (3.9).$$

Assuming a quite conservative rupture stress of 3×10^8 Pa [Che97], the maximum acceleration that a device can survive for the most sensitive direction can be calculated from equation 3.9. For the fabricated in-plane structure presented above, the calculated maximum acceleration is about 300g for the sensitive direction. For other directions the maximum acceleration is orders of magnitude higher.

Experimentally, we found that the beams of the lateral masses will break at a force of at least 0.35N, corresponding to an acceleration of 350g, which agrees well with the theoretical result. Depending on the beam dimensions and the mechanical sensitivity (0.02µm/g - 1µm/g), this corresponds to a displacement between 10µm and 300µm. For the vertically sensitive mass, almost the same values have been measured.

Therefore, if the device should operate as an accelerometer, one need to include overrange stoppers or to operate the device in a liquid damping medium to avoid breakage of the device due to shocks.
While for the out-of-plane mass overrange stoppers can be included by an additional etching step or by the deposition of such stoppers on the counter substrate, the forming of such devices for in-plane structures could be realized at the same time as the main etching process without the need of an additional process step. However, due to the large underetching of the {100} silicon planes, gaps smaller than the wafer thickness are not achievable when aligning the pattern parallel to the <100> direction. Therefore, the pattern for realizing the overrange stopper should be aligned parallel to the <110> direction taking advantage of the slow etching {111} planes. First tests have been undertaken (see figure 3.24) using this alignment in combination with overetching. However, the gap between seismic mass and fixed substrate is difficult to control by this technique. Fortunately, the size of the gap is not very critical a long as it is small enough to avoid breakage and large enough to allow movement within the measurement range. Of course, other types of overload protection structures are possible, but in general with the cost of an extra process step.

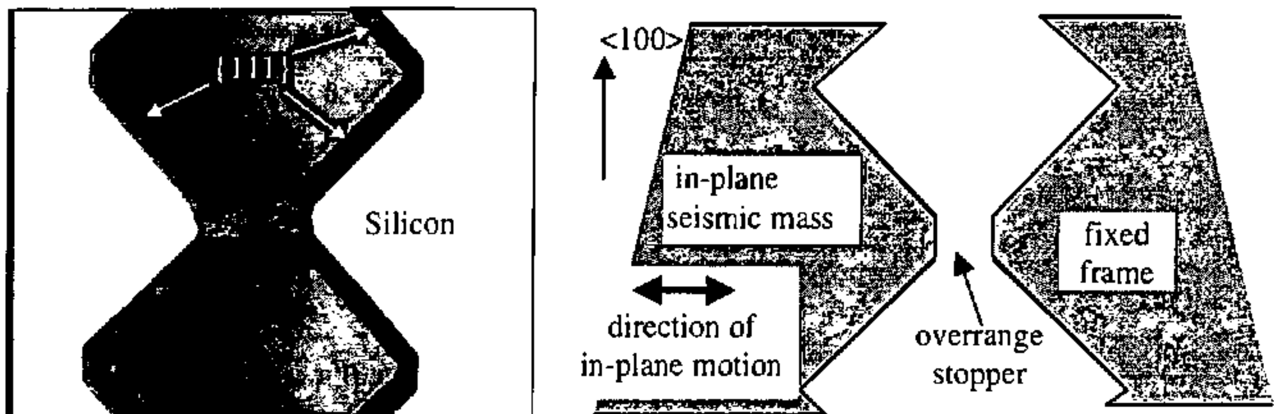

Figure 3.25: Overrange stopper for in-plane accelerometer: silicon structure (left) and schematic (right). The stopper is fabricated at the same time as the seismic mass and the suspension beams.

3.5 Some other micromachined structures

Apart from the fabrication of accelerometer structures, the above described unconventional etching techniques can also be employed to micromachine other mechanical, electromechanical or optical devices.

3.5.1 Micromirror

Torsional micromirror has been completely fabricated by maskless etching. After a pre-etching of several µm, the etching mask has been removed in the region of the mirror plane and of the torsional suspension beams. The realized structure can be seen in figure 3.26 (top). The silicon oxide at the border is here not removed. The thickness of the rotating mirror is about 4-5µm. for electrostatic actuation of the mirror two electrodes can be implemented under the mirror surface. For first tests, the silicon mirror has been mounted on a PCB board containing electrodes for

electrostatic actuation. The tilt angle was measured with help of an focused laser beam (figure 3.26 right).

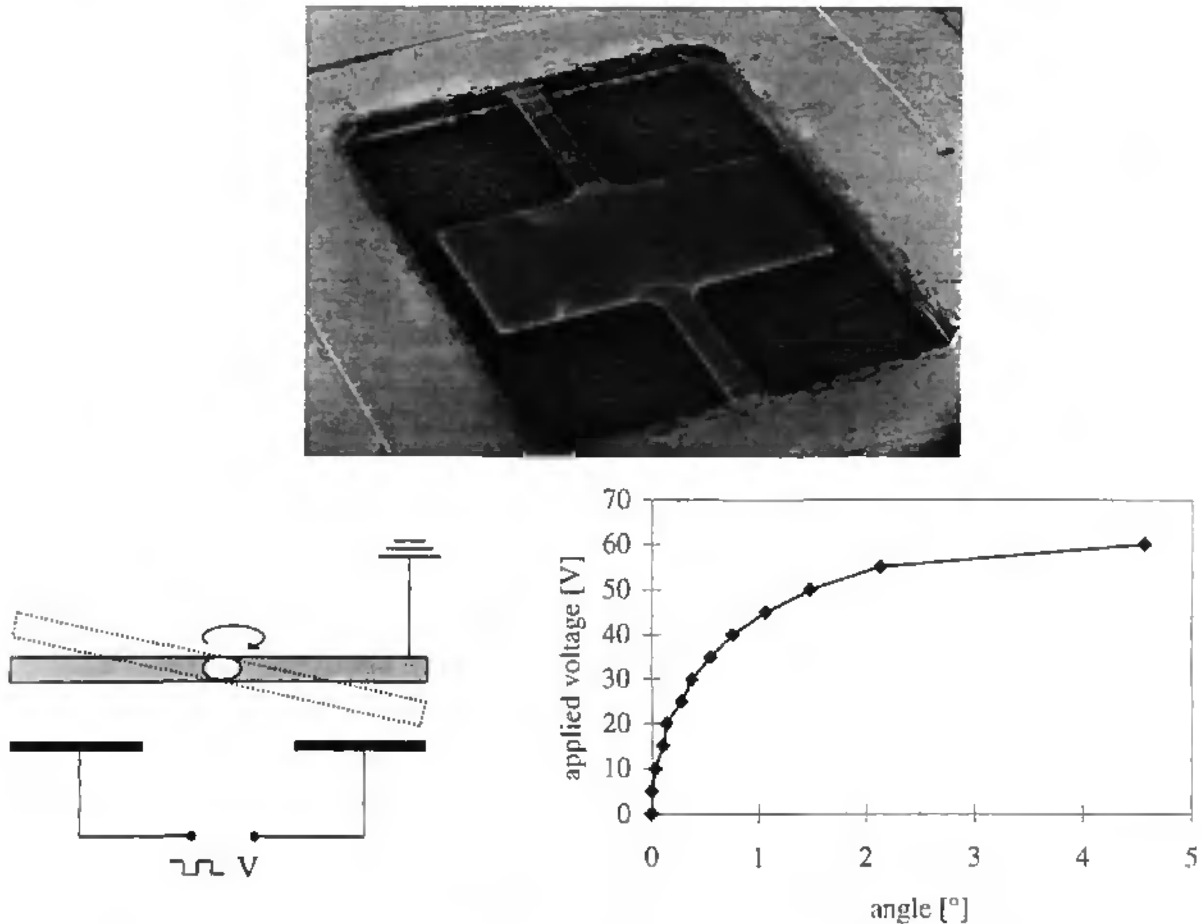

Figure 3.26: SEM view of the torsional micromirror (top), view of cross-section illustrating the electrostatic actuation (left), and measured tilt angle (right).

3.5.2 3D Gyroscope

In 1997 David Wood [Wo97] presented a design for a three-dimensional gyroscope, a device being able to measure angular rates for three axis. The device has a 90° rotational symmetry and each of the four sides has a central mass connected at the corner sections via four beams. The beams are thin and deep so that the central masses are able to move radially outwards, while remaining rigid for flexing our of plane. The device has one primary mode of excitation and three secondary modes to detect the angular rates due to Corolis forces. In order to achieve the desired performance, a frequency matching is necessary between excitation and detection modes. This implies a beam width accuracy higher than ±0.1μm. Unfortunately, the presented etching technique is not sufficient precisely in order to provide this accuracy in lateral beam width. However, the device in figure 3.27 demonstrates excellently the three-dimensional orthogonality of the proposed etching using {100} silicon planes.

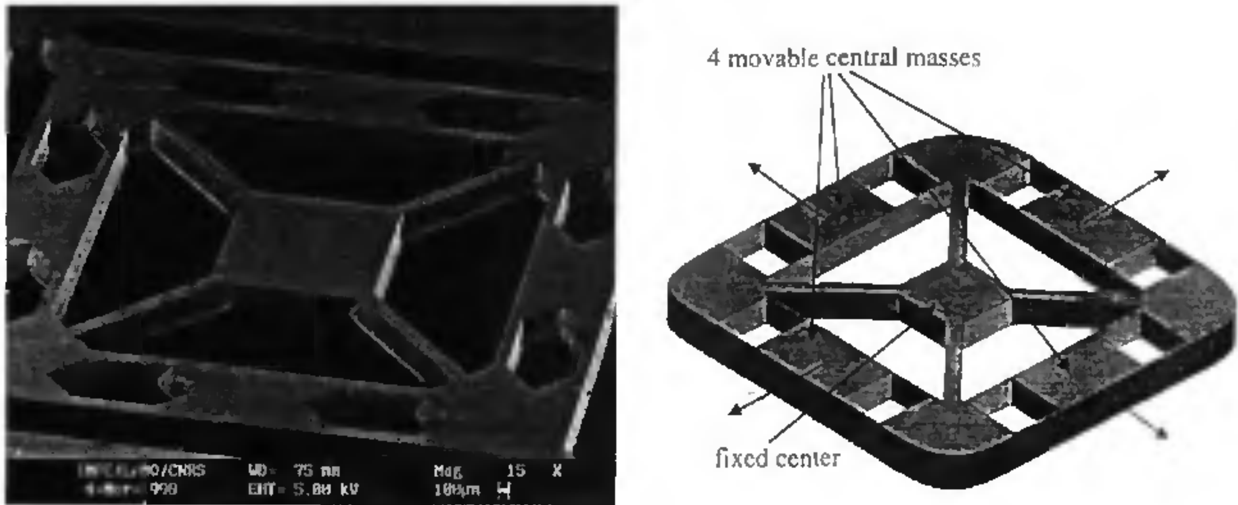

Figure 3.27: A 3D gyroscope-structure. Design proposed by D. Wood [Wo97]. On the right there is a schematic shown demonstrating the primary mode used for excitation (courtesy of D. Wood).

3.5.3 Multi-axial accelerometer with a single seismic mass

As described in section 2, apart from uni-axial accelerometers in lateral or vertical direction, other designs are possible which are sensitive in all three directions (design 8 and 9). With the same fabrication technique, structures, corresponding to these designs, can be made as shown below in figure 3.28.

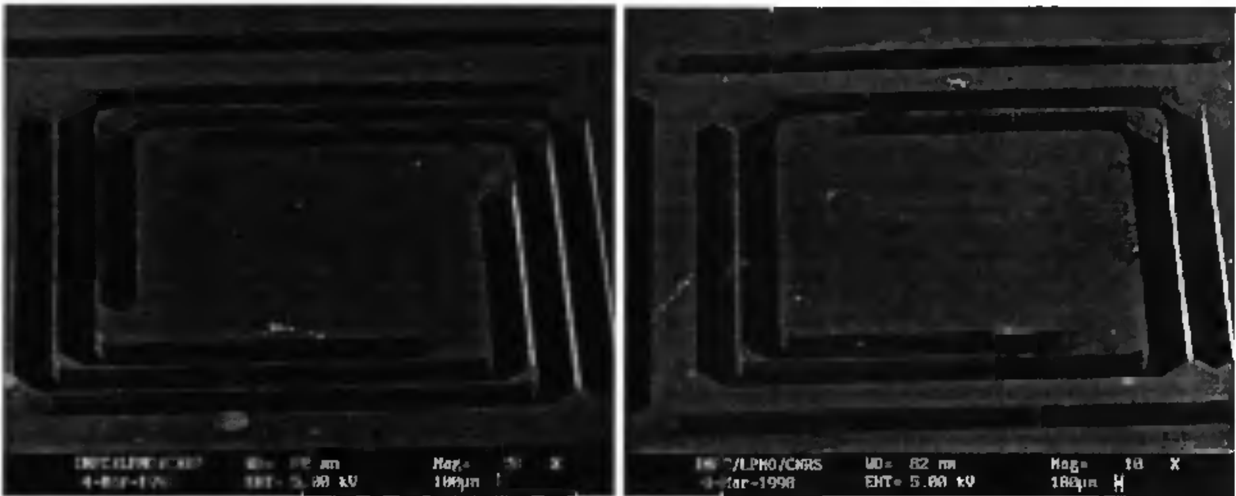

Figure 3.28: Seismic mass systems sensitive to in- and out-of-plane accelerations.

3.5.4 Seismic mass structure with octagonal shaped or double suspension beams

Apart from beams with flat surfaces, vertically or horizontally orientated, also more complicated shaped beams can be micromachined. In this paragraph two of such complex suspended seismic mass configurations are demonstrated.

In figure 3.29 one can see a seismic mass suspended by round, or more precisely, octagonal shaped beams. This structure is realized by double side maskless-etching very similar to the process of manufacturing flat horizontally located beams. But in this case the beam width for the

mask w_M was smaller than two times the edge recession d_{rec}. Therefore the {100} plane disappeared during etching. This {100} plane bounds the horizontally located beam in the vertical direction. Similar beam structures, used for a torsion spring, have been very recently presented by Birgit Hannemann and Joachim Frühauf [Han98].

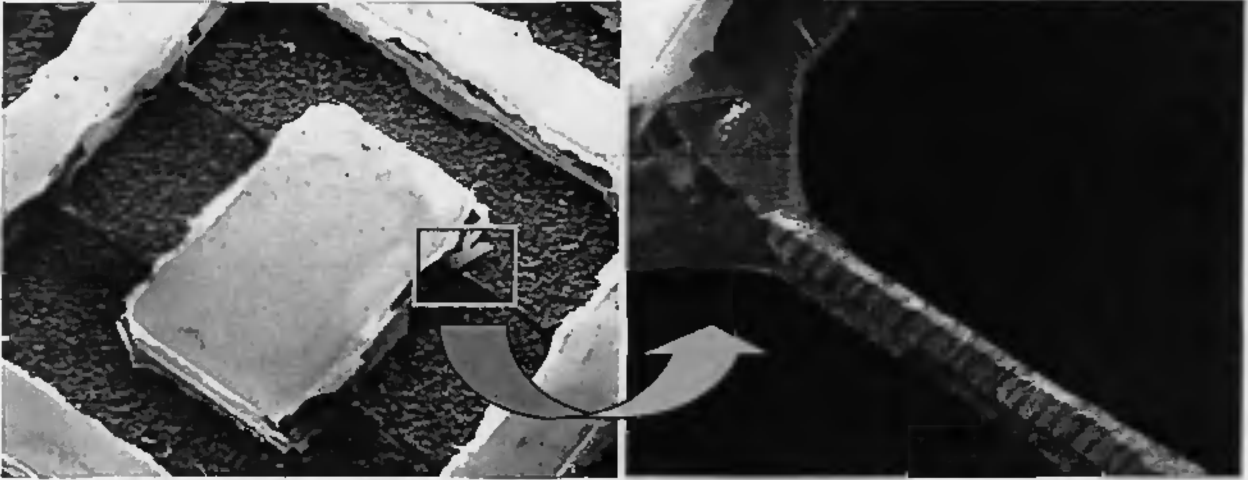

Figure 3.29: SEM view of a seismic mass suspended by octagonal shaped beams (a). Detail of one beam (b). In a) the masking SiO_2 is not removed.

Another sophisticated mass-beam-configuration is presented in figure 3.30. This structure with double suspension beams was simply micromachined by shifting the upper and lower mask (as shown in figure 3.12), instead of aligning them accurately face on face. After wafer perforation, these double-beams appear.

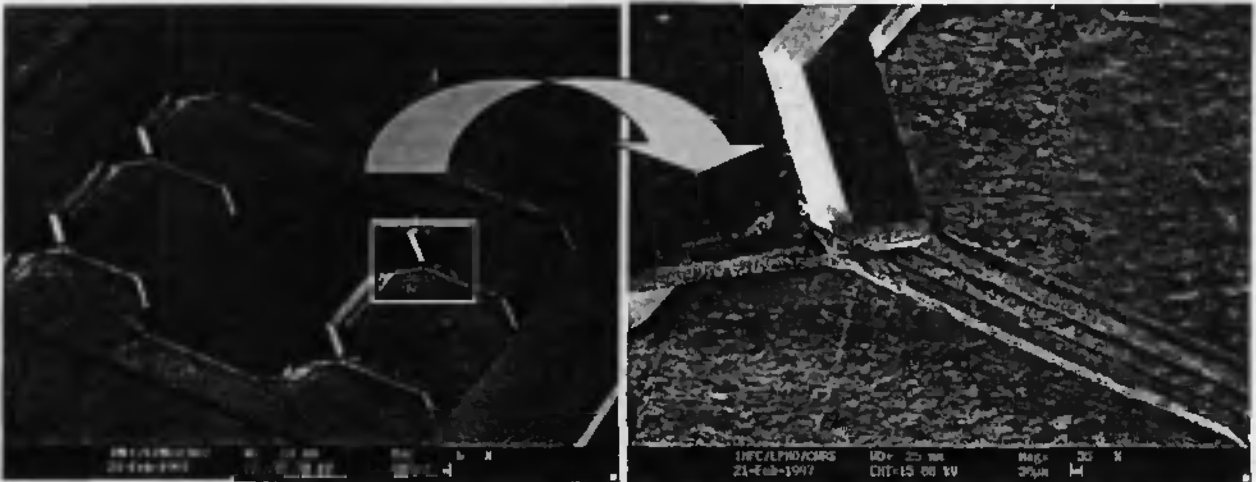

Figure 3.30: SEM view of a seismic mass suspended by double beams (left). Detail of one double-beam (right). One can identify clearly the shift of the upper and lower mask by regarding the step in the middle of the seismic mass.

3.6 Conclusion of chapter 3

Fabrication of in-plane accelerometer-structures
A non conventional fabrication method using the underetching of {100} silicon planes was demonstrated. With the help of this silicon bulk-micromachining process on a (100) wafer, the fabrication of thin vertical beams with flat sidewalls is possible. The seismic mass and the suspending beams were fabricated within the same etching step. The fabricated structures offer aspect ratios (beam thickness over beam width) up to 35. The directions of undercutting as well as design rules for the mask layout were determined. The in-plane structures are highly symmetrical, thus having very low mechanical cross-axis sensitivities. The unconventional fabrication method is fairly simple and allows to build a two-axis accelerometer-system in a single etching step, by simultaneously building two sensor elements rotated by 90° with respect to each other. Moreover, the 90° angle is precisely defined by the intrinsic crystal orientation.

Etching simulation and limitations for in-plane structures
From the simulations of the anisotropic etching we can conclude that the simple technique of underetching vertical {100} planes can be employed to micromachine mechanical devices within a reproducibility in the order of a few percent if simple precautions are taken. For that, the important points are: firstly, an adapted design, and secondly, a pre-etching to reveal the crystal orientation.

Fabrication of a monolithic tri-axial seismic mass system
For the third direction, another accelerometer sensing vertical accelerations can be included, resulting in a three-dimensional monolithic accelerometer system, with intrinsic alignment due to the perpendicular {100} crystal planes. This third device is micromachined by a technique called maskless etching. For this structure, the suspension beams are horizontally located and can be aligned parallel or with an angle of 45° to the wafer flat.
We can summarize that the fabrication of a monolithic system, comprising three seismic masses sensitive in three different directions, has been successfully demonstrated. The advantages of the described process principle are the simplicity of the two step etching, the almost perfect orientation of the devices along the <100> directions of the silicon crystal, and the symmetrical suspension of the masses, resulting in low cross-sensitivities. The structures exhibit the excellent material qualities of single crystal silicon, such as good long term stability, no hysteresis, etc. No stress is induced into the suspension beams due to doping. The occurrence of large undercutting is, of course, a disadvantage of using (100)-oriented wafers instead of (110)-oriented wafers. However, two perpendicular devices cannot be made on (110) wafers. A summary of the advantages and disadvantages of the presented micromachining method is given in table 3.3.

Advantages	Disadvantages
□ simple and inexpensive	□ large undercutting (takes spacc on chip)
□ all advantages of pure crystal silicon as a mechanical material (no hysteresis, long term stability, etc.)	□ accuracy of etching depends on variation of wafer thickness
□ perfect orthogonal orientation along <100> silicon axes	□ no closely-spaced beams possible (due to underetching)
□ highly symmetrical structures (if double sided etched)	□ accuracy of etching depends on initial crystal orientation in wafer and on alignment at lithography
□ full 3d structures in combination with other techniques such as mask-less etching	□ no electrochemical etch-stop
□ high aspect ratios possible, e.g., for vertical beams height/width > 35	
□ no stresses due to doping	

Table 3.3: Advantages and disadvantages of bulk-micromachining using underetching of vertical {100} silicon planes.

Some other micro-machined structures

All designs for in- and out-of-plane accelerometers presented in chapter 2 can be fabricated by the proposed micromachining technique. Of course, this technique is not limited to accelerometers. Other silicon devices, such as optical mirrors, gyroscopes or more complex suspension structures can also be realized using this etching method.

CHAPTER 4

4. Multi-axial capacitive accelerometers

4.1 Introduction

4.2 Principles

4.3 Modeling of the capacitive transducers

4.4 Fabrication of the capacitive accelerometers

4.5 Capacitive measurement circuits

4.6 Characterization and limitations of the capacitive accelerometers

4.7 Conclusion of chapter 4

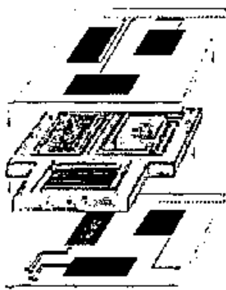

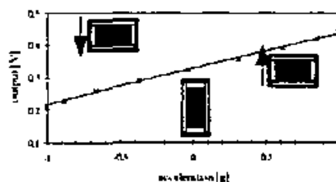

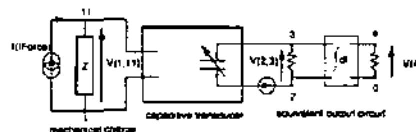

4. Multi-axial capacitive accelerometers

4.1 Introduction

Electrostatic principles are commonly used in microsensors as well as in microactuators. In the case of capacitive sensors for detection of mechanical quantities, i.e. accelerometers, one can find that they all rely on a displacement measurement [Zhu92]. The principle of capacitive sensors inherently offers some distinct advantages: high sensitivity, low power consumption, better temperature performance, less sensitive to drift, etc. [Pu98]. Capacitive accelerometers can be seen as a combination of mechanical system (suspended seismic masses) and corresponding capacitive transducer. Apart from the piezoresitive effect capacitive detection is the most employed technique in accelerometer design, e.g. [Ah97, Bur91, Cha96, Kra97, Lem97, Löt97, Min96, Mot97, Pue98, Rud83, Sei90, Str94, Ya90].
The main topics of this chapter are the design, fabrication and characterization of multi-axial capactive accelerometers. The mechanical design is given by the anistropic etched silicon seismic mass systems presented in chapter 3. Their mechanical behavior was already modeled in chapter 2. In the next section of this chapter the basic principles of the corresponding capacitive transducers will be explained. We can distinguish mainly between two different types: a lateral electrostatic transducer for the read-out of the in-plane accelerometer devices and a vertical capacitive configuration to detect the out-of-plane accelerations. Differential sensing and closed-loop operation are also discussed.
Then different models are investigated to predict the capacitive response. Firstly, a linear electrostatic field between the electrodes is assumed, so called Simplified Field Assumption (SFA). While in the case of the vertical capacitive transducer this method leads to a satisfying model, in the case of the lateral transducer this approach is not sufficient. In order to consider the electrostatic fringing fields at the electrodes edges a more sophisticated analytical model is developed. Finally, numerical tools, i.e. 2D and 3D Finite Element Methods (FEM), were also used to simulate the capacitive change due to accelerations. All three different modelisation techniques are compared. Electrostatic forces for feedback and electrostatic damping are analyzed. In addition, global simulation was performed to adequately predict the system performance, including preliminary electronics. Behavioral models written in hardware description language are therefore generated from FEM simulations or analytical formulae. This part was mainly done at the EPFL Lausanne in a collaboration with Yannick Ansel ea.
Then, the device batch fabrication is described. Here, topics as micromachining of sensor elements, structuring of electrodes, glass technology, assembling of the device by anodic bonding and also mounting and connecting are discussed. Basically, two process sequences are developed and compared. Some realized capacitive multi-axial accelerometers are presented.
Different types of capacitive measurement circuits are shortly presented in section 4.5. The fundamental noise limits of these circuits are identified. Apart from the capacitive AC bridge circuit and the charge/discharge circuits, a current project for the development of an ASIC using sigma-delta modulation is shortly described. This project is a collaboration in the framework of the CNRS program "*microsystèmes*" between the CMP/TIMA in Grenoble, and the LPMO in Besançon.

Finally, the capacitive accelerometers are characterized. Static and dynamic behavior are discussed. Possible optimizations and limitations are considered.
The global simulation of the capacitive accelerometer has been published in [14-18]. Other aspects, such as analytical modeling of the capacitive transducer, fabrication issues or performance limitations have been published in [6, 10-12].

4.2 Principles

To evaluate the capacitive response, different modelisation methods are used which will be discussed in detail in section 4.3. Now, the fundamental physical principles, which are employed in the capacitive transducers, are explained.

4.2.1 Definition of capacitance

In a configuration made up of any number of electrodes, the capacitance between two of the electrodes (i.e. i and j) is determined by the quotient of the charge, induced on one of the electrodes due to the potential difference between the two electrodes, and the difference in potential [Her86]. This can be written as

$$C_{ji} = \frac{q_{ji}}{U_j - U_i} \qquad (4.1)$$

where C_{ji} is the capacitance between the electrodes i and j. q_{ji} is the charge on electrode j induced by the potential difference U_j - U_i. One important conclusion one can derive from equation 4.1 is that for all the other electrodes their presence and not their potential contributes to the capacitance between the electrodes i and j. This relation should be considered in the design of sensing and guarding electrodes.

4.2.2 Simplified field approximation

A simple approach to calculate a capacitance is to use Simplified Field Approximation (SFA). The distance d between two electrodes is assumed to be small compared to the circumference of the electrode surface ($d \ll a, b$), so that fringe fields occuring at the electrode's edges can be neglected. In this case the electrostatic field between the two electrodes is uniform. If a voltage V is applied across the capacitor, the electric field intensity E is given by

$$E = \frac{V}{d} \qquad (4.2).$$

This assumption leads to the well known formula for a parallel plate capacitor:

$$C(A,d) = \varepsilon_0 \cdot \frac{A}{d} \qquad (4.3)$$

with capacitance C, dielectric permitivity ε_0, overlapping surface of electrodes A, and gap d between the electrodes (see figure 4.1a). As mentioned in the defintion of capacitance, formula

4.3 points out that a capacitance is a function, depending only on geometrical variables. Here, on the electrode surface A and the distance d.

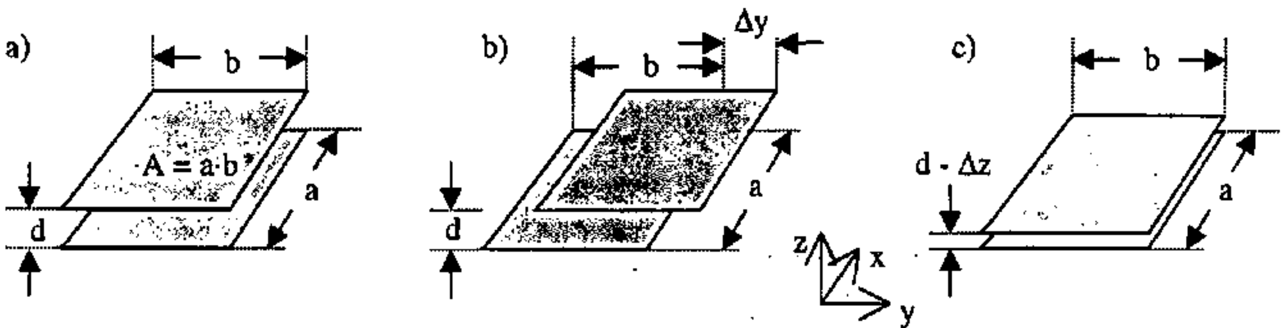

Figure 4.1: Two conducting parallel plates forming a capacitor (4.1a). The capacitance can change either due to a parallel displacement of one plate regarding the other (4.1b) or by an increase/decrease in the distance (4.1c).

4.2.3 Lateral capacitive transducer

In order to use a capacitive read-out for the micromachined accelerometer structures, one has to integrate one electrode on the seismic mass. The capacitor is built with help of a second electrode that is fixed on a counter substrate. In the case of the in-plane accelerometer, the movement due to accelerations is mainly parallel to the electrodes. The electrostatic detection method for lateral or in-plane sensitive seismic mass is represented by figure 4.2. The capacitance between the two comb or meander shaped electrodes changes due to a mechanical displacement of the seismic mass. The electrode placed on the mass is either made by thin film deposition or structured into the silicon seismic mass. Thin film electrodes need a nonconductive layer between metal electrodes and silicon seismic mass in order to isolate them from each other. In the following this accelerometer type is called Sensor *#C1*. If the electrodes are directly formed into the silicon mass, this accelerometer prototype is entitled Sensor *#C2*.

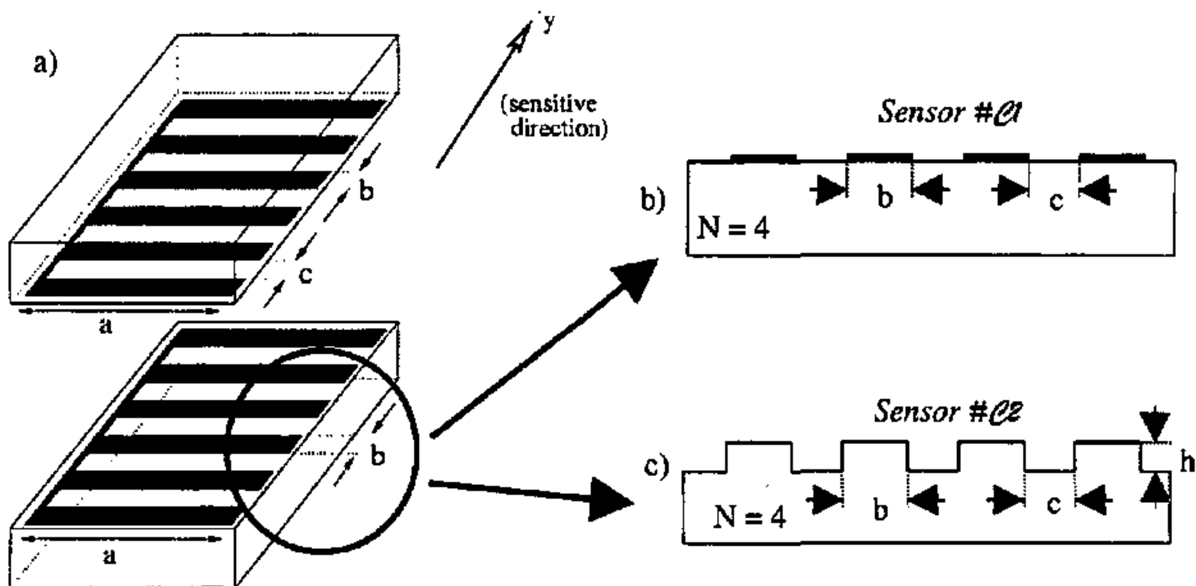

Figure 4.2: Basic principle for a lateral capacitive read-out: a meander or comb shaped electrode fixed on the moveable seismic mass and a non moveable counter electrode build up the sensing capacitor (4.2a). The electrodes on the moveable seismic mass can either be realized by thin film deposition (4.2b) or by silicon 3D micromachining, i.e. wet or dry etching (4.2c).

As demonstrated in figure 4.1b) a parallel mass displacement due to lateral accelerations changes the overlapping surface between electrodes. Considering movement in y-direction, this results in a capacitive change given by

$$C_y = N \varepsilon_0 a (b - \Delta y) d^{-1} \qquad (4.4)$$

where a and b are electrode width and length and N is the number of electrodes (see figure 4.2). The capacitive change is linearly related to the displacement Δy and thus proportional to acceleration.

4.2.4 Vertical capacitive transducer

The displacement Δz of the seismic mass with out-of plane-sensitivity can be sensed by a capacitor C_z which is formed by the bulk silicon mass and one counter-electrodes like shown in figure 4.1c). Due to vertical (z-direction) accelerations the gap d between mass and counter-electrode increases or decreases. The overlapping surface A remains constant. The relationship between displacement Δz and capacitance C_z can be generally expressed with sufficient precision by the SFA (equation 4.2):

$$C_z = \varepsilon_0 A (d - \Delta z)^{-1} \qquad (4.5).$$

The relationship between capacitance and displacement (or acceleration) is in this case not linear but inversely proportional.

4.2.5 Differential sensing

Differential sensing techniques are a common tool, not only for capacitive devices, to overcome undesired effects such like temperature drift, nonlinearity or cross-sensitivities. We can employ differential capacitor designs to both transducers: lateral and vertical type.

Vertical capacitive transducer
The displacement Δz of seismic mass with out-of plane-sensitivity can be sensed by a differential capacitor ($C1_z$, $C2_z$) which is formed by the bulk silicon mass placed between two counter-electrodes. The relationship between displacement Δz and capacitances can be expressed by

$$C1_z = \varepsilon_0 A \ (d - \Delta z)^{-1} \qquad (4.6) \qquad \text{and} \qquad C2_z = \varepsilon_0 A (d + \Delta z)^{-1} \qquad (4.7)$$

A linear relationship between Δz and the capacitive response can be obtained by subtracting the two capacitances $\Delta C_z = C1_z - C2_z$:

$$\Delta z = \Delta C_z (C1_z + C2_z)^{-1} d \qquad (4.8).$$

Lateral capacitive transducer
To implement a differential read-out for in-plane accelerometers, the following method can be used: for each electrode on the seismic mass two electrodes have to be placed on the counter substrate, forming two comb or meander shaped capacitors $C1_y$ and $C2_y$. Due to lateral

accelerations the overlapping surface between electrodes changes, resulting in an increase of $C1_y$ and a decrease in $C2_y$ or vice versa. The capacitors are ideally described by

$$C1_y = N\,\varepsilon_0\,a\,(b+\Delta y)\,d^{-1} \quad (4.9) \qquad \text{and} \qquad C2_y = N\,\varepsilon_0\,a\,(b-\Delta y)\,d^{-1} \quad (4.10).$$

Combining these expressions we obtain:

$$2\,\Delta y\,b^{-1} = (C1_y - C2_y) / (C1_y + C2_y) \qquad (4.11)$$

The capacitive change $\Delta C_y = C1_y - C2_y$ is thus linearly related to the displacement Δy. Furthermore, ΔC_y does not depend on the initial gap d and it's variations. This reduces cross-sensitivities regarding vertical accelerations.

4.2.6 Capacitive transducer as actuator for closed loop operation

One significant advantage of capacitive sensors is that they can be used as actuators, without any change in design. An external electrostatic force can be applied on the structure. This force can be used to compensate the inertial force on the seismic mass due to acceleration, thus keeping the seismic mass at zero displacement ($\Delta y = 0$, $\Delta x = 0$ and $\Delta z = 0$, respectively).
The displacement of the seismic mass is sensed and converted into a voltage. This voltage is used to generate a feedback force in opposite direction to the acceleration force.
The closed loop operation offers some benefits for accelerometers [Kra97, vKa95]. In open loop systems the sensitivity is proportional to the square of the resonance frequency. In feedback mode, this relationship is not important as sensitivity depends on the loop gain and the form of compensation. Possible nonlinearities or fabrication tolerances of the mechanical suspension can be adjusted or tuned. Also electrostatic damping can be applied. Furthermore the bandwidth of the device can be increased and self-test features can also be implemented. Of course, electronic signal processing becomes more complex. Principally, two different techniques are possible for feedback operation. Firstly, the excitation and the feedback signals are continuously applied to the capacitors and are separated in the frequency domain. Secondly, separate sensing and feedback phases can be used, meaning separation in the time domain. The first approach results generally in an analog output, while the second one is more suitable for the design of digital accelerometers.

Capacitive actuators are governed by their energy W contained in the electrostatic field:

$$W = -\tfrac{1}{2}\, C \cdot V^2 \qquad (4.13).$$

C represent the capacitance of the device and V the on the electrodes applied voltage. Electrostatic forces can be derived by calculating the derivatives of energy W in respect to the direction of motion:

$$F_{el,x} = -\frac{\partial W}{\partial x}, \qquad F_{el,y} = -\frac{\partial W}{\partial y} \qquad \text{and} \qquad F_{el,z} = -\frac{\partial W}{\partial z} \qquad (4.14).$$

Taking relation 4.13 and 4.14, we see that for capacitors, electrostatic forces are essentially a function of change in capacitance

$$F_{el,x} = \frac{1}{2}\frac{\partial C}{\partial x}V^2, \qquad F_{el,y} = \frac{1}{2}\frac{\partial C}{\partial y}V^2 \qquad \text{and} \qquad F_{el,z} = \frac{1}{2}\frac{\partial C}{\partial z}V^2 \qquad (4.15).$$

The forces are proportional to the square of the voltage. Hence, they are always positive and thus attractive.

4.3 Modeling of the capacitive transducers

The above discussed formulae for the capacitances are based on the simplified field approximation (SFA) of the electrostatic field between the electrodes. This becomes insufficient as far as fringe fields become important. For the vertical capacitive transducer the electrode distance is quite small compared to the electrode dimensions ($d \ll a, b$) and thus SFA gives reasonable results. But for the lateral transducer the electrode width b is not considerably larger than the electrode distance d. For this case a more precise analytical model or numerical simulation using the Finite Element Method (FEM) should be applied. Both methods and their results are subject of this section.

4.3.1. Definition of capacitive sensitivity

The sensitivity of the capacitive accelerometer is the product of the mechanical sensitivity S_{mech} defined in section 2 and the capacitive sensitivity S_{cap} given by the change of capacitance ΔC due to displacement, e.g. Δy. The total sensitivity S can be written for a displacement in y-direction as

$$S = S_{mech} \cdot S_{cap} = \frac{\Delta y}{a_y} \cdot \frac{\Delta C_y}{\Delta y} = \frac{\Delta C_y}{a_y} \qquad (4.16).$$

More general, the capacitive sensitivity is given by the derivative of the capacitance in respect of the direction of displacement, e.g.

$$S_{cap} = \frac{\partial C_y}{\partial y} \qquad (4.17).$$

4.3.2 Analytical modeling

The electrostatic field can be described by the Laplace equation [Her86]. The solution of the Laplace equation gives the potential distribution inside the capacitor. By using the potential gradient perpendicular to the electrode surfaces, the electrode's charge density can be derived. After integration over the total electrode, one obtains expressions for the induced charge. Finally, in order to calculate the capacitance, one has to divide the induced charge by the applied potential difference (voltage). In general it is difficult or even impossible to find an analytic solution of the Laplace equation for a three-dimensional electrostatic field problem [Zhu92]. Therefore, we have to simplify our electrode arrangement to a two-dimensional parameter dependent configuration

[Her86]. In the case of a biplane capacitor with inter-electrode-distance d we can derive, with help of the fundamental relation given in formula 4.1, the following analytical expression of the capacitance:

$$C = \frac{q}{U_1 - U_2} = \frac{\iint \varepsilon_0 E ds}{V} = \frac{\varepsilon_0}{V} \iint \left.\frac{\partial U}{\partial z}\right|_{z=d} ds \qquad (4.18)$$

where $\varepsilon_0(\partial U/\partial z)|_{z=d}$ is the surface charge density on one electrode.

In case of SFA the surface integral over this charge density equals $A \cdot V \cdot d^{-1}$ which leads to the well known formula 4.3 of a parallel plate capacitor. By assuming that one of the bottom electrode has an infinite length (see figure 4.3), Heerens ea. [Her86] derived a more precise analytical formula:

$$C = \frac{\varepsilon_0 a}{\pi} \ln\left(\frac{\cosh\left[\frac{\pi}{2d}(\Delta y - b)\right] \cdot \cosh\left[\frac{\pi}{2d}(b + \Delta y)\right]}{\cosh\left[\frac{\pi}{2d}\Delta y\right] \cdot \cosh\left[\frac{\pi}{2d}\Delta y\right]} \right) \qquad (4.19).$$

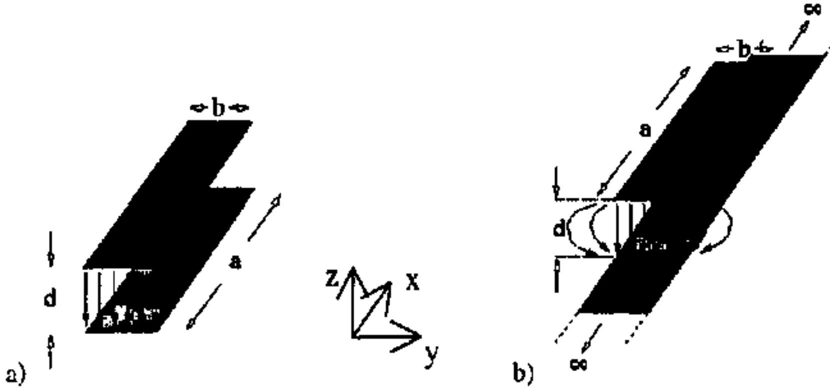

Figure 4.3: Schematic representation of the electrostatic field of a two electrode capacitor in case of a simplified field assumption (a) and an analytical model with the assumption that the bottom electrode has an infinite length (b).

Formula 4.19 can be rewritten for the lateral comb-shaped transducer with N electrodes as

$$C = \frac{\varepsilon_0 \cdot a \cdot N}{\pi} \ln\left(\frac{\left(1 + \exp\left[\frac{\pi}{d}(\Delta y - b)\right]\right)\left(1 + \exp\left[\frac{\pi}{d}(\Delta y + b)\right]\right)}{\left(1 + \exp\left[\frac{\pi}{d}\Delta y\right]\right)^2} \right) \qquad (4.20).$$

Differential detection

For b>>d and $\Delta y \approx 0$ one can simplify formula 4.20 to the SFA expression 4.3. In contrast to SFA-formulas 4.3 and 4.4, equation 4.20 takes into account nonlinearities due to fringe fields. We apply now this analytical formula to transducer *#C2* (etched electrodes, see figure 4.2). We consider a differential read-out scheme shown in figure 4.4. In the case of sensor type *#C2* we have not only taken into account the electrode distance and surface, but also the influence of the limited height h of the etched electrodes. This results in a higher zero capacitance. In addition, the

gap c between the lower counter electrodes can not be infinitely small due to the limitation by the photolithographic fabrication process (see figure 4.4).
In the model proposed in figure 4.4 (bottom), apart from the two main capacitances C1' and C2', also the parasitic capacitances are considered coming from the silicon mass: C1'', C1''' and C2'', C2''', respectively. The difference of the capacitors can thus be expressed by:

$$\Delta C = C1 - C2 = [(C1' + C1'' + C1''') - (C2' + C2'' + C2''')]\,. \quad (4.21)$$

where all the individual capacitances are calculated by equation 4.20. The electrostatic fields coming from the vertical walls of the etched electrode are difficult to describe analytically, and are thus neglected. Since their contribution to the capacitive response might be important, they are considered in the numerical simulations, presented in the following.

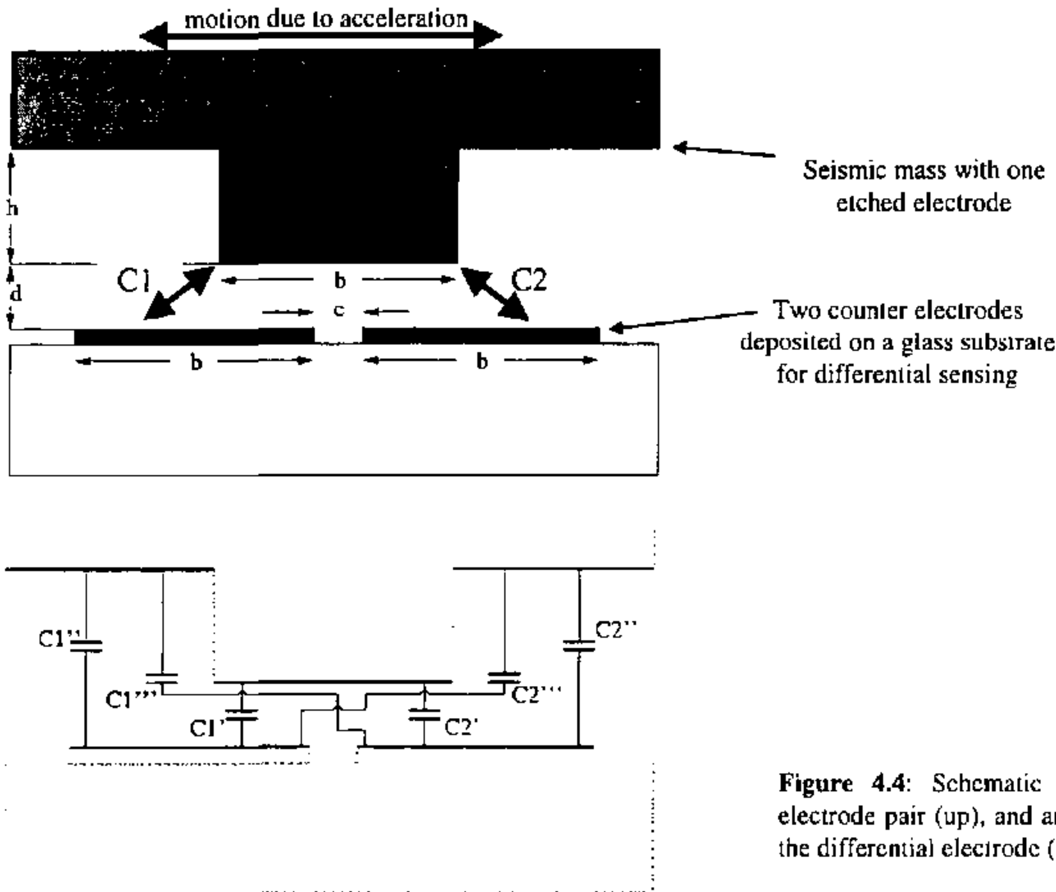

Figure 4.4: Schematic of a differential electrode pair (up), and analytical model of the differential electrode (low).

The static behavior of the lateral accelerometer is simulated in figure 4.5. It becomes visible that the capacitive response is not perfectly linear (which is in opposite to results obtained by SFA). However, we can conclude in this case that at least in the range of ±10g the capacitive change is quite linear with a slope of about 2pF/g. Zero Capacitance Co is about 17pF. In reality we are faced to further parasitic capacitances (wires, packaging...). Since an alignment error between upper and lower electrode will occur in practical realizations, the linearity of the capacitance versus displacement plays an important role (the measurement range plus a margin due to alignment errors should lie in the linear displacement range).

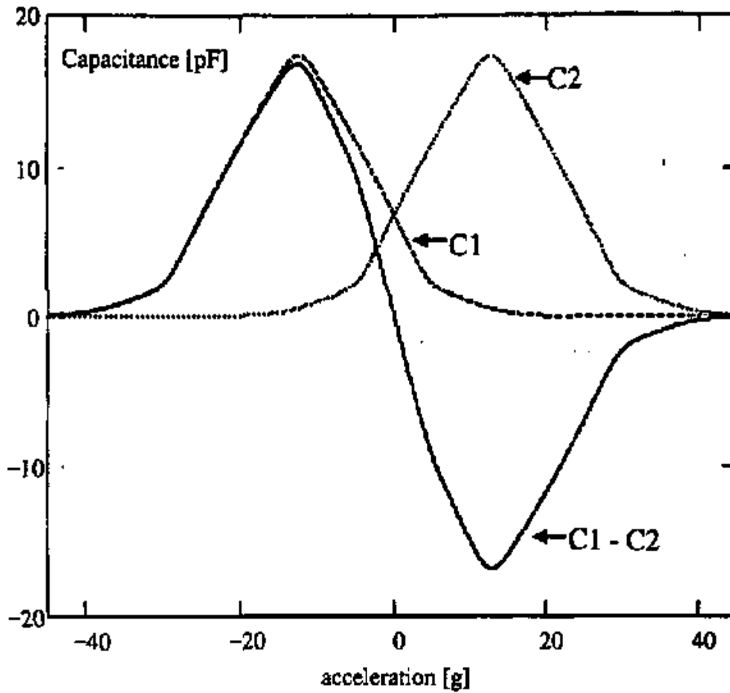

Figure 4.5: Calculated capacitive change for a differential configuration of lateral transducer #C2 based on the model shown in figure 4.4. The used parameters are: b = 17μm, c = 8μm, a = 5700μm, N = 55, d = 2.7μm, Sy = 1μm/g. C1 and C2 respectively represents the single capacitive response, while C1 - C2 is the differential output signal.

The above analytical modeling gives us the possibility to optimize quickly the system sensitivity, and to investigate further the dependence of the sensitivity dC/dy versus design parameters. Results calculated analytically with formula 4.20, regarding the capacitive sensitivity and it's dependence from the device parameters, are discussed more in detail in the two following sections.

4.3.3 Finite element simulation

In addition to analytical calculations, numerical simulations have been performed. From the electric field simulations using Finite Element Methods (FEM) one can derive the capacitance response [Bon95]. The disadvantage of FEM is that it can be quite time consuming. Analytical calculations based on approximations are faster. However, these calculations cannot be universally applied. In general, FEM models are well adapted to realized devices and can thus give estimations closer to real performance. Two-dimensional FEM simulations have been done with the help of the software package MODULEF and three-dimensional FEM calculations with the commercial tool ANSYS. The results obtained from FEM simulations will be compared with the those obtained from analytical modeling in order to evaluate the relevance of the analytical approach.

2D FEM simulation (MODULEF)

In a first approach a two-dimensional model is used to simulate the capacitive transducer (figure 4.6). Computing was done by MODULEF. Capacitance was calculated between two electrodes. One of them was successively shifted parallel in order to obtain a capacitance vs. displacement curve. The model is very simple, but can give a good estimation of the capacitive sensitivity,

defined as $\partial C/\partial y$, as far as fringe fields are constant. However, the total capacitance can not be correctly calculated due to the two-dimensional simplification.

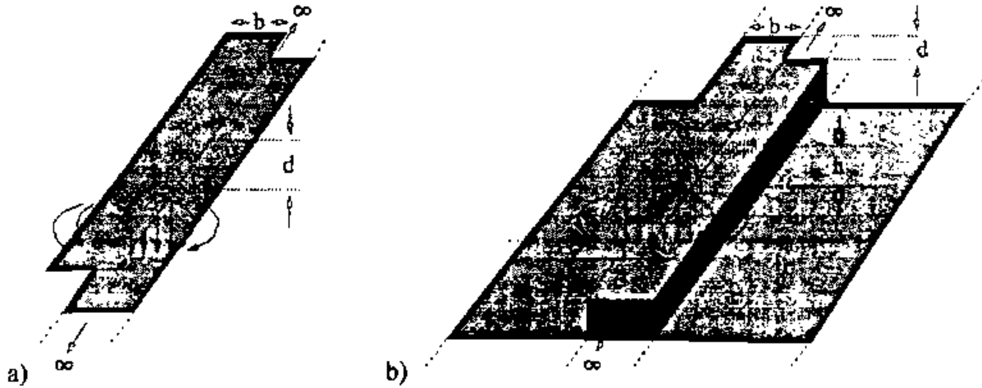

Figure 4.6: First simplified Structure simulated by FEM: 2D model using software MODULEF. The electrodes are assumed to be inventively long (a). A second two-dimensional electrodes structure corresponding to an etched electrode as used in sensor type #C2 (b).

A comparison between results obtained from SFA, analytical formula 4.20 and MODULEF is shown in figure 4.7. In this case, only one electrode is taken into account. One can see that the capacitive sensitivity $\partial C/\partial y$ is around an overlap Δy of 5μm constant. Here, 5μm corresponds to the half-electrode with a width b/2. Also, the sensitivities are similar around b/2, $\partial C/\partial y$ is slightly larger for the SFA. The sensitivities mainly differ by a constant capacitance offset which is due to the stray or fringe fields.

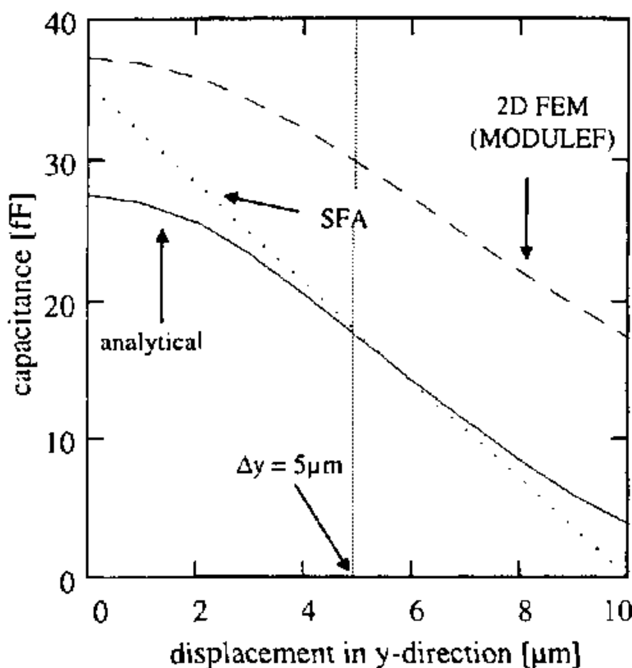

Figure 4.7: Simulation of the capacitance of only one electrode (N=1) using three different approaches: SFA, analytical formula 4.20, and 2D FEM simulations (MODULEF). A displacement $\Delta y = 0$ means exact alignment between upper and lower electrode; b = c = 10μm, d = 5μm, a = 2000μm). Simulation is performed with model in figure 4.6a).

In addition, we performed simulation on a second simple model corresponding to etched electrodes (see figure 4.6b). Thus parasitic capacitances from the electrode's sidewalls and the silicon seismic mass add to the total capacitance. The capacitive response versus lateral

displacement is shown in figure 4.8 for different electrode heights. While the capacitive sensitivity varies only slightly as a function of electrode height h ($S_{cap} \approx$ 1pF/μm to 1.5pF/μm), the total capacitance increases significantly with decreasing h. Analytical calculations are also made for this case. The corresponding analytical model neglects the electrostatic fields coming from the vertical walls of the etched electrode. These fields are considered in the MODULEF-model, which explains an offset in total capacitance between the two models. However, as in figure 4.7, the capacitive sensitivity (slope) is nearly identical for analytical and 2D FEM modelisation.

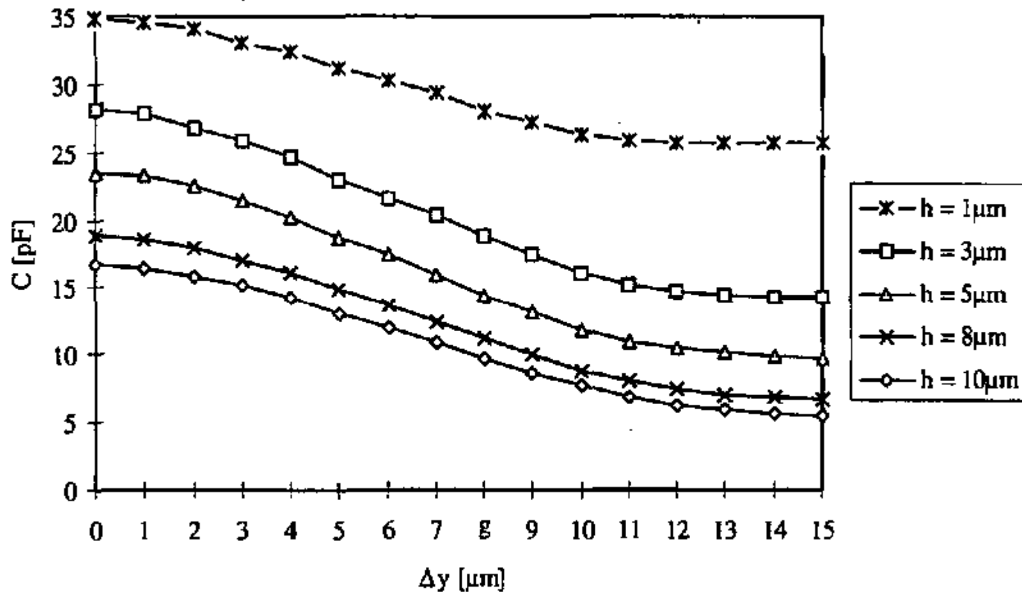

Figure 4.8: Simulation of the capacitance response using the MODLEF model of figure 4.5b) for different electrode heights h. Used parameters: b = 20μm, c = 30μm, d = 2μm, a = 5000μm, N = 45, electrode height h = 5μm.

3D FEM simulation

A three-dimensional FEM simulation was performed using the software ANSYS [15, 17, 18]. In the case of capacitance calculation , ANSYS element type SOLID122, a 3D 20-node electrostatic element with a VOLT degree of freedom at each node is used to model the device. Known voltages are applied to the boundary of the electrodes of the model. After solution, the electric flux density is available at corner nodes for postprocessing. A physical parameter extractor tool, developed at the EPFL [Ro97], calculates the capacitance between electrodes by evaluating the electric flux density integral over equipotential electrode surfaces. The general concept is similar to the analytical modelisation given in formula 4.18.

Figure 4.9: 3D FEM model using ANSYS. In this case an isolating layer and the silicon seismic mass are also taken into account (like sensor #∅).

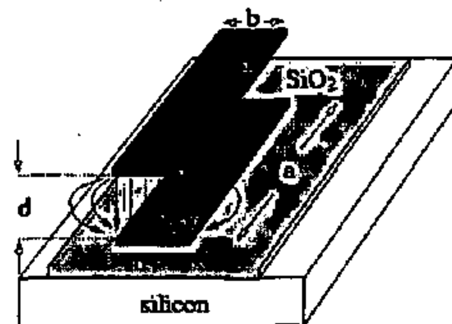

Sensor #01 with flat electrodes was modeled for simulation. Thus we considered in addition an isolating SiO_2-layer between silicon mass and thin-film electrodes (see figure 4.9). Three electrodes sets are taken into account in the evaluation of the capacitance: the fixed upper metal electrode deposited on glass, the lower movable metal electrode deposited on a silicon oxide layer, and the silicon mass as another electrode. The electric potential and the charge of the upper electrode are respectively V_{up}, V_{lo}, V_{si}, Q_{up}, Q_{lo}, Q_{si}. The three interconnected capacitors C_{ul}, C_{us} and C_{ls} between the electrodes are shown on figure 4.10. The link between these nine quantities is given by

$$\begin{pmatrix} Q_{up} + Q_{lo} \\ Q_{lo} + Q_{Si} \\ Q_{Si} + Q_{up} \end{pmatrix} = \begin{bmatrix} V_{lo} - V_{Si} & V_{up} - V_{Si} & 0 \\ 0 & V_{Si} - V_{up} & V_{lo} - V_{up} \\ V_{Si} - V_{lo} & 0 & V_{up} - V_{lo} \end{bmatrix} \cdot \begin{pmatrix} C_{ls} \\ C_{us} \\ C_{ul} \end{pmatrix} \qquad (4.22).$$

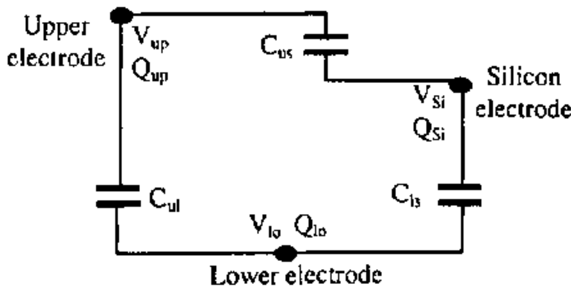

Figure 4.10: Schematic of the capacitor circuit used in the 3D ANSYS simulation.

If the potentials and the charges can be measured or calculated, the three capacitances can be calculated with equation 4.22. Estimations based on SFA applying formula 4.3, are for this case:

$$C_{ul} = \varepsilon_{air} \frac{N \cdot a \cdot (b - \Delta y)}{d} \qquad (4.23)$$

$$C_{us} = \frac{N \cdot a \cdot b}{d / \varepsilon_{air} + e / \varepsilon_{SiO2}} \qquad (4.24)$$

$$C_{ls} = \varepsilon_{SiO2} \frac{N \cdot a \cdot b}{e} \qquad (4.25)$$

where ε_{air} and ε_{SiO2} are the dielectric permitivity of air and silicon oxide, e the thickness of the oxide layer and a, b and d as above defined. Of course, capacitance calculations based on the ANSYS Electrostatic Field Analysis package allows better accuracy to be achieved. The charges are extracted using the physical parameter extractor after electrostatic analysis (figure 4.11).

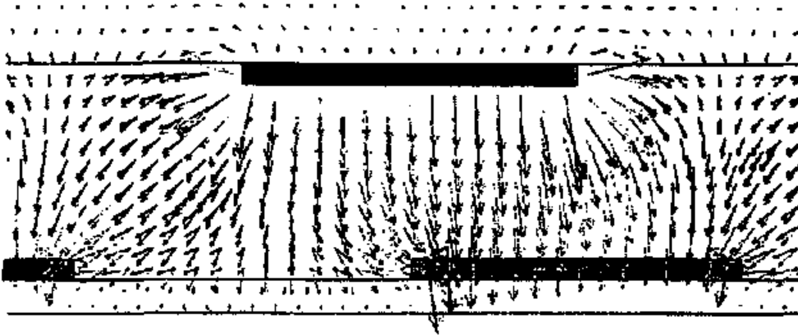

Figure 4.11: Cross section of the finite-element model (ANSYS) and the dielectric flux density represented by arrows (in this case a = 10μm, b = c = 10μm, d = 5μm, e = 1μm, N = 5, V_{up} = 10V, V_{lo} = 0V, and V_{Si} = 0V).

Assuming that b = c = 10μm is the displacement range, figure 4.12 displays the calculated capacitance C_{ul} obtained by analytical, SFA and ANSYS. The stray fields of neighbor electrodes is taken into account. Note, that the analytical and SFA result is offset-compensated by adding the constant value of 4.8pF. If C_{ul} + C_{us} is calculated, one founds that the analytical and SFA calculations overestimate the capacitance value because C_{ul} and C_{us} are calculated independently. FEM results are more accurate but time consuming. The precision is linked to the fineness of the mesh and thus to the computing time. In this case, the results vary less than ± 10% when the meshing size of the electrostatic finite-element model is halved. ANSYS results confirm that a good linear response of the capacitive transducer is obtained around the middle of the displacement range.

Very remarkable is the good agreement in capacitive sensitivity $\partial C/\partial y$ for ANSYS and analytical calculations. This allows to use the analytical formula instead of time consuming FEM calculations to optimize the capacitive response. However, in that case, the total capacitance might be not well estimated.

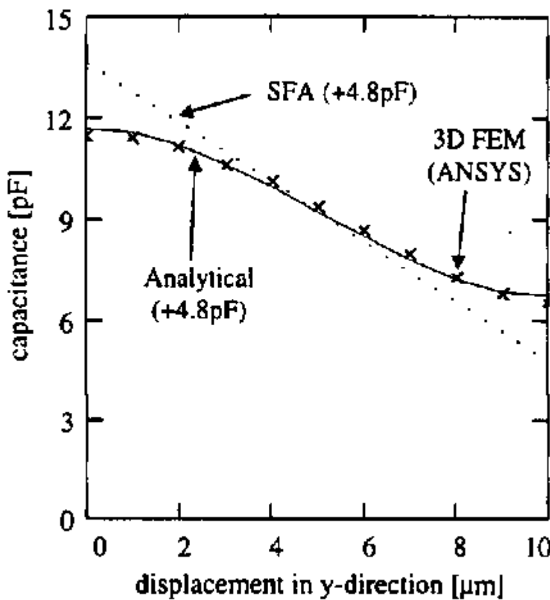

Figure 4.12: Comparison between analytical (solid line), SFA (dotted line), and ANSYS (crosses) results for the capacitance change (N=250, b=c=10μm, d=5μm, a=2000μm). The analytical and SFA results are corrected by adding a constant capacitance of 4.8pF. Note: the electrostatic strayfield of the neighbor electrodes is included in all calculations.

As mentioned earlier, sensor #C1 needs an isolating layer to separate seismic mass and metal electrodes. This is taken into account in the above simulations. However, neither the FEM nor the analytical models take into account possible free charges in this silicon oxide layer, which can disrupt the accelerometer detection operation. This can be avoided in case of accelerometers of type #C2.

4.3.4 Investigations concerning the capacitive sensitivity

After having verified the accuracy of the analytical model, which is quite precise for estimating $\partial C/\partial y$, we can now investigate further the dependence of the sensitivity $\partial C/\partial y$. The analytical model offers the advantage of studying easily and fast a large range of design parameters. The effect of nonlinearity is additionally investigated. For a fixed gap d of 5μm we find a maximum sensitivity for a parameter b of 10μm (see fig. 4.13), corresponding to twice the gap d. This relation, maximum sensitivity at $b \approx 2d$, was also approximately obtained for gap values of 2μm and 3μm.

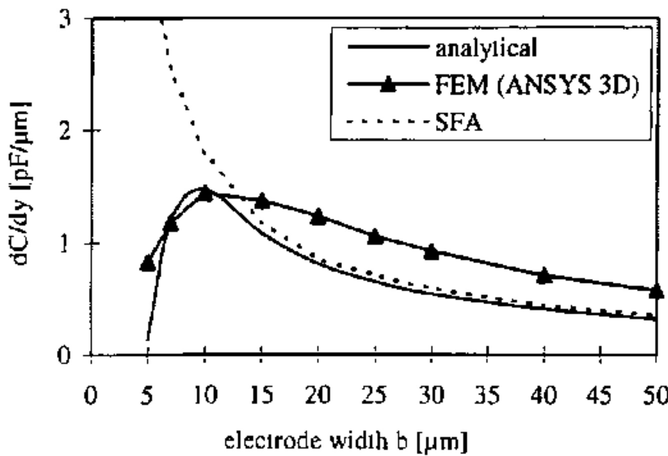

Figure 4.13: Capacitive sensitivity $\partial C/\partial y$ as a function of the electrode width b (c=h, d=5μm, N(b+c)=8000μm, a=4000μm).

By reducing the gap d the results from the analytical formula 4.20 approach the results based on SFA, relating to an improvement in the linearity (see table 4.1 and fig. 4.14). For example, by decreasing the gap from 5μm to 1μm, the nonlinearity is reduced by a factor of 10^4 (in a 1μm displacement range). The linearity of the capacitive sensitivity plays an important role regarding the fact that in the practical realization an alignment error between upper and lower electrode will occur. Therefore, the measurement range plus a margin due to alignment errors should cover a linear displacement range.

Displacement range	*Nonlinearity in capacitive sensitivity*		
	d=5μm	d=3μm	d=1μm
1μm	0.29%	0.1%	0.00003%
3μm	2.6%	1%	0.0006%
5μm	7.6%	3.3%	0.09%

Table 4.1: Nonlinearity in the capacitive sensitivity $\partial C/\partial y$ as a function of the gap d and the displacement.

In conclusion, the most important parameter is the gap d, which should be as small as possible in order to reduce nonlinearity and to increase sensitivity. On the other side, the electrode width b is more dependent from the available alignment accuracy between lower and upper electrode.

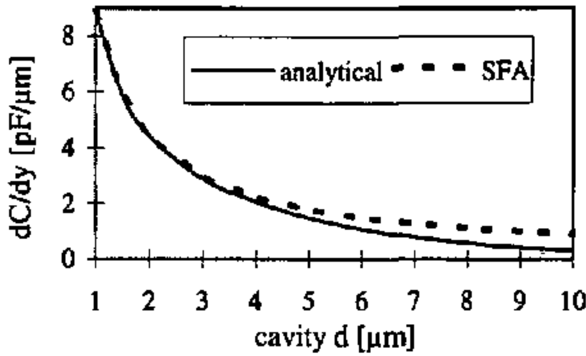

Figure 4.14: Capacitive sensitivity ∂C/∂y as a function of the gap d (here b=c=10µm , a=4000µm, N=500).

Considering electrodes fabricated by anisotropic etching in KOH, one can find an optimum relation between electrode height and width. Due to the underetching of vertical {100} silicon planes the height cannot be increased without decreasing the electrode width. In order to find an optimum electrode height h in this case of the etched electrodes, the capacitive sensitivity was calculated as a function of h for different electrode distances d.
From Figure 4.15, we can conclude that the capacitive sensitivity mainly depends on the electrode distance d, and less on the electrode height h.

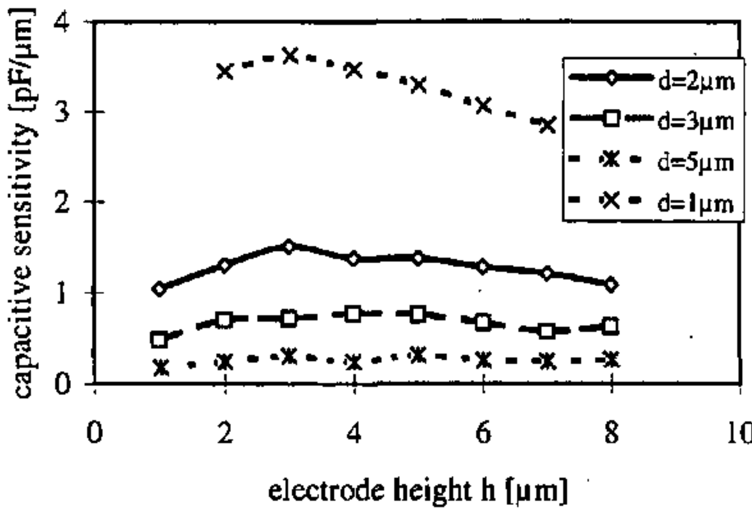

Figure 4.15: Capacitive sensitivity for the in-plane transducer with etched electrodes as a function of electrode height h for different electrode distance d (simulated with MODULEF).

4.3.5 Global simulation

Earlier in chapter 2 mechanical modeling for the accelerometer structure was presented. In the sections above, models have been developed for the capacitive response. Using both mechanical and capacitance data, a global model for the lateral accelerometer is generated with behavioral models written in Hardware Description Language used for Analog electronics (HDL-A) [Ans98]. Finally, these behavioral models are used in SPICE-like circuit simulators, to perform system simulations together with the read-out electronics. The procedure of the global modeling process is shown in figure 4.16.

Figure 4.16: Behavioral global modeling flow process

Mechanical model generation

The accelerometer device modeling has been split into two elements. The first element is modeled as a mechanical harmonic resonator directly obtained from the structural finite element simulation presented in chapter 2. The mathematical model used to describe the mechanical behavior of the accelerometer is a linear differential equation. From the network theory point of view, this model is a passive one-port element. The nature of the signal going through and across the pins of the one-port model are respectively the force F and the displacement Δy corresponding to the *mechanical2* nature in HDL-A.

The harmonic simulation has been done with an excitation force applied on the gravity center of the mechanical structure of the accelerometer. The displacement of this gravity center is picked up and implemented into a mechanical energy received by the accelerometer. The parameters of the mechanical model are calculated automatically from finite element simulation results, the amplitude response of the model is modulated in the case of large deflection. The modulation of the amplitude response is implemented into the accelerometer HDL-A model.

Capacitive model generation

The electrical part of the model is a variable capacitor load implemented as a piecewise linear lookup table, or as a analytical function. The nature in HDL-A of the input variables are *mechanical2* and *electrical* for the output variables. At first, the capacitance data was extracted from finite element simulations performed by ANSYS [17, 18]. Later the data was taken from the above developed analytical model (formula 4.20 and 4.21) [10] in order to simulate the etched electrodes and differential detection. In each case, the capacitance response is implemented into a two-port model. This two-port model written in HDL-A is acting like a transducer converting the displacement of the seismic mass of the accelerometer into a capacitance. Equation 4.26 links the output current I and the output voltage V of the two-port model:

$$C\frac{dV}{dt} + V\frac{dC}{dt} = I \qquad (4.26)$$

Global simulation

Figure 4.17 is a schematic view of the global model accelerometer architecture. The resultant behavioral model of the whole accelerometer is used in an analog circuit simulator to perform simulations together with the detection electronics. Generation of behavioral HDL-A models of devices characterized using finite elements or analytical formulae results in fast system simulation. This method prevents convergence problems often encountered when coupling different field solvers.

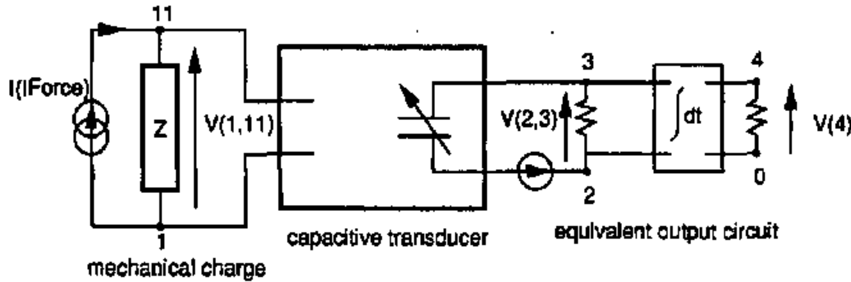

Figure 4.17: Schematic of the electric accelerometer circuit using HDL-A models.

In order to illustrate the global model of the accelerometer, the electric circuit shown in figure 4.17 is employed to detect accelerations. A constant bias voltage and a resistor are connected in series with the accelerometer model. A capacitance change induces a current change in the resistor and a resistor's bias signal, which is integrated to obtain a signal proportional to the acceleration. Network simulations are performed on ELDO, a SPICE-like simulator with a transient force signal. Simulations results for a differential electrode configuration of sensor type #C2 are displayed in figure 4.18.

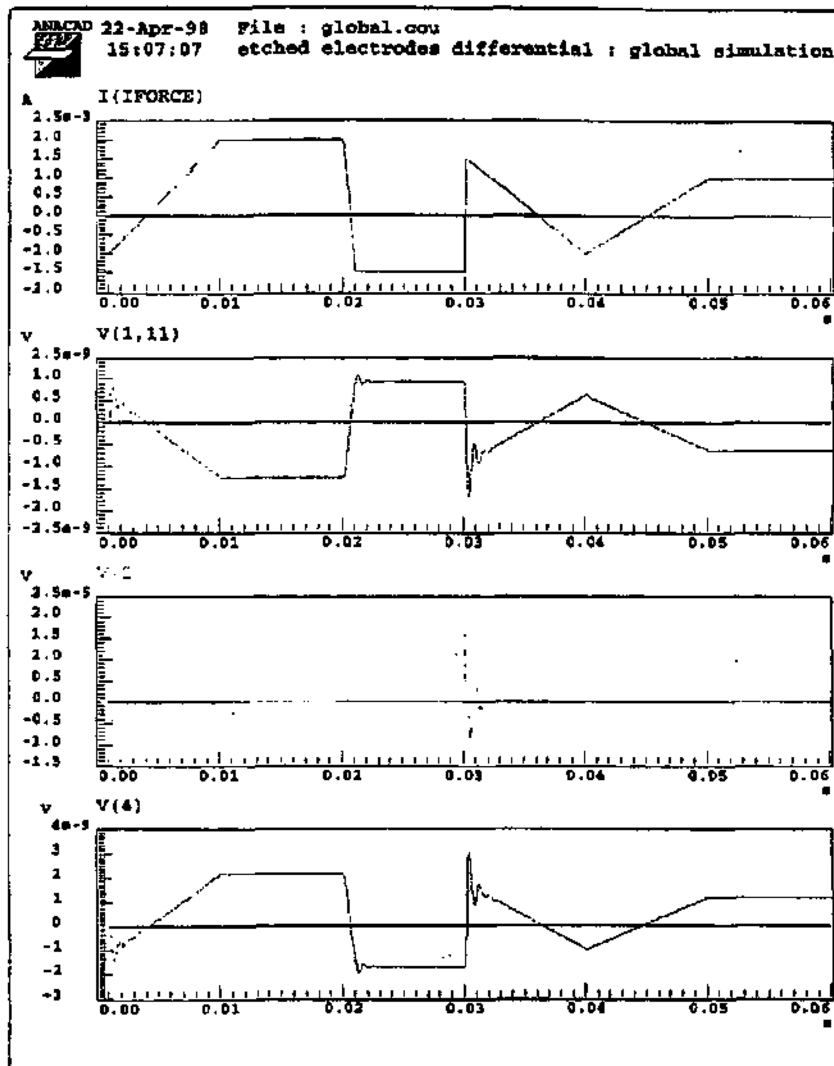

Figure 4.18: Transient global simulation results of the accelerometer circuit represented in figure 4.17: upper graph, applied current/force I(IFORCE); second and third graph, intermediate voltage taken at the mechanical charge V(1,11) and at the resistance V(2,3); and finally lowest graph, transient output voltage V(4). Quality factor Q = 2.

In order to improve the global model, feedback forces generated by the potentials on the seismic mass can be calculated either by ANSYS or analytically, and implemented in the model. Including electrostatic feedback forces in the model, a possible closed looped accelerometer electronic circuit can be tested in order to increase acceleration range and bandwidth of the sensor.

4.3.6 Electrostatic force analysis

We have already discussed the advantages of the electrostatic force feedback above and in section 4.2.6. A schematic of a closed-loop system is shown in figure 4.19.

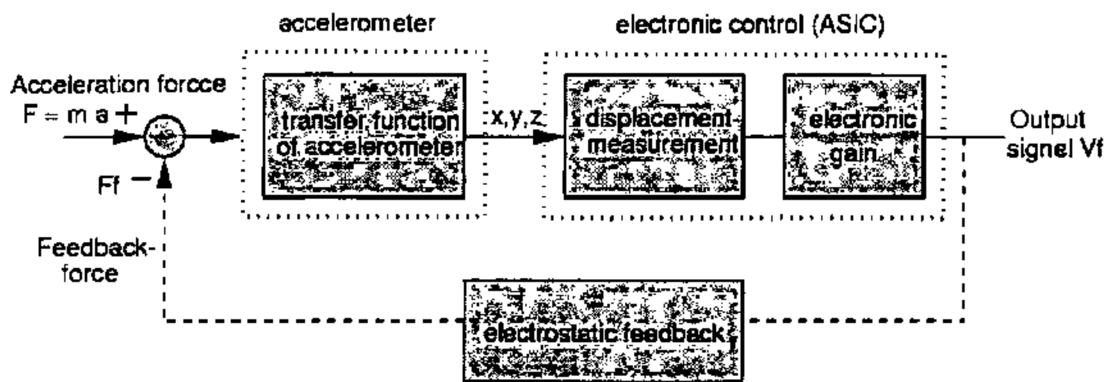

Figure 4.19: Schematic of a closed-loop system using electrostatic feedback to compensate the inertial forces.

Now we investigate more in detail the electrostatic forces for the lateral capacitive transducer. For this case, the components in y- and z-direction are relevant. Remembering equation 4.15, they are given by

$$F_{el,y} = \frac{1}{2}\frac{\partial C}{\partial y}V^2 \qquad \text{and} \qquad F_{el,z} = \frac{1}{2}\frac{\partial C}{\partial z}V^2 .$$

An applied voltage V generate always an attractive force in vertical and lateral direction. The forces are dependent from the capacitive sensitivities. Fortunately, we can profit from the previous analytical and FEM modeling in order to calculate $\partial C/\partial y$, $\partial C/\partial z$ and thus the electrostatic force. In figure 4.20 we present electrostatic forces for the lateral direction ($F_{el,y}$) and for the vertical direction ($F_{el,z}$) as a function of the lateral electrode position ($y = 0\mu m$: no displacement regarding two opposite electrodes, $y{=}b$: two opposite electrodes are shifted by electrode width b). The forces have been calculated by analytical formulae and SFA. To explain the arising forces in a general way, we consider SFA. With formula 4.4 the forces in lateral and vertical direction are given respectively

$$F_{el,y} = -\tfrac{1}{2}\, N\, \varepsilon_0\, a\, (d-\Delta z)^{-1}\, V^2 \qquad (4.27)$$

$$F_{el,z} = -\tfrac{1}{2}\, N\, \varepsilon_0\, a\, (b-\Delta y)\, (d-\Delta z)^{-2}\, V^2 \qquad (4.28)$$

As pointed out in figure 4.20 and equation 4.27, for SFA the lateral force is constant regarding displacement Δy, and the vertical force is proportional to $-\Delta y$. More precise analytical analysis takes fringe effects into account, showing that the lateral force vanishes at the electrode's edges. Generally for our structures, vertical forces are higher than lateral forces. In the presented case, inertial forces up to an equivalent acceleration of 4g could be compensated by an applied voltage of 20V. However, electrostatic vertical forces should also be compensated. For this reason an additional counter electrode could be placed on the opposite side of the seismic mass. This counter electrode does not consist of meander shaped electrodes, but only of one plane plate. The almost same voltage would be applied to this electrode. Such a formed capacitor could thus only be sensitive to vertical, and not to lateral forces.
In case of an accelerometer that is only sensitive in vertical directions, higher electrostatic forces can be generated compensating accelerations up to 40g for 20V (if the electrodes are not shifted). As the electrostatic force is always attractive, both, vertical and lateral devices have to operate with a differential electrode configuration in order to compensate positive and negative accelerations.

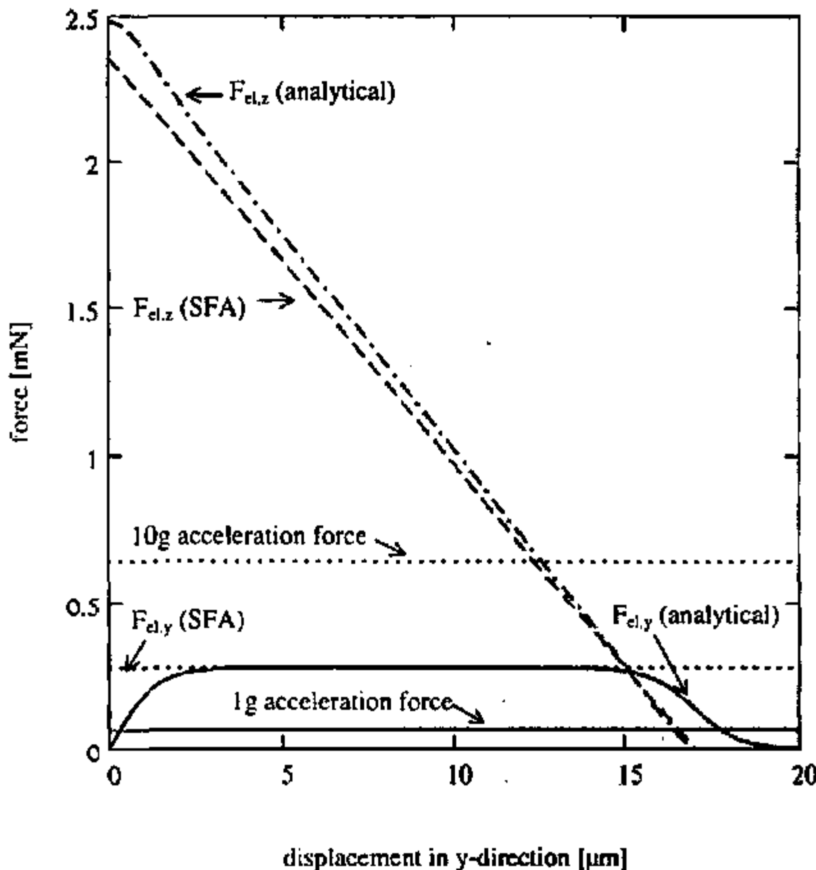

Figure 4.20: Electrostatic force calculation regarding lateral forces in the lateral direction ($F_{el,y}$) and for the vertical direction ($F_{el,z}$) as a function of the lateral electrode position. Used parameters: a=5700µm, b=17µm, c=8µm, d=2µm, N=55. Applied voltage is 20V.

4.4 Fabrication of the capacitive accelerometers

The bulk-micromachining of 3D seismic mass elements has been described in chapter 3. Some essential process steps have to be added in order to fabricate the complete capacitive sensor. Cavities have to be formed in order to ensure the movement of the seismic masses. Also, electrodes on the movable mass and fixed counter-electrodes have to be provided. Finally, assembling by anodic bonding, chip separation, mounting and wire bonding complete the fabrication sequence.

Electrode fabrication can be achieved by thin-film deposition or silicon etching. Both possibilities have been applied and are discussed. In the following we present two devices, which differ by their fabrication process and their design: a two-dimensional accelerometer (*2D #C1*), and a three-dimensional device (*3D #C2*).

4.4.1 Silicon process for the accelerometer using thin film electrodes

The first realized prototype consists of two seismic masses oriented perpendicular to each other and sensitive parallel to the wafer. One keyelement in capacitive sensor fabrication is the forming of electrodes. For this device, comb-shaped electrodes have been provided by thin-film deposition. As the wafer is difficult to process after KOH wet etching, electrodes have to be fabricated before the structuring of seismic mass elements. If metal films are used as electrode material, the metal should be either resistant to the etching solvent or the deposited metal has to be protected by another layer, e.g. silicon oxide or silicon nitride. Employment of a chuck as protective tool is not possible in our case, due to the double side etch process. In order to minimize the number of process steps we have chosen to use the KOH resistant metals nickel and chromium.

The complete process is listed and illustrated in figure 4.21. It starts from a double side polished (100) silicon wafer. The first step is thermal oxidation. The obtained silicon oxide (SiO_2) is used as a masking layer for KOH etching and also as isolating layer between the seismic mass and the metal electrodes. Nickel or chromium is than sputtered on the oxidized wafer. This metal layer is afterwards structured in order to form electrodes and conductors. As the metal should remain several hours during the KOH wet etching process, a very good adhesion to the wafer is required in addition to a good resistivity against KOH. Our laboratory experience shows that sputtered metal layers tend to exhibit better adhesion than thin films deposited by evaporation. Also when nickel is used, a thin chromium layer is used as adhesive film between SiO_2 and Ni. Adhesion can be improved by heating the substrate during deposition [Ren97]. After wet etching of the metal layer, the photolithography for silicon wet etching is performed. As only suspended masses sensitive to in-plane accelerations are contained in the 2D device, no maskeless etching is necessary, therefore only one KOH etching step is performed. Finally, the remaining silicon oxide is removed in Buffered HydroFluoric acid (BHF). One advantage of chrome and nickel is that they are also resistant to BHF. Thus, as the SiO_2 under the electrodes is protected by the metal, the oxide layer can function as isolating layer (see figure 4.22). A scanning electron microscope image of the total 2D device *#C1* after completed silicon micromachining is shown in figure 4.23. The silicon wafer fabrication sequence is, in the case of this sensor, simple and quite short. However, the following glass processing steps are more complicated and will be explained in the next section. Before, the silicon process for the 3D accelerometer *#C2* will be described.

As mentioned in the discussion on the capacitive simulation, free charges could be generated in the isolating silicon oxide layer. This can disturb the accelerometer detection operation. The problem can be avoided for accelerometers of type *#C2*.

Step	Process	Mask
1	Thermal oxidation of double side polished Si, 1.3μm SiO_2	
2	Sputtering of Cr-Ni or Cr (~200nm)	
3	Double side photolithography for electrodes and conductors	mask 1, 2
4	Wet etching of electrodes	
5	Stripping of photoresist	
6	Double side photolithography for suspended seismic mass elements	mask 3, 4
7	Oxide opening in BHF	
8	Stripping of photoresist	
9	Wet etching in KOH 41%wt.	
10	Removing of remaining oxide	

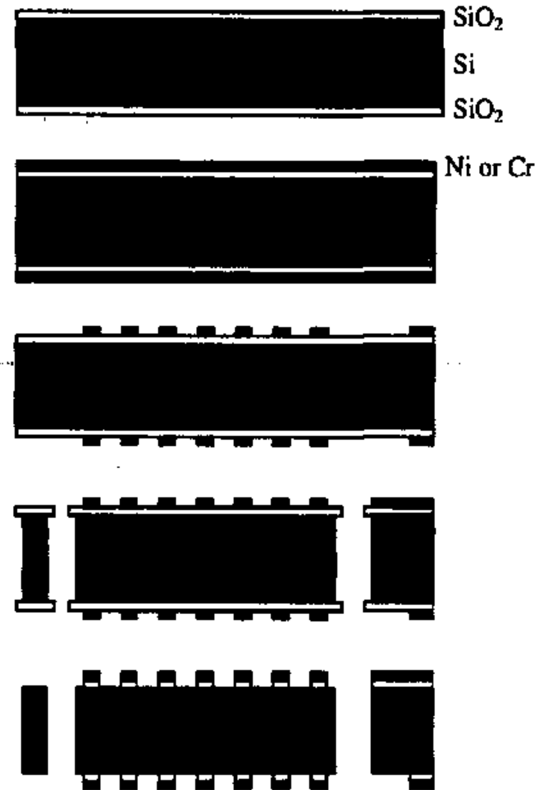

Figure 4.21: Fabrication sequence of the silicon wafer for 2D accelerometer #① (thin-film electrodes).

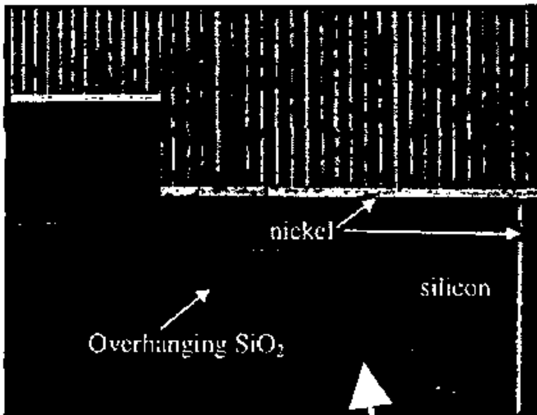

Figure 4.22: Nickel electrodes deposited on the silicon seismic mass. The isolating SiO_2 film used as etch mask and as isolating layer is not yet removed.

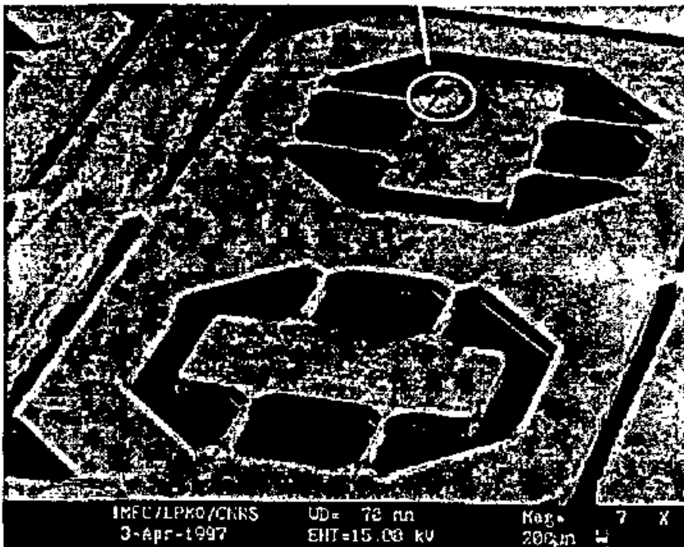

Figure 4.23: SEM image of a total 2D device #① after having completed the silicon wafer process (SiO_2 is still to be removed).

4.4.2 Silicon process for the accelerometer using etched electrodes

In the case of sensor type #C2. the electrodes are directly formed into the silicon. Thus, the whole silicon seismic mass and the associated frame works as an electrode. In this way, the parasitic influence of the seismic mass to the sensor capacitance is canceled. The starting material is again a double side polished 3inch (100) silicon wafer. As the silicon is in this case not only a mechanical material, but also a conductor, one has to pay special attention on type and concentration of doping. P-type silicon with a resistance of 2-3Ωcm was chosen. The overall device contains three seismic masses.
Figure 4.24 illustrate the process sequence for the silicon wafer in case of device #C2. The first photolithographic step is performed in order to micromachine a cavity to enable the movement of the seismic mass, and also to adjust the lateral and squeeze film damping. Etching was done in KOH-solution, but could also be replaced by dry etching. As this first etching step is only some micrometers deep (typically 2μm-5μm), the initial masking oxide layer can be relatively thin (~ 0.3μm). This is identical in the case of the second etching step. The second photolithography defines the electrodes for two capacitive in-plane seismic masses. Bulk-micromachining can be either performed in KOH using the underetching of {100} silicon planes, or by dry etching (RIE). In the first case, due to the underetching, we are limited in the variation of the design parameters: increasing the electrode height h by a longer etching time means also increasing the distance c between two etched electrodes (see figure 4.25).
Before performing long time KOH etching in order to release the suspended seismic masses, the pre-etched wafer is thermally oxidized with a thick 1.3μm layer. Despite the first two etching steps, the following photolithographic processes are not critical because the pre-etched structures show only a depth of some micrometers. However, a thick photoresist (SJR 5740) has to be used for both wafer sides in order to protect well the etched cavities and electrodes. After an etching depth corresponding to the half-height of the horizontally located suspension beams of the vertical seismic mass, the wafer is withdrawn from the KOH, to be submitted to a last photolithographic step. This is the maskless etching step to release the horizontal beams. The lateral structures are not influenced by this step. Re-oxidation is not necessary, and KOH wet etching is continued after a short BHF etch and stripping of the photoresist. As in the maskless etching step no high precision is required, the lithography of the structured wafer does not cause any difficulty.
The final silicon chip is pictured in figure 4.26. It contains two lateral seismic masses, each having N silicon electrodes, and one device sensitive to vertical accelerations. The silicon process consists of more photolithographic steps than in case of device #C1. However, in accelerometer #C2 three sensing elements are contained and subsequently glass processing is easier as no etching into the glass is necessary.

Step	Process	Mask
1	Thin thermal oxidation (0.3μm) of double side polished Si	
2	Double side photolithography for cavity (2-5μm)	mask 1, 2
3	Oxide opening in BHF	
4	Stripping of photoresist	
5	Wet or dry etching of cavity	
6	Removing of remaining oxide	
7	Thin thermal oxidation (0.3μm)	
8	Double side photolithography for electrodes	mask 3, 4
9	Oxide opening in BHF	
10	Stripping of photoresist	
11	Wet or dry etching of electrodes	
12	Removing of remaining oxide	
13	Thick thermal oxidation(1.3μm)	
14	Double side photolithography for suspended seismic masses	mask 5, 6
15	Oxide opening in BHF	
16	Stripping of photoresist	
17	Wet etching in KOH 41%wt.	
18	Double side photolithography for maskless etching	mask 7, 8
19	Oxide opening in BHF	
20	Stripping of photoresist	
21	Continuing etching in KOH	
22	Removing of remaining oxide	

SiO_2
Si
SiO_2

Lateral mass with etched electrodes:

Vertical mass (maskless etching):

Figure 4.24: Fabrication sequences of the silicon wafer for 3D accelerometer #C2 (etched silicon electrodes).

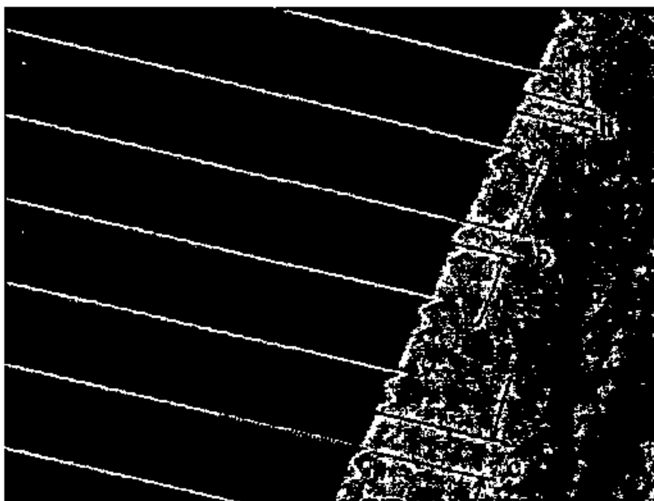

Figure 4.25: Electrodes with vertical sidewalls directly etched in to the silicon seismic mass. In the presented case etching was performed in KOH solution.

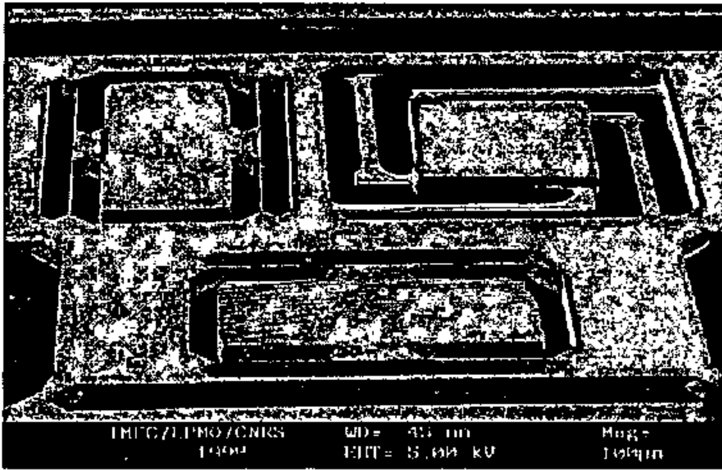

Figure 4.26: The final silicon chip of 3D accelerometer #C2 with etched electrodes for capacitive in-plane detection.

Alternatively to the proposed 3D design of accelerometer #C2 containing three individual seismic masses, a three-axis accelerometer consisting of a single seismic mass has been fabricated within the same process. The device is entitled accelerometer #C3 and shown in figure 4.27. The mechanical analysis of this design have been discussed in chapter 2. Comb-shaped electrodes are formed into the silicon and arranged in four quadratic areas. Counter electrodes are provided on an upper and a lower glass substrate. In-plane accelerations are detected by comb-shaped electrodes on one glass substrate. Vertical accelerations are sensed by one plane electrode positioned on the opposite glass substrate.

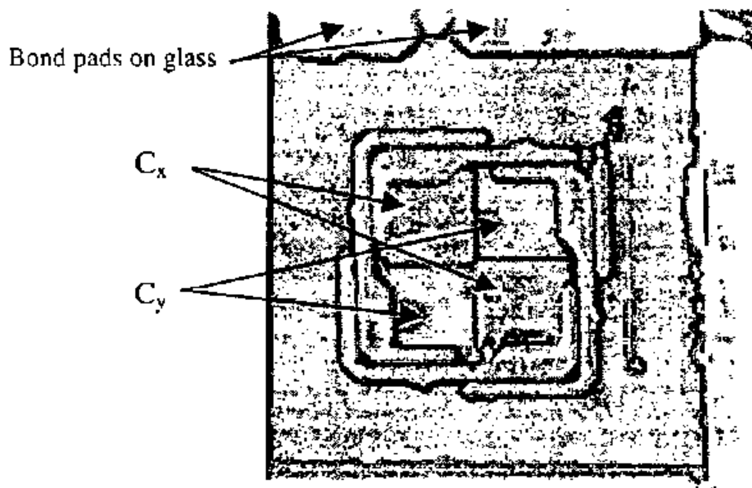

Figure 4.27: Silicon chip of accelerometer #C3 using a singnle seismic mass for tree axis capacitive detection.

4.4.3 Glass wafer processing

Glass processing is necessary in order to perform two different tasks. Firstly, to provide fixed counter and shielding electrodes, and secondly to encapsulate the silicon die. A schematic view of the 3D capacitive accelerometer is shown in figure 4.28. The lower glass wafer contains the comb-shaped detection electrodes for the lateral masses and one electrode of the vertical mass. The upper glass wafer provides the second electrode for the vertical mass to ensure differential sensing. Also additional plane electrodes are used for the in-plane devices in order to compensate vertical electrostatic forces, i.e. in case of closed-loop operation. Shielding electrodes positioned on the glass wafers are not represented in figure 4.28, but are considered in the realized devices.

Several types of glass can be used to provide fixed electrodes and encapsulation. An often used type is Pyrex glass 7740 [Pyr97]. It is especially suitable for anodic bonding of silicon-glass, because the thermal expansion coefficient of this glass nearly equals that of silicon for a wide temperature range. This permits a low-stress bond between the glass and silicon wafer.

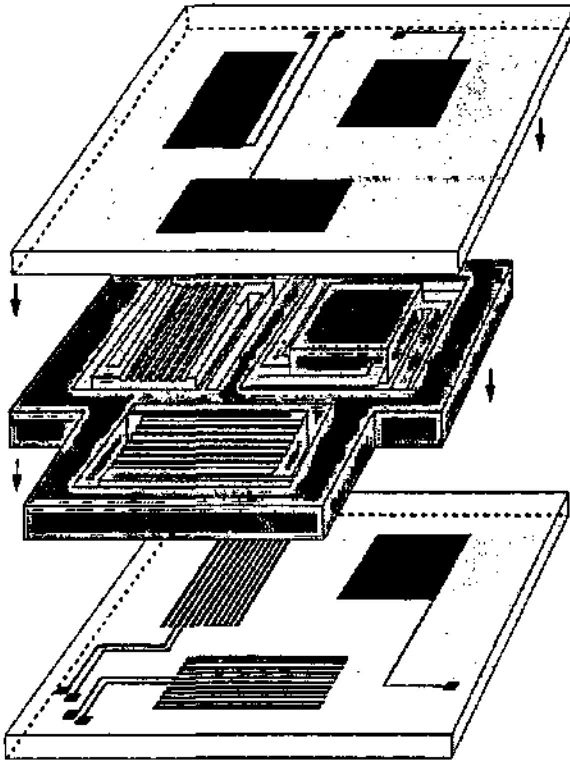

Figure 4.28: Schematic view of the 3-layer-sandwich consisting of one structured silicon chip, an upper and a lower glass chip. (3D accelerometer #C2).

From figure 4.28 and preceding chapters, we can set the following requirements for glass processing: Metal electrodes have to be structured on the glass substrates. In case of accelerometer #C1 recesses are needed in the glass for proper device operation (movement of the seismic mass and damping). Encapsulation of the device by anodic bonding will be discussed in the next section. As the glass processing for accelerometer #C2 is quite simple, we mainly focus on the fabrication module concerning sensor #C1. The two complete process sequences for glass wafers are illustrated in figure 4.29.

Etching of glass

Cavities have to be etched for the suspended seismic masses (to ensure their mobility and damping) and also for conductors (to avoid short circuits and to permit later narrow contact between silicon and glass for anodic bonding). The used etchant is Buffered HydroFluoric acid (BHF). The etch-rate of Pyrex 7740 glass depends on the temperature and concentration of the etchant. In our case etching was performed at ambient temperature leading to an experimental etch-rate of 0.029 ($\pm$0.003)µm/min. This is similar to elsewhere reported etch-rates for Pyrex 7740 [Sta94]. In order to protect the covered areas of the glass from the etchant, two different masking layers have been tested: standard photoresist (Hoechst AZ 5214) and chromium layer. Good protection of the glass areas during etching is very important, because damaged glass surfaces are not suitable for anodic bonding.

As photoresist is easy to handle and resistant to BHF, we tried firstly to use it as masking layer for glass etching. However, the main problem when using photoresist as masking layer, is the

adhesion of this layer to the Pyrex wafers. Even when using the adhesion promoter HDMS (HexaMethylDiSilizane), the photoresist layer peels off after about 20 minutes. 20 minutes etching results in an etch depth of 0.5µm - 0.6µm, which is not sufficient for our application. More promising results have been reported by Strato ea. [Sta94] using the photoresist HPR 504. Using a 100nm thick sputtered chromium layer as etch mask, satisfying protection has been achieved. The adhesion of the metal layer was sufficient to protect the glass wafer during several hours. Cavities up to 10µm are possible. Deeper etching with good protection is possible by heating the substrate during metal deposition. The profile of an etched recess is shown in figure 4.30. The profile was measured using an alpha-step surface profilometer.

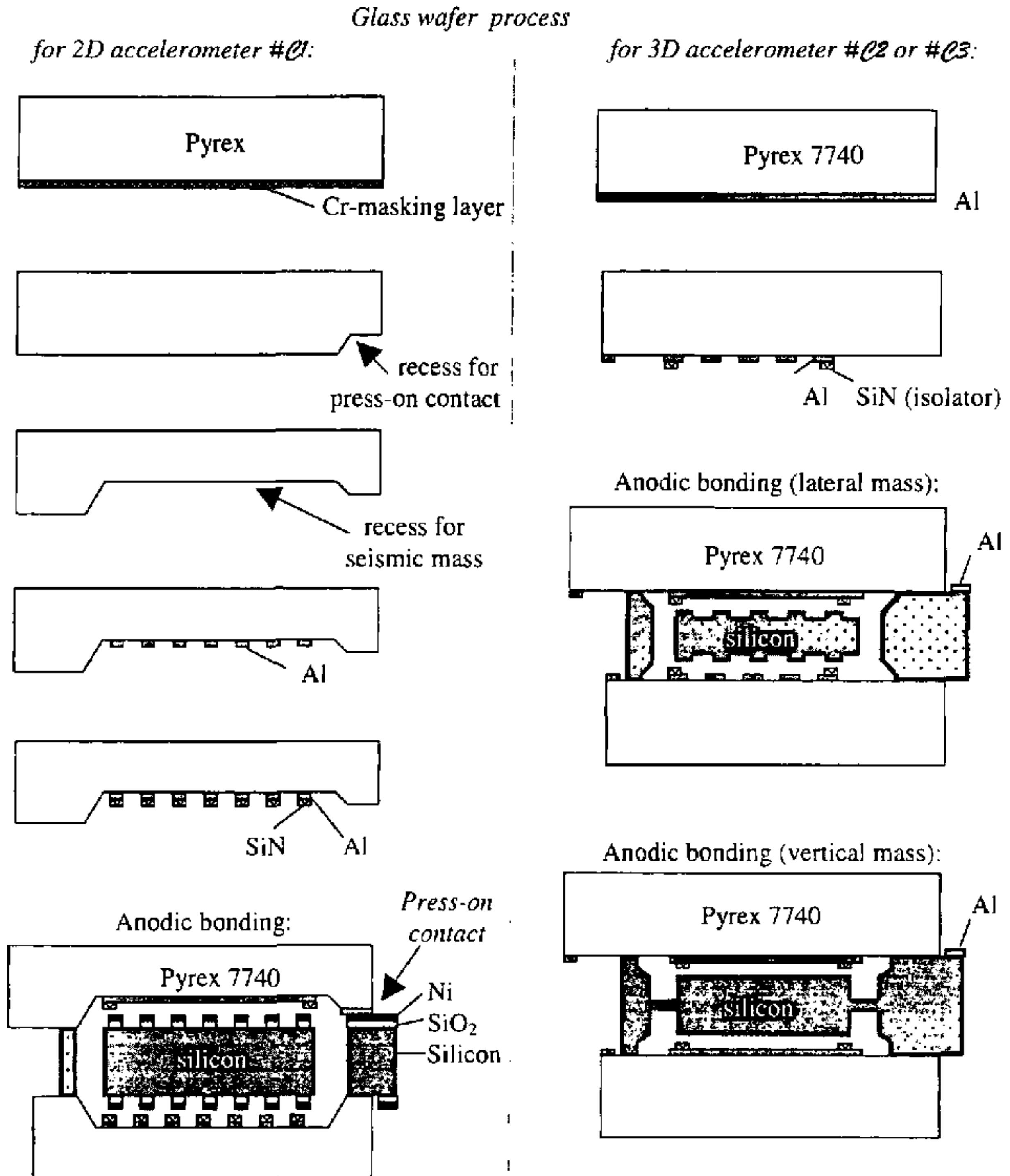

Figure 4.29: Process sequences for glass wafers of both sensor types: 2D accelerometer #C1 (left) and 3D accelerometer #C2 or #C3 (right).

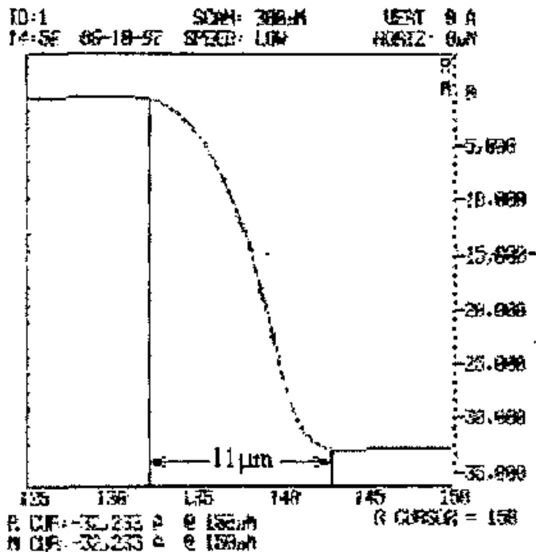

Figure 4.30: Measured profile of a recess etched into Pyrex glass. An undercut of 11µm and a depth of 3.3µm lead to an aspect ratio of approximately 3.3.

Press-on contacts

The contacting of the glass top electrode can be realized by aligning two metal pads, one on the silicon wafer, and the other one on the top glass wafer. During anodic bonding, these layers will be pressed together, forming a so called press-on contact (see figure 4.29 left side, bottom). During the bonding the wafers will be deformed elastically around the press-on contacts and unbonded regions appears. Experimental results show that the diameter of an unbonded region around an outstanding contact can be in the range of several millimeters and thus, glass bonding can even be prevented. This experience has been confirmed by T. Geßner [Geß94].

To overcome this problem, a shallow recess is etched into the glass in the region of the press-on contact. Thus for fabrication sequence of device #C1 the glass has to be etched twice (see figure 4.29 left side, top). One time for the suspended mass (cavities of 2µm-5µm) and recesses for the press-on contact (~0.2µm-0.4µm) depending on the thickness of the used metal layers). The depth of the recess of the press-on contact has to be very accurately controlled, in order to firstly avoid unbonded regions, and secondly to ensure a low ohmic resistance of the press-on contact. In addition, the step coverage of the metal leads across the edge of the recess is important. This step coverage depends on the thickness of the on glass sputtered metal (here aluminum) and on the recess profile. The thicker the aluminum layer, the better the step coverage. The recess profile should not be steep. The aspect ratio between undercutting and recess depth should be larger than 1 to ensure metallic step coverage. In case of the BHF etchant and chromium masks, a corresponding experimental aspect ratio of more than 3 was found (see figure 4.30).

The glass processing module for device #C1 has some critical steps. Especially, the silicon oxide layer in combination with the press-on contact causes isolation problems. Thus, a simpler process for glass treatment was developed for accelerometer #C2 (see figure 4.29, right side).

4.4.4 Anodic bonding

The developed glass processes end up with anodic bonding of the silicon-glass sandwich. Anodic bonding is a well known technique in microtechnology to join hermetically metals or semiconductors with glass [Wa69]. As earlier mentioned, Pyrex 7740 is especially interesting for silicon, because their temperature expansion coefficients are almost identical between 0°C and 400° C. The two substrates to be bonded are assembled on a hot plate and heated, typically between 300°C and 400°C. At this temperature, many glasses contain movable positive ions (e.g. sodium), which are compensated by almost immobile positive oxygen ions. If a high DC voltage is applied in such a way that the glass is at the negative potential with respect to the metal, positive sodium ions drift towards the cathode where they are neutralized. The immobile oxygen ions in the Pyrex glass form a negative space charge layer adjacent to the silicon surface. The resultant electrostatic forces pull the substrates into intimate contact, thus allowing chemical bonds to form [Alb88].

The surfaces of the two wafers to be bonded must be smooth and clean. Contaminations and dust particles have to be removed. In order to reduce the disturbance by dust particles the bonding surface can be minimized. This has been realized through forming of recesses in the first etching step (in glass for accelerometer #*C1* and in silicon for device #*C2*). A reduced bonding surface also leads to a faster bonding process.

The bonded silicon-glass sandwiches have been already shown schematically in figure 4.28 and 4.29 (bottom). In the fabrication process for the lateral accelerometers, a precise alignment between movable and fixed comb-shaped electrodes is necessary. A special bonding equipment was developed in our laboratory. It consists of three different modules, represented in figure 4.31. Firstly, a cassette module to hold glass and silicon wafer together. Secondly, an alignment module in order to align the two wafers accurately. And thirdly, a substrate bonding module consisting basically of electrodes, hot plate and voltage supply.

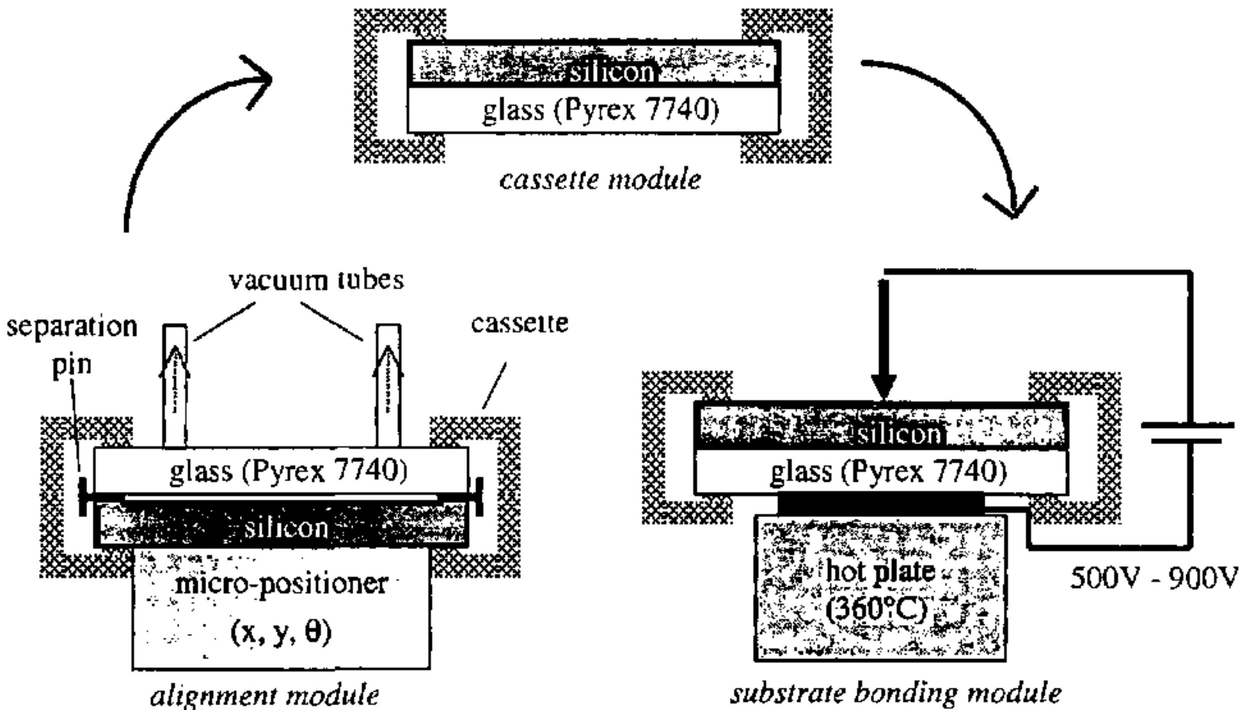

Figure 4.31: Schematic of the developed bonding equipment: alignment module, cassette module and substrate bonding module.

As can be seen in figure 4.31, initially three thin metal pins separate the silicon and glass wafer, both contained and fixed in a cassette. These pins ensure a separation between both substrates in order to permit mobility. While the silicon wafer is fixed into the cassette, the glass wafer is hold in the alignment module with help of vacuum. A micro-positioner allows to align accurately both wafers. To achieve precise orientation, alignment marks have been provided: metallic squares on the Pyrex wafer and KOH etched cross-like structures on the silicon (see figure 4.32). The creation of these alignment marks has been integrated in the fabrication sequence, so that no additional process steps are necessary. For the used set-up, the achieved alignment accuracy is a few microns (~5μm).

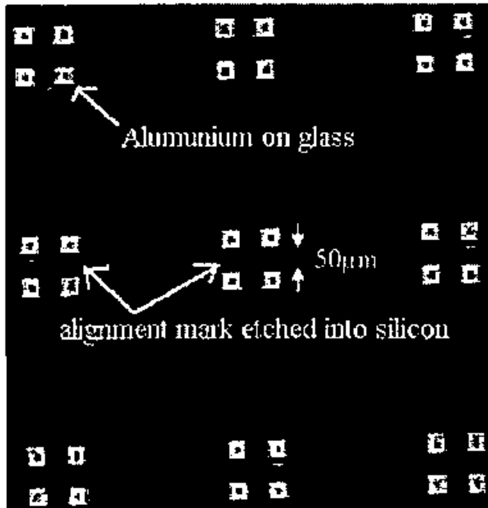

Figure 4.32: Close-up view of silicon-glass sandwich after anodic bonding: alignment marks on silicon (etched cross) and on glass (metalic squares).

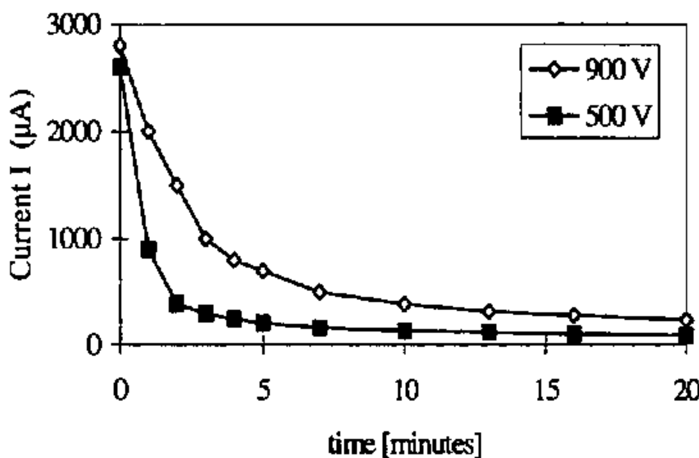

Figure 4.33: Typical variation in current during the anodic bonding process. The bond curves have been measured for two different wafers at DC voltages of 500V and 900V, respectively.

Once the alignment of the two wafers is finished the separations pins are withdrawn and both substrates are fixed together in the cassette module. This module can now be transported to the anodic bonding site (substrate bonding module). In the performed bonding processes only a point contact as cathode was used, which is quite sufficient for 3inch wafers. In case of larger wafers more electrodes should be used, preferably in a star-like configuration as proposed by J. Plaza [Plaza]. In the used set-up, the bonding temperature can be precisely regulated. A temperature of 360°C was chosen. Applied DC voltage was varied for different wafers between 500°C and 900°C. No significant difference in bonding quality could be observed. However, quantitative tests have not been performed. The typical variation in current between the two substrates during

the anodic bonding process can be seen in figure 4.33. After twenty minutes the hot plate was turned off to cool down the wafers.

One problem encountered with silicon-glass bonding in the case of micromachined movable structures is the sticking of the silicon elements due to electrostatic attraction (in our case seismic masses and vertical suspension beams). The sticking problem was successfully avoided by forming a metal layer (at the same time as the electrodes) on the glass areas that should not be bonded.

4.4.5 Mounting and connecting

In case of the fabrication process for accelerometer *#C2* or *#C3* press-on contacts have been avoided. Thus, before separating the individual chips by sawing, contact pads have to be formed. In order to form the connecting pads on the silicon, aluminum is sputtered through a physical mask. A silicon wafer in which holes are etched through serves as physical mask. Since precisely defined position of the contact pads is not needed, the alignment of silicon-glass sandwich and sputter-mask is not critical. After sputtering, subsequent annealing at 400°C lead to ohmic contacts. Since p-type silicon was used, the doping concentration is less important. In case of n-type silicon doping should be not lower than 10^{20} atoms cm^{-3} [Sze69]. As shown in figure 4.34 proper annealing is very important to achieve ohmic contacts.

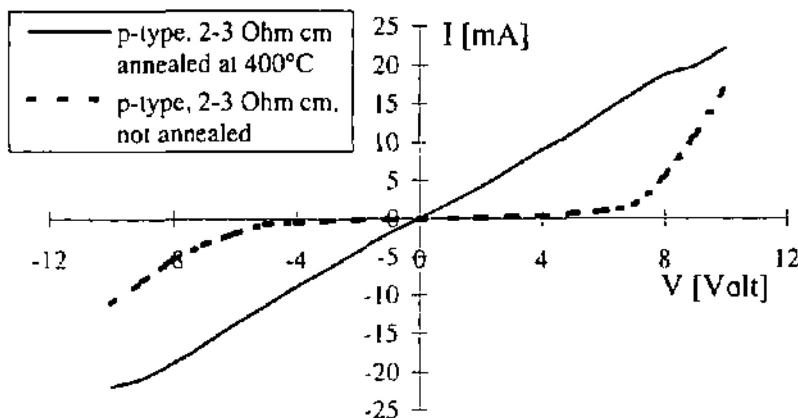

Figure 4.34: Experimental current-voltage diagram for two different Al-Si contacts showing the characteristics of the contact. In both cases, p-type silicon was used. However, an ohmic contact is achieved only in case of annealing.

As the Pyrex wafer protects well the structured and fragile silicon wafer, sawing is not critical. If only one glass wafer is bonded, which was the case for the first prototypes, wax or photoresist can be used to protect the silicon structures and additionally to fix the wafer sandwich on a sawing support. Alternatively, the substrate can be attached to an adhesive plastic. This depends on the employed saw. In any case, after separation, the glass-silicon dies have to be carefully cleaned (standard RCA cleaning or at least trichlorethylene-acetone-alcohol cleaning sequence).

Finally the single chips were fixed with epoxy glue into standard metal packages or simply on Printed Circuit Board (PCB) boards. As the dies are very large in comparison to other electronic or micromachined sensors, other standard packages could not be used, such as 24-pin package or lead frames. In case of the first devices, the bonding pads have been connected to the contacts on

the package by using silver glue. Alternatively, standard wire bonding is possible. Also, the epoxy glue should be substituted by a nonconductive silicone adhesive in order to avoid package induced stress [Nys97].

Figure 4.35: Packaged 2D accelerometer.

4.5 Capacitive measurement circuits

Several kinds of circuits for the measurement of small capacitive changes have been developed and commercialized, not only for the readout of capacitive accelerometers, but also for capacitive pressure sensors, displacement and absolute position transducers. Most of the capacitive measurement circuits belong to one of the following categories [Zhu]:

- capacitive AC bridge
- charge/discharge
- impedance comparison
- resonance
- oscillation

Generally, the zero capacitances C_0 of mircomachined accelerometers (sensor capacitance at no applied acceleration) ranges from 0.1pF to 100pF, mainly depending on the sensor fabrication technology (surface- or bulk-micromachined). The above presented accelerometers show typically zero capcitances between 15pF and 25pF with sensitivities ranging from 0.3pF/g to 5pF/g, basically depending on the chosen electrode distance. In order to measure accelerations in the µg-domain, capacitive changes have to be detected up to 1aF, showing the need for very sensitive electronic measurement circuits.

For sensor applications, the capacitive ac bridge circuit and the charge/discharge circuits are mainly used. Therefore the discussion will be limited to these techniques. In addition, a recent measurement technique based on sigma-delta conversion is presented.

4.5.1 Capacitive AC bridge circuits

A typical capacitance bridge circuit [Bos97] is illustrated in Figure 4.36. Here, two excitation signal sources, $+V_0$ and $-V_0$ (phase shifted by 180°), and the two sensing capacitors, C1 and C2,

are arranged in a symmetrical circuit. Any change in the sensing capacitances disturbs the balance of the bridge and gives an output signal. C_{p1} and C_{p2} represent parasitic capacitances, coming from wiring and packaging. Using $\Delta C = C1-C2$, the voltage at the buffer input is:

$$V_x = 4\ V_0\ \Delta C\ (\ 2C_0 + C_{p1}\ )^{-1} \qquad (4.29)$$

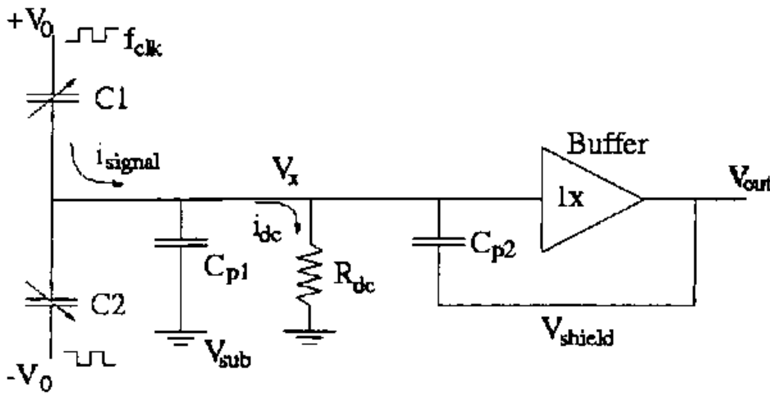

Figure 4.36: Capacitive position measurement circuit using an AC bridge [Bos97].

4.5.2 Charge/discharge circuits

Based on charge transfer, various capacitance measurement circuits have been developed. The most common of those are the CMOS switched capacitor circuits (switched controlled charge/discharge capacitance measurement circuits). Here, the sensing capacitances C1 and C2 are connected in series and are switched alternatively to the supply voltage V_0 and the output voltage V_{out} (see figure 4.37). At the series connection point of C1 and C2 the resulting charge difference ΔQ is then fed to a charge amplifier. This charge difference is :

$$\Delta Q = C_0\ V_0\ \Delta C\ (C_0 + C_{p1} + C_{p2})^{-1} \qquad (4.30)$$

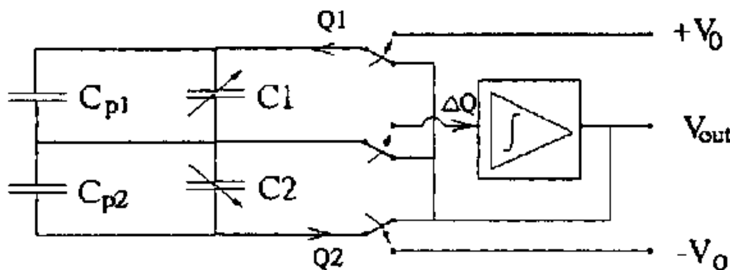

Figure 4.37: Example of a switched capacitor circuit of a differential capacitor with parasitic capacitances C_{p1} and C_{p2}, similar as in [Leu90].

Existing capacitive interface circuits

In table 4.2 five examples of highly sensitive capacitive interface circuits are given, which are all used in accelerometer microsystems. Two of them are three-dimensional devices [Löt97, Lem97]. Only in the case of full integrated single chip systems, capacitances under 1aF could be sensed.

However, resolution in acceleration measurement is essentially higher for bulk-micromachined devices due to their higher sensitivity.

category	*Zero cap.* $2 \times C_0$	*resolution [aF/√Hz]*	*measurement range*	*fabrication technology of sensor system*	*ref.*
cap. AC bridge[1]	2 × 12pF	17	± 1% C_0	discrete components	[Löt97]
cap. AC bridge[2]	2 × 5pF	5	± 20% C_0	multi chip module	[Krö95]
cap. AC bridge[2]	2 × 120fF	0.08	± 1% C_0	full integrated	[Cha96]
charge/discharge[2]	2 × 98fF	0.17	± 3% C_0	full integrated	[Lem97]
charge/discharge[1]	2 × 22pF	40	± 50% C_0	2 chip hybrid	[Leu90]

[1] open loop [2] closed loop (feedback)

accelerometer technology	*bandwidth [Hz]*	*resolution [µg/√Hz]*	*measurement range*	*fabrication technology of sensor system*	*ref.*
Tungsten cube	DC-400	100	> ± 5g	discrete components	[Löt97]
LIGA (Nickel)	DC-400	1	± 1g	multi chip module	[Krö95]
Poly Si surface	DC-4000	600	± 5g	full integrated	[Cha96]
Poly Si surface	DC-7000	730	± 11g	full integrated	[Lem97]
Crystal Si bulk	DC-1000	1	± 0.1g	2 chip hybrid	[Leu90]

Table 4.2: Five examples of highly sensitive capacitive interface circuits (upper part), which are all used in accelerometer systems (lower part).

4.5.3 Sigma-delta modulation

In this section, the development of an integrated read-out circuit specially adapted to the developed 3D accelerometer is described. The underlying principle is based on sigma-delta modulation. This Application Specific Integrated Circuit (ASIC) would build up together with the silicon accelerometer a complete microsystem. The work is performed in the frame of a joint collaboration recently established between the CMP/TIMA in Grenoble and the LPMO in Besançon. As the main work has still to be accomplished and as this is also not the main motivation of this thesis, only basic issues are described in this section.

Principle of sigma-delta modulation

The basic function of a sigma-delta (Σ-Δ) modulator is analog to digital signal conversion [Can92]. A first order sigma-delta converter is schematically shown in figure 4.38. In general, a sigma-delta modulator uses a sampling frequency that is much higher than Shanon-frequency of the analog input signal V_{in}. This is called oversampling. As a result of the oversampling process the average of the output bit stream is a measure of the analogue input signal V_{in}. Refering to figure 4.38, the output of the Analog to Digital Converter (ADC) is a one bit signal and passes to a Digital to Analog Converter (DAC) from where it is fed back to the analog input.

High order modulators can be employed to obtain an improved signal to noise ratio. However, due to their high order, such systems may only be conditionally stable [Kra97]. General advantages of sigma-delta modulators are a high linearity (based upon the principle), no sample and hold circuitry is necessary and, of course, they are very suitable for digital systems (DSP-applications) [Kau97].

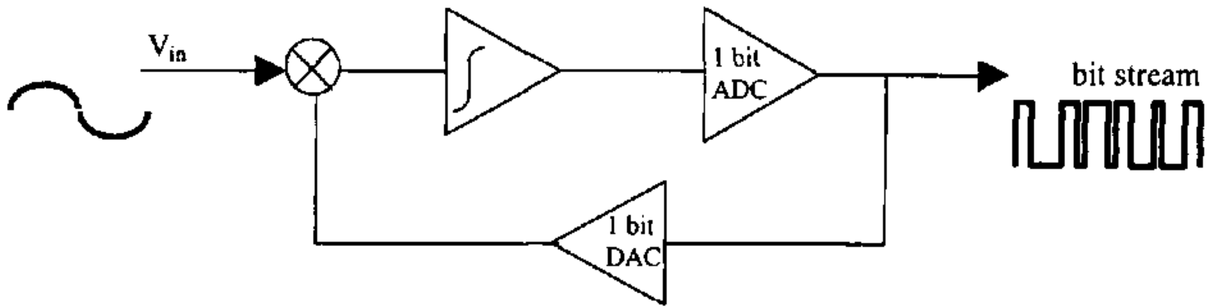

Figure 4.38 : Schematic of a first order sigma-delta (Σ-Δ) modulator [Kra97].

Application to the 3D accelerometer system: micromechanical sigma-delta modulator
A micromechanical capacitive accelerometer can be employed in such a sigma-delta modulator, basically by substituting the analog part of the schematic in figure 4.38 by a capacitive read-out circuit. The accelerometer would be sensed by a switched capacitor circuit (like shown in figure 4.37). The output voltage of this capacitive detection circuit is used as the analog input signal of a sigma-delta converter. Now the digital signal can be used to measure acceleration in an open loop system. Alternatively, the bit stream could be fed back (via a control module and a digital to analog converter) in order to apply electrostatic forces to the accelerometer. Such a digital servo accelerometer can be seen as a mechanical sigma delta modulator, and has been already realized on a PCB for an uni-axial device sensitive to vertical acceleration [Kra97]. Such a mechanical sigma-delta modulation can be applied to the three axis accelerometers developed in this thesis as schematically shown in figure 4.39. The microsystem combines the advantages of sigma delta conversion with the benefits of electrostatic force feedback. However, sigma delta modulation can also be applied for open loop detection.

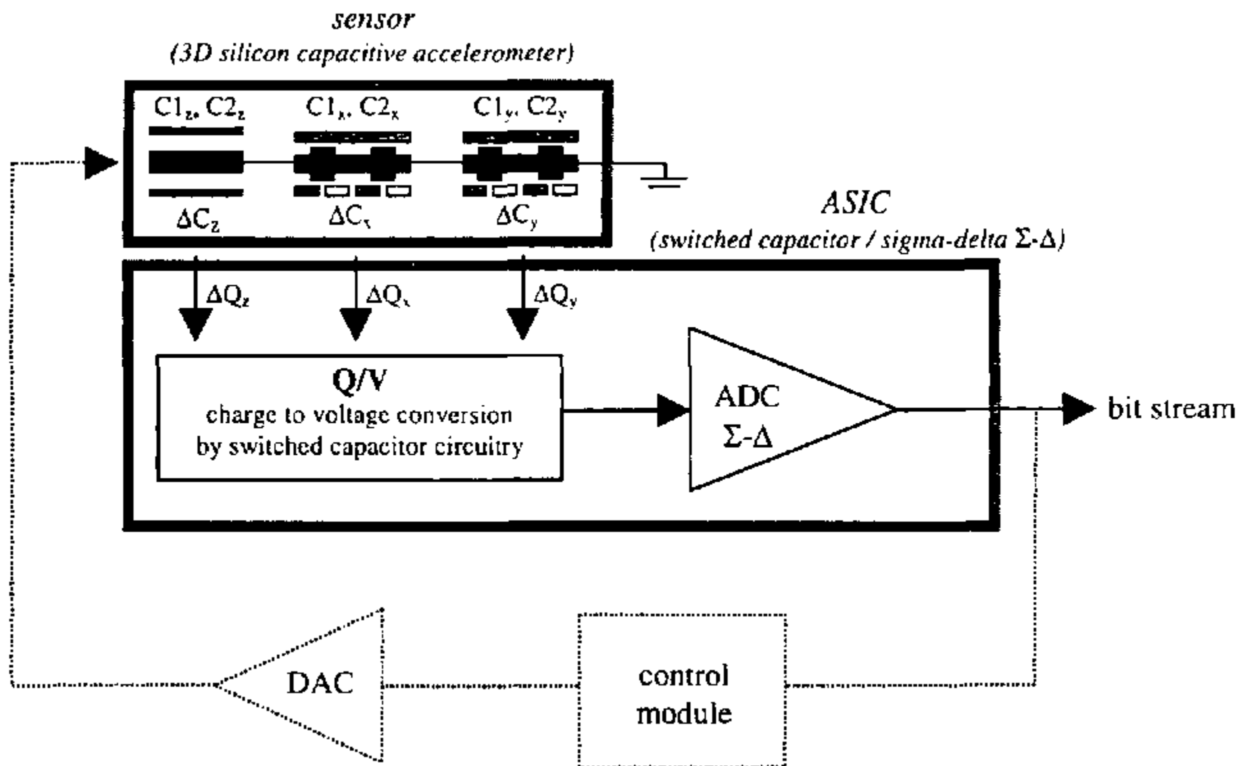

Figure 4.39: Principle of a 3D accelerometer system employing differential sensing, switched capacitor detection circuitry, and first order sigma-delta modulation with possible force feedback (dotted line).

The developed HDL-A model for global simulation presented in section 4.3 is very suitable to simulate the complete microsystem of figure 4.39 consisting of a micromechanical silicon chip and an application specific integrated circiut.

Preliminary sensor specifications for the ASIC have been established and are illustrated in table 4.3. Zero capacitances of 20pF are assumed for all three accelerometers. In order to measure accelerations 10μg/√Hz, a resolution of the read-out electronic up to 10aF/√Hz is necessary.

	$C1_x$, $C2_x$	$C1_y$, $C2_y$	$C1_z$, $C2_z$
Zero capacitance C_0	20pF (±5pF)	20pF (±5pF)	20pF (±5pF)
Capacitive sensitivity	1pF/g	1pF/g	4pF/g
Measurement range	±2g	±2g	±2g
Resolution	10μg/√Hz	10μg/√Hz	10μg/√Hz

Table 4.3: Preliminary specifications for the ASIC concerning accelerometer performance ($C1_x$, $C2_x$, $C1_y$, $C2_y$, $C1_z$ and $C2_z$ as shown in figure 4.39).

4.5.4 Noise of capacitive detection

As far as the thermo-mechanical noise limit due to the Brownian molecular movements is not reached, the resolution of the capacitive accelerometer depends mainly on the performance of the capacitance measurement circuit. Despite the large variety of detection circuits, the electronic thermal noise represents in each case the ultimate lower limit, however, in practice other noise sources are often more relevant, e.g. variation of supply voltage. The fundamental lower limit regarding the resolution of the AC bridge circuit in figure 4.36 is set by the thermal noise of the amplifier. From [Bos97], one can derive the following formula for the minimum detectable capacitance :

$$\Delta C\, \Delta f^{-1/2} = 2.6\, V_0^{-1}\, [\, k_B T\, f_T^{-1}\, (C_0 + C_{p1} + C_{p2})\,]^{1/2} \qquad (4.31)$$

Where f_T is the sampling frequency which is limited by the cutoff frequency of the underlying circuit technology. Taking the values of the realized bulk-micromachined accelerometers with typically C_0 = 20pF and parasitic capacitances of not more than $C_{p1} + C_{p2}$ = 20pF, as well as V_0=1V, Δf=100 Hz, f_T=100 MHz and T=300 K, the resolution of the circuit shown in figure 4.36 is approximately 1aF/√Hz. This is typically one order of magnitude higher than for surface-micromachined devices, which have integrated read-out electronics and C_0 around 100fF (see table 4.2).

For a switched capacitor circuit (figure 4.37), the fundamental noise limit is given by the equivalent noise charges (ENC) [Spe88]:

$$ENC = (2\, k_B\, T)\, (C_0 + C_{p1} + C_{p2})^{1/2} \qquad (4.32)$$

Setting ENC equal to the charge variation ΔQ (see equation 4.30), and considering the noise reduction due to averaging with a sample frequency, one can calculate the ultimate resolution of such a switched capacitor circuit. The theoretical resolution limits for these circuits are comparable to the case of AC bridge circuits. Typically, one finds also 1aF/√Hz for a two chip solution (with bulk-micromachined capacitive transducers), and around 0.1aF/√Hz for fully

integrated surface-micromachined devices. In case of the proposed micromechanical sigma-delta converter, the first electronic module is a switched capacitor circuit. Thus a charge amplifier sets also the fundamental thermal limit for this technique regarding resolution. Basically, the same relation as 4.32 can be established. Of course, the achieved resolution depends in this case additionally on the order of the sigma-delta converter and on the oversampling frequency.
As it can clearly be seen, parasitic capacitances reduce resolution and sensitivity. For microaccelerometers, these parasitic capacitances are therefore very critical and should be minimized, especially in case of two-chip systems. One mean to reduce such parasitic capacitances, as well as disturbances from electromagnetic fields, is the implementation of shielding electrodes.

4.6 Characterization and limitations of the capacitive accelerometers

After device simulation, presentation of the microfabrication of capacitive accelerometers and discussion of different possible measurement circuits, first measurements on the realized sensors are described in the following sections.

4.6.1 Employed evaluation methods

Generally, evaluation of accelerometer performance can be divided in static and dynamic test methods. These methods will be applied to the vertical as well as to the lateral capacitive accelerometers.

Evaluation of static accelerations
The static response of an accelerometer can be measured by applying constant acceleration to the sensor. Accelerations up to ±1g ($9.81ms^{-2}$) can be applied by tilting the device in the gravity field. Static tests at higher accelerations than 1g can be made by rotating the sensor using a high speed rotating disk. As in our case the desired measurement range is in the low g-range, typically 1g-2g, the simple method of tilting the accelerometer is employed. Depending on the mounting, the sensor can be rotated around all three axes. In this way main and also cross-sensitivities as well as linearity can be determined.
To measure the static capacitive changes two devices have been used. Firstly, a LCR-meter (Phillips PM6303) with a accuracy of 0.1pF. Since this device is quite limited for small capacitive changes, secondly a capacitance meter (Fogale MC900) was employed. The maximum measurement range for this capacitance meter is 10pF with a resolution of 0.01% at 400Hz (50aF/√Hz for a 10pF range) [Fog98]. As the realized accelerometers have typically zero capacitances between 15pF-25pF one have to add a fix capacitor in series in order to reduce the maximum capacitance to smaller than 10pF. However, in this way the capacitive sensitivity of the accelerometers is also reduced.

Evaluation of dynamic response
The frequency responses of the acceleration sensors can be measured by vibrating the device with many sinusoidal waves of different frequencies. The measurement set-up for dynamic measurements that was used is illustrated in figure 4.40. The accelerometer to be tested is attached to the moving coil of a loudspeaker. Since the resonance modes of the loudspeaker's

membrane appear in the measured spectrum, the speaker's resonance should be measured. The first resonance frequency was found to be at 130Hz. The weight of the attached sensor reduces this value to about 100Hz depending on the package size (PCB). This measurement set-up can be improved by replacing the loudspeaker by a vibrating table or pot and by controlling the applied acceleration with the help of a reference accelerometer.

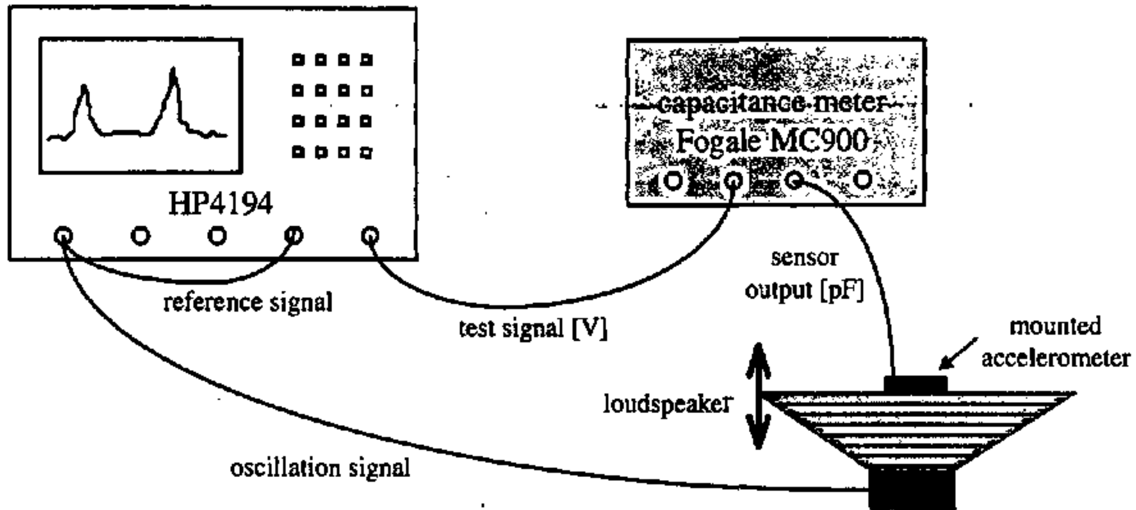

Figure 4.40: Employed measurement set-up to determine the frequency response of accelerometers.

From the measured gain/frequency curve, one can derive directly the accelerometer's quality factor [Bur95]. The Q factor is obtained by dividing the resonance frequency by the width of the peak at an attenuation of 3dB ($1/\sqrt{2}$).
Another possibility to test the accelerometer's dynamic behavior consists in measuring the sensor response due to an applied shock [Um90]. By Fourier transformations one can obtain the frequency signal from the measured impulse response in the time domain.
The 3D accelerometers which have been tested consist of three individual seismic masses, two sensitive to in-plane accelerations, and one sensitive to out-of-plane accelerations. A number of sensors have been tested. In case of response curves, typical measurements are represented and, in case of table 4.4, average values are listed. The gap between electrodes is 2.9µm (±0.2µm) for both, in- and out-of-plane sensors.

4.6.2 Measurements of the in-plane accelerometers

Two different mechanical sensor configurations have been fabricated to measure in-plane accelerations. One using design 2 (a seismic mass suspended by four vertical beams) and a second sensor type based on design 3 (mass suspended S-like by two beams). Design 2 and 3 have been presented and analyzed in chapter 2. As expected from the mechanical model, the two sensors differ in their mechanical sensitivity. However by using the fabrication type #C2 (electrodes etched into silicon), the electrode configuration is the same for both in-plane accelerometer types.

Static behavior

The sensor output of the most sensitive lateral accelerometer with two suspension beams (design 3) is illustrated in figure 4.41. Acceleration from 0g to 1g is successively applied by rotating the device around 90°. As expected, the change in capacitance is linear. The measured sensitivity is around 1.2pF/g. This agrees almost with a value of 1pF/g obtained from simulations (calculated mechanical sensitivity is 1μm/g and capacitive sensitivity is 1pF/μm, respectively)

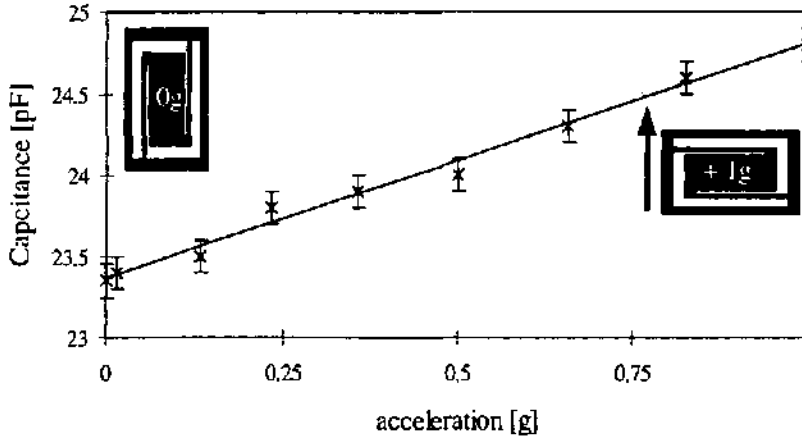

Figure 4.41: Static response of a lateral accelerometer (mechanical *design 3*, electrode type #C2) measured with Phillips PM6303 LCR-meter.

The sensitivity of sensors with design 2 is lower than 1pF/g. Thus, due to the precision of the LCR-meter, these accelerometers have been measured with the Fogale MC900 capacitance meter, as shown in figure 4.42. In this case, sensitivities vary between 0.3pF/g and 0.6pF/g. The diffrence in sensitivity. The error in linearity is around 1%. Since this nonlinearity could also come from the capacitance meter, further investigations have to be done.

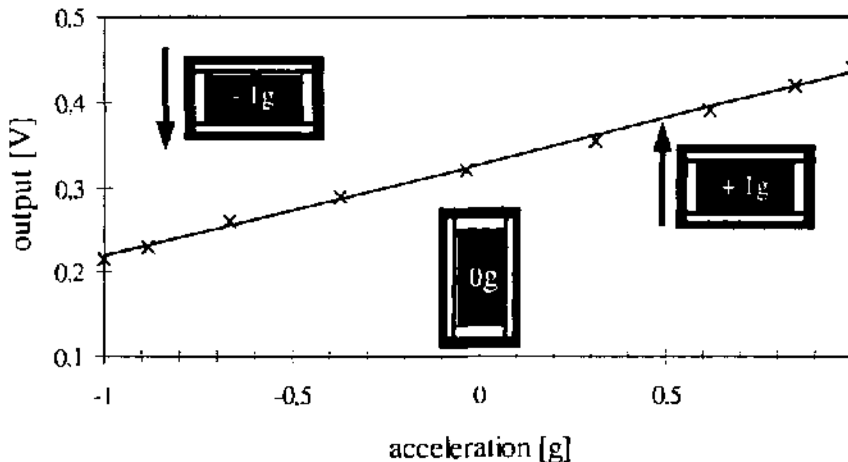

Figure 4.42: Static response of a lateral accelerometer (mechanical *design 2*, electrode type #C2) measured with capacitance meter Fogale MC900.

Since only simple, and no differential electrode configurations have been tested and also no counter electrode on the opposite side of the seismic mass has used for electrostatic force compensation, the cross-sensitivity regarding accelerations perpendicular to the wafer plane are quite large due to variations in the gap size d. As shown earlier (section 4.2.5) by subtracting two inverse changing capacitances, this effect can be canceled out.

Dynamic behavior

The measured gain/frequency plots of the two different lateral accelerometer types are shown in figure 4.43 and 4.44, respectively. One can clearly see in both spectra two resonance peaks, one for the resonance of the loudspeaker membrane, the other one representing the first resonance mode of the accelerometer. The slight difference in the loudspeakers resonance frequency (100Hz ±20Hz) is due to the different size of the employed accelerometer's PCB.

The second resonance peak observed in the dynamic response is situated around 680Hz and 460Hz, respectively. Using the relation between mechanical sensitivity and resonance frequency, the mechanical sensitivity can be derived and is given in table 4.4. Sensors with mechanical design 3 are twice as sensitive as accelerometers of design 2. Comparing these values to the static measurements, one can conclude that the obtained experimental results are coherent. In addition, the developed capacitive model as well as the mechanical model agree very well with the experimental measurements.

The difference in the amplitudes of the resonance peaks originates not only from different sensitivities, but also from different high AC voltages (0.1V-1V) to excite the loudspeaker. Experimentally derived quality factors are around 10, indicating an underdamping.

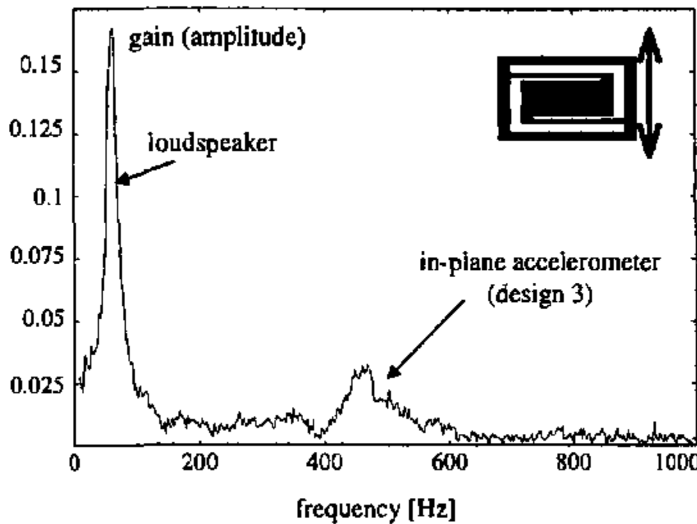

Figure 4.43: Dynamic response of a lateral accelerometer (*design 3*, electrode type #C2) measured with set-up of figure 4.40.

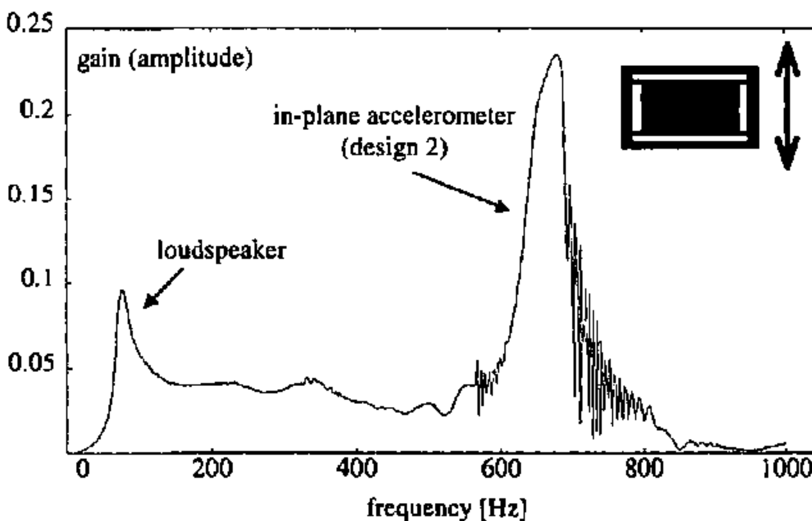

Figure 4.44 Dynamic response of a lateral accelerometer (*design 2*, electrode type #C2) measured with set-up of figure 4.40.

A summary of the measured static and dynamic performance for the in- and out-of-plane accelerometers is given in table 4.4. One can see that the obtained experimental characteristics are close to the theoretical values calculated for the specifications. The resolution in acceleration measurement is determined by the capacitive resolution specified in the data sheet of the employed capacitance meter Fogale MC900 [Fog98].

Measured performance	**In-plane accelerometers** (design 2 / design 3) C_x, C_y	**Out-of-plane accelerometer** (design 7) C_z	**Specifications** (see table 4.3) C_x, C_y	C_z
Zero capacitance C_0	19.1pF (±5pF)	18.0pF (±5pF)	20pF (±5pF)	20pF (±5pF)
Capacitive sensitivity	0.5pF/g / 1.1pF/g	4pF/g (±1.2pF)	1pF/g	4pF/g
Measurement range	> ±1g	~ ±0.8g	±2g	±2g
Resolution (with MC900)	400µg/√Hz / 160µg/√Hz	40µg/√Hz	10µg/√Hz	10µg/√Hz
Resonance frequency	681Hz / 460Hz	436Hz	500Hz	500Hz
Mechanical sensitivity	0.54µm/g / 1.17µm/g	1.3µm/g	-	-
Q-factor	12 / 9	8	-	-

Table 4. 4: Summary of measured performance (average) for in-plane and out-of-plane capacitive accelerometers, compared to some preliminary specifications established for the ASIC development.

4.6.3 Measurements of the out-of-plane accelerometers

In case of the out-of-plane sensors, one mechanical structure type (design 7) was employed in all tested 3D accelerometer systems. In the following measurements only the capacitance between seismic mass and bottom electrode is considered, because the top glass containing the counter electrodes was not yet bonded. Thus no experimental differential capacitive responses are presented

Static behavior

In general, the capacitive variations of the out-of-plane accelerometers for applied accelerations in the range of ±1g are significantly higher than for the in-plane sensors. As shown in figure 4.45, the change in capacitance is typically in the order of several pF/g for small accelerations up to 1g. However, due to the physical principle of the variations in electrode distance d, the capacitive response in not linear, but inversely proportional to acceleration. As shown in figure 4.46, the sensor output can be linearized by differential detection using a second electrode on the opposite side of the seismic mass (the graph in figure 4.46 was calculated based on the measurements shown in figure 4.45).

The mechanical displacement of the seismic mass is limited to about 1µm (~1/3 d) in direction to the bottom electrode. For larger displacements no change in capacitance could be observed, which can be explained by an electrostatic pull-in effect of the two electrodes. Thus the measurement range is limited for the realized out-of-plane devices to about ±0.8g (equivalent to ±1µm displacement). To increase the measurement range to ±0.8g the electrode distance can be

increased or the mechanical sensitivity decreased. Alternatively, the measurement range can be significantly improved by using a counter electrode and electrostatic force feedback.

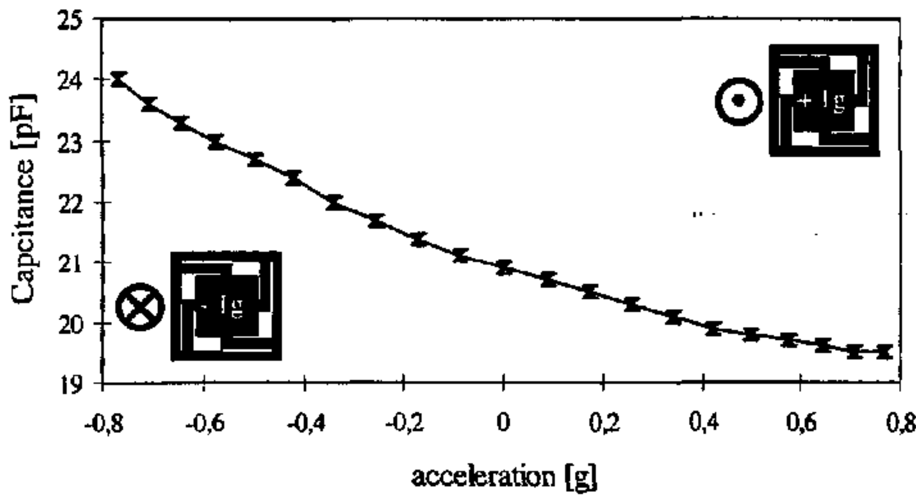

Figure 4.45:
Static response of an out-of-plane accelerometer (mechanical *design 7*) measured with Phillips LCR-meter.

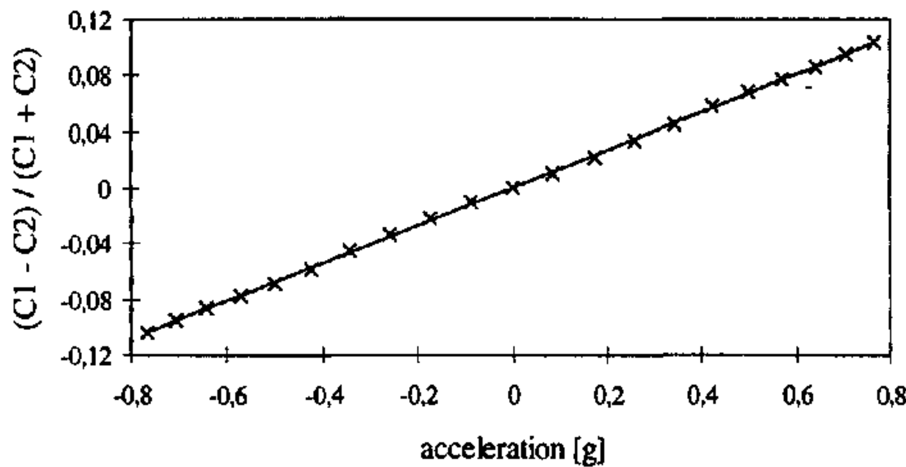

Figure 4.46:
Differential response of the out-of-plane accelerometer (mechanical *design 7*), calculated from the measurements presented in figure 4.45.

To illustrate furthermore the static response of the capacitive out-of-plane accelerometers, the sensor was rotated with small angles, which are equivalent to static accelerations in the range of 1mg to 5mg (shown in figure 4.47).

Figure 4.47:
Accelerometer response to various static accelerations steps.

Dynamic behavior

From the resonance peak at 436Hz observed in figure 4.48, one can derive a mechanical sensitivity of 1.3µm/g and a quality factor around 8. Joining the top glass containing the second electrode would significantly reduce the damping.

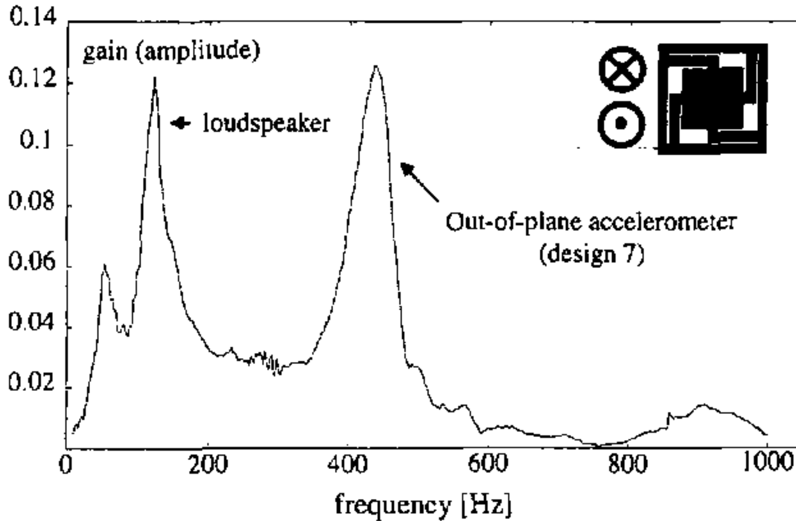

Figure 4.48: Dynamic response of an out-of-plane accelerometer (mechanical *design 7*) measured with set-up of figure 4.40.

4.6.4 Possible optimizations of the capactive accelerometers

Refering to the performed measurements and to theoretical results presented in section 4.3, one can conclude that the developed models are coherent with the experimental results. In case of the in-plane accelerometers a linear measurement range is obtained. The range depends on the width b of the single comb electrodes and also on the distance d between seismic mass and counter electrodes on glass. For the realized accelerometers having an electrode width of b = 17µm (±1µm) and a cavity of 2.9µm (±0.2µm), a linear measurement range of about ±10g can be estimated if perfect alignment between upper and lower electrodes is achieved. In reality, such a perfect alignment is not achievable and the measurement range is reduced to about ±5 g by the alignment error of the bonding system (in our case ±5 µm). By improving the employed fabrication technology, it should be feasible to reduce the gap d between the electrodes to 1µm, and the electrode design parameters to b = 8µm and c = 1µm, which would increase the sensitivity to 8pF/g. Employing a high-performance wafer bonding equipment [KS98] with an accuracy better than ±1µm, would improve the electrode alignment, thus increasing the measurement range.

By using an external measurement unit (capacitance meter Fogale MC900) resolution in the range of 100µg have already been achieved. However, resolution can be improved by employing an integrated read-out circuit placed close to the silicon sensor in order to reduce disturbance in signal transmission. In addition, by using the sensed acceleration in three directions, the specific measurement circuit could be adapted to compensate still appearing cross-sensitivities which have not been canceled out by differential detection methods.

4.7 Conclusion of chapter 4

Chapter 4 presents the design, modelisation and simulation, fabrication and finally the experimental characterization of silicon capacitive sensors suitable for multi-axis acceleration measurements.

Principles

Basically, two different sensor types are contained in one monolithic system. Firstly, two device which detect in-plane accelerations due to the change in the overlapping electrode surfaces. Secondly, a seismic mass, which is sensitive to out-of-plane accelerations, by measuring the distance between mass and counter electrodes. For both sensing principles, differential read-out can be applied in order to reduce cross-axis sensitivities and other disturbing effects, e.g. influence of temperature.

Modeling

In the case of the out-of-plane or vertical accelerometer, a simplified field assumption leads to a satisfying accelerometer model. For the in-plane designs two different types of electrode configurations are proposed. Comb shaped electrodes structured in sputtered metallic thin film or comb shaped electrodes etched vertically into the silicon seismic mass. In any case, electrostatic fringe fields are to be considered and thus adapted analytical models have been developed. Simulations using finite element analysis have also been performed in order to estimate the capacitive change due to a mechanical displacement of the seismic mass. Finally, the capacitive sensitivity and thus the response of the lateral accelerometers can be well described. Analytical and FEM calculations are compared. In conclusion, the analytical formula describes well the capacitive change due to mechanical displacements. This gives access to exact modeling of the transducer and offers the possibility to investigate easily a large range of parameters to find, considering technological aspects, the best geometries regarding capacitive sensitivity and linearity.
Using the developed models, the electrostatic forces due to an applied voltage have been calculated to demonstrate the feasibility of an electrostatic servo accelerometer employing force feedback. In addition to analytical and finite element modelisation, a global model written in a hardware description language has been developed. This global simulation combines not only mechanical and electrostatic models, but also allows the simulation of the complete microsystem including read-out electronics.

Fabrication

For the realization of the electrodes of the in-plane accelerometers two different silicon process have been developed and are described in detail. One process for the fabrication of a capacitive accelerometer employs thin-film electrodes structured into a sputtered nickel or chrome film. A silicon oxide layer, needed to isolate metal electrodes and silicon seismic mass can produce undesired charges and makes also the used press-on contacts difficult to realize. Therefore, a second process has been developed for the realization of electrodes etched into the silicon seismic mass. The counter electrodes are deposited on Pyrex glass wafers. For the structuring of these glass wafers, processes have been developed. Joining silicon and glass wafers is performed by anodic bonding. In order to align silicon and glass wafers with a high accuracy, a bonding

equipment consisting of alignment module, cassette and substrate bonding module has been employed. Finally, the silicon-glass chips are separated by sawing, then mounted and connected.

Measurement circuits

In order to detect small capacitive changes in the order of a view pF and below, three types of measurement methods are considered: capacitive AC bridge, charge/discharge and also sigma delta modulation. The last one is devoted to be used in an application specific integrated circuit adapted to the realized 3D capacitive accelerometer. Typical advantages of such a micromechanical sigma delta modulator are the high linearity and the digital output. Sensor specifications are a zero capacitance of 20pF, a capacitive sensitivity of more than 1pF/g, with a measurement range of ±2g. General investigation of the detection noise shows that for all measurement circuits a capacitive resolution of 1aF/√Hz can be achieved for the read-out of the realized bulk-micromachined accelerometer. This opens the way for a two-chip solution accelerometer system for three-dimensional acceleration measurement with a resolution in the μg-range.

Experimental characterization

Finally, the fabricated 3D silicon capacitive accelerometer was tested. Static accelerations have been applied by rotating the sensors in the gravity field. The dynamic response was measured by using the vibrating coil of a loudspeaker, and an HP4194 network analyzer. Average zero capacitances for in- and out-of plane accelerometers are between 18pF and 19pF with sensitivities ranging from 0.5pF/g to 4pF/g depending on the mechanical design. Deviations from linearity are around 1% and have to be further investigated. First resonance occurs around 500Hz. Using a commercial capacitance meter, resolutions up to 40μg/√Hz can be obtained. In conclusion, the measured accelerometer performance is close to the theoretical estimations expressed in the specifications. The resolution is expected to be improved by using an integrated read-out circuit placed close to the accelerometer chip.

Conclusion

One general advantage of the capacitive transducers is its double function of sensor and actuator. Operating as an actuator by applying an electrostatic force to the electrodes, offers the advantage of closed loop operation, electrostatic damping and stiffness adjustment. Furthermore, a low power operation and a wide temperature range are characteristics of most electrostatic sensors. Different from most capacitive accelerometers, the change in capacitance for the presented in-plane device is linear versus acceleration. Concerning fabrication, the capacitive device offers the advantage of a full batch process (meaning possible low cost). However, the cost reduction is limited by the critical fabrication steps of electrode alignment, and small gap etching.

CHAPTER 5

5. Multi-axial optical accelerometers

5.1 Introduction

5.2 Fabrication concepts for opto-mechanical sensors

5.3 Principles

5.4 Modeling of the optical accelerometer

5.5 Fabrication process of the optical accelerometer

5.6 Experimental characterization

5.7 Noise and optimized performance

5.8 Conclusion of chapter 5

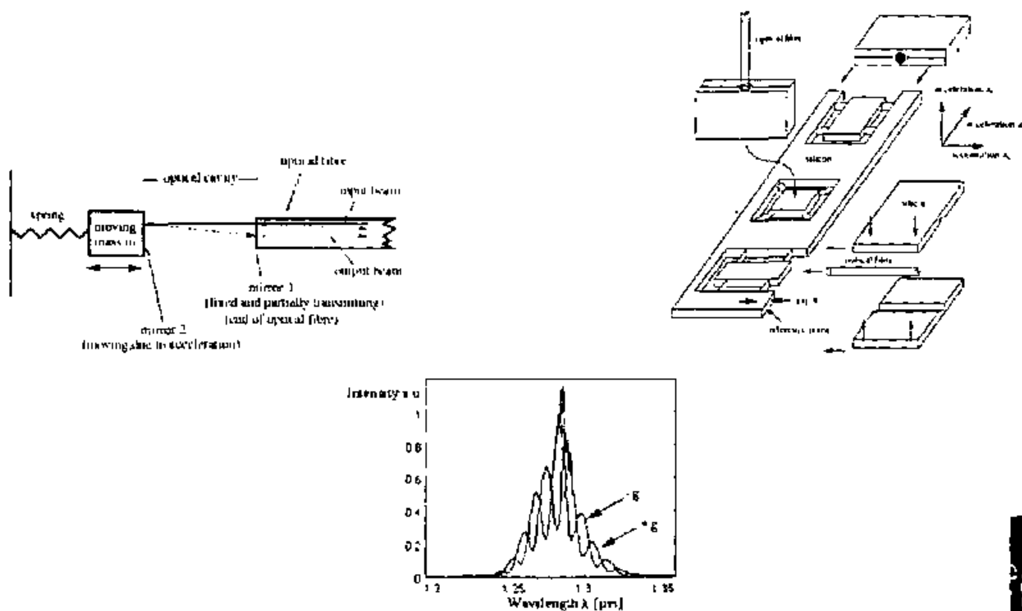

5. Multi-axial optical accelerometers

This chapter deals with optical sensors for multi-axial measurement of acceleration designed and realized in frame of the thesis project. After an introduction into some general aspects of fiber optic sensors, we explain the concept of fiber optic interrogation and the principle of operation used for the presented accelerometer. Then follow sections focusing on device modeling, fabrication and experimental characterization. Finally, this chapter concludes with an analysis of the noise in the system and with the possible optimizations and limitations of the optical accelerometers.
The general optical technique based on coherence modulation and employed for the accelerometers has been developed at the optical laboratory LOPMD in Besançon (Laboratoire d'optique Pierre-Michel Duffieux). Thus, the scientific results of this chapter are born in a collaboration between the LPMO and the LOPMD (Wilhelm Elflein and Henri Porte). The main content of this chapter has been published in [3, 4, 7, 11].

5.1 Introduction

Over the last two decades fiber optic sensors have been subject to continuous development. Typical applications of these optical devices are the sensing of chemical, biochemical and environmental properties, structural monitoring, and measurements of electrical and magnetic fields [Cul95, Cro94]. Also in the domain of micromachined optical accelerometers several papers have been published during the last years [Abb95, Bur92, Chn97, Deg98, Lis94, Mar95, Pei98, Sto96, Utt92].
Optical fiber sensors are known to have some attractive features, such as immunity to electromagnetic interference, chemical passivity, electrical isolation, no fire hazards and often potential high sensitivity and large bandwidth. Although fiber optic sensors have these advantageous features, relatively little commercial exploitation has occurred compared to their electro-mechanical counterparts [Cro95]. Some reasons for this lack of commercial interest could be attributed to the often high costs, the complex packaging technology, the requirement of precise alignment during fabrication, temperature and vibration induced intensity and phase noise, or the lack of conformity of design and signal processing, which makes sensor interchangeability difficult, if not impossible [Jac94]. In this chapter we describe an optical fiber sensor for multi-axial acceleration measurement, which overcomes some of the above mentioned obstacles, e.g. precise alignment.
As presented in chapter 1, where an overview of possible read-out techniques is given, fiber optic accelerometers can be generally divided into two categories [Sto95]. Firstly, in devices based on intensity modulation and secondly, interferometric or phase modulated sensors. While intensity modulated transducers are associated with simplicity and low cost, interferometric devices are often more sensitive and have a larger dynamic range. However they are more expensive due to their more complex electronic signal processing. Considering the aim of the PICS project (searching for the limits in microtechnology), we have chosen to focus on an interferometric type of accelerometer in order to achieve a high sensitivity.

5.2 Fabrication concepts for opto-mechanical sensors

Different technologies for the fabrication of the opto-mechanical sensing element will be now discussed. Once decided, which fabrication concept should be taken, the different designs feasible with this technology are investigated.

5.2.1 Fabrication technologies

In general, one can divide the fabrication processes for MOEMS (Micro-Opto-Electro-Mechanical-Systems) into two main categories: fully integrated in silicon and hybrid concepts. The most important difference between these two categories lies in the realization of the medium for optical light transmission. In the case of an integrated device, the light is transmitted via a planar optical waveguide which is integrated into the silicon chip with help of photolithography and thin film deposition, e.g. Si_xN_y, SiO_2. In a hybrid system the mechanical element is formed out of silicon, while the optical interrogation is realized by an attached optical fiber. For both fabrication technologies one can find several advantages and disadvantages. Most of them are summarized in table 5.1. One of the main obstacles for both technologies lies in the assembling procedure. For an integrated device a coupling between the planar waveguide and the optical fiber is necessary. In the case of the hybrid type, there is no such coupling necessary, making it easier to use. However, a precise attachment of the optical fiber to the mechanical element has to be provided.

	Integrated	Hybrid
Benefits:	☺ no assembling between mechanical element and optical interrogation ☺ geometrical precision defined in layout ☺ electronics on same chip possible ☺ small devices ☺ batch process for device	☺ simple fabrication process ☺ no coupling between waveguide and external optical fiber necessary, thus „ easy to use "
Drawbacks:	☹ complicated process technology ☹ coupling between waveguide and external fiber necessary (with precise alignment) ☹ potential high Fresnel losses when coupling to an external optical fiber	☹ potential low reproducibility ☹ large devices (e.g., difficult to reduce the diameter of the optical fiber)

Table 5.1: Benefits and drawbacks for two different fabrication technologies for MOEMS (Micro-Opto-Electro-Mechanical-Systems): integrated versus hybrid.

5.2.2 Different concepts for a fiber-optic interrogation

Since the development of a fabrication process for an integrated optical devices requires a too long time to be finished in the framework of this thesis, it was chosen to focus on the development of an opto-mechanical accelerometer with a fiber-optic read-out.

There are various designs possible which allow to combine the etching technology proposed in chapter 3, an interferometric optical cavity as the detection mechanism, and a fiber-optic interrogation. In general, optical fibers are fixed into etched V-grooves aligned along the {110}-direction. Due to this alignment these V-grooves have {111} silicon planes as sidewalls. In our case the alignment is along the <100>-direction. This is not compatible with the developed etching process. For this reason we propose alternatives to the conventional V-groove devices.

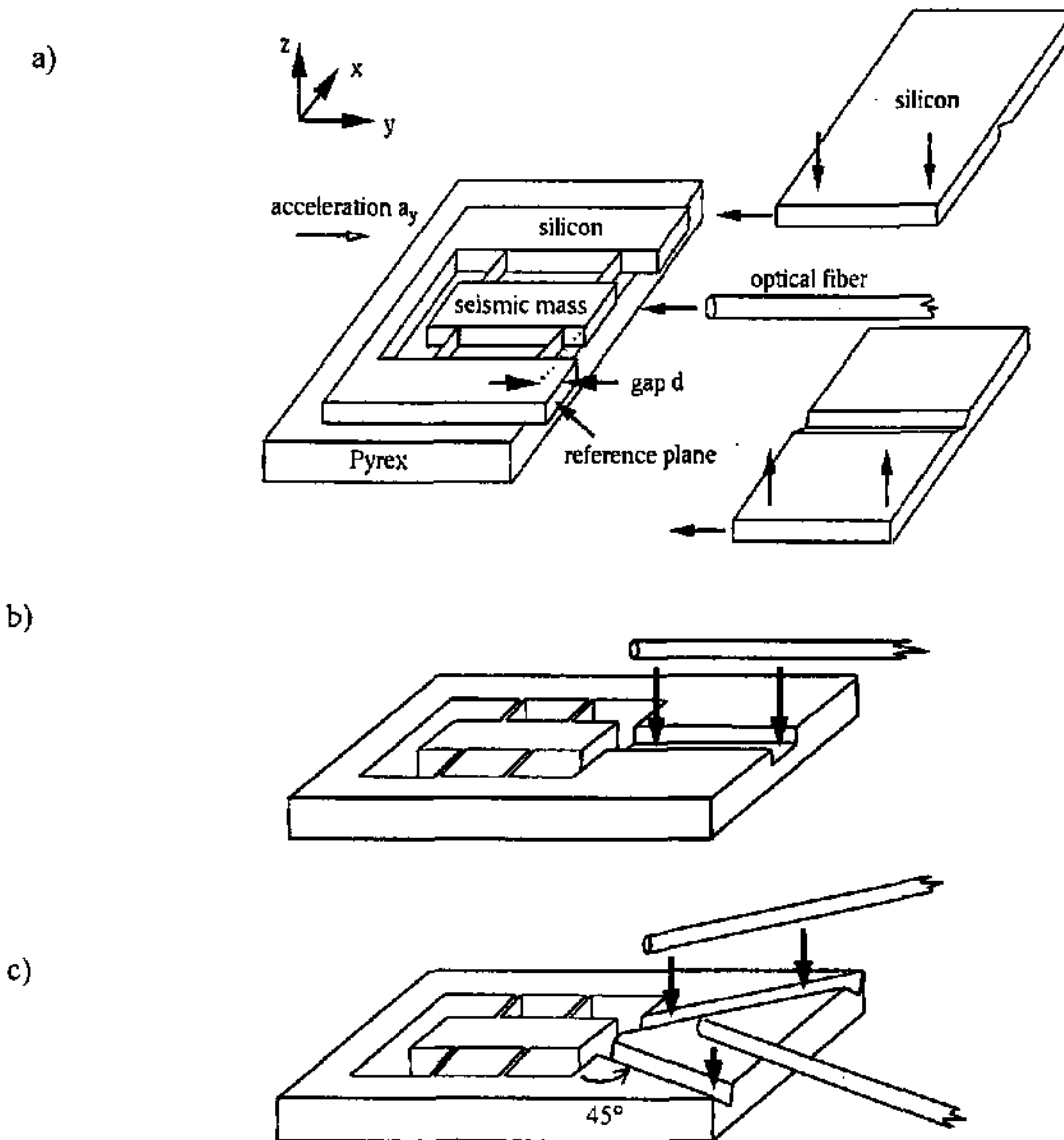

Figure 5.1 : Different concepts for the fiber-optic interrogation of an uni-axial accelerometer: a) Schematic of a mechanical silicon sensor with an attached fiber-silicon sandwich; b) Seismic mass including a U-groove for the alignment of an optical fiber; c) Two V-grooves aligned with an angle of 45° to the seismic mass element.

In figure 5.1 three different concepts for a fiber-optic accelerometer are shown. In each case an optical cavity is formed between the silicon mass and the fiber. Figure 5.1a) shows a schematic of a mechanical silicon sensor with an attached fiber-silicon sandwich. As this device consists of two silicon dies, the lithography process is independent for both silicon parts. V-grooves can be formed in the conventional way, in order to fix precisely the optical fiber. Fig. 5.1b) represents a seismic mass including an U-groove for the alignment of an optical fiber. The U-groove is bounded by {100} silicon planes. In this case, a precisely parallel alignment between fiber and U-groove is more difficult, since the groove is quite large (≥ wafer thickness) due to the

underetching of the vertical {100} planes (seismic mass and U-groove are assumed to be etched within the same fabrication step). In design 5.1c) two V-grooves are aligned with an angle of 45° to the seismic mass element. Another possibility exists in forming a V-shaped groove within the silicon seismic mass element by changing the etch solvent from KOH to EDP in an additional etching step [Ros94, Frü97]. In order to keep the etching process as simple as possible, this possibility was not explored.

Structure shown on Fig. 5.1a) has two advantages compared to the other concepts (5.1 b and 5.1 c): firstly, a more precise formation of the optical cavity and secondly, a more adapted design to build a 3D accelerometer system. Both will be explained in more detail in the following sections, where we focus on this structure.

5.3 Principles

This part describes the basic detection principle used for the read-out of the optical accelerometers. The sensor element represents a low-finesse Fabry-Perot interferometer which is remote controlled by a technique called coherence modulation. The method allows to detect signals from different sensors at one time using one single light source. This is called optical multiplexing.

5.3.1 General detection principle using a Fabry-Perot cavity

To measure the displacement of the seismic mass, an optical fiber is added in the structure as shown in figure 5.1. The vertical surfaces of the seismic mass and the optical fiber form thus a low-finesse Fabry-Perot cavity (FPC). This cavity works as a two beam interferometer with an optical path difference equal to twice the fiber-to-mass distance. The general principle of such a Fabry-Perot interferometer is shown in 5.2. The readout beam is sent through the optical fiber and reflects on the FPC. The reflected beam from the fiber end (reference reflection) and the reflected beam coming from the seismic mass (sensing reflection) interfere in the input-output fiber. When one of the mirrors is moved, the length of the FPC is changed. This changes the phase difference between the reference reflection and the sensing reflection.

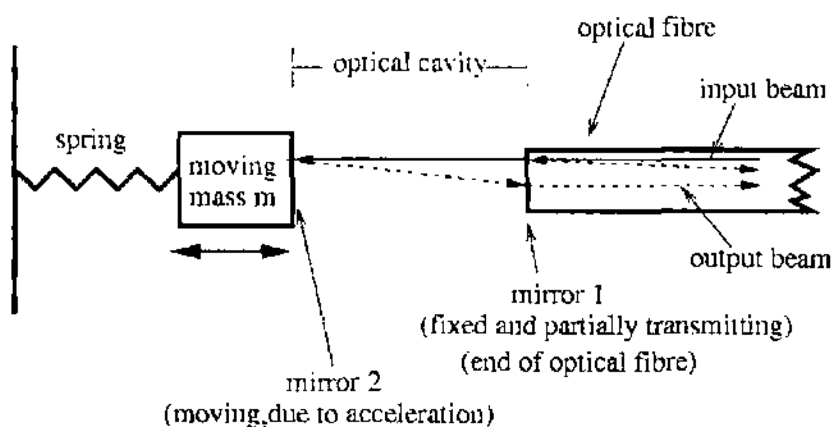

Figure 5.2: Principle of the accelerometer with a Fabry-Perot cavity as detection mechanism.

The general transmission function of such an optical cavity is the ratio between the reflected and the initial light intensity (I_R and I_0, respectively). It can be described by

$$T = \frac{1}{2} \alpha [1 + v \cos(\Phi_1)] \qquad (5.1).$$

(with wavelength λ, α is a factor related to optical losses, and v is the interference visibility with $0 < v < 1$) Φ_1 represents the optical phase difference of the FPC. The FPC's optical path length D_1 equals twice the fiber-to-mass distance d_1. The optical phase is a function of the used wavelength and of the fiber-to-mass distance d_1

$$\Phi_1 = 2\pi D_1 \lambda^{-1} = 4\pi d_1 \lambda^{-1} \qquad (5.2).$$

If a broadband light is sent through the optical fiber, the spectrum of the light reflected by the FPC through the fiber is modulated by the FPC spectral response. Any movement of one mirror, i.e. Δy, changes the FPC optical path, and leads to a shift $\delta\lambda = \lambda (\Delta y / d)$ of the FPC reflected spectrum. Thus the FPC's optical phase becomes a function of the mirror displacement

$$\Phi_1 = 4\pi (d_1 + \Delta y) \lambda^{-1} \qquad (5.3).$$

5.3.2 Remote read-out based on coherence modulation

Coherence modulation is a technique which is applied to the optical path change of a light beam with a small coherence length L_c. In other words, the transmitted information is coded in an optical path change. To retrieve the information one has to determine the relevant path change. One general possibility to realize such a system is shown in figure 5.3. Two interferometers are connected in serie. Interferometer 1 acts as modulator and interferometer 2 as demodulator. The light coming from a broadband source has a small coherence length. This emitted light can be seen as a serie of wave packets.

The first interferometer separates one wave packet into two. The distance between them is given by the optical path difference D_1 of the employed interferometer. A shift of the interferometer's mirrors introduces a variation into the path length and thus into the distance between the wave packets. If the optical path length of the first interferometer is larger than the coherence length of the transmitted light ($D_1 > L_c$), the interference does not occur anymore.

The light is then coupled via an optical fiber into the detection unit (opto-electronic central processing unit). This unit contains a second (receiver-) interferometer, a photo detector and eventually an electronic signal processing unit. By going through the second interferometer with an optical path difference of D_2, the initial signal, which is coded as an optical path change, is converted into an intensity modulation. When the two separated wave packets are introduced in the second interferometer, they are divided into four parts. If, as shown in the schematic of figure 5.3, the static path differences of the two interferometers are nearly identical ($D_2 \approx D_1$), two from the four wave packets will superpose. Interference fringes appear when one optical path difference of the interferometers is modified.

At the output of the second interferometer, the detected intensity contains now a term that depends on the difference between the two path length. With $D_2 \approx D_1$, the interference function can be expressed as (optical phases of the two interferometers Φ_2, Φ_1)

$$I = \frac{1}{4} I_0 (1 + \frac{1}{2} \cos(\Phi_2 - \Phi_1)) \qquad (5.4).$$

From equation 5.4 one can clearly see that the signal depends on the phase shift $\Phi_2 - \Phi_1$ between the two interferometers. One can control the first interferometer on the measurement site with help of the second interferometer in the detection unit regulating the total phase $\Phi_2 - \Phi_1$.

Such a system provides all the typical advantages of optical measurement, i.e. immunity to electromagnetic interference, no power supply at the measurement site, etc. In addition, coherence modulation has some advantages which are specially interesting for the applications of sensors with remote read-out:

Firstly, the information coded in the optical path difference can be retrieved by local demodulation. The second interferometer can control the total interferometric phase. This opens the way to several different demodulation principles.

Secondly, these demodulation principles allow to cancel out some possible influences on the transmitted light during the propagation in the optical connection fibers. In fact, the light intensity and polarization is generally altered during transmission. However, the mutual phase shift remains unchanged.

Thirdly, the proposed technique of coherence modulation allows to multiplex several sensors within one network. The interrogation of many devices with one detection and transmission system can simplify the installation and reduce the costs.

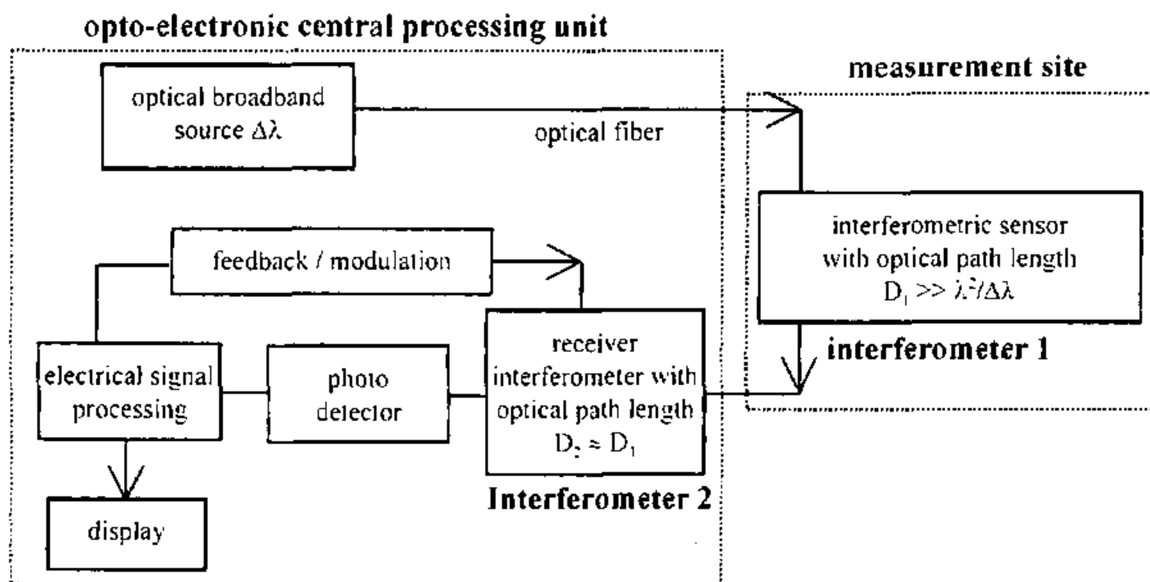

Figure 5.3: General schematic of an optical measurement set-up using an interferometric sensor and read-out based on coherence modulation.

5.3.3 Optical multiplexing of several sensors

The possibility to use coherence modulation to multiplex several interferometric sensors was proposed by Brooks [Bro85] based on principles earlier developed by Delisle [Del75] and Goedgebuer [Goe82]. Theoretically it is possible to multiplex a high number N of signals in only one transmission channel with one single light source. The demodulation could be performed by N parallel interferometers, each having an optical path difference associated to the corresponding interferometric sensor (see figure 5.4). The choice of the optical path difference depends on the network topology, the number of interferometers, the coherence length of the light source and the cross-talk and coupling between the different channels.

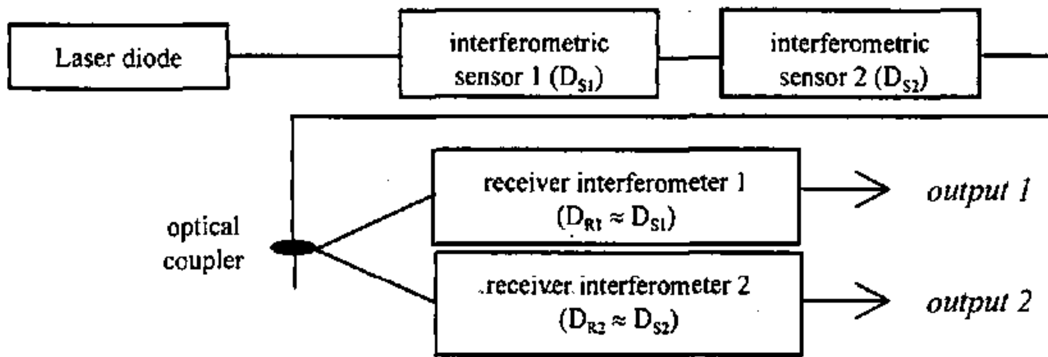

Figure 5.4: Topology for multiplexing of two interferometric sensors (proposed by [Bro85]). The two sensor interferometers have optical path differences of D_{S1} and D_{S2}, respectively, which are matched to those of the receiver interferometers (D_{R1} and D_{R2}, respectively).

In the case of a multi-axial accelerometer system, the technique of coherence modulation allows to multiplex two (and three) accelerometer signals to one single fiber (see figure 5.5). For that purpose, the second (and third) seismic mass systems are part of a second (and third) Fabry-Perot cavity with another optical delay. Both signals could then be multiplexed into the same fiber. At the fiber output, a fiber optic coupler allows to split the signal between two (or three) receiver-interferometers which are matched to the corresponding Fabry-Perot cavities. The fabrication method presented in chapter 3 allows to build three independent suspended seismic masses on one silicon chip with precise orthogonal alignment along the {100} silicon crystal axis.

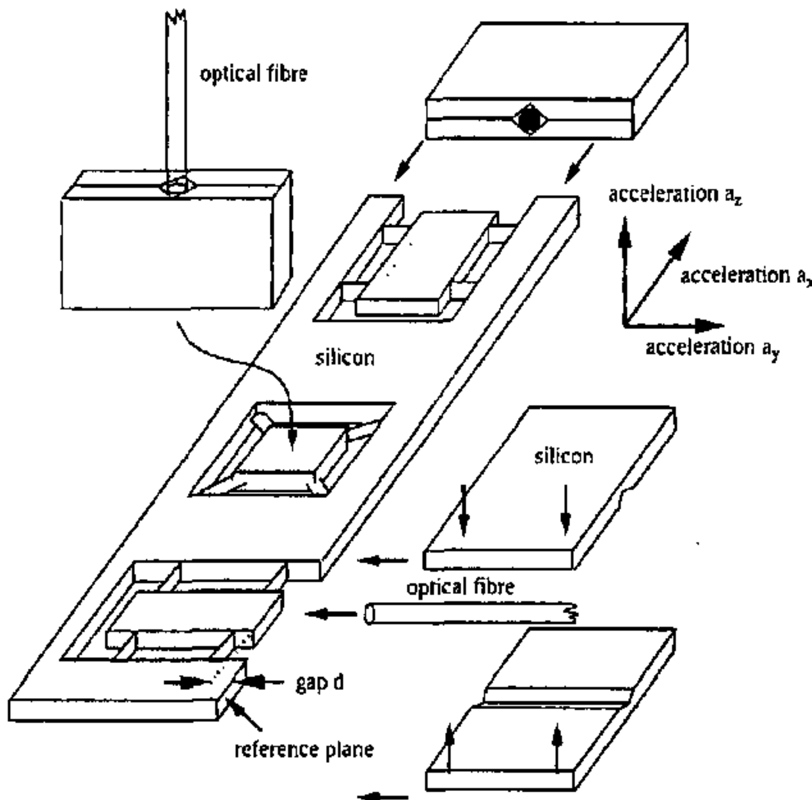

Figure 5.5 : Schematic view of a 3D microsystem composed of three independent accelerometers. Using three different Fabry-Perot cavities, the three signals can be multiplexed via one single fiber.

5.4 Modeling of the optical accelerometer

In the following we present the modeling of the opto-mechanical sensing element. The modelization can be divided into three parts: mechanical structure, optical transmission function of the sensing element, and the theoretical description related to coherence modulation and multiplexing

5.4.1 Mechanical structures for optical detection

Different mechanical designs and their mechanical models have been earlier described in this thesis in a general way. Now, we give a short presentation of the devices having been realized for optical detection. The mechanical element of an optical accelerometer is symmetrical and consists of a seismic mass supported by four thin, vertical beams (i.e. see figure 5.1). Accelerations parallel to the wafer-plane and perpendicular to the suspension beams cause the seismic mass to move in the wafer-plane. The displacement of the mass is proportional to the applied acceleration and given by formula 2.10. The spring constant is a function of the geometry and number of suspension beams and given by equation 2.2 ($N = 4$). The main advantage of this structure is that displacements along other directions than the sensitive direction are very small due to the structure's geometry and symmetry. Therefore, cross-sensitivities are very small.
We have fabricated four different accelerometers (named Sensor#O1, Sensor#O2, Sensor#O3_1 and Sensor#O3_2). Some of the mechanical characteristics are summarized in table 5.2. Sensor#O1 and Sensor#O2 are uni-axial devices and have beam lengths of 1325μm, beam heights of 340μm and a beam thickness between 20μm and 10μm. The beam thickness can be adjusted in the etching process without changing the lithography mask. For Sensor#O1 with a beam thickness of 17μm the calculated mechanical sensitivity (displacement per unit acceleration) in the sensitive direction is 143 nm/g. The mass m is calculated as $6.1 \cdot 10^{-6}$ kg. Resonance frequencies are given in table 5.3.

	Sensor #O1	*Sensor #O2*	*Sensor #O3-1*	*Sensor #O3-2*
Seismic mass m (calculated):	$6.1 \cdot 10^{-6}$ kg	$6.1 \cdot 10^{-6}$ kg	$6.0 \cdot 10^{-6}$ kg	$6.0 \cdot 10^{-6}$ kg
Fabry-Perot cavity d (theoretical):	45 μm	135 μm	45 μm	135 μm
Mechanical sensitivity (theoretical):	143 nm/g	462 nm/g	171 nm/g	171 nm/g

Table 5.2: Overview of the dimensions and mechanical characteristics of the sensing elements realized for optical read-out.

Mode for *Sensor #O1*	Resonance frequency (analytical)	Resonance frequency (ANSYS)
Vibration along main sensitive axis	1.3 kHz	1.4 kHz
Vibration along vertical direction	19.1kHz	22.7 kHz
Rocking mode	24.1 kHz	31.1 kHz
Vibration along suspension beams	98.5 kHz	98.0 kHz

Table 5.3: Resonance frequencies calculated analytically or with ANSYS for the uni-axial sensor#1.

Sensor#O3_1 and Sensor#O3_2 are included in one chip and represent a monolithic 2D device. Beam dimensions are 2000μm × 24μm × 353μm and seismic mass dimensions are 4600μm × 1600μm × 353μm (length × width × thickness). The mechanical sensitivity of the suspended mass is 171nm/g. It should be emphasized that we do not aim to fabricate very small devices, but we rather seek for a large seismic mass associated with thin suspension beams in order to increase the mechanical sensitivity. The transverse sensitivities are much smaller than the main sensitivity. For instance, with the above numerical values, the mechanical sensitivity along the z-axis is 104 times smaller than along the main sensitive direction.

5.4.2 Optical transmission function of the accelerometer

The polished endface of the optical fiber and the silicon seismic mass build together a low-finesse Fabry-Perot cavity. The reflectivity of the surfaces is small. This allows us to describe approximately the reflected light by only two beams which superpose to each other (see figure 5.2 and 5.6). The beams are also enlarged due to diffraction.

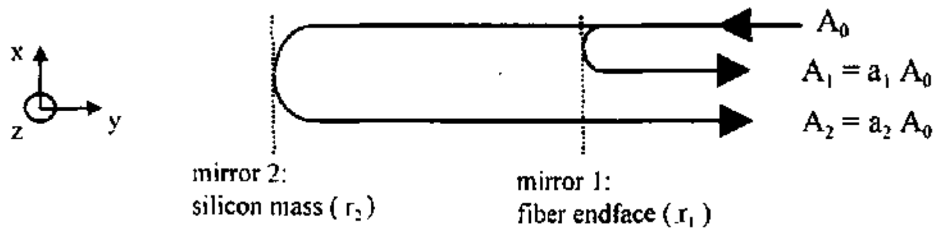

Figure 5.6: Description the reflected light by to superposing beams with amplitudes A_1 and A_2.

Assuming a Gaussian distribution. the amplitude's spatial distribution of the mode propagating inside the fiber is given by

$$A_0 = E_0 \exp\left(-\frac{x^2 + z^2}{em_0^2}\right) \qquad (5.5).$$

em_0 is the half-width of the fiber's eigenmode and E_0 a constant. The reflection at the polished endface of the fiber gives a first reflected beam of amplitude A_1 (r_1 is the reflection coefficient of the fiber's endface)

$$A_1 = r_1 A_0 \qquad (5.6).$$

The coupling coefficient is defined as $a_1 = A_1 / A_0 = r_1$. The light is then transmitted through the fiber's endface in the cavity. It is reflected at the seismic mass and returns to the fiber. Neglecting the curvature of the reflected optical field, the amplitude of this second reflected beam can be described by (r_2 is the reflection coefficient of {100} silicon plane) [Vat85]

$$A_2 = A_0\, r_2 \left(1 - r_1^2\right) \frac{2\,em_0^2}{em_2^2 + em_0^2} \exp\left(\frac{-j\,4\pi \cdot d}{\lambda}\right) \qquad (5.7).$$

em_2 represents the enlargement due to diffraction of the Gaussian field. The coupling coefficient for the second reflected beam is $a_2 = A_2 / A_0$. Consequently, limiting the number of reflected beams to two, the intensity of the reflected light $I_R = (a_1 + a_2)^2\, I_0 = (a_1^2 + a_2^2 + 2\, a_1\, a_2)\, I_0$ is given by

$$I_R = I_0 (r_1^2 + r_2^2 (1 - r_1^2)^2 \left(\frac{2\,em_0^2}{em_2^2 + em_0^2}\right)^2 + 2\, r_1\, r_2 (1 - r_1^2) \left(\frac{2\,em_0^2}{em_2^2 + em_0^2}\right) \cos\left(\frac{4\pi d}{\lambda}\right) \qquad (5.8).$$

Thus, we obtain a classical optical transmission function ($T = I_R / I_0$, see also equation 5.1)

$$T(\lambda) = \tfrac{1}{2}\, \alpha\, [\, 1 + v \cos(4\pi\, \lambda^{-1}\, d)\,] \qquad (5.9).$$

The optical losses in the system can be expressed by $\alpha = 2\,(a_1^2 + a_2^2)$, and the interference visibility by $v = 2 \cdot a_1 \cdot a_2 / (a_1^2 + a_2^2)$. The static optical path length is 2 d. In our case the reflectivity of the polished fiber's endface is $r_1^2 = 4\%$ and for the silicon plane about $r_2^2 = 30\%$. The half-width of the fiber's eigenmode em_0 is 5.1 μm. Taking these values, we can calculate the relevant parameters of the optical accelerometer as an interferometric filter (see table 5.4).

Optical path difference D (twice the fiber-to-silicon distance d)	90μm	270μm
Optical losses α	- 6.4dB	- 10.6dB
Interference visibility v	0.95	0.51

Table 5.4: Theoretical parameters of the optical accelerometer as an interferometric filter.

5.4.3 Coherence modulation and multiplexing

After the discussion of the transmission function of the optical accelerometer, we investigate now its application to a measurement system using coherence modulation and multiplexing.

Coherence modulation

A broadband source has a spectral power distribution P_0 associated with a spectral width $\Delta\lambda$. The coherence length L_c of a broadband source equals $L_c = \lambda_0^2/\Delta\lambda$. The total power P_S of the source that can be detected at the systems output is given by integration over the total spectrum. If the radiation is transmitted into an optical filter with a transmission function $T_1\,(\lambda)$ (i.e. accelerometer), the spectral power density is given by $P_0 \cdot T_1\,(\lambda)$. In out experimental set-up (figure 5.14) the light passes through a 50:50 directional coupler leading to a loss factor of ¼ . The spectral integral over $\tfrac{1}{4} \cdot P_0 \cdot T_1\,(\lambda)$ giving the total detectable power P_S remains constant if the optical path difference D_1 ($D_1 = 2$ d) of the accelerometer is larger than the coherence length of the source ($D_1 >> L_c$). If $D_1 < L_c$ one observes periodic fringes as a function of D_1.

Referring to figure 5.3 the light passes into a second filter (i.e. receiver interferometer having a optical path difference of D_2) with a transmission function $T_2(\lambda)$. In this case, we can describe the output spectrum as ¼ $P_0 \cdot T_1(\lambda) \cdot T_2(\lambda)$, leading to

$$P(\lambda) = P_0 \frac{\alpha_1}{8}\left(1 + v_1 \cos\left(\frac{2\pi D_1}{\lambda}\right)\right)\frac{\alpha_2}{2}\left(1 + v_2 \cos\left(\frac{2\pi D_2}{\lambda}\right)\right) \qquad (5.10).$$

After some simplifications with help of trigonmetrical functions and assuming that the distributed spectral density of the light source is gaussian, as well as the assumption $D_1 \approx D_2$, we can finally write the total transmitted power as [Elf98]

$$P_S = P_0 \frac{\alpha_1\alpha_2}{16}\left(1 + \frac{v_1 v_2}{2}\cos\left(\frac{2\pi}{\lambda_0}(D_1 - D_2)\right)\right) \qquad (5.11).$$

In addition, if we choose a working point at the half-maximum of a fringe, that is at $D_1 = D_2 + \lambda/4$ and use modulation of low amplitude ($\Delta D_1 < \lambda/8$), we can linearize equation 5.11:

$$P_S = P_0 \frac{\alpha_1\alpha_2}{16}\left(1 + \frac{v_1 v_2}{2}\frac{2\pi}{\lambda_0}\Delta D_1\right) \qquad (5.12).$$

Under an applied acceleration the seismic mass of the accelerometer is shifted by Δy equivalent to a change in the optical path difference D_1 by ΔD_1 ($\Delta D_1 = 2\ \Delta y$). Δy and thus ΔD_1 are proportional to the applied acceleration. The change in the optical path leads to a wavelength shift $\delta\lambda$ in the accelerometer's transmission function:

$$\delta\lambda = 2\ \lambda\ (\Delta y / D_1) \qquad (5.13).$$

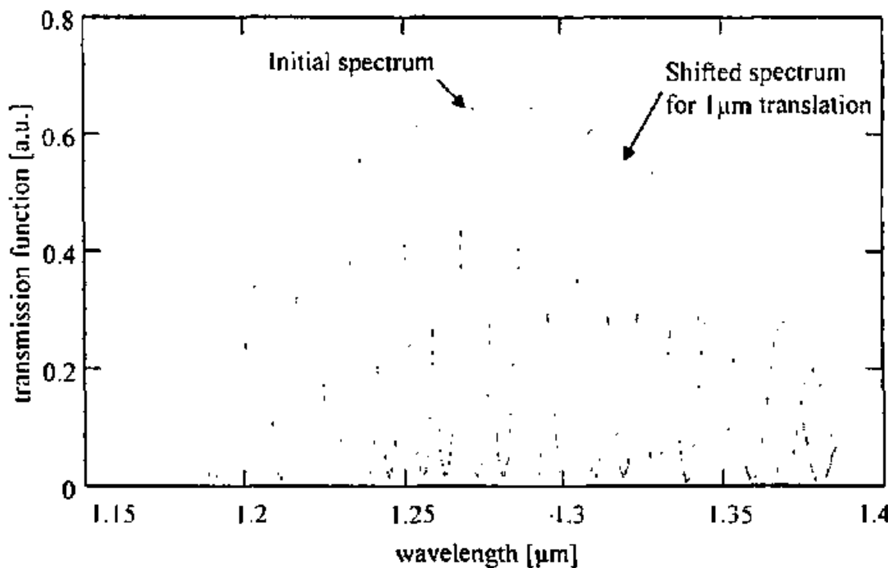

Figure 5.7: Simulated wavelength shift of the sensors's transmission function due to a 1µm displacement of one FPC mirror (the power distribution of a 1.285µm center wavelength laser-diode is assumed).

Coherence Multiplexing

We consider a network of two interferometric sensors, i.e. two accelerometers with optical path differences of D_1 and D_2, as proposed in figure 5.4. The individual transfer functions of the two accelerometers are given by

$$T_1(\lambda) = ½\, \alpha_1 [\, 1 + v_1 \cos(2\pi\, \lambda^{-1} D_1) \,] \text{and} \qquad T_2(\lambda) = ½\, \alpha_2 [\, 1 + v_2 \cos(2\pi\, \lambda^{-1} D_2) \,].$$

where α_1 and α_2 represent again the optical losses, v_1 and v_2 the interference visibilities. In addition, we take into account one receiver interferometer with an optical path difference of D_R and a transmission function as follows:

$$T_R(\lambda) = ½\, \alpha_R [\, 1 + v_R \cos(2\pi\, \lambda^{-1} D_R) \,] \qquad (5.14).$$

Assuming $D_R \approx D_1$, one can derive the total transmitted power [Elf98]

$$P_S = P_0 \frac{\alpha_1 \alpha_R}{16} \left(1 + \frac{v_1 v_R}{2} \cos\left(\frac{2\pi}{\lambda_0} (D_1 - D_R) \right) + \frac{\alpha_2}{\alpha_1} \right) \qquad (5.15).$$

P_S becomes independent from the second accelerometer and is only sensitive to variations of the first accelerometer's optical path difference D_1. Taking another receiver interferometer with $D_R \approx D_2$ a similar expression can be found

$$P_S = P_0 \frac{\alpha_2 \alpha_R}{16} \left(1 + \frac{v_2 v_R}{2} \cos\left(\frac{2\pi}{\lambda_0} (D_2 - D_R) \right) + \frac{\alpha_1}{\alpha_2} \right) \qquad (5.15).$$

Equations 5.15 and 5.16 demonstrate that by choosing carefully the optical path differences of the receiver interferometers, one can access to each accelerometer signal without cross-talk. The optical path differences of the receiver interferometers should be chosen according the following linear law in order to provide operation with minimum cross-talk:

$$D_{R1} = {}^1/_2\, D_{R2} = {}^1/_3\, D_{R3} \quad \text{etc.}$$

The devices presented in this thesis have path differences of 90µm or 270µm enabling a network of two multiplexed accelerometers. For a three-dimensional multiplexed accelerometer system a third sensor should be included with an optical path difference of 180µm.

5.5 Fabrication process of the optical accelerometer

After describing the basic principles of operation and the corresponding analytical models, now the employed fabrication technology is presented.

5.5.1 Fabrication of mechanical elements and silicon-fiber-sandwich

Unlike other lateral accelerometers, the structure in our case is fabricated by anisotropic etching of (100) silicon in a KOH solution . The thin suspension beams with vertical sidewalls were achieved by aligning the mask pattern with an angle of ± 45° from the <110> wafer flat as demonstrated in chapter 3. This non conventional alignment and the orthogonal orientation of the {100} silicon crystal planes give the possibility to fabricate two perfectly perpendicular devices on one chip in the same etching step. It should be emphasized that conventional wet-etching techniques have demonstrated vertical sidewalls fabrication using (110) wafers, but in such cases, the {111} vertical sidewalls that can be fabricated are not perpendicular to each other and the masses are not perfectly symmetrical suspended. By adding a third accelerometer which is sensitive to vertical accelerations, a 3D accelerometer system on one single chip can be achieved. Due to double side etching, the structure is highly symmetrical. A Scanning Electron Microscope (SEM) view of the silicon structure for an uni-axial optical accelerometer is shown in figure 5.8. A device enabling a multiplexed two-axis detection is presented in Figure 5.9.

Figure 5.8 : SEM view of the suspended mass.

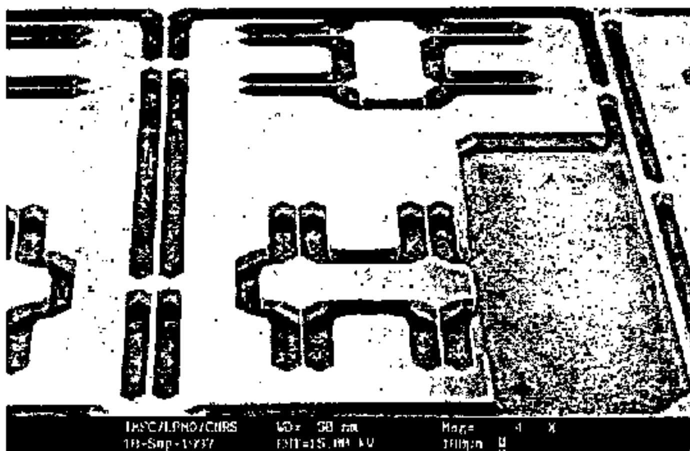

Figure 5.9 : SEM view of the micromachined 2D seismic mass system.

5.5.2 Assembling of the opto-mechanical sensor

In order to insure movability of the seismic mass after anodic bonding on a Pyrex glass (Corning 7740), the silicon mass and the suspension beams are etched 10 µm along the vertical direction in an additional KOH etching step. The fiber is fixed in a V-groove, polished, and then epoxied to the open end of the sensor structure (see figure 5.10). We used a standard singlemode fiber.
The vertical walls of the seismic mass consists of {100} crystal silicon planes and enables a good light reflection (see figure 5.11). The gap between the mass and the optical fiber should be precisely set in order to optimize the detection sensitivity. Fortunately, since the reference plane (see figure 5.10) is etched at the same time as the mass, this gap is defined by the photolithography mask pattern. Therefore, thanks to the high precision of the micromachining process and the large alignment tolerances, this simple assembly procedure allows to define the optical gap within a precision of a few microns (as shown in the experimental results) without any dynamic adjustment during the assembly process. For the uni-axial device the FPC is designed to be 45µm, equivalent to an interferometer's optical path difference of 90µm. In case of the 2D accelerometers the gaps are defined to be 45 µm and 135 µm, respectively. The overall 2D chip containing two suspended seismic masses is 19 mm x 10 mm large. A photo of a assembled uni-axial accelerometer is shown in figure 5.12. The opto-mechanical sensor is completely passive (no electrical supply is provided at the accelerometer).

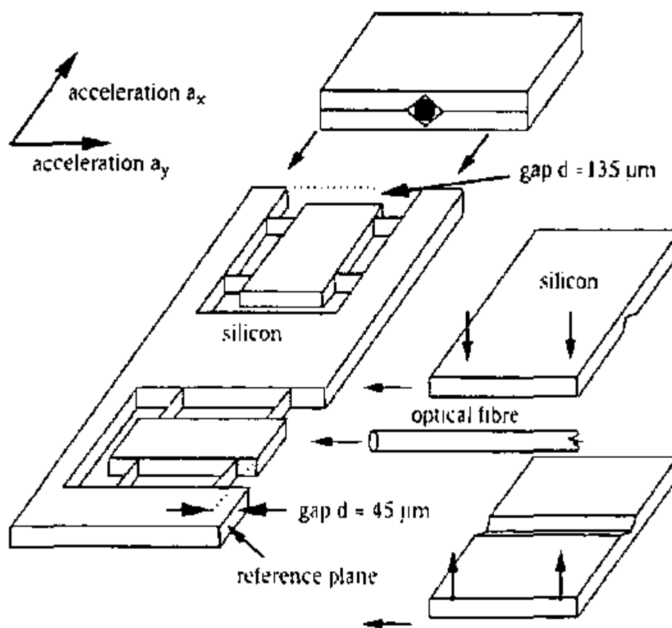

Figure 5.10: Schematic of the assembling of a micromachined optomechanical 2D accelerometer with two different Fabry-Perot cavities of 45µm and 135µm, respectively.

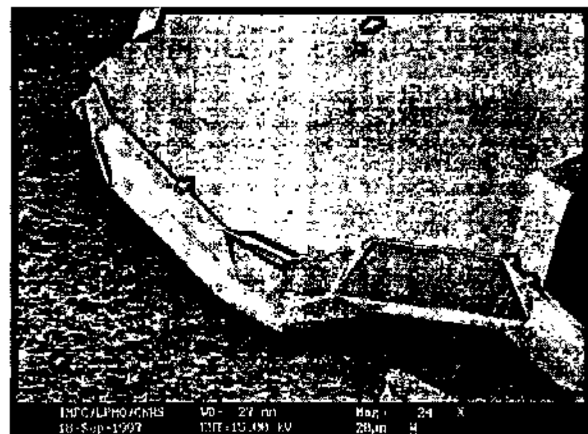

Figure 5.11: Detail of the fabricated 2D structure, showing the suspended seismic mass with a vertical sidewall used for light reflection.

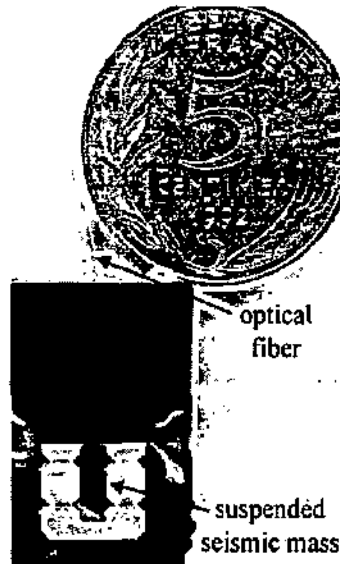

Figure 5.12 : Photo of a completely assembled opto-mechanical sensor (suspended seismic mass with attached optical fiber). The device is fully electrical passive.

5.6 Experimental characterization

Acceleration was applied on the seismic mass by rotating the sensor in the gravity field. Static measurements were performed, firstly by using a commercial optical spectrum analyzer, and secondly by employing the detection unit based on coherence modulation. We have tested three different sensor designs (labeled #O1, #O2 and #O3), whose theoretical features have been given in table 5.2. Apart from various mechanical sensitivities, the Fabry-Perot cavities are different. The accelerometers are designed to match with the optical delays of the receiver interferometers (twice 45μm = 90μm and twice 135μm = 270μm, respectively), which are used in the opto-electronic detection unit.

5.6.1 Measurements with spectrum analyzer

Measurements with a commercial spectrum analyzer have been performed to check experimentally the mechanical sensitivities and the optical gaps of the fabricated devices.

1D accelerometer

The reflection spectrum, measured on sensor #O1 with the optical spectrum analyzer, is shown in figure 5.13 for two orientations of the accelerometer, corresponding to +1g and -1g acceleration ($1g = 9.81 m\,s^{-2}$). The reflection minima are spaced by $\Delta\lambda$ = 18.8nm, indicating a fiber-to-silicon distance

$$d = \tfrac{1}{2} D = \tfrac{1}{2} (\lambda^2/\Delta\lambda) \qquad (5.16)$$

of 44μm, which is close to the designed value of 45 μm. Therefore, no additional adjustment of this gap is required. The shift of the reflected light spectrum for a 2g variation of acceleration is $\delta\lambda$ = 8.4nm or 4.2nm/g. Thus, the corresponding mirror displacement is

$$\Delta d = (\delta\lambda/\lambda)\, d \qquad (5.17).$$

In this case Δd=144nm per 1g, which is in the vicinity of the predicted mechanical sensitivity of 143nm/g.

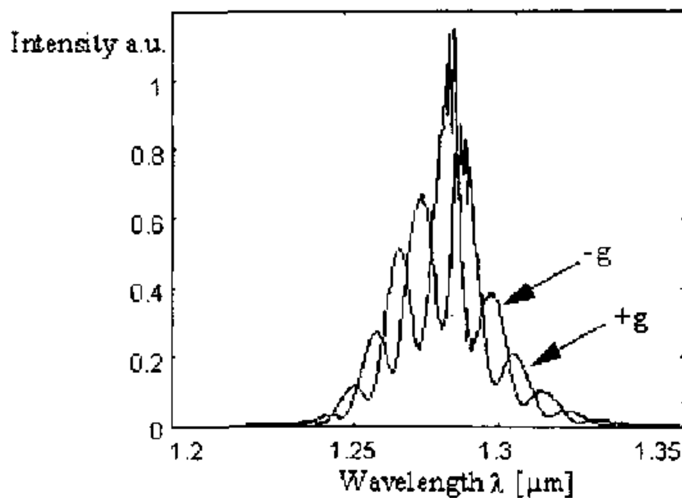

Figure 5.13 : Shift in optical reflection spectrum of $\delta\lambda = 8.4$nm (= 4.2nm/g) for applied accelerations of +1g and -1g. The used center wavelength was 1.285 μm.

In figure 5.14 one can see the very linear displacement behavior of the silicon seismic mass (sensor #O2) due to accelerations ranging from -1g to +1g. For a sensor with the design #O2, the measured shift $\delta\lambda$ in the spectrum is 8.5nm/g equivalent to a mass displacement of 906nm/g.

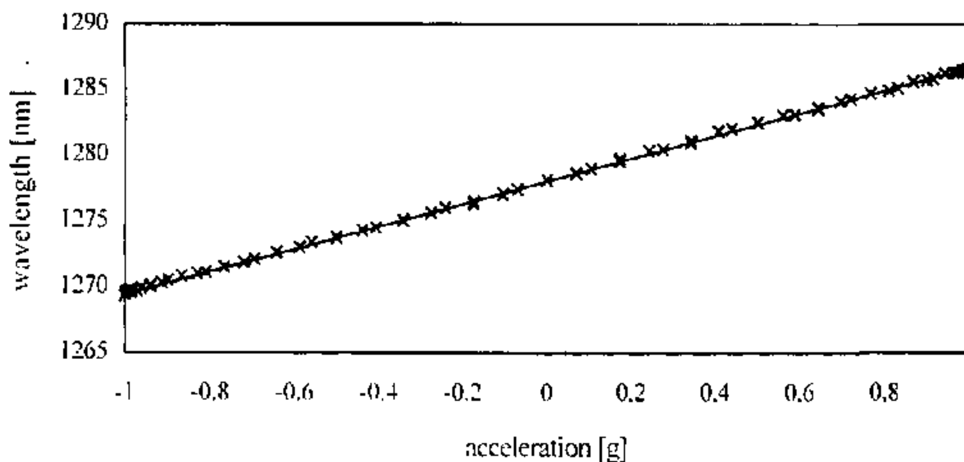

Figure 5.14 : Measured output (wavelength) of a sensor with an optical cavity of 135μm (design #2). The output is due to applied accelerations ranging from -g to +g. The measurement was done using an optical spectrum analyzer.

2D accelerometer

The shift in the reflection spectrum of the first mass (45 μm gap) was $\delta\lambda_1/g = 4.92$nm/g and the measured distance between two minima was $\Delta\lambda_1 = 18.1$nm. For the second seismic mass, the sensitivity to accelerations was $\delta\lambda_2/g = 1.62$nm/g with a distance between two reflection minima of $\Delta\lambda_2 = 6.1$nm. From these measurements, one can calculate with formula 5.16 the corresponding optical gaps. The mechanical sensitivity of the suspended mass can be derived from the relation give in equation 5.17.

A comparison between the theoretical and measured values is given in table 5.5 for all tested devices. A good agreement is observed between theoretical values and experimental measurements. In case of mechanical sensitivity and optical gap the deviations are smaller than 2.3%.

	Sensor #O1	Sensor #O2	Sensor #O3-1	Sensor #O3-2
Fabry-Perot cavity d (theoretical):	45 µm	135 µm	45 µm	135 µm
Fabry-Perot cavity d (measured):	44 µm	137 µm	45.5 µm	135.3 µm
Mechanical sensitivity (theoretical):	143 nm/g	924 nm/g	171 nm/g	171 nm/g
Mechanical sensitivity (measured):	144 nm/g	906 nm/g	174 nm/g	170 nm/g

Table 5.5: Comparison between the expected values and those derived from experimental data for the all optical device (Sensor #O1 and #O2 are uni-axial devices, sensor #O3-1 and #O3-2 are the mechanical sensing elements for the 2D device).

5.6.2 Measurement set-up using coherence modulation

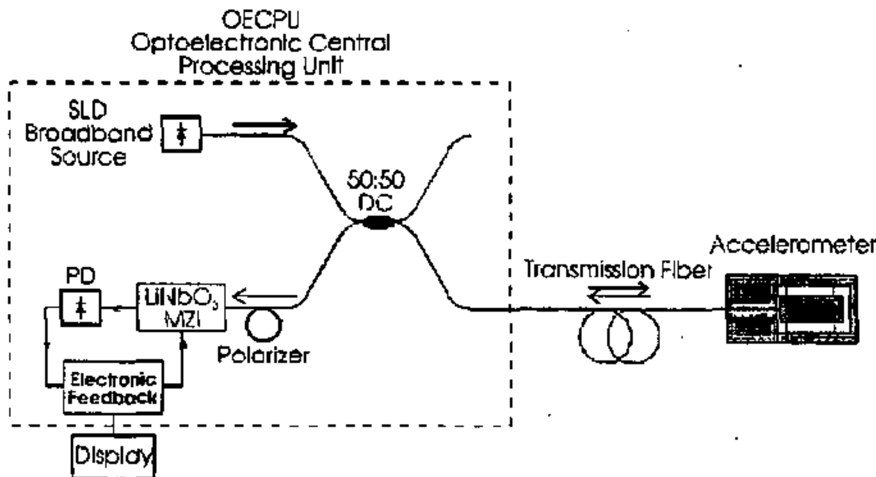

Figure 5.15 : Experimental set-up for the optical read-out of an uni-axial accelerometer.
The accelerometer is linked with an optical fiber to an opto-electronic central processing unit (OECPU).

Figure 5.15 shows the detailed set-up of the detection system. The light source is a superluminescent diode (SLD) with an optical power of 500µW, 1.285µm central emission wavelength, and 33µm coherence length. The emitted light is not polarized. A 50:50 non-polarizing directional coupler injects the light into the standard singlemode fiber of the accelerometer. The light reflected from the device is again split in the directional coupler and directed to the active detection opto-electronics unit. First, the light is polarized by a fiber polarizer, and then launched into a receiver interferometer, in our case a Ti:$LiNbO_3$ integrated optics Mach-Zehnder-Interferometer (MZI) (see figure 5.16). The MZI's optical delay should be equal to the FPI's optical delay. Two kinds of MZI have been constructed, with optical path delays of 90µm and 270µm, respectively. The accelerometers optical delays were matched to these detection units. For TM polarization, the MZI has total insertion losses of 9.4dB, and a $V_\pi = 4.6V$ half-wave voltage. At the interferometer output, a photodiode detects the transmitted light power.

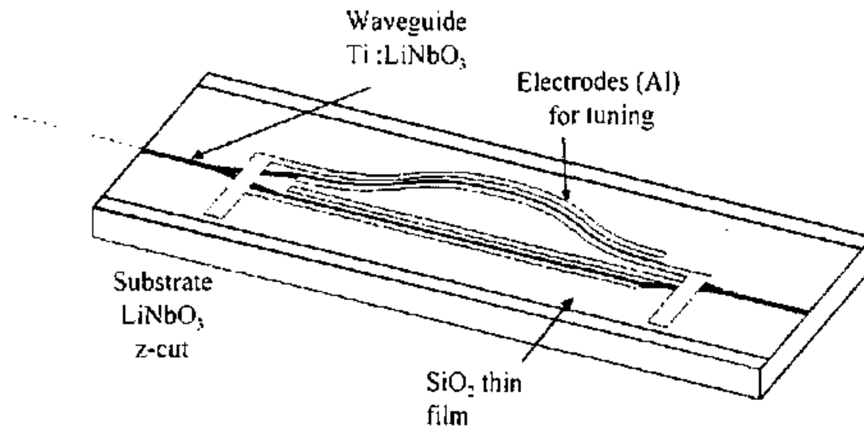

Figure 5.16: Schematic view of an integrated Mach-Zehnder interferometer (MZI) contained in the OECPU. The optical path difference of the MZI is tunable. It is used as a receiver interferometer in order to detect the wavelength shift of the reflection spectrum. (courtesy of Wilhelm Elflein)

In order to produce a signal which varies linearly with the seismic mass displacement, the tunability of the MZI can be used to track the spectral shift of the light reflected from the device using an electronic feedback loop, and following detection scheme proposed in reference [Por96]. The intensity modulation at the $LiNbO_3$ interferometer output is, according equation 5.4, proportional to $\cos(\theta_1 - \theta_2)$, where $\theta_1 = 4\pi \cdot (d+\Delta d)/\lambda$ is the phase shift due to the mirror displacement, and $\theta_2 = \pi \cdot V_{drive}/V_\pi$ is the phase shift induced by the drive voltage V_{drive} applied to the MZI. The optical intensity transmitted through the MZI is maintained at its maximum, which happens when the MZI filter is aligned with the accelerometer's FPC spectrum (i.e. $\theta_1 = \theta_2$). In order to detect the maximum condition, a dither voltage at about 10kHz is applied to the tuning terminal of the MZI. The MZI output optical intensity is therefore dithered at the same10kHz frequency, except when it reaches its maximum. A detection of this 10kHz signal with a lock-in amplifier produces an error signal that is used to correct the MZI tuning voltage in order to keep both spectra coincident. Since the spectral shift of the MZI varies linearly with its input voltage, the correction signal applied to the MZI varies linearly with mass displacement Δd once the feedback loop is locked. Therefore, this correction voltage V_{drive} under locked conditions is the output voltage proportional to sensed accelerations.

5.6.3 Measurements using coherence modulation

A static measurement for sensor design #O1 using the OECPU of figure 5.15 is shown in figure 5.17. It shows the linear behavior of the sensor system. The overall sensitivity of the demonstrated system is 1.8 V/g. The measurement range given by the maximum detectable phase-shift and thus depends on the detection principle. In the demonstrated sensor system it is about ± 10g for sensor#O1. In this range the displacement of the seismic mass versus acceleration is still very linear. In figure 5.18 we measured the response of the fiber-optic accelerometer to an acceleration step of 10mg. From this measurement performed with an approximately 1s integration time, an estimation of the residual noise shows that the resolution of sensor #O1 is about 500µg/√Hz for static acceleration fields.

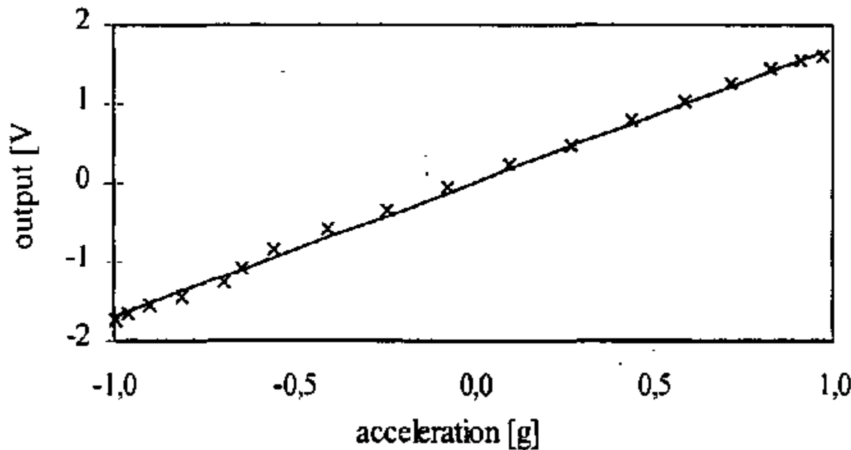

Figure 5.17: Output-voltage (V_{drive}) of a sensor with an optical cavity of 45µm (design #O1). The output is due to applied accelerations ranging from -g to +g. The measurement was done using the opto-electronic central processing unit (OECPU).

The sensor sensitivity due to accelerations perpendicular to the sensitive direction could not be observed with the used measurement set-up. We can conclude that experimental cross-sensitivities are lower than 1% of the main sensitivity. The measurement signal does not depend on the light intensity variations, because it is only based on the spectral shift of the light reflected from the seismic mass. Thus, no effects on the measurement signals could be observed due to bending or twisting of the fiber.

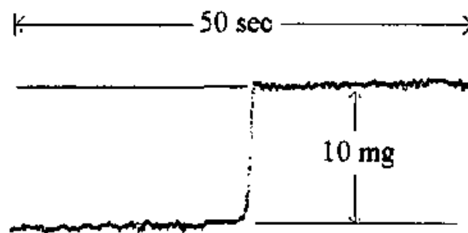

Figure 5.18: Response of the fiber-optic accelerometer to a static acceleration step of 10mg.

5.6.4 Multi-axial and multiplexed measurements

The measurement set-up for a 2D multiplexed accelerometer

The experimental setup for the 2D multiplexed device is shown in figure 5.19. It contains two accelerometers with FPC of 45µm and 135µm (x-FPC corresponding to Sensor #O3-1 and y-FPC to sensor #O3-2). Both reflected spectra are produced by the same optical source and mixed in the optical fiber. Their spectral shifts are then detected independently by two MZI fabricated on the same $LiNbO_3$ substrate (x-MZI for detection in x-direction and y-MZI for detection along y), but with optical delays of 270µm for the x-MZI and 90µm for the y-MZI. With such a configuration, the signal corresponding to the spectral shift of the x-FPC should be highly rejected through the y-MZI, which means that the output of the y-MZI gives only the information relative to the y-accelerometer.

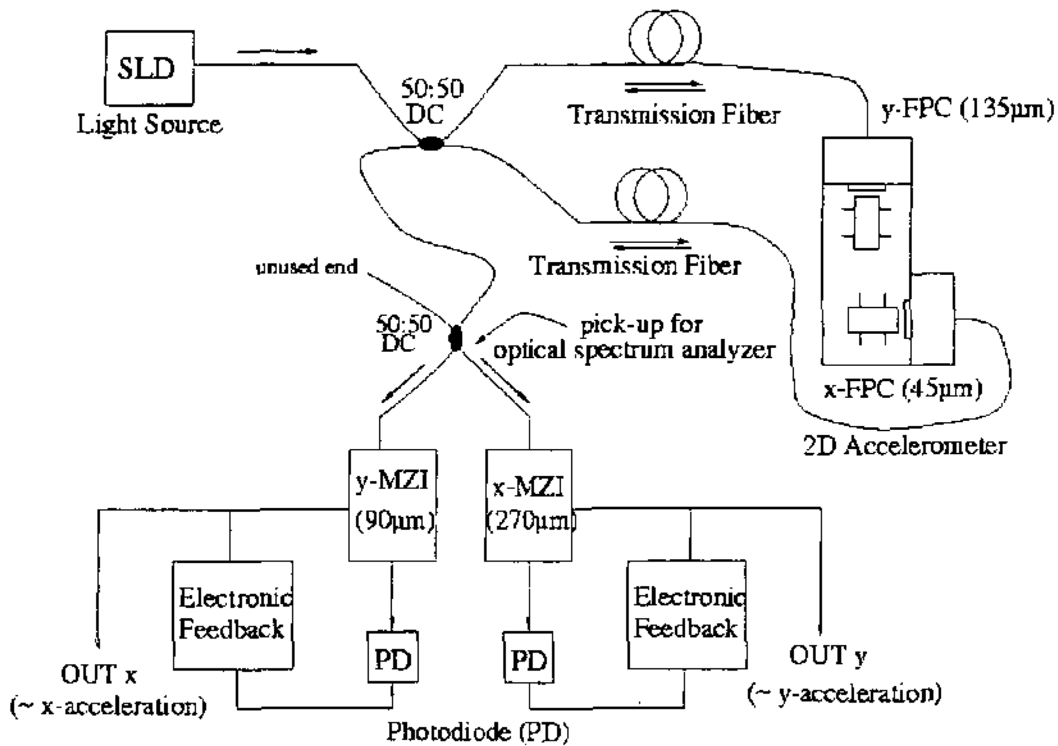

Fig. 5.19: Experimental setup for the 2D multiplexed detection of small seismic mass movements (x-FPC corresponds to sensor #O3-1 and y-FPC to sensor #O3-2).

When the MZI filter function coincides with the spectrum of the light reflected from the FPC, almost all reflected intensity can be transmitted whereas it is almost totally blocked when the MZI filter is spectrally shifted by half a period (see figure 5.20). For a movement Δd of the seismic mass, the total optical intensity transmitted through the MZI has a periodic variation with a period $\lambda/2$. When the spectral period of the detection filter (MZI) is different from the spectral period of the FPC spectrum, the intensity variations are much smaller. In that case, the transmitted intensity is never totally blocked or totally transmitted and its spectral integration does not vary a lot with the shift of the FPC spectrum.

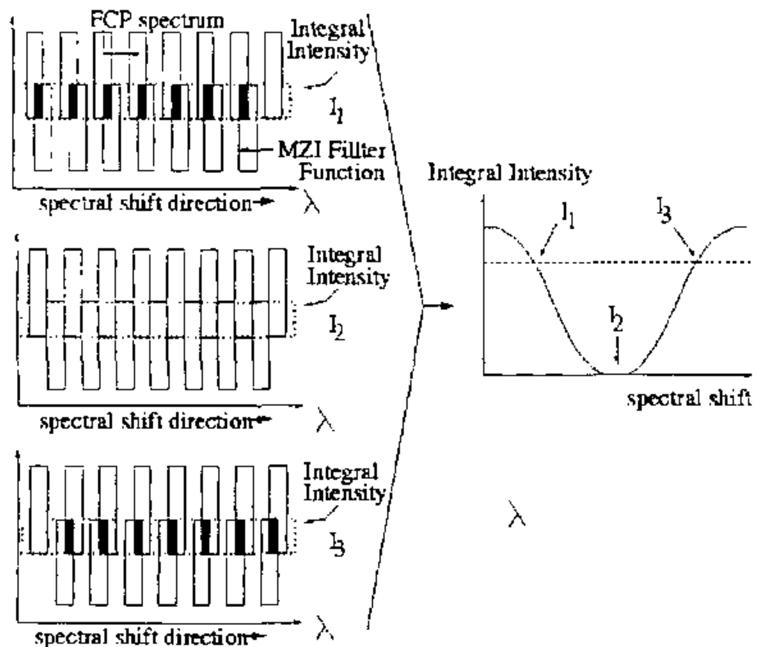

Fig. 5.20: Principle of the FPC spectral shift detection using an integrated optics MZI spectral filter : the spectral integration of the FPC spectrum through the "mask" provided by the MZI leads to a periodic output intensity variation versus spectral shift $\delta\lambda$.

2D multiplexed acceleration measurements

Multiplexed measurements have been performed with one sensor of the 2D chip (135µm FPC) and one uni-axial sensor (45µm FPC). The sensors have been rotated in the gravity field. The corresponding output signals are cosine functions of the rotation angle shifted by 90°. They are shown in figure 5.21. The corresponding sensor response curve versus acceleration is derived from the previous measurement and shows (see fig. 5.22) a linear behavior for both sensors between -g and +g.

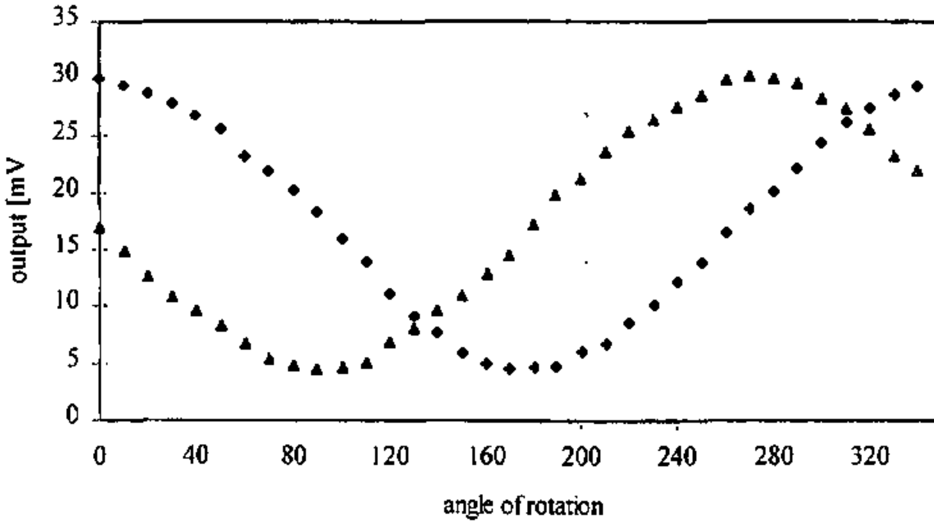

Fig 5.21: Experimental results for the two-dimensional acceleration sensing by rotating the sensors in the gravity field. Note : the output of the sensor with an optical gap of 135 µm (triangles) is multiplied by 2.5.

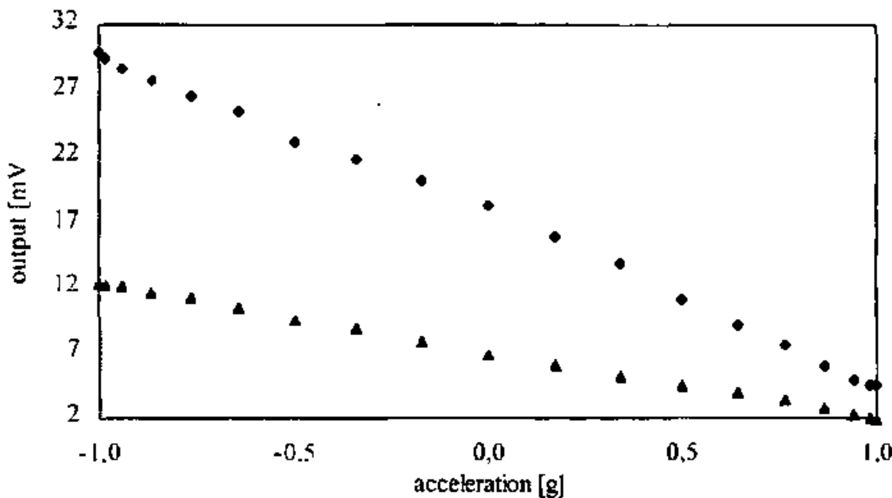

Fig. 5.22: Output-voltage of the multiplexed sensor system with optical cavities of 45µm (triangles) and 135µm (squares), for applied accelerations between -g and +g.

Attempts were made to estimate the cross-talk between both signals. For that purpose the sensors were uncoupled and the spectral shift of one sensor's output was measured while the other was rotated by 360° in the gravity field. No signal variations (phase shifts) could be detected with the resolution of these measurements. This gives us an upper limit of about 1% to the possible influence of cross-talk in the 2D multiplexing system.

5.7 Noise and optimized performance

After realization and characterization, now the limitations of the optical accelerometers concerning noise and performance are discussed.

5.7.1 Noise sources in the optical detection system

To derive an ultimate limit for the detection noise, we define the sensitivity S_{opt} of the optical transducer as :

$$S_{opt} = \Delta\varphi/a = 4\pi\,\lambda^{-1}\,S_y \qquad (5.18).$$

where $\Delta\varphi$ is the phase shift due to the acceleration a. The mechanical sensitivity S_y of the 2D accelerometer presented before is $S_y = \Delta y/a = 171$nm/g corresponding to $S_{opt} = 1.66$rad/g. The resolution limit is given by the Smallest Detectable Phase Shift (SDPS) $\Delta\varphi_{min}$. The above mentioned resolution of 500µg corresponds to a phase shift of 0.8mrad. Three main contributions to noise will be considered. Firstly, the employed laser diode is represented by a thermal source with a phase noise $\Delta\varphi_{th}$. Secondly, a shot noise $\Delta\varphi_{shot}$ is associated with the creation of a photocurrent in the photodiode. And thirdly, the electronic noise $\Delta\varphi_{elec}$ of the photodetector is taken into account. In all these cases, a white noise is assumed, although deviations from this assumption can be expected – due to flicker noise – at low frequencies. Following reference [Wen89], these noises, for a system comprising N sensors/accelerometers (N=1,2, or 3) are given by :

$$(\Delta\varphi_{th})^2 = 24\,X^2\,(1 + \tfrac{1}{2}X^{-2})^N\,\Delta f\,L_c\,c^{-1} \qquad (5.19)$$

$$(\Delta\varphi_{shot})^2 = 32\,N\,X^2\,(1 + X^{-1})^N\,\Delta f\,h\nu\,(\chi\,P_{diode}\,\eta)^{-1} \qquad (5.20)$$

$$(\Delta\varphi_{elec})^2 = 32\,N^2\,X^2\,(1 + X^{-1})^{2N}\,\Delta f\,NEP^2\,\chi^{-2}\,P_{diode}^{-2} \qquad (5.21).$$

$X = v^{-2}$ is a parameter related to the interference visibility (in our case the measured $X \approx 6.25$), the system intensity losses are described by χ=0.02. L_c is the coherence length (here 33µm) of the laser diode whose optical power is P_{diode} = 500µW. c is the velocity of light, and $h\nu$ the photon energy. The photodiode has a quantum efficiency η of 0.3, and a noise equivalent power NEP of 10^{-12} W/√Hz.

The total SDPS is related to these individual contributions by

$$\Delta\varphi_{min} = [\,(\Delta\varphi_{th})^2 + (\Delta\varphi_{shot})^2 + (\Delta\varphi_{elec})^2\,]^{1/2} \qquad (5.22).$$

Further, we have to consider how many sensors are multiplexed, in order to calculate the ultimate detection limit. In table 5.5, the different noise contributions and the resulting resolutions are summarized for a one and three axis accelerometer system. The mismatch between the theoretical and the experimental resolution a_{min} is mainly due to the addition of noise in the feedback loop.

SPDS $\Delta\varphi$, a_{min}	N = 1, X = 1.25	N = 1, X = 6.25	N = 3, X = 1.25
$\Delta\varphi_{min}$	3 µrad/√Hz	12.3 µrad/√Hz	13.4 µrad/√Hz
a_{min} (S_{opt} = 1.66rad/g)	1.8 µg/√Hz	7.4 µg/√Hz	8.1 µg/√Hz
a_{min} (S_{opt} = 9.7rad/g)	0.3 µg/√Hz	1.2 µg/√Hz	1.4 µg/√Hz

Table 5.5: Theoretical smallest detectable phase shifts $\Delta\varphi_{min}$ and accelerations a_{min}, for one and three sensors (N = 1 or 3), and for various coupling parameters X. S_{opt} = 1.66rad/g corresponds to a mechanical sensitivity S_y = 171nm/g and S_o = 9.7rad/g to S_y = 1µm/g.

5.7.2 Optimized performance and limitations of the optical accelerometers

Optimum coupling parameters

From equation (5.19 - 5.21) we can derive separately for each noise source optimum coupling parameters X_{opt}, which also depend on the number of multiplexed accelerometers N. The optimum coupling parameter for each noise contribution is given by [Wen89]:

$$X_{th}^2 = \begin{cases} 1, & N = 1,2,3 \\ (N-1)/2, & N \geq 3 \end{cases} \qquad (5.23)$$

$$X_{shot}^2 = \begin{cases} 1, & N \leq 4 \\ N/2-1, & N \geq 4 \end{cases} \qquad (5.24)$$

$$X_{elec}^2 = \begin{cases} 1, & N = 1.2 \\ N-1, & N \geq 2 \end{cases} \qquad (5.25).$$

Thus, for a 3D accelerometer system. we can find $X_{opt,N=3} = (1 + 1 + 2)/3 \approx 1.3$.

Optimized measurement range

The measurement range of the optical transducer is given by the maximum detectable phase-shift $\Delta\varphi_{max}$. Experimentally, the optical phase was tracked over a range of 7π radians [Por96]. This range is related to the half-wave voltage of the MZIs and is wider for a lower half-wave voltage. In systems using lower half-wave voltages [Duc84], a maximum detectable phase-shift $\Delta\varphi_{max}$ of 25π radians has been demonstrated and calculations show that 50π radians could be feasible [Por96]. With formula 5.18 and a mechanical sensitivity between 0.1µm/g and 1µm/g (corresponding to an optical sensitivity of 1rad/g - 10rad/g) we can derive a maximum acceleration measurement range between ±80g and ±8g.

Bandwidth and reflection coefficients

The feedback loop bandwidth of the realized system was limited to about 10Hz. The circuit design of the electronic system could be improved in order to reduce the detection noise and to increase the bandwidth.

The performance of the sensor system can be improved in different ways. The reflection coefficients of both, the fiber and the seismic mass, can be increased by deposition of suitable coatings (see figure 5.22). The optimized reflection coefficients would be 50% for the fiber's endface and 100% for the silicon seismic mass.

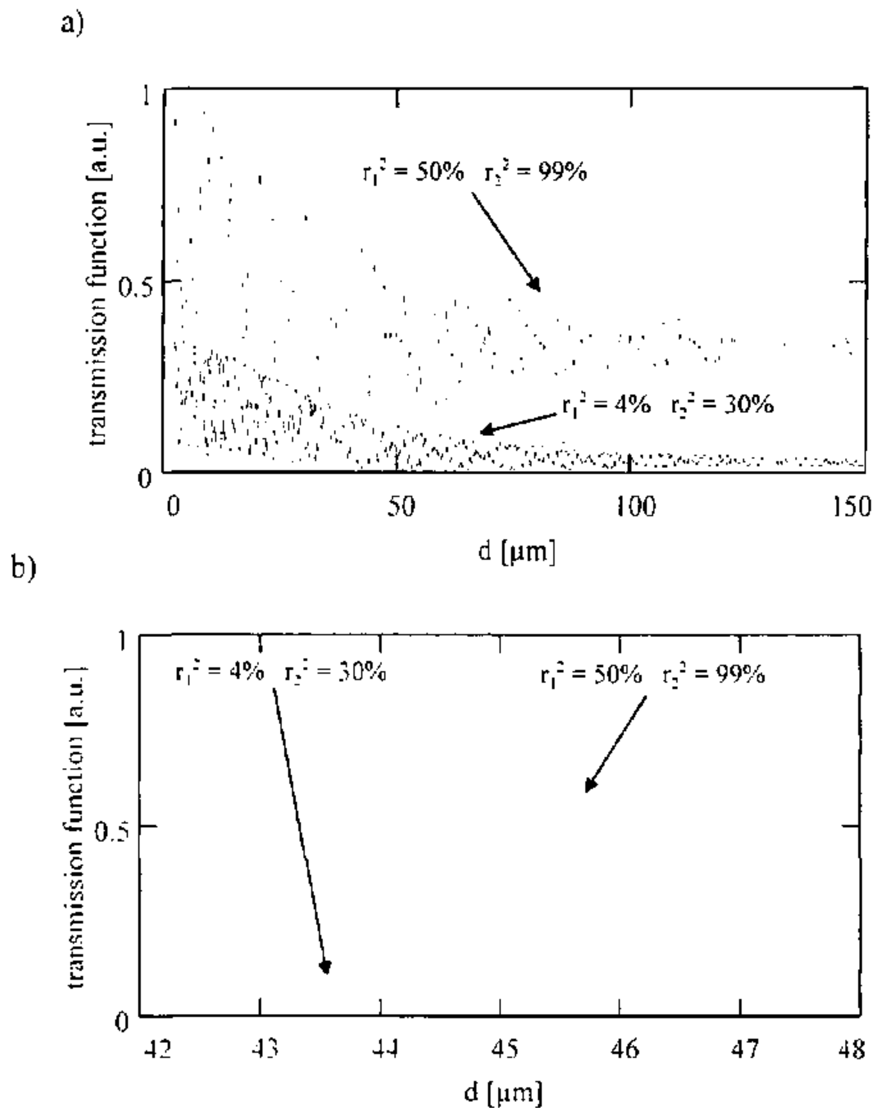

Figure 5.22: Optical transmission function for the Fabry-Perot cavity as a function of the fiber-to-silicon distance d. Parameter d equals half the optical path difference. Two different sets of reflections coefficients are assumed: $r_1^2 = 4\%$, $r_2^2 = 30\%$ corresponding to the realized device, and $r_1^2 = 50\%$, $r_2^2 = 99\%$ corresponding to an optimized configuration.

Benefits

The demonstrated fiber-optic accelerometer system is completely passive at the measurement site. The system features the corresponding advantages, like immunity to electromagnetic interference and possible operation in hazardous environments. The measurement signal does not depend on light intensity variations, because it is only based on the spectral shift of the light reflected from the seismic mass. In addition, this detection technique allows to multiplex two (or three) accelerometer signals to one single fiber. Such an optical 2D/3D sensor system does not require any power supply at the measurement site.

Fabrication and commercial issues

The fabrication of the sensor is simple, because no active optical alignment between the fiber and the silicon seismic mass is necessary. However, assembly is done device by device, with no advantage of a wafer batch process. But, due to the large alignment tolerances, an automated assembling procedure is feasible. To reduce costs, the integrated Mach-Zehnder interferometers, which are used in the remote opto-electrical read-out unit, and which are fabricated in $Ti:LiNbO_3$, could be replaced by silicon based devices.

Recently the British company BOOKHAM has released an active silicon integrated optical circuit for sensing applications, mainly pressure sensing [Boo97]. This integrated optical detection circuit is devoted to the read-out of Fabry-Perot sensors and uses path imbalanced Mach-Zehnder interferometers to interrogate fiber-optic sensors. Thus, this circuit could also replace our optoelectronic detection unit. However, low cost of few US-dollars, as demanded for airbag-accelerometers, cannot be achieved with such an optical system.

Comparison with other optical accelerometers

Torben Storgaard-Larsen [Sto95] proposed in his Ph.D.-thesis a 3D accelerometer system micromachined in (110) silicon with stress sensitive Bragg-gratings as a detection mechanism. But he only realized an uni-axial device. To the best knowledge of the author no other multi-axial optical accelerometers have been presented. Of course, many optical devices for single-axis acceleration measurement have been presented [Abb95, Bur92, Chn97, Deg98, Lis94, Mar95, Pei98, Sto96, Utt92], but only few of them were able to detect accelerations in the sub-mg domain [Lis94, Pei98, Utt92].

5.8 Conclusion of chapter 5

Principles

Among various concepts for fiber optic accelerometers one was chosen, which seems to be very promising regarding sensor performance and fabrication complexity. In addition, the design uses the earlier presented technique of (100) silicon underetching. In order to measure the displacement of a seismic mass due to acceleration, an optical fiber was integrated into a micro-mechanical structure. The vertical surfaces of the seismic mass and the optical fiber form a low-finesse Fabry-Perot cavity (FPC). This cavity functions as a two beam interferometer with an optical path difference equal to twice the fiber-to-mass distance. If a broadband light is sent through the optical fiber, the spectrum of the light reflected by the FPC through the fiber is modulated by the FPC spectral response. Any movement of the mass changes the FPC optical path, and leads to a wavelength shift proportional to acceleration. We control the Fabry-Perot accelerometer on the measurement site with a second interferometer in the detection unit by regulating the phase difference between them. The measurement technique is based on so called coherence modulation and allows the multiplexing of the three sensor outputs.

Modeling

An analytical model of the opto-mechanical accelerometer is presented. The modelization was divided into three parts: micro-mechanical seismic mass structure, optical transmission function of the Fabry-Perot cavity, and theoretical description related to coherence modulation and multiplexing. The mechanical model gives the displacement of the seismic mass mirror as a function of applied acceleration. The optical transmission function describes the shift of the optical reflection spectrum due to the seismic mass displacement. The reflected light is simulated by two beams which are superimposed. Finally, the modelisation of the detection mechanism explains analytically how we can retrieve the information coded in the spectrum shift with the help of a receiver interferometer. It also describes the multiplexing of several accelerometers.

Fabrication

1D and 2D optical accelerometer systems have been fabricated. One sensor consists of a seismic mass with an attached silicon-fiber sandwich. With this technique no active optical alignment between the fiber and the silicon seismic mass is necessary. However, the optical cavity can be defined precisely with an accuracy of typically ± 1 μm. In order to permit multiplexing with a broadband source the accelerometer was adapted to the receiver interferometers. FPCs of 45μm and 135μm have been realized. For the third detection axis, the FPC should be 90μm.

Experimental characterization

The characterization started with the experimental investigation of an opto-mechanical accelerometer sensitive in only one direction. The measured sensitivity of the device agree well with the developed model, and it appears that the fabrication method allows to control the sensor sensitivity within a few percent. Measurement results are reported and show for devices with a mechanical sensitivity of 143nm/g a resolution of 500μg and a ± 10g dynamic range. This corresponds, for a device with a higher mechanical sensitivity of 1μm/g, to a resolution of 70μg in measurement range of ± 1.5g. Cross-sensitivities are lower than 1% of the main sensitivity.

In addition, a 2D accelerometer was demonstrated using one optical fiber link and two suspended micromachined silicon seismic masses, which are sensitive in the directions parallel to the substrate plane. The detection method based on coherence modulation allows the multiplexing of the two sensor signals, and hence remote 2D acceleration sensing through one optical fiber link. There is no electrical link between the measurement region and the signal output. Performance are equivalent to the uni-axial accelerometer and cross-talk due to multiplexing is lower than 1% of the main sensitivity.
To the best knowledge of the author no other realized multi-axial optical accelerometers have been presented up to now.

Noise and optimized performance
To calculate the ultimate optical noise floor, three main contributions have been considered. Firstly, the employed laser diode is represented by a thermal source. Secondly, a shot noise is associated with the creation of a photocurrent in the photodiode. And thirdly, the electronic noise of the photodetector is taken into account. The theoretical noise depends on the number of multiplexed accelerometers and can be estimated to be in the vicinity of 1 μg.
The realized devices can be optimized for different parameters, e.g. optical coupling parameter and measurement range. Also, the circuit design of the electronic system could be improved in order to reduce the detection noise and to increase the bandwidth.

Discussion
The realized accelerometer system provides all the typical advantages of optical measurement, i.e. immunity to electromagnetic interference, no power supply at the measurement site etc. In addition, coherence modulation has some advantages which are specially interesting for the application of sensor with remote read-out. Firstly, the information coded in the optical path difference can be retrieved by local demodulation. The interferometer in the detection unit can control the total interferometric phase. This opens the way to several different demodulation principles. Secondly, these demodulation principles allow to cancel out some possible influences on the transmitted light during the propagation in the optical connection fibers. In fact, the light intensity and polarization could be altered during transmission. However, the mutual phase shift remains unchanged. Thirdly, the proposed technique of coherence modulation allows to multiplex several sensors and to realize in this way a 3D accelerometer system. The interrogation of three sensors with one detection and transmission system can simplify the installation and reduce the costs.

CHAPTER 6

6. Conclusions and further work

6.1 Comparison between the capacitive and optical accelerometers

6.2 Suggestions for further work

6.3 General conclusions

6. Conclusions and further work

6.1 Comparison between the capacitive and optical accelerometers

In order to compare the presented multi-axial capacitive and optical accelerometers, a mechanical sensitivity for the lateral seismic mass of 1µm/g is assumed for both devices. This corresponds to a first resonance frequency of approximately 500Hz. Therefore, from the sensor side, we are limiting the bandwidth to about 150 Hz. In table 6.1 four different cases are compared. Firstly, an optical accelerometer (OA1) which corresponds to the fabricated and measured device but adapted to a mechanical sensitivity of 1µm/g. Secondly, device (OA2) is constructed by assuming that the theoretical noise limits are reached, with a maximum detectable phase-shift $\Delta\varphi_{max}$ of 25π radians. Thirdly, a fabricated and tested capacitive accelerometer is considered and entitled CA1. Finally, an optimized capacitive accelerometer (CA2) is assumed with optimized parameters (1µm gap, sensitivity dC/dy = 8pF/g, etc.), and the feasible noise floor for such a device using an integrated read-out circuit (1aF/√Hz).

Sensor parameter	**Optical accelerometer OA1 (realized/tested)**	**Optical accelerometer OA2 (optimized)**	**Capacitive accelerometer CA1 (realized/tested)**	**Capacitive accelerometer CA2 (optimized)**
Measurement range	± 1.5g *	± 5g	± (0.8 - 2) g	± 7g
Resolution a_{min}	85 µg/√Hz *	(0.3 -1.4) µg/√Hz**	(40-160) µg/√Hz***	0.2 µg/√Hz
a_{min} / a_{therm}	425	1.5 - 7	500	1
Dynamic range	43dB	72dB	43dB	75dB
Cross-sensitivity	< 1%	< 1%	< 1%****	< 1%

* derived from measurements **depending on number of multiplexed sensors N=1.2 or 3
*** using capacitance meter Fogale MC900 ****only when employing differential sensing

Table 6.1: Comparison between fabricated transducers and optimized transducers. For all devices a mechanical sensitivity of 1 µm/g is assumed.

The comparison in table 6.1 demonstrates that with both sensors, acceleration in the range of 100µg can be detected. However, by dividing the experimental achieved resolution a_{min} by the limit given due to thermal-mechanical noise a_{therm}, one can see the potential that can be still exploited in optimizing both accelerometers leading to a high resolution in the sub-µg range. Basically, both acceleration sensors show similar performance regarding resolution, measurement range and cross-sensitivities. This conclusion differs significantly from other studies [Gar95], where interferometeric methods are often pointed out as the most sensitive techniques. The reason for this discrepancy lies in the difficulty to compare different transducer techniques in a general way. Our test case is a device with a quite large electrode surface, which enables to obtain a large capacitance. Such a large surface allows improving the capacitive detection method, without any advantage for the case of optical detection. In addition, the recent achievements on the design and technology of capacitive measurement

circuits allow to measure small capacitive changes, down to the aF-range. In the case of very small devices, the optical detection, which does not require an object with a large area, would have given a better sensitivity (in accordance with the case studied in reference [Gar95]).
Long- and short-term stability are sometimes more important than the sensor parameters compared in table 6.1. However, stability is often related to technological processes and not to measurement principles, therefore this feature is difficult to predict and to compare globally.
The demonstrated fiber-optic accelerometer system is completely passive at the measurement site. The system features the corresponding advantages, like immunity to electromagnetic interference and possible operation in hazardous environments. The measurement signal does not depend on light intensity variations, because it is only based on the spectral shift of the light reflected from the seismic mass. In addition, this detection technique allows to multiplex two (or three) accelerometer signals to one single fiber. Such an optical 2D/3D sensor system does not require any power supply at the measurement site. The fabrication of the sensor is simple, because no active optical alignment between the fiber and the silicon seismic mass is necessary. However, assembly is done device by device, taking not advantage of a low cost batch process.
One important advantage of the capacitive transducers is its double function of sensor and actuator. Operating as an actuator by applying an electrostatic force to the electrodes, offers the advantage of closed loop operation, electrostatic damping and stiffness adjustment. Furthermore, a low power operation and a wide temperature range are characteristics of most electrostatic sensors. Different from most capacitive accelerometers, the change in capacitance for the lateral device is linear versus acceleration. Concerning fabrication, the capacitive device offers the advantage of a full batch process (meaning possible low cost). However, the cost reduction is limited by the critical fabrication steps of electrode alignment and small gap etching.
For an optimized accelerometer system, both methods give nearly the same performance in terms of measurement range and resolution. Both techniques have a potential high sensitivity (down to the μg), low transverse sensitivities, a high dynamic range, and can be used to build a 3D accelerometer system. No technique results in fundamentally better performance. Therefore, the choice between each detection method will depend on other factors, such as cost and application requirements. The benefits and drawbacks of both methods are summarized in table 6.2.

	Optical accelerometer	Capacitive accelerometer
Benefits:	• passive, inherently immune to EMI • operates in hazardous environments • remote read-out • simple fabrication process (no active alignment) • multiplex capability (one source for 1..N sensors) • high potential resolution	• capacitors can operate as sensors and actuators : closed loop operation, electrostatical damping, stiffness adjustment • low consumption • batch process (low cost possible) • high potential resolution
Drawbacks:	• costly (laser diode, optical coupler) • no batch process (device by device assembling) • difficult to integrate	• critical fabrication steps (small gap required, alignment of electrodes)

Table 6.2: Key factors (advantages and disadvantages) for the two presented transducers.

6.2 Suggestions for further work

Some suggestions for further work are not difficult and time consuming to realize. Other one are more labor intensive and can probably only be done in frame of a student or Ph.D. project.

Micromachining using underetching of {100} silican planes

Simulations concerning the effects of mask misalignment and wafer intrinsic crystal misorientation have been performed. An experimental verification of misalignment could be undertaken with help of beam-like structures slightly rotated on the mask in a range of ±2°.
To control the width of the vertical suspension beam, test structures have been implemented. This could also be implemented for the horizontally located beams that are fabricated by maskless etching.

Multi-axial capacitive accelerometers

First performance results of the capacitive sensors have been presented. Sensitivity and resonance frequencies have been measured. More investigation concerning the linearity have to be done. The dynamic behavior, and thus damping, can further be investigated by using the briefly mentioned method of impulse detection and subsequent Fourier transformation of the signal. For application in measurement systems, the sensors must be also studied, for example, regarding long and short term stability, temperature and offset drift. The silver glue used for wiring is certainly not the best choice regarding good stability and aging. It should be substituted by ultrasonic or other wire bonding techniques.
The developed HDL-A models support the global simulation of the capacitive accelerometer and the application specific read-out circuit using sigma-delta modulation is to be performed. Closed-loop operation and electrostatic damping could be investigated for both, in- and out-of-plane devices. Finally, once the integrated circuit is realized, measurements of the microsystem have to be done, opening the way for redesign of sensor and electronic.

Multi-axial optical accelerometers

For the optical accelerometer further experimental characterizations, as proposed similarly for the capacitive sensor (stability, dynamic behavior, etc.), should he made. In addition, to reduce cost, the integrated Mach-Zehnder interferometers, which are used in the remote opto-electrical read-out unit and that are fabricated in Ti:$LiNbO_3$, could be replaced by silicon based devices.
Apart from the presented accelerometer, the developed opto-mechanical techniques could be used in other microsystems. The frequency of a laser diode can be influenced by a mirror mounted in opposite of its backside. An electrostatic actuator replacing the mirror can be employed to tune the laser diode [Bro98]. A similar configuration could also be used as actuator, but as displacement sensor, e.g. an accelerometer's seismic mass movement.

6.3 General conclusions

In January 1996, this thesis started by searching new possibilities regarding detection principles and fabrication methods of accelerometers. In frame of the PICS project a navigation system based on inertial sensor should be studied. Accelerations well under 10^{-3}g should be measured, if possible along three axes.

The proposed mechanical design consists of a monolithic chip containing three individual seismic masses, each sensitive in only one direction. Different designs have been discussed that are sensitive to accelerations regarding the in- or out-of-plane directions. In order to transfer these designs in working acceleration sensors, unconventional microfabrication methods based on standard anisotropic etching of (100) silicon have been developed. The feasibility of the etching technique has been demonstrated on several micromechanical seismic mass systems, and also on other microelectromechanical or optical devices. Simulation of the etching process has been performed to investigate the influences on the fabricated structures due to the inaccuracy of the etching. In designing the accelerometer structure, compromises have to be found considering sensitivity, etching accuracy, cross-sensitivities and resonance frequencies.
In order to achieve high resolution, two detection principles, optical and capacitive sensing, have been studied and implemented into multi-axial accelerometers. Their general advantages and disadvantages have been summarized in table 6.2. Each accelerometer type was analytically modeled and numerically simulated bringing the mechanical and the transducer principle together. Global accelerometer modeling opens the way to simulate the complete microsystem containing an accelerometer chip and an integrated read-out electronic. Emphasis was put in the development of fabrication processes using, in case of the optical accelerometers, piece by piece assembling, and in case of the capactive accelerometers, a batch process of complete wafers.
Finally, both developed accelerometer types have been characterized and are compared above. In conclusion, the accelerometer models have been confirmed and the feasibility of the developed fabrication sequences has been proven. Accelerations up to 40μg could have been measured with, in a typical measurement range of ±1g. However, improvements up to resolution under 1μg are possible.

In this thesis all aspects of accelerometer development are considered such as design, modeling, fabrication and characterization. However, three years are not enough to investigate all these aspects in detail. Thus suggestions for work, which could not have been done due to the limited time, have been made in the previous section.

7. Summary

This thesis describes the research work towards some new possibilities in silicon wet etching and their application to the design and fabrication of accelerometers with capacitive and optical read-out. The general principle of accelerometers is the measurement of the displacement of a seismic mass due to inertial force. In chapter 1 a general introduction into accelerometers and microfabrication technologies is given. Existing multi-axial accelerometers are briefly reviewed. Up to now, resolutions below 100µg/√Hz, cross-sensitivities lower than 1% for a measurement ranges between ±1g and ±10g have not been achieved in 3D monolithic accelerometer microsystems.

Design and modeling of new accelerometer structures

Chapter 2 presents nine different mechanical designs for accelerometers, so called seismic mass systems. Four of them are devoted acceleration measurements parallel to the waferplane and three to measure accelerations that are perpendicular to the waferplane. Combining two lateral accelerometers and one vertically sensitive accelerometer in one substrate offers the three-dimensional measurement of accelerations with one monolithic chip. Due to the highly symmetrical suspension with high-aspect ratio beams the movements of the masses are purely translational and mechanical cross-sensitivities are very small (<0.1%). Alternatively, two designs are presented for measuring accelerations in- as well as out-of-waferplane, opening the way to a 3D accelerometer consisting of one single seismic mass. However, this possibility leads to higher mechanical cross-sensitivities.
The analytical modeling of these structures is based on a second order spring-mass-system. Explicit formulae for the spring stiffness allows to calculate the mechanical sensitivity of these designs. The damping for the in-plane structures is caused mainly by lateral film damping, while for the out-of-plane structures the dominant damping type is squeeze film damping. Finally, the mechanical transfer function describing the dynamical behavior is given. The analytical model is very suitable to describe the mechanical response of the accelerometer structures for small displacements. However, to calculate effects such as nonlinearity due to large displacements (displacement > beam width), mechanical cross-sensitivities, higher resonance modes or more complicated shaped beams, finite element simulations (FEM) are preferable. Using ANSYS the static and dynamic behavior of the proposed designs is computed. In general, considering small displacements, predictions from the FEM analysis and from the analytical model agree within 10%. In addition, static measurements with an external optical comparator have been performed to confirm the theoretical calculation. Here, analytical and experimental results agree well for small dispalcements. However, nonlinear displacements due to higher forces are overestimated by ANSYS.
Comparing the different mechanical designs, we have to find a tradeoff between cross-sensitivities, chip size, variation of sensitivity due to fabrication tolerances and linearity. Designs offering longer instead of thinner beams seem to be the best choice to improve the main sensitivity. As one fundamental aspect in designing accelerometers, one has to consider that mechanical sensitvity and first resonance frequency are related. Limiting the first resonance frequency to 500Hz to operate in a bandwidth of at least 100Hz, we can increase the mechanical sensitivity up to 1µm/g.

Finally, investigating the level of thermal-mechanical noise, one can derive that for bulk-micromachined accelerometers the detection limit is not determined by mechanical-thermal noise, but by the read-out mechanism. Therefore, bulk-micromaching of silicon is very suitable to obtain accelerometers with resolutions in the μg-range and even below.

Unconventional bulk-micromachining using underetching of (100) silicon

A non conventional fabrication method using the underetching of {100} silicon planes was demonstrated. With the help of this silicon bulk-micromachining process on a (100) wafer the fabrication of thin vertical beams with flat sidewalls is possible. The seismic mass and the suspending beams were fabricated within the same etching step. The fabricated structures offer aspect ratios (beam thickness over beam width) up to 35. The directions of undercutting as well as design rules for the mask layout were determined. The in-plane structures are highly symmetrical, thus having very low mechanical cross-axis sensitivities. The unconventional fabrication method is fairly simple and allows one to build a two-axis accelerometer-system in a single etching, by simultaneously building two sensor elements rotated by 90° with respect to each other. Moreover, the 90° angle is precisely defined by the intrinsic crystal orientation.
The accuracy of the etching depends on the initial crystal orientation in the silicon wafer and on the alignment at lithography. From the simulations of the anisotropic etching we can conclude that the simple technique of underetching vertical {100] planes can be employed to micromachine mechanical devices within a reproducibility in the order of a few percent if precautions are taken. The important points are: firstly, an adapted design, and secondly, a pre-etching to reveal the crystal orientation.
For the third direction, another accelerometer sensing vertical accelerations can be included, resulting in a three-dimensional monolithic accelerometer system, with intrinsic alignment due to the perpendicular {100} crystal planes. This third device is micromachined by a technique called maskless etching. For this structure the suspension beams are horizontally located and can be aligned parallel or in an angle of 45° to the wafer flat.
We can summarize that the fabrication of a monolithic system has been successfully demonstrated comprising three seismic masses sensitive in three different directions. The advantages of the described process are the simplicity of the two step etching, the almost perfect orientation of the devices along the <100> directions of the silicon crystal, and the symmetrical suspension of the masses, resulting in low cross-sensitivities. The structures exhibit the excellent material qualities of single crystal silicon, such as good long term stability, no hysteresis, etc. No stress is induced into the suspension beams due to doping. The occurrence of large undercutting is, of course, a disadvantage of using (100)-oriented wafers not experienced with, e.g. (110)-oriented wafers. However, two perpendicular devices cannot be made on (110) wafers.
All the designs presented in chapter 2 for in- and out-of-plane accelerometers can be fabricated by the proposed micromachining technique. Of course, this technique is not limited to accelerometers. Other silicon devices, such as optical mirrors, gyroscopes or more complex suspension structures can also be realized using this etching method.

Multi-axial capacitive accelerometers

Chapter 4 presents the design, modelisation and simulation, fabrication and finally the experimental characterization of silicon capacitive sensors suitable for multi-axis acceleration measurements.

Basically, two different sensor types are contained in one monolithic system. Firstly, two devices which detect in-plane accelerations due to the change in the overlapping electrode surfaces. Secondly, a seismic mass, which is sensitive to out-of-plane accelerations, by measuring the distance between mass and fixed counter electrodes. For both sensing principles differential read-out can be applied in order to reduce cross-axis sensitivities and other disturbing effects, e.g. influence of temperature.
In the case of the out-of-plane or vertical accelerometer, a simplified field assumption leads to a satisfying accelerometer model. For the in-plane designs, two different types of electrode configurations are proposed. Comb shaped electrodes structured in sputtered metallic thin film or comb shaped electrodes etched vertically into the silicon seismic mass. In any case electrostatic fringe fields are to be considered and thus adapted analytical models have been developed. Simulations using finite element analysis have also been performed in order to estimate the capacitive change due to a mechanical displacement of the seismic mass. Finally, the capacitive sensitivity and thus the response of the lateral accelerometers can be well described. Analytical and FEM calculations are compared. In conclusion, the analytical formula describes well the capacitive change due to mechanical displacements. This gives access to exact modeling of the transducer, and offers the possibility to investigate easily a large range of parameters in order to find, with consideration of technological aspects, the best geometries regarding capacitive sensitivity and linearity.
Using the developed models, the electrostatic forces due to an applied voltage have been calculated to demonstrate the feasibility of an electrostatic servo accelerometer employing force feedback. In addition to analytical and finite element modelisation, a global model written in a hardware description language has been developed. This global simulation combines not only mechanical and electrostatic models, but also allows the simulation of the complete microsystem including read-out electronics.
For the realization of the electrodes of the in-plane accelerometers two different silicon process have been developed and are described in detail. One process for the fabrication of a capacitive accelerometer employs thin-film electrodes structured into a sputtered nickel or chromium film. A silicon oxide layer, needed to isolate metal electrodes and silicon seismic mass can produce undesired charges and makes also the used press-on contacts difficult to realize. Therefore, a second process has been developed for the realization of electrodes etched into the silicon seismic mass. The counter electrodes are contained on Pyrex glass wafers. For the structuring of these glass wafers processes have been developed. Joining silicon and glass wafers is performed by anodic bonding. In order to align silicon and glass wafers with a high accuracy, a bonding equipment consisting of alignment module, cassette and substrate bonding module has been employed. Finally, the silicon-glass chips are separated by sawing, then mounted and connected.
In order to detect small capacitive changes in the order of a view pF and below, three types of measurement methods are considered: capacitive AC bridge, charge/discharge and also sigma delta modulation. The last one is devoted to be used in an application specific integrated circuit adapted to the realized 3D capacitive accelerometer. Typical advantages of such a micromechanical sigma delta modulator are the high linearity and the digital output. Sensor specifications are a zero capacitance of 20pF, a capacitive sensitivity of more than 1pF/g, and a measurement range of $\pm 2g$. General investigation of the detection noise shows that for all measurement circuits a capacitive resolution of $1aF/\sqrt{Hz}$ can be achieved for the read-out of the realized bulk-micromachined accelerometer. This opens the way for a two-chip solution accelerometer system for three-dimensional acceleration measurement with a resolution in the µg-range.
Finally, the fabricated 3D silicon capacitive accelerometer was tested. Static accelerations have been applied by rotating the sensors in the gravity field. The dynamic response was

measured by using the vibrating coil of a loudspeaker and a network analyzer. Average zero capacitances for in- and out-of plane accelerometers are between 18pF and 19pF with sensitivities ranging from 0.5pF/g to 4pF/g depending on the mechanical design. Deviation from linearity are around 1%. First resonance occurs around 500Hz. Using a commercial capacitance meter, resolutions up to 40μg/√Hz can be obtained. In conclusion, the measured accelerometer performance is close to the theoretical estimations expressed in the specifications. The resolution is expected to be improved by using an integrated read-out circuit placed close to the accelerometer chip.

Multi-axial optical accelerometers

Among various concepts for fiber optic accelerometers one was chosen, which seems to be very promising regarding sensor performance and fabrication complexity. In addition, the design uses the earlier presented technique of (100) silicon underetching. In order to measure the displacement of a seismic mass due to acceleration, an optical fiber was integrated into a micro-mechanical structure. The vertical surfaces of the seismic mass and the optical fiber form a low-finesse Fabry-Perot cavity (FPC). This cavity works as a two beam interferometer with an optical path difference equal to twice the fiber-to-mass distance. If a broadband light is sent through the optical fiber, the spectrum of the light reflected by the FPC through the fiber is modulated by the FPC spectral response. Any movement of the mass changes the FPC optical path, and leads to a wavelength shift proportional to acceleration. We control the Fabry-Perot accelerometer on the measurement site with a second interferometer in the detection unit by regulating the phase difference between them. The measurement technique is based on the so called "coherence modulation" and allows the multiplexing of the three sensor outputs.
An analytical model of the opto-mechanical accelerometer is presented. The modelization was divided into three parts: micro-mechanical seismic mass structure, optical transmission function of the Fabry-Perot cavity, and theoretical description related to coherence modulation and multiplexing. The mechanical model gives the displacement of the seismic mass mirror as a function of applied acceleration. The optical transmission function describes the shift of the optical reflection spectrum due to the seismic mass displacement. The reflected light is simulated by two beams which are superimposed. Finally, the modelization of the detection mechanism explains analytically how we can retrieve the spectrum shift coded information with the help of a receiver interferometer. It also describes the multiplexing of several accelerometers.
1D and 2D optical accelerometer systems have been fabricated. One sensor consists of a seismic mass with an attached silicon-fiber sandwich. With this technique no active optical alignment between the fiber and the silicon seismic mass is necessary. However, the optical cavity can be defined precisely with an accuracy of typically ± 1μm. In order to permit multiplexing with a broadband source the accelerometer was adapted to the receiver interferometers. FPCs of 45μm and 135μm lengths have been realized. For the third detection axis, the FPC length should be 90μm.
The characterization started with the experimental investigation of an opto-mechanical accelerometer sensitive in only one direction. The measured sensitivity of the device agree well with the developed model, and it appears that the fabrication method allows to control the sensor sensitivity within a few percent. Measurement results are reported, and show for devices with a mechanical sensitivity of 143nm/g a resolution of 500μg and a ± 10g dynamic range. This corresponds, for a device with a higher mechanical sensitivity of 1μm/g, to a

resolution of 70μg in a measurement range of ± 1.5g. Cross-sensitivities are lower than 1% of the main sensitivity.
Additionally, a 2D accelerometer was demonstrated using one optical fiber link and two suspended micromachined silicon seismic masses, which are sensitive in the directions parallel to the substrate plane. The detection method based on coherence modulation allows the multiplexing of the two sensor signals, and hence remote 2D acceleration sensing through one optical fiber link. There is no electrical link between the measurement region and the signal output. Performance are equivalent to the uni-axial accelerometer and cross-talk due to multiplexing is lower than 1% of the main sensitivity. To the best knowledge of the author no other realized multi-axial optical accelerometers have been presented up to now.
To calculate the ultimate optical noise floor, three main contributions have been considered. Firstly, the employed laser diode is represented by a thermal source. Secondly, a shot noise is associated with the creation of a photocurrent in the photodiode. And thirdly, the electronic noise of the photodetector is taken into account. The theoretical noise depends on the number of multiplexed accelerometers and can be estimated to be in the vicinity of 1μg.
The fabricated devices can be optimized for different parameters, e.g. optical coupling parameter and measurement range. Also, the circuit design of the electronic system could be improved in order to reduce the detection noise and to increase the bandwidth.
The realized optical accelerometer system provides all the typical advantages of optical measurement, i.e. immunity to electromagnetic interference, no power supply at the measurement site, etc. In addition, coherence modulation has some advantages which are specially interesting for the application of sensor with remote read-out. Firstly, the information coded in the optical path difference can be retrieved by local demodulation. The interferometer in the detection unit can control the total interferometric phase. This opens the way to several different demodulation principles. Secondly, these demodulation principles allow to cancel out some possible influences on the transmitted light during the propagation in the optical connection fibers. In fact, the light intensity and polarization could be altered during transmission. However, the mutual phase shift remains unchanged. Thirdly, the proposed technique of coherence modulation allows to multiplex several sensors and to realize in this way a 3D accelerometer system. The interrogation of three sensors with one detection and transmission system can simplify the installation and reduce the costs.

Conclusions

In this thesis all aspects of accelerometer development are considered such as design, modeling, fabrication and characterization. A comparison of the realized capacitive and optical accelerometer demonstrates that with both sensors acceleration in the range of 100μg can be detected. However, there is still a potential that can be exploited in optimizing both accelerometers leading to a high resolution in the sub-μg range. Since no technique results in fundamentally better performance, the choice between each detection method will depend on other factors, such as cost and application requirements.

8. Résumé

Cette thèse décrit une étude sur de nouvelles possibilités de micro-usinage de volume du silicium et leurs applications aux accéléromètres multi-axiaux avec lecture capacitive et optique. Le principe physique général des capteurs d'accélération est de mesurer le déplacement d'une masse sismique provoqué par la force inertielle. Le premier chapitre donne une introduction générale sur les accéléromètres et les technologies de micro-usinage. Les accéléromètres multi-axiaux existants sont brièvement résumés. Jusqu'à maintenant des résolutions, inférieures à 100µg/√Hz, et des sensibilités transverses, bien en dessous de 1% pour une gamme de mesure entre ±1g et ±10g, n'ont pas encore été obtenues par des accéléromètres 3D monolithiques.

Conception et modélisation des nouvelles structures accéléromètriques

Dans le deuxième chapitre, neuf configurations mécaniques différentes sont proposées pour les masses sismiques. Quatre structures sont conçues pour mesurer des accélérations parallèles au substrat et trois pour des mesures perpendiculaires au substrat. La combinaison de deux accéléromètres latéraux et d'un accéléromètre sensible selon la direction verticale sur le même substrat, permet de mesurer des accélérations selon trois directions au moyen d'une puce monolithique. Chaque masse sismique est sensible à une seule direction et insensible aux autres directions. Grâce à la suspension très symétrique avec des poutres fines, le mouvement des masses est purement latéral et les sensibilités mécaniques transverses sont très faibles (< 1%). Par ailleurs, deux types de dispositifs sont présentés pour mesurer des accélérations parallèles et normales au substrat avec une seule masse. Cela ouvre la voie à la réalisation d'un accéléromètre 3D utilisant une seule masse sismique. Cependant, cette possibilité introduit des sensibilités transverses plus importantes.
La modélisation analytique de ces structures est basée sur un système ressort-masse d'ordre deux. Les formules analytiques pour la raideur de ressort permettent de calculer la sensibilité mécanique de ces architectures. L'amortissement par l'air des structures, qui sont sensibles parallèlement au substrat, est provoqué par l'amortissement visqueux d'air comprise entre la masse et le substrat et sollicitée en cisaillement. Par contre pour les structures verticales, l'amortissement est dominé par un amortissement de type « couche comprimés » (angl. « squeeze film damping »). La fonction de transfert qui décrit la réponse mécanique limitée aux déplacements faibles est explicitée. Pour évaluer des effets, comme la nonlinearité due à des grands déplacements (déplacement > largeur de poutres), les sensibilités mécaniques transverses, les modes de résonance élevés, ou les poutres de suspension plus complexes, la simulation par méthode d'éléments finis (FEM) est préférable. En utilisant le logiciel ANSYS la réponse statique et dynamique des structures proposées est calculée. En général, les estimations par FEM et le modèle analytique sont identiques avec une précision de 10% pour un faible déplacement. En plus, nous avons mesuré expérimentalement les déplacements statiques en utilisant un comparateur optique pour confirmer le calcul théorique. Les résultats analytiques et expérimentaux sont proches pour les faibles déplacements. Cependant, dans le cas d'un déplacement nonlinaire dû à des forces élevées, ce déplacement est surestimé par ANSYS.
En comparant les différentes structures mécaniques, on voit qu'il existe un compromis entre les sensibilités transverses, la largeur de puce, la variation de sensibilité due aux tolérances de fabrication et la linéarité. Des structures avec des poutres plus longues au lieu d'être plus fines sont le meilleur choix pour augmenter la sensibilité principale. Un aspect fondamental à considérer est la

relation entre la sensibilité mécanique et la première fréquence de résonance. Si la première fréquence de résonance est limitée à 500Hz (pour travailler dans une bande d'au moins 100Hz), on peut atteindre une sensibilité mécanique de 1µm/g.
Finalement, nous avons étudié le niveau de bruit thermomécanique qui est de l'ordre de 0.1µg/√Hz. On peut en conclure que, pour les accéléromètres micro-usinés en volume, la résolution n'est pas limitée par le bruit thermomécanique, mais plutôt par la méthode de lecture. Donc, l'usinage de volume du silicium est bien approprié pour obtenir des accéléromètres très sensibles avec une résolution dans le domaine de µg et même en dessous.

Micro-usinage non conventiannel de volume utilisant la sous-gravure du (100) silicium

Une méthode de fabrication non conventionnelle, utilisant une sous-gravure des plans (100) du silicium, a été démontrée. Avec un procédé d'usinage de volume d'une plaque (100) de silicium il est possible de fabriquer des poutres fines avec des murs verticaux. La masse sismique et les poutres de suspension sont usinées dans la même étape de gravure. Les structures fabriquées ont un rapport de forme (relation entre hauteur et largeur de poutre) qui peut atteindre 35. Les directions de sous-gravure et les règles de dessin du masque ont été déterminées. Les structures latérales sont fortement symétriques et grâce à cela les sensibilités transverses sont faibles. La méthode de fabrication non conventionnelle est assez simple et permet de construire un système accélérométrique à deux axes dans une seule étape de gravure. L'angle de 90° entre les deux dispositifs est précisément défini par l'orientation intrinsèque du cristal de silicium.
La précision de la gravure dépend de l'orientation cristalline initiale du plan du substrat, et de l'alignement pendant la lithographie. L'attaque anisotrope a été simulée. Grâce à cela, on peut démontrer que la simple technique de sous-gravure des plans verticaux {100} peut être utilisée pour le micro-usinage de dispositifs mécaniques avec une reproductibilité de l'ordre de quelque pour-cent, si des précautions sont prises. Les points importants sont premièrement une conception adaptée et deuxièmement une pré-gravure pour identifier l'orientation cristalline du silicium.
Pour détecter des accélérations selon la direction normale au substrat, on peut ajouter un troisième accéléromètre avec une sensibilité verticale. Dans un tel microsystème accélérométrique 3D, toutes les masses sismiques sont précisément alignées grâce à la perpendicularité des plans cristallins {100}. Le troisième dispositif est micro-usiné avec une technique appelée « gravure sans masque ». Les poutres de suspension sont localisées horizontalement et peuvent être alignées parallèlement ou encore avec un angle de 45° degrés par rapport au méplat du substrat.
Nous pouvons donc conclure que la fabrication d'un système monolithique avec trois masses sismiques a été démontrée. Les avantages du procédé sont la simplicité de la gravure en deux étapes. une orientation quasiment parfaite des dispositifs suivant les directions cristallines <100> du silicium et une suspension symétrique des masses. Les structures ont les qualités excellentes du silicium cristallin. une bonne stabilité à long terme et pas d'hysteresis. Aucune contrainte n'est présente dans les poutres de suspension en raison de l'absence de dopage. La grande sous-gravure est un inconvenient. Dans le cas des plaques (110) du silicium on peut s'affranchir de cet effet. Cependant, on ne peut pas usiner deux dispositifs perpendiculaires dans une telle plaque (110).
Tous les types d'accéléromètres latéraux et verticaux présentés dans le chapitre 2 peuvent être fabriqués par la technique de micro-usinage proposée. Bien sûr, cette technique n'est pas limitée aux accéléromètres. D'autres dispositifs sur silicium, comme un miroir optique, un gyromètre ou des structures avec des poutres plus complexes ont été fabriqués par cette méthode de gravure.

Accéléromètres capacitifs multi-axiaux

Le quatrième chapitre donne une description de la conception, de la modélisation, de la simulation, de la fabrication, et de la caractérisation expérimentale d'accéléromètres capacitifs dédiés à des mesures multi-axiales. Il existe deux types différents de capteurs dans ce système monolithique. D'une part, des dispositifs pour détecter des accélérations latérales avec un changement de capacité provenant d'un décalage des électrodes, d'autre part, une masse sismique sensible aux accélérations verticales, destinée à mesurer la variation de distance entre masse et contre électrode. Pour les deux principes on peut utiliser une détection différentielle pour réduire les sensibilités transverses et d'autres effets, comme par exemple l'influence de la température.
Dans le cas des accéléromètres verticaux, un modèle simplifié de champ électrostatique permet d'obtenir une description satisfaisante de l'accéléromètre. Pour les accéléromètres latéraux les électrodes sont en forme de peigne ou méandre. Deux types différents d'électrodes sont proposés : elles sont soit élaborées dans une couche métallique déposée, soit gravées verticalement sur le silicium. Dans chaque cas les effets électrostatiques au bord des électrodes doivent être pris en compte. Pour cette raison, des modèles analytiques adaptés ont été développés. En outre, des simulations par la méthode des éléments finis ont été utilisées pour calculer le changement capacitif dû au déplacement mécanique de la masse sismique. Finalement, la sensibilité capacitive et la réponse des accéléromètres latéraux peuvent être parfaitement estimées. Les calculs analytiques et numeriques sont comparés. En conclusion, la formule analytique décrit très bien la réponse capacitive. On peut donc facilement modéliser le capteur et étudier une gamme large de paramètres pour trouver les meilleures géometries en ce qui concerne la sensibilité capacitive et la linéarité, et ce, en considérant les différents aspects technologiques.
En utilisant les modèles développés, nous avons calculé les forces électrostatiques nécessaires pour démontrer la faisabilité d'un accéléromètre en boucle fermée. En complément de la modélisation analytique et numérique, nous avons développé un modèle global écrit dans le langage HDL-A (Hardware Description Languange for Analog electronics). La simulation globale assemble les modèles mécanique et électrostatique, et permet de plus de simuler le microsystème complet dans son environnement électronique.
Deux procédés différents de fabrication sur silicium ont été développés pour les électrodes des accéléromètres latéraux. Ils sont décrit en détail. Un procédé pour la fabrication d'accéléromètre capacitif utilise des électrodes élaborées dans une couche mince de nickel ou chrome. Une couche de silice est nécessaire pour isoler les électrodes métalliques de la masse sismique de silicium. Cette couche peut être à l'origine de l'apparition de charges parasites et rendre également la réalisation des contacts difficile. A cause de cela un deuxième procédé a été développé pour la réalisation d'électrodes gravées dans le silicium. Les contre-électrodes sont localisées sur un substrat de verre du type Pyrex. Pour les élaborer différents procédés ont été développée. L'assemblage des plaques de verre et de silicium est fait par soudage anodique. Pour aligner les plaques de silicium et verre avec une haute précision l'équipement de soudage se compose d'un module d'alignement, d'un module de fixation et d'un module de soudage. Finalement, les puces silicium-verre sont séparées par sciage puis encapsulées et connectées.
Pour détecter des petits changements de capacités de l'ordre de quelques pF et moins, trois méthodes de mesure différentes sont étudiées : pont AC capacitif, charge/décharge, et modulation sigma-delta. La dernière méthode est prévue pour être utilisée dans un circuit intégré adapté à l'accéléromètre 3D capacitif réalisé. Les avantages d'un tel modulateur sigma-delta sont la linéarité élevée et le signal numérique. Dans les spécifications pour le capteur on trouve une capacité à accélération nulle de 20pF, une sensibilité capacitive plus grande que 1pF/g et une gamme de mesure de ±2g. Une étude générale de bruit de détection démontre qu'on peut arriver à une

résolution capacitive de 1aF/√Hz pour tous les circuits de mesure. Cela permet d'envisager une solution à deux puces pour un système accélérométrique 3D avec une résolution de l'ordre du µg. Finalement, les accéléromètres capacitifs 3D réalisés ont été testés. Des accélérations statiques ont été appliquées en tournant les capteurs dans le champ de gravité. La réponse dynamique a été mesurée en utilisant un haut-parleur et un analyseur de réseau. En moyenne, les capacités pour les accéléromètres latéraux et verticaux varient de 18pF à 19pF avec des sensibilités entre 0.5pF/g et 4pF/g selon la structure mécanique. L'erreur de linéarité est approximativement 1%. La première résonance est observé vers 500Hz. En utilisant un capacimètre commercial, des résolutions de 40µg/√Hz ont été obtenues. En conclusion, la performance de l'accéléromètre mesuré est conforme aux estimations théoriques des spécifications. La résolution pourrait être améliorée en plaçant un circuit intégré au plus prés de l'accéléromètre.

Accéléromètres optiques multi-axiaux

Après avoir étudié des différents concepts d'accéléromètres optiques, nous avons choisi la méthode de réalisation qui paraît la plus efficace au niveau de la performance du capteur et au niveau de la complexité d'assemblage. La structure choisie utilise la technique de sous-gravure du silicium (100) présentée dans le chapitre 3. Pour mesurer le déplacement de la masse sismique, une fibre optique a été intégrée dans la structure micromécanique. Le mur vertical de la masse sismique et la face polie de la fibre optique forment une cavité de Fabry-Perot (FPC) de faible finesse. Cette cavité agit comme un interféromètre à deux faisceaux avec un retard optique qui est équivalent à deux fois la distance fibre-masse. Le mouvement de la masse sismique change le retard optique de la FPC et on observe un décalage de longueur d'onde dans le spectre réfléchi, proportionnellement à l'accélération. La FPC du capteur est contrôlée par un deuxième interféromètre, dans l'unité de détection, qui régule la phase entre les deux. La méthode basée sur la modulation de cohérence permet une lecture à distance et en outre, de multiplexer trois signaux issus des accéléromètres sur une seule fibre.
Un modèle analytique de l'accéléromètre opto-mécanique est présenté. La modélisation est divisée en trois parties: structure micro-mécanique de la masse sismique, fonction de transfert optique de la FPC, et la modélisation liée à la modulation de cohérence et au multiplexage. Le modèle mécanique donne le déplacement entre le miroir et la masse sismique en fonction de l'accélération appliquée. La fonction de transfert optique décrit le décalage du spectre réfléchi, dû au déplacement de la masse sismique. La lumière réfléchie est modélisée par deux ondes qui se superposent. Finalement, la modélisation de la méthode de détection explique analytiquement comment on peut interpréter l'information codée dans le décalage du spectre par un deuxième interféromètre de réception. De plus, le multiplexage de plusieurs accéléromètres est théoriquement expliqué.
Nous avons fabriqué des systèmes 1D et 2D d'accéléromètres optiques. Le capteur est composé d'une masse sismique et d'une pièce de maintien de la fibre. L'alignement de la fibre ne requiert pas de contrôle optique actif. Cependant, la cavité optique a été réalisée avec une précision de ±1µm grâce au procédé de lithographie. Pour réaliser le multiplexage avec une source à spectre large les accéléromètres doivent être bien adaptés aux interféromètres de réception. Des FPC de 45µm et 135µm ont été réalisées. Pour prendre en compte un troisième axe de détection, la longueur de la FPC serait de 90µm.
La caractérisation commence avec une étude expérimentale de la sensibilité de l'accéléromètre optique-mecanique selon une direction. La sensibilité mesurée est très proche de celle calculée par le modèle développé. La méthode de fabrication permet d'ajuster la sensibilité du capteur avec une précision de quelques pour-cent. Les résultats des mesures sont présentés et indiquent pour un

dispositif ayant une sensibilité de 143nm/g une résolution de 500μg dans une gamme de mesure de ±10g. Cela correspond, pour un capteur ayant une sensibilité mécanique plus élevée de 1μm/g, à une résolution de 70μg dans une gamme de mesure de ±1.5g. Les sensibilités transverses sont inférieures à 1% de la sensibilité principale.
Par ailleurs, nous avons également réalisé un accéléromètre 2D ayant deux masses sismiques micro-usinées sensibles aux deux directions parallèles aux côtes du substrat. La méthode de détection basée sur la cohérence de modulation permet de multiplexer les deux signaux des capteurs et de mesurer l'accélération 2D par une lecture à distance. Il n'y a pas de connexion électrique entre le site de mesure et l'unité de détection. Les performances sont similaires à l'accéléromètre uniaxial et la diaphonie due au multiplexage est inférieure à 1% de la sensibilité principale. A notre connaissance, aucun autre accéléromètre multi-axial optique n'a été réalisé jusqu'à maintenant.
Dans le calcul du bruit fondamental du capteur optique, trois contributions principales sont considérées. Premièrement, le bruit de phase de la source laser qu'on a modélisé par un bruit d'origine thermique , deuxièmement le bruit de grenaille associé à la création d'un courant dans la photodiode et troisièmement le bruit électronique du photodétecteur. Le bruit théorique dépend du nombre d'accéléromètres multiplexés, et on peut l'estimer à environ 1μg/√Hz.
On peut optimiser les dispositifs fabriqués selon différents paramètres, comme par exemple, le paramètre de couplage optique et la gamme de mesure. Le circuit électronique peut être amélioré afin de réduire le bruit de détection et d'augmenter la bande passante.
Le système d'accéléromètre optique qui a été réalisé, présente tous les avantages d'une mesure optique : immunité aux interférences électromagnétiques, pas d'alimentation électrique sur le site de mesure, etc. En plus, la modulation de cohérence présente des avantages particulièrement intéressants dans le cas d'un capteur avec une lecture à distance : premièrement, l'information codée sur le retard optique peut être restituée par une démodulation locale. L'interféromètre de l'unité de détection nous donne accès à la phase interférométrique. Ceci permet différents schémas de démodulation. Deuxièmement, ces schémas de démodulation permettent de s'affranchir des influences éventuelles que peut subir le faisceau lumineux pendant sa propagation à travers les fibres de liaison. En effet, tandis que l'intensité lumineuse et la polarisation de la lumière peuvent être affectées au cours de la propagation, le décalage mutuel des impulsions reste inaltéré. Et troisièmement, la modulation de cohérence permet en outre la mise en réseau de plusieurs accéléromètres par multiplexage. L'interrogation de trois capteurs d'accélération par un même système de détection et de transmission permet la simplification de l'installation d'un système, et la réduction de son coût.

Conclusions

Dans cette thèse, tous les aspects du développement d'un accéléromètre sont considérés : la conception, la modélisation, la fabrication et la caractérisation. Une comparaison entre les accéléromètres réalisés, notamment un dispositif capacitif et un capteur optique, démontre qu'avec les deux capteurs on peut détecter une accélération jusqu'à environ 100μg. Par ailleurs, il est encore possible d'optimiser les deux accéléromètres. En particulier on pourrait obtenir une haute résolution en dessous de μg. Du fait de la similarité des performance obtenues par les deux techniques, le choix de la méthode de détection sera effectué en prenant d'autres critères en compte, comme par exemple le coûts ou le domaine d'utilisation.

Remerciements

Cette thèse synthétise la recherche réalisée surtout au sein du Laboratoire de Physique et Métrologie des Oscillateurs du CNRS/IMFC à Besançon dans le cadre du projet PICS entre les instituts de microtechnique franco-suisse.

Très nombreux ont été ceux qui ont contribué à rendre agréables et fructueuses ces trois années passées.

Travailler sous la direction de Monsieur ***Michel de Labachelerie*** *a été un réel plaisir ; sa nature intuitive, sa disponibilité, son efficacité et son implication dans mon travail sans être toutefois directif, m'a apporté beaucoup d'esprit et de liberté pour réaliser ce travail de thèse. Je veux lui exprimer ici ma sincère gratitude.*

Je tiens également à exprimer ma gratitude à Monsieur ***Daniel Hauden****, Professeur à l'ENSMM et Directeur du LPMO, qui m'a accueilli au sein du laboratoire et m'a donné l'opportunité de présenter mon travail à de nombreux congrès internationaux.*

Je remercie les autres membres du jury de me faire l'honneur d'examiner cette thèse:

> *Monsieur* ***Philippe Renaud****, Professeur à l'EPFL, qui a bien voulu être rapporteur et qui m'a accueilli plusieurs fois au sein de son institut à Lausanne. Les conseils qu'il m'a donné aux différentes réunions « PICS » étaient très fructueux pour mon travail.*
>
> *Monsieur* ***Daniel Estève****, directeur de recherche au LAAS à Toulouse, qui a volontairement accepté d'être rapporteur de cette étude et qui vient de très loin pour assister à ma soutenance.*
>
> *Monsieur* ***Nico de Rooij****, Professeur à l'Université de Neuchâtel, qui a bien accepté d'être codirecteur de thèse dans le cadre d'une cotutelle établie entre l'Université de Franche-Comté et l'Université de Neuchâtel. Il a suivi et examiné ces travaux avec beaucoup d'intérêt.*
>
> *Monsieur* ***Charles Dussurgey****, Chef du Département Technique, section Capteurs chez Sextant Avionique, Valence, en tant qu'expert dans le domaine de capteurs industriels, il a bien voulu examiner ce projet de thèse.*

« Ein Herzliches Dankeschön » à ***Sylvain Ballandras****. Je lui suis très reconnaissant de m'avoir fait bénéficier de ses connaissances, surtout au début de ma thèse, et d'avoir toujours fait preuve de beaucoup de dynamisme et d'enthousiasme. Je me rappelle qu'il ma donné tout son soutien pour chercher un appartement et également ma carte de séjour.*

Je remercie également ***Yannick Ansel****, qui était thésard à l'EPFL Lausanne, pour notre collaboration au niveau de la simulation. Je n'oublie pas l'accueil chaleureux qui m'a été réservé à l'EPFL et chez lui lors de mes « stages de formation autour de FEM et HDL-A ».*

J'exprime ma gratitude à Monsieur ***Pascal Blind****, ingénieur au CETEHOR à Besançon pour nos nombreuses discussions sur le micro-usinage de silicium et surtout pour avoir effectué la gravure humide de mes dispositifs.*

*Merci beaucoup à nos collaborateurs du laboratoire d'optique à Besançon, **Wilhelm Elflein** et **Henri Porte**, instigateurs de la modulation de cohérence.*

*Mes remerciements s'adressent également à Madame **Collette Tellier**, Professeur à l'ENSMM. Elle a effectué des simulations de la gravure anisotrope, qui se sont avérées fondamentales pour le travail présenté.*

*Un remerciement spécial à **Catherine Marselli** et **Jean-Pierre Amann** du IMT Neuchâtel. Malgré tous les problèmes administratifs, ils se sont engagés beaucoup à établir une cotutelle entre les deux universités et mon inscription à l'Université de Neuchâtel.*

*Merci beaucoup à mes collègues au niveau des accéléromètres, **Torben Storgaard-Larsen** (Brüel & Kjoer, Danemark) et **José Plaza** (CNM Barcelone) pour les discussions par courrier électronique et les images fournies.*

*Je voudrais remercier Messieurs **Daniel Gillet** et **Jean-Claude Jeannot** du LPMO, ainsi que **Jean-Michel Karam** et **Jérome Goy** (TIMA/CMP) pour m'avoir expliqué la méthode de la modulation sigma – delta. Je crois que le projet d'ASIC va devenir un succès.*

*Merci à **William Daniau**, ingénieur de recherche à l'IMFC/LPMO, pour plusieurs dépôts métalliques. Je remercie **Hervé Fourré** pour sa collaboration et ses efforts pour développer l'équipement du soudage anodique et également **Jean-François Manceau** du LPMO et **Florence Grétillat** du IMT Neuchâtel pour plusieurs discussions autour des accéléromètres et des autres microsystèmes.*

*Mes collègues **Emmanuelle Briot** et Neila **Kaou** et Mesdames **Anne Basrour** et **Corinne Martin** sont assurées de ma reconnaissance pour l'efficacité et la gentillesse avec laquelle elles se sont acquittées de la correction de mes transparentes et textes français. Je remercie **Fathia Doudou**, **Christiane** Hisleur et **Madame Carquille** pour s'être occupées de mes dossiers administratifs.*

*Enfin, je n'oublie pas de remercier tous les **thésards et autres personnes du** LPMO à Besançon, du **IMS à Lausanne** et **du IMT** à **Neuchâtel** qui ont contribué à rendre ce travail et les trois années passées très agréables.*

*Finalement, tout ce travail et mon séjour en France n'aurait pas été possible sans la complicité et le soutien de mon épouse, **Katharina**, que je remercie très profondément.*

10. References

[Abb94] E. Abbaspour-Sani, R. Huang, C.Y. Kwok, A linear electromagnetic accelerometer, Sensors and Actuators A44, 1994, pp. 103-109

[Abb95] E. Abbaspour-Sani. R. Huang, C.Y. Kwok, A novel optical accelerometer. IEEE Electron device letters. Vol.16, No 5, May 1995, pp. 166-168

[Ah97] H. Ahmad, A. Al-Khalili, L. Landsberger, M. Kahrizi, A two-dimensional micromachined accelerometer, IEEE Transaction on Instrumentation and Measurement, Vol.46, No1, February 1997, pp.18-26

[Alb88] K.B. Albaugh and P.E. Cade, Mechanism of anodic bonding of silicon to Pyrex glass, tech. Digest. IEEE Solid-state sensor and actuator workshop, Hilton Head Island, SC, 1988. p.109

[All89] H.V. Allen, S.C. Terry, D.W. de Buin, Accelerometer systems with built-in testing, Proc. Transducer'98. 1989. pp. 1-10

[An93] M. Andrews, I. Harris. G. Turner, A comparison of squeeze-film theory with measurements on a microstructure. Sensors and Actuators A36, 1993, pp.79-87

[And95] G.I. Andersson. A novel 3-axis monolithic silicon accelerometer, Proc. Transducers'95, Stockholm, Sweden, June 25-29, 1995

[Ans98] Y. Ansel. Operational limits of micromachined inertial sensors, Ph.D. thesis, Institute of Microsystems. Swiss Federal Institute of Technology Lausanne. September 1998

[BA98] British Aerospace Systems and Equipment, Product information on motion sensors. accelerometer C3A-02, Plymouth, UK, 1998

[Bal97] Ballandras S. Basrour S. Robert L. ea., Microgrippers fabricated by LIGA techniques. Sensors and Actuators , 1997

[Bar88] P.W.Barth. F.Pourahemi. R.Mayer. J.Poydock and K.Petersen. A monolithic silicon accelerometer with integrated air damping and overrange protection. Tech. Dig. IEEE Solid State and Sensor Workshop. Hilton Head Island. 1988. pp.35-38

[Bou97] C.Bourgeois. F.Porret, A. Hoogerwerf. Analytical modeling of squeeze-film damping in accelerometers. Proc.Transducers'97, Chicago, June 16-19, 1997, pp.1117-1120

[Bon95] M.H.W. Bonse. C. Mul. J.W. Spronck, Finite-element modelling as a tool for designing capacitive position sensors. Sensors and Actuators A46-47, 1995. pp.266-269

[Boo97] S.F. Knowles. J.S. McKenzie. R.D. Pechstedt, Active Silicon integrated Optical Circuit (ASOCTM) for sensing applications. Fiber Optic Sensors Technical Interchange Meeting. NASA-Kennedy Space Center. Florida. USA, 20th November 1997

[Bos97] B. Boser. Electronics for micromachined inertial sensors. Proc.Transducers'97, Chicago. June 16-19. 1997. pp.1169-1172

[Box90] B. Boxenhorn, P. Greiff, Monolithic silicon accelerometer, Sensors and Actuators A21-23, 1990, pp. 273-277

[Bro85] J.L. Brooks, R.H. Wentworth, R.C. Younggquist, M.T. tur, B.Y. Kim, H.J. Shaw, Coherence multiplexing of fiber-optic interferometric sensors, IEEE Journal of Lightwave Technology, Vol. LT-3, No. 5, 1985, pp. 1062-1071

[Bro98] M. Brounais, D. Gaspar Rodrigues, Conception d'un microsystème optomécanique pour le contrôle spectral de diode laser, projet de fin d'études, Ecole Nationale Supérieure d'Ingénieurs de Mécanique et des Microtechniques, Besançon, Juin 1998

[Bun96] D.W.Burns, R.D.Horning, W.R.Herb ea., Sealed-cavity resonant microbeam accelerometer, Sensors and Actuators A53, 1996, pp. 249-255

[Bur91] C. Burbaum, J. Mohr, P. Bley and W. Ehrfeld, Fabrication of capacitive acceleration sensors by the LIGA technique, Sensors and Actuators A 25-27, 1991, pp. 559-563

[Bur92] K.E. Burcham, G.N. de Brabander, J.T. Boyd, Micromachined silicon cantilever beam accelerometer incorporating an integrated optical waveguide, SPIE Vol. 1793 Integrated Optics and Microstructures, 1992, pp.12-18

[Bur95] Chr. Burrer, Design, fabrication and characterization of resonant silicon accelerometers, Ph.D.-thesis, Univeresity of Barcelona, Spain, February 1995

[Bra91] A. Brahim-Bounab, J.Y. Amaudrut, C.R. Tellier, Dissolution slowness surfaces of cubic crystals: Part I Theory and three-dimensional representation for class 2 3, Journal of Material Science 26 (1991), pp. 5585-5594

[Can92] J.C. Candy, G.C. Temes, Oversampling Delta-Sigma Data Converters, New York, IEEE Press, 1992

[Cha90] S.C.Chang, M.W.Putty, D.B. Hicks, C.H.Li, R.T.Howe, Resonant-bridge two-axis microaccelerometer, Sensors and Actuators A21-A23, 1990, pp. 342-345

[Cha96] K.H.-L. Chau, S.R. Lewis, Y. Zhao, e.a., An integrated force-balanced capacitive accelerometer for low-g applications, Sensors and Actuators A54 (1996), pp. 472-476

[Che82] P.L.Chen, R.S. Muller, R.D.Jolly ea., Integrated silicon microbeam PI-FET accelerometer, IEEE transactions on electron devices, ED-29, pp. 27-33

[Che84] P.L.Chen, R.S. Muller, A.P. Andrews, Integrated silicon microbeam PI-FET accelerometer with proof mass, Sensors and Actuators 8, 1984, pp. 119-126

[Che97] H. Chen, M. Bao, H. Zhu, S. Shen, A piezoresitive accelerometer with novel vertical beam structure, Sensors and Actuators A63, 1997, pp. 19-25

[Chn97] Y.H. Chen, C.H. Cheng, H.W. Lee, A.Q. Liu and N.C. Tien, A Polysilicon surface micomachined accelerometer based on optical intensity modulation, Proc. MOEMS97 International conference on optical MEMS and their applications, Nara, Japan, November 18-21, 1997, pp. 121-125

[Cho92] W.Choi, J.G.Slits, A method to etch undoped silicon cantilever beams, J. of Microelectromechanical Systems, Vol. 2, No. 2, June 1993, pp. 82-86

[Cho94] Y-H. Cho, A.P. Pisano, R. Howe, Viscous damping model for laterally oscillating microstructures, Journal of Micromechanical Systems, Vol. 3, NO. 2, June 1994, pp. 81-86

[Cho97] B. Choi, E.G. Lovell, Improved analysis of microbeams under mechanical and electrostatic loads, J.Micromech. and Microeng. 7, 1997, pp. 24-29

[Cle98] P.-A. Clerc, L. Dellmann, F. Grétillat, M.-A. Grétillat ea., Advanced deep reactive ion etching a versatile tool for microelectromechanical systems, presented at MircoMechanicsEurope'98, Ulvik, Norway, June 4-6, 1998

[Cra93] H. Crazzolara, G. Flach, W. von Munch, Piezoresistive accelerometer with overload protection and low-cross-sensitivity, Sensors and Actuators, A39, 1993, pp. 201-207

[Cro95] S.D. Crossley, Commercially available fibre optic sensors - 10 years of progress?, Optical Fibre Sensors 94, Proc. SPIE Vol. 2360, Glasgow 1994, pp. 249-252

[Cul95] B. Culshaw, Fibre optic sensor: integration with micromachined devices, Sensors and Actuators A46-47, 1995, pp. 463-469

[Dar97] R.B. Darling, C. Hivick, J. Xu, Compact analytical models for squeeze film damping with arbitrary venting conditions, Proc.Transducers'97, Chicago, June 16-19, 1997, pp. 1113-1116

[Dau95] U.A.Dauderstädt, P.H.S. de Vries, R.Hiratsuka, P.M.Sarro, Silicon accelerometer based on thermopiles, Sensors and Actuators A46-47, 1995, pp. 201-204

[Deg98] O.Degani, D.Seter, E.Socher,S.Kaldor,Y.Nemirovsky, Micromachined accelerometer with modulated integrative differential optical sensing, Electronics Letters, 2nd April 1998, Vol.34 NO.7, pp.654-655

[Del75] C. Delisle, P. Cielo, Multiplexage en communication optique par interférométrie à grande différence de marche en lumière blanche, Canadien Journal of Physics, Vol.54, No.23, 1975, pp. 2322-2331

[Del87] Delapierre G, Danel J S, Michel F, Bost J L, Boura A, Aujay O, A quartz micromachined closed loop accelerometer, Proc. Eurosensors'87, Cambridge, Great Britain, 1987, pp. 223-224

[Del96] Delapierre G 1996 Microtechnology: limits and opportunities through the example of accelerometers, Proc. Eurosensors'96, Leuven, Belgium, pp. 1083-1092

[dRe98] R. de Reus, J. Gullov, P. Scheeper, Fabrication and characterization of a piezoelectric accelerometer, Proc. MircoMechanicsEurope'98, Ulvik, Norway, June 4-6, 1998, pp.202-205

[Duc84] C. Duchet, R. Martin, Electro-optic modulator on Ti:LiNbO3 with very low drive voltage, Electronic Letters, Vol. 20, No. 13, June 21, 1984, pp. 567-568

[Elf97] W. Elflein, Contribution à l'étude d'un réseau de capteurs distribués: microdispoditifs optique integrés adaptés à une architecture de multiplexage de cohérence, Ph.D.-thesis, Université de Franche-Comté, February 1998

[Ens96] Ensell G, Alignment of mask patterns to crystal orientation, Sensors and Actuators A53, 1996, pp. 345-348

[Fog98] Data sheet MC900, Documentation technique du système de mésure capacitive MC900, FOGALE nanotech, Nimes, France, 1998

[Fre97] French P.J., Sarro P 1997 Surface versus bulk micromachining: the contest for suitable applications Proc. MircoMechanicsEurope 1997, Southampton, September 1-2, 1997

[Frü97] J. Frühauf, B. Hannemann, Anisotropic multi-step etch processes of silicon, J. of Micromechanics and Microengineering 7, 1997, pp. 137-140

[Gab93] T.B. Gabrielson, Mechanical-thermal noise in micromachined acoustic and vibration sensors, IEEE Transaction on Electron Devices, Vol. 40, NO. 5, May 1993, pp.903-909

[Gab95] T.B. Gabrielson, Fundamental noise limits for miniature acoustic and vibration sensors, Journal of Vibration and Acoustics, Vol. 117, October 1995, pp.405-410

[Gal89] D. Galler, A. Booth, The shocking truth of accelerometer selection, Machine Design, July 6 (1989), pp.85-89

[Gar95] Garcia-Valenzuela, M. Tabib-Azar, Comparative study of piezoelectric, piezoresistive, electrostatic, magnetic, and optical sensors, Integrated optics and microstructures II, vol. SPIE-2291, 1995, pp. 125-142

[Ger90] U.E. Gerlach-Mayer. Capacitive accelerometer made by silicon micromechanics, MicroSystem Technologies. 1990. pp. 623-628

[Ger91] J.M. Gere. S.P. Timoshenko. Mechanics of Materials. Third SI Edition. Chapman & Hall. London. 1991

[Geß94] T. Geßner. E. Vetter. M. Wiener. Technology tools for a high precision accelerometer in bulk-micromachining. Microsystem Technologies 1 (1994). Springer-Verlag. 1994, pp. 10-13

[Goe82] J.-P. Goedgebuer. J. Salcedo. J.Ch. Vienot. Multiplex communication via electrooptic phase modulation of white light. Optica Acta. Vol.29. No.4. 1982. pp.471-477

[Gré98] F. Grétillat. "Silicon Micromachined Vibrating Gyroscopes with Piezoresistive Detection and Electromagnetic Excitation". PhD thesis. University of Neuchâtel. Institute of Microtechnology. Sensors Actuators and Microsystems Laboratory. Neuchâtel (CH). 1998.

[Han98] B. Hannemann. J. Frühauf. New and extended possibilities of orientation dependent etching in microtechnics. Proc. MEMS'98. Heidelberg. Germany. January 1998. pp. 234-239

[Har98] P.G. Hartwell. F.M.Bertsch. S.A.Miller e.a., Single mask lateral tunneling accelerometer, Proc. MEMS'98. Heidelberg. Germany. January 1998, pp. 340-344

[Hee86] Heerens W C. Application of capacitance techniques in sensor design J.Phys.E:Sci.Instrum. 19. 1986. pp.897-906

[Hen90] W. Henrion. L. DiSanza. M. Ip ea., Wide dynamic range direct digital accelerometer, IEEE solid-state sensor and actuator workshop. 1990, pp.153-157

[Hir91] R. Hiratsuka, D.C. van Duyn, T. Otaredian, P. de Vries, A novel accelerometer based on thermopile, Proc. Transducers'91, 1991, pp.420-423

[Hir92] R. Hiratsuka, D.C. van Duyn, T. Otaredian ea., Design considerations for the thermal accelerometer, Sensors and Actuators A32, 1992, pp. 380-385

[Hua95] Huang R S. Abbaspour-Sani and Kwok C Y 1995 A novel accelerometer using silicon micromachined cantilever supported optical grid and pin photodetector, Proc. Transducers'95, Stockholm, Sweden, pp. 663-666

[Jac94] D.A. Jackson, Recent progress in monomode fibre-optic sensors, Meas. Sci. Technolol. Vol. 5, 1994. pp. 621-638

[Joh88] S. Johansson, Micromechanical properties of silicon, Ph.D. thesis, Uppsala University, Sweden, ISBN 91-554-2223-3, 1988

[Jon94] K. Jono, H. Hashimoto, M. Esashi, Electrostatic servo system for multi-axis accelerometers, Proc. IEEE MEMS 1994, pp. 251-256

[Kan87] Y. Kanda, K. Yamaura, Silicon pressure sensors and an accelerometer with four-terminal-gauge utilizing the shear stress, Proc. Transducers'87, Tokyo, 1987, pp. 406-409

[Kau97] J. Kaufmann, Untersuchungen eines mikromechanischen Delta-Sigma-Wandlersystems, Diploma thesis at Hochschule für Technik und Wirtschaft, Mittweida, Germany, 1997

[Ken75] D.L. Kendall, On etching very narrow grooves in silicon, Applied Physics Letters, Vol. 26, No 4, 1975, pp. 195-198

[Kla95] Klaassen E, Petersen K et al. 1995 Silicon fusion bonding and deep reactive ion etching: a new technology for microstructures, Proc. Transducers'95, Stockholm, Sweden, pp. 556-559

[Kra97] M. Kraft, Closed loop digital accelerometer employing oversampling conversion, Ph.D.-Thesis, University of Coventry, July 1997

[Krö95] O. Krömer, O. Fromheim, H. Gemmeke ea., High-precision read-out circuit for LIGA acceleration sensors, Sensors and Actuators A 46-47, 1995, pp. 196-200

[Kru98] E.J.J. Kruglick, B.A. Warneke, K.S.J.Pister, CMOS 3-axis accelerometers with integrated amplifier, Proc. MEMS 98, Heidelberg, Germany, January 1998, pp. 631-636

[KS98] SUSS BA6 Bond Aligner, Data sheet from Karl SÜSS KG GmbH & Co, München, Germany, 1998

[vKa95] R. van Kampen, Bulk-micromachined capacitive servo-accelerometer, Ph.D.-thesis, University of Delft, September 1995

[Kw97] K.Kwon, S.Park, Three axis piezoresistive accelerometer using polysilicon layer, Proc. Transducers 97, Chicago, USA, 16-19 June 1997, pp. 1221-124

[Le98] A.M.Leung, J.Jones, E.Czyzewska, J.Chen, B.Woods, Micromachined accelerometer based on convection heat transfer, Proc. MEMS 98, Heidelberg, Germany, January 1998, pp.627-630

[Lee69] D.B. Lee, Anisotropic etching of silicon, Journal of Applied Physics, Vol. 40, No 11, 1969, pp. 4569-4574

[Lem97] M. Lemkin, B. Boser, D. Auslander, J. Smith, A 3-axis force balanced accelerometer using a single proof-mass, Proc.Transducers'97, Chicago, June 16-19, 1997, pp.1185-1188

[Leu90] H. Leuthold, F. Rudolf, An ASIC for high-resolution capacitive microaccelerometers, Sensors and Actuators A 21-23, 1990, pp. 278-281

[Li95] Li Y X, French P J, Sarro P, Wolffenbuttel R 1995 Fabrication of a single crystalline capacitive lateral accelerometer using micromachining based one single step plasma etching MEMS'95 398-403

[Li96] X. Li, M. Bao, S. Shen, Maskless etching of three-dimensional silicon structures in KOH, Sensors and Actuators A57, 1996, pp. 47-52

[Li97] X. Li, M. Bao, S. Shen, Maskless anisotropic etching - a novel micromachining technology for multilevel microstructures, Proc. Transducers'97, Chicago, USA, June 16-19, 1997, pp.699-702

[Lis94] A.V. Listvin, T.V. Potapov, S.V. Tverdov, Passive fiber-optic accelerometer with silicon sensing element. tech. Phys. 39 (10), October 1994, pp. 1066-1068

[Lit96] B-290 TRIAD Three Axis Accelerometer, data sheet, LITEF GmbH, Freiburg, Germany, 1996

[Lor96] H.Lorenz. M.Despont. N.Fahrni. N.Labianca, P.Renaud and P.Vettinger. EPON SU-8: A low-cost negative resist for MEMS. Proceedings MME'96, Barcelona, Spain, October 1996

[Löt97] Lötters J.C., A highly symmetrical capacitive triaxial accelerometer. PhD-thesis. University of Twente, ISBN 90-365-0982-3, August 1997

[Mar95] J. Marty. A. Malki. C.Renouf. P.Lecoy. F. Baillieu. Fibre-optic accelerometer using silicon mircomachining techniques. Sensors and Actuators A46-47. 1995. pp. 470-473

[Mar98] C. Marselli. "Data Processing for a Navigation Microsystem". PhD thesis. University of Neuchâtel. Institute of Microtechnology. Electronics and Signal Processing Laboratory. Neuchâtel (CH). 1998

[Mat93] Y. Matsumoto. M. Esashi. Low drift integrated capacitive accelerometer with PLL servo technique. The 7th international conference on solid-state sensors and actuators, 1993. pp.826-829

[Mc95] N.C. MacDonald. SCREAM MicroElectroMechanical Systems. Microelectronic Engineering 32. 1996. pp. 49-73

[Min96] T.Mineta. S.Kobayashi. Y.Watanabe. e.a.. Three-axis capacitive accelerometer with uniform axial sensitivities. Journal of Micromechanics and Microengineering 6. 1996. pp. 431-435

[Mo68] P. Morse. K.U. Ingard. Theoretical acoustics, McGraw-Hill, New York, 1st edition, 1968

[Mot97] Sensor Data/Handbook from MOTOROLA, 4th Edition, 1997

[Mun98] U.Munch, N.Schneeberger, O.Paul, H.Baltes, E.Doering, Thin film protection of CMOS wafers against KOH. Proc. SPIE Vol. 3514, Conference on micromachined devices and components IV, Santa Clara, California, USA, September 1998, pp.124 - 133

[Nas95] Naseh S. Experimental investigation of anisotropic etching of Silicon in Tetra-Methyl Ammonium Hydroxide, M.Sc. Thesis, Concordia University Montreal. Quebec, 1995

[Nik96] Nikpour B, Landsberger L M, Haroun B and Kahrizi M, Process to achieve vibrating beams for an angular rate measurement sensor, Canadian Conference on ECE, Calgary, May 26-29, 1996

[Nik97] B. Nikpour, L.M. Landsberger, T.J. Hubbard, M. Kahrizi, A. Iftimie, Patterns for concave compensation between vertical (010)-(001) planes on Si(100) Anisotropically etched in TMAH. Proc. Transducers'97, Chicago, USA, June 16-19, 1997, pp. 691-694

[Nys97] J.B. Nysaether, A. Larsen, B. Liverd, P. Ohlckers, Measurement of package induced stress and thermal zero shift in transfer moulded silicon piezoresistive pressure sensors, Proc. MircoMechanics'97, Southampton, UK, September 1997, pp. 219-222

[Off95] Offenberg M. Lärmer F, Elsner B, Münzel H and Riethmüller, Novel process for a monolithic integrated accelerometer, Proc. Transducers'95, Stockholm, Sweden, 1995, pp. 542-545

[Ohl96] Ohlkers P. EMSTO Country Reports: Norway, http://www.nexus-emsto.com/country/Norway.html, 1996

[Oka92] K. Okada, Tri-axial piezoresitive accelerometer, Technical digest of the 11th sensor symposium, 1992, pp.245-248

[Pal85] E.D.Palik, V.M. Bermudez, O.J. Glembocki, Ellipsometric study of orientation-dependent etching of silicon in aqueous KOH, Journal of Electrochemical Society, Vol 132, No 4, 1985, pp. 871-884

[Pet82] K.E.Petersen, A.Shartel, N.F. Raley, Micromechanical accelerometer with MOS detection circuitry, IEEE transaction on electron devices, ED-29, 1982, pp. 23-27

[Pei98] E.Peiner, D. Scholz, A. Schlachetzki, P. Hauptmann, A micromachined vibration sensor based on the control of power transmitted between optical fibres, Sensors and Actuators A65, 1998, pp.23-29

[Pla96] J.A.Plaza, M.A.Benitez, L.Svenson ea., New FET accelerometer based on surface micromachining, Proc. Eurosensors X, Leuven, Belgium, 8-11 September 1996, pp.437-440

[Pla97] J.A.Plaza, H. Chen, J.Esteve, New bulk accelerometer for triaxial detection, Proc.Transducers'97, Chicago, June 16-19, 1997, pp.1231-1232

[Pla98] J.A.Plaza, J.Esteve, E.Lora-Tamayo, Cantilever Beam Accelerometer with Selftest System. Simulation, Technology and Experimental Results, Proc. Micromechanics Europe'98, Ulvik, Norway, June 1998, pp.135-138

[Plaza] J.A.Plaza, μ Acelerómetros de silicio, PhD-thesis, University of Barcelona, Bellaterra, Spain, October 1997

[Por96] H. Porte, J.-P. Goedgebuer, W. Elflein, A. Terras, F. Ledeventec, N. Butterlin, Linear Phase Tracking in a Coherence Modulation Electrical Sensor System Using Integrated LiNbO3 Modulator/Demodulator, IEEE Journal of Selected Topics of Quantum Electronics, Vol. 2, No. 2, June 1996

[Pu98] R. Puers, Sensor, sensorinterfacing and front-end data management for stand alone microsystems, Proc. MME'98, pp. 123-129

[Pue88] R. Puers, L. Reynaert, W. Snoeys, W.M.C. Sansen, A new uniaxial accelerometer in silicon based on the piezojunction effect, IEEE transaction on electron devices, 35, 1998, pp. 764-769

[Pue98] R. Puers, S. Reyntjens, The characterization of a miniature silicon micromachined capacitive accelerometer, Journal of Micromechanics and Microengineering 8, 1998, 127-133

[PuS98] R.Puers and S. Reyntjens, Design and processing experiments of a new minaturized capacitive triaxial accelerometer, Sensors and Actuators A68, 1998, pp. 324-328

[Pyr97] Corning Pyrex 7740, Data sheet, Corning S.A., Global business operation, Avon, France, 1997

[Ren97] P. Renaud, Communication at PICS meeting, Neuchâtel, January 1997

[Ric94] H. Richert, A simple monolithic accelerometer, Micro Structure Bulletin No.1, February 1994, pp. 2-3

[Ro97] B. Romanowicz. Methodology for the modeling and simulation of microsystems, Ph.D.-thesis, Institute of Microtechnology, Swiss Federal Institute of Technology of Lausanne, June 1997

[Roc71] Y. Rocard, Dynamique generale des vibrations, Masson et Cie, Paris, 1971, pp. 44-56

[Roc96] H.K.Rockstad, T.K.Tang, J.K..Reynolds ea, A miniature, high-sensitivity, electron tunneling accelerometer, Sensors and Actuators A53, 1996, pp. 227-231

[Ros94] L. Rosengren, Silicon Microstructures for Biomedical Sensor Systems, Ph.D.-thesis, Uppsala University, ISBN 91-554-3317-0, 1994

[Rou79] J.E. Roughton, W.S. Jones, Electromechanical transducers in hostile environments, Proc. IEE, Vol. 126, No. 11R, IEE Reviews, November 1979, pp.1029-1052

[Roy79] Roylance L.M., Angell J.B., A batch-fabricated silicon accelerometer, IEEE Transaction on Electron Devices, ED-26, 1979, pp. 1911-1917

[Rud83] F.Rudolf, A micromachined capacitive accelerometer with a two-point inertial-mass suspension, Sensors and Actuators 4, 1983, pp. 191-198

[Rud90] F.Rudolf., A.Jornod, J.Bergqvist, H.Leuthold, Precision accelerometer with micro-g resolution, Sensors and Actuators, A21-A23, 1990, pp. 297-302

[SA20] SA20 Crash sensor, Product information from SensoNor asa, Horten Norway, 1996

[SA30] SA30 Crash sensor. Product information from SensoNor asa. Horten Norway. 1998

[Sag97] F.Pressecq. Les innovations dans les microsystèmes spatiaux. Microtechnolgies & Microsystèmes, No 12. ISSN: 1260-6391, 1997, p.3

[San87] H. Sandmaier. K. Kuhl. E. Obermeier. A silicon based micromechanical accelerometer with cross acceleration sensitivity compensation, Proc. Transducers'87. 1987. pp.399-402

[Sat89] D.W.Satchell and J.C. Greenwood. A thermally-excited silicon accelerometer. Sensors and Actuators 17 (1989). pp. 241-245

[Sch90] H.F. Schlaak. F. Arndt. A. Steckenborn ea. Micromechanical capacitive acceleration sensor with force compensation. MicroSystem Technologies. 1990, pp. 617-622

[Sch96] P.Scheeper. J.O.Gullov. L.M.Kofoed, A piezoelectric triaxial accelerometer. Journal of Micromechanics and Microengineering, 6, 1996, pp.131-1336

[Sei87] H. Seidel. The mechanism of anisotropic silicon etching and its relevance for micromachining. Proc. Transducers 87 ISBN 4-88686-010-9, Tokyo, Japan, June 2-5n, 1987, pp. 120-125

[Sei90] H.Seidel. H.Riedel. R.Kolbeck. G.Mück. W.Kupke and M.Königer. Capacitive silicon accelerometer with highly symmetrical design, Sensors and Actuators. A21-A23, 1990. pp. 312-315

[Son97] Song C. Commercial vision of silicon based inertial sensors. Proc. of Transducers'97. Chicago. USA. 16-19 June 1997. pp. 39-842

[Spe88] R. Spencer. B. Fleischer. P. Barth ea., A theoretical study of transducer noise in piezoresistive and capacitive silicon pressure sensors. IEEE Transaction on Electron. Devices. Vol. 35. No.8. August 1988. pp.1289-1298

[Sta94] H.R.C. Strato. Glass technology: recess etching. electrode fabrication and anodic bonding. Master of Science thesis. Delft Technical University. August 1994

[Sto95] T. Storgaard-Larsen. Opto-mechanical accelerometer based on strain sensing by a Bragg grating in a planar waveguide. Ph.D.-thesis at Technical University of Denmark. ISBN 87-89935-02-0. December 1995

[Sto96] T. Storgaard-Larsen. S. Bouwastra. O. Leitisko. Opto-mechanical accelerometer based on strain sensing by a Bragg grating in a planar waveguide. Sensors and Actuators A52. 1996. pp. 25-32

[Str94] Strohmann M. Bley P. Fromhein O and Mohr J. Acceleration sensor with integrated compensation of temperature effects fabricated by the LIGA process. Sensors and Actuators A 41-42. 1994. pp. 426-429. Sensors and Actuators. A21-23. 1990. pp. 316-319

[Sus90] S. Suzuki. S. Tuchitani. K. Sato ea., Semiconductor capacitive-type accelerometer with PWM electrostatic servo technique.

[Sys72] P.H. Sydenham. Microdisplacement transducers. Journal of Physics E: Scientific Instruments. Vol. 5. 1972. pp.721-733

[Tak96] H. Takao, Y. Matsumoto, H. Seo ea., Analysis and design considerations of three-dimensional vector accelerometer using SOI structure for wide temperature range, Sensors and Actuators, A55, 1996, pp. 91-97

[Tak97] H. Takao, Y. Matsumoto, M.Ishida, A monolithically integrated three axial accelerometer using stress sensitive CMOS differential amplifiers, Proc.Transducers'97, Chicago, June 16-19, 1997, pp.1173-1176

[Tel91] C.R. Tellier, J.Y. Amaudrut, A. Brahim-Bounab, Dissolution slowness surfaces of cubic crystals: Part 2 Applications to class 2 3 and to combined etching and lithography techniques, Journal of Material Science 26, 1991, pp. 5595-5607

[Tel97] C.R. Tellier, S. Durand, Micromachining of (hhl) silicon structures: experiments and 3D simulation of etched shapes, Sensors and Actuators A60, 1997, pp. 168-175

[Ten89] L. Tenerz, Silicon micromachining with applications in sensors and actuators, Ph.D.-thesis, Uppsala University, ISBN 91-554-2418-X, 1989

[Ter88] S. Terry, A minature silicon accelerometer with built-in damping; IEEE solid-state sensor and actuator workshop, 1988, pp. 114-116

[Tir95] Tirole N, Hauden D, Blind P. Froelicher M and Gaudriot L, Three-dimensional silicon electrostatic linear microactuator ,Sensors and Actuators A48, 1995 , pp. 145-150

[Tsc91] T.Tschan, N.de Rooij. A.Bezinge. S. Ansermet. J.Berthoud. Characterization and modelling of silicon piezoresistive accelerometers fabricated by a bipolar-compatible process. Sensors and Actuators. A25-A27. 1991. pp.605-609

[Tsc92] T.Tschan. N.de Rooij. A.Bezinge. Damping of piezoresistive silicon accelerometer. Sensors and Actuators A32. 1992. pp.375-379

[Tsu87] M.Tsugai. M.Bessho. Semiconductor accelerometer for automotive controls. Transducers'87. 1987. pp.403-405

[Um90] A. Umeda. K. Ueda. Study on the dynamic force/acceleration measurements. Sensors and Actuators. A21-A23. 1990. p. 285-288

[Utt92] D.Uttamanchani. D.Liang. B.Culshaw. A micromachined silicon accelerometer with fiber optic interrogation. SPIE Vol.1793 Integrated Optics and Microstructures. 1992. pp. 27-33

[Vat85] S. Vatoux. Y. Combemale. E. Enard. J.M. Arnoux, M. Papuchon. Le couplage de l'énergie lumineuse entre guides optiques monomodes. in L'optique guidée et ses applications, edition Masson. 1985. p.668

[Vei95] T. Veijola. T. Ryhänen. H. Kuisma. J. Lahdenperä, Circuit simulation model of gas damping in microstructures with nontrivial geometries, Proc. Transducers'95. Stockholm. Sweden. June 25-29. 1995. pp. 36-39

[Vel96] Th. Velten. P.Krause. E.Obermeier. Two-axis micromachined accelerometer for gesture recognition. Proc. MircoMechanicsEurope'96. Barcelona, Spain, 21-22 October 1996. pp.247-250

[vKa95] R. van Kampen, Bulk-micromachined capacitive servo-accelerometer, Ph.D.-thesis, Technical University of Delft, September 1995

[Wa69] G. Wallis, D.I. Pommerantz, Field assisted glass-metal sealing, Journal of Applied Physics, Vol. 40, 1969, pp. 3946-3949

[We89] R. Wentworth, Theoretical noise performance of coherence multiplexed interferometric sensors, Journal of lightwave technology, vol. 7, no. 6, June 1989, pp. 941-596

[Wo97] D. Wood, G. Cooper, M. Yang ea., A monolithic three dimensional micromachined gyroscope, Proc. MicroMechanicsEurope'97, Southampton, UK, Sep. 1-2, 1997, pp. 164-167

[Yam90] K.Yamada, K.Higuchi, H.Tanigawa, A novel silicon accelerometer with surrounding mass structure, Sensors and Actuators A21-A23, 1990, pp. 308-311

[Yun92] W. Yun, R.T. Howe, P.R. Gray, Surface micromachined, digitally force-balanced accelerometer with integrated CMOS detection circuitry, IEEE, 1992, pp. 126-131

[Zhu92] F. Zhu, Developement of capacitive position transducers through a mechatronic approach, Ph.D.-thesis, Delft University of Technology, ISBN 90-9005114-7, April 1992, pp.41-81

11. Publications by the author (related to the work described in this thesis)

First author:

[1] G. Schröpfer, S. Ballandras, M. de Labachelerie, P. Blind, Y. Ansel, Fabrication of a new highly symmetrical in-plane accelerometer-structure by anisotropic etching of (100) silicon, Journal of Micromechanics and Microengineering 7, 1997, pp. 71-78

[2] G. Schröpfer, M. de Labachelerie, S. Ballandras, P. Blind, Collective wet etching of a 3d monolithic silicon seismic mass system, MME'97, Southampton, *UK*, September 1-2, 1997, pp. 43-46

[3] G. Schröpfer, W. Elflein, M. de Labachelerie, H. Porte, S. Ballandras, (100) silicon in-plane microaccelerometer with remote optical read-out based on coherence modulation, EUROSENSORS XI, Warsaw, *Poland*, September 21-24, 1997, pp. 1021-1024

[4] G. Schröpfer, W. Elflein, M. de Labachelerie, H. Porte, S. Ballandras, Lateral optical accelerometer micromachined in (100) silicon with remote read-out based on coherence modulation, Sensors and Actuators A68, 1998, pp. 344-349

[5] G. Schröpfer, M. de Labachelerie, S. Ballandras, W. Elflein, Y. Ansel, Neuartiger lateraler Beschleunigungssensor mit symmetrischem Design, MikroSystemTechnik'97, Chemnitz, *Germany*, October 13-14, 1997, pp. 131-140

[6] G. Schröpfer, M. de Labachelerie, S. Ballandras, P. Blind, Y. Ansel, W. Elflein, Vers des mesures accéléromètriques triaxiales au moyen d'un microdispositif en silicium, 8e Congrès International de Métrologie, Besançon, *France*, October 20-23, 1997, pp. 208-213

[7] G. Schröpfer, M. de Labachelerie, S. Ballandras, W. Elflein, H. Porte, 2D optical accelerometer with multiplexed distant read-out, MOEMS'97 International Conference on Optical MEMS and their Applications, Nara, *Japan*, November 18-21, 1997, pp. 126-131

[8] G. Schröpfer, M. de Labachelerie, S. Ballandras, P. Blind, W. Elflein, Y. Ansel, Accéléromètre triaxial micro-usiné sur silicium, journée club Nanotechnologie, Paris, *France*, November 19, 1997 et Second forum national ADEMIS, Paris, *France*, November 20-21, 1997

[9] G. Schröpfer, M. de Labachelerie, S. Ballandras, P. Blind, Collective wet etching of a 3d monolithic seismic mass system, Journal of Micromechanics and Microengineering 8, 1998, pp. 77-79

[10] G. Schröpfer, M. de Labachelerie, Y. Ansel, Investigations concerning the mechanical and capacitive sensitivity of a lateral bulk accelerometer, Proc. Micromechanics Europe'98, Ulvik, *Norway*, June 4-6, 1998, pp. 295-298 (also accepted for publication in Journal of Micromechanics and Microengineering)

[11] G. Schröpfer, M. de Labachelerie, Comparison between an optical and a capactive transducer for a novel multi-axial bulk-micromachined accelerometer, SPIE Conference on micromachined devices and components IV, Santa Clara, *California, USA*, September 1998, pp. 199-209

[12] G. Schröpfer, M. de Labachelerie, Multi-axial bulk-micromachined silicon accelerometers with capacitive or optical read-out, Proc. 4th Japan-France/ 2nd Asia-Europe Congress on Mechatronics, Kitakyushu, *Japan*, October 6-8, 1998

[13] G. Schröpfer, M. de Labachelerie, C. Tellier, Unconventional bulk-micromachining using underetching of (100) silicon planes, its fabrication tolerances and application to some MEMS and MOEMS, MicroSystem Technologies, Potsdam, *Germany*, December 1-3, 1998 also submitted to Journal of MicroSytemTechnologie (Springer Verlag)

Co-author:

[14] B. Romanowicz, Y. Ansel, M. Laudon, Ch. Amacker, P. Renaud, A. Vachoux, G. Schröpfer, VHDL-1076.1 modeling examples for microsystem simulation, 2nd workshop on libraries, component modeling and quality assurance, accompanying computer hardware description languages symposium'97, Toledo, *Spain*, April 1997

[15] Y. Ansel, B. Romanowicz, M. Laudon, P. Renaud, G. Schröpfer, Capacitive detection method for a silicon accelerometer by physical parameter extraction from finite element simulations, 1997 International conference on simulation of semiconductor processes and devices, Cambridge, MA, *USA*, September 8-10, 1997

[16] Y. Ansel, Ph. Lerch, Ph. Renaud, F. Paoletti, M-A. Grétillat, N.F. de Rooij, G. Schröpfer, S. Ballandras, M. de Labachelerie, C. Marselli, H.P. Amann, F. Pellandini, Simulation and design of a three axis navigation microsystem based on micromachined sensors, MICROSIM'97, Lausanne, *Switzerland*, September 17-19, 1997

[17] Y. Ansel, B. Romanowicz, P. Renaud, G. Schröpfer, Optimisation of a linear capacitive transducer for a silicon accelerometer by finite element simulation, EUROSENSORS XI, Warsaw, *Poland*, September 21-24, 1997, pp. 39-42

[18] Y. Ansel, B. Romanowicz, P. Renaud, G. Schröpfer, Global model generation for a capacitive silicon accelerometer by finite element analysis, Sensors and Actuators A67, 1998, pp. 153-158

RESUME

Cette thèse décrit une étude sur de nouvelles possibilités de micro-usinage de volume du silicium et ses applications aux accéléromètres multi-axiaux avec lecture capacitive et optique.
Le principe physique général des capteurs d'accélération est de mesurer le déplacement d'une masse sismique provoqué par la force inertielle. Différentes configurations mécaniques sont proposées. La combinaison de deux accéléromètres latéraux et d'un accéléromètre sensible selon la direction verticale dans le même substrat permet de mesurer des accélérations selon trois directions au moyen d'une puce monolithique. Chaque masse sismique est sensible à une seule direction.
Pour la fabrication, une technique non conventionnelle de gravure sur silicium a été développée. Les avantages du procédé sont la simplicité de la gravure en deux étapes, une orientation quasiment parfaite des dispositifs suivant les directions cristallines <100> du silicium, et une suspension symétrique des masses.
La conception, la modélisation et la simulation, puis la fabrication et la caractérisation expérimentale d'accéléromètres 3D capacitifs sont présentées. Les performances mesurées sont conformes aux estimations théoriques obtenues analytiquement ou par simulation numérique.
Pour mesurer les accélérations par une méthode optique, on a intégré une fibre optique dans une structure micro-mécanique d'accéléromètre. La méthode basée sur la modulation de cohérence permet une lecture à distance et permet en outre de multiplexer trois signaux issus des accéléromètres sur une seule fibre.
Une comparaison des accéléromètres capacitifs et optiques réalisés démontre qu'avec les deux capteurs on arrive à détecter des accélérations en dessous de 100 µg. Du fait de la similarité des performances obtenues par les deux techniques, le choix de la méthode de détection sera effectué en prenant d'autres critères en compte comme par exemplé le coût ou le domaine d'utilisation.

Mots-clés : Micro-usinage sur silicium, microsystèmes, accéléromètre, détection capacitive, détection optique, gravure anisotrope

ABSTRACT

This thesis describes the research work towards some new possibilities in silicon wet etching and their application to the design and fabrication of multi-axial accelerometers with capacitive and optical read-out.
The general principle of accelerometers is the measurement of displacement of a seismic mass due to the applied inertial force. Different mechanical accelerometer designs are proposed. Combining two lateral accelerometers and one vertically sensitive accelerometer in one substrate offers the three-dimensional measurement of accelerations with one monolithic chip. The movements of the seismic masses are purely translational and mechanical cross-sensitivities are very small.
For the device fabrication a non conventional silicon wet etching technique has been developed. The advantages of the process are the simplicity of the two step etching, the almost perfect orientation of the devices along the <100> directions of the silicon crystal, and the symmetrical suspension of the masses.
The design, modelisation and simulation, fabrication and also the experimental characterization of silicon capacitive 3D accelerometers. The measured accelerometer performance is very close to the theoretical estimations obtained analytically or by numerical simulations.
In order to measure accelerations optically, an optical fiber was integrated into a micro-mechanical accelerometer structure. The detection method based on coherence modulation allows the multiplexing of three sensor signals, and hence remote 3D acceleration sensing through one optical fiber link.
A comparison of the realized capacitive and optical accelerometer demonstrates that with both sensors acceleration below 100 µg can be detected. Since no technique results in fundamentally bener performance, the choice between each detection method will depend on other factors, such as cost and application requirements.

Keywords: Silicon micromachining, microsystem, accelerometer, capacitive detection, opticol detection, anisotropic etching